HEAT TREATMENTS OF A MICROWAVE SINTERED SILICON NITRIDE

THE EFFECTS OF HEAT TREATMENT CONDITIONS ON A MICROWAVE SINTERED SILICON NITRIDE CERAMIC

By

JOHN ALEXANDER NYCHKA, B.Sc.

A Thesis

Submitted to the School of Graduate Studies

in Partial Fulfillment of the Requirements

for the Degree

Master of Engineering

McMaster University

MASTER OF ENGINEERING (1999)
(Materials)

McMaster University
Hamilton, Ontario

TITLE: The Effects of Heat Treatment Conditions on a Microwave Sintered Silicon Nitride Ceramic.

AUTHOR: John Nychka, B.Sc. (Metallurgical Engineering, University of Alberta)

SUPERVISOR: Dr. D.S. Wilkinson

NUMBER OF PAGES: xiv, 267

ABSTRACT

The sintering of silicon nitride ceramics follows the rationale that the final mechanical properties of the material are directly linked to the thermo-mechanical history of the liquid phase of sintering. Post sinter heat treatments performed on the as sintered material have the potential to alter the character of the secondary phase, and therefore modify the mechanical properties of the material.

In the present study a mixed α/β SiAlON ceramic was manufactured by microwave sintering, then post sinter heat treated under various conditions. Analysis of the microstructure as a function of the heat treatment conditions of temperature, pressure, and time was performed using quantitative x-ray analysis, and scanning and transmission electron microscopy. The properties of hardness and fracture toughness were also classified as a function of the said processing conditions. Microstructural mechanisms responsible for the changes in mechanical properties were identified and their implications explored.

Increasing temperature and time were found to degrade the hardness of the material due to an increase in the $\alpha \rightarrow \beta$ phase transformation. Pressure was found to have no effect on the hardness.

The β SiAlON grain size increased with increasing temperature. The increase in grain size followed grain coarsening behaviour, and was found to effect a small increase in fracture toughness when time was increased from 30 to 120 minutes; longer times had no similar effect. The grain size was predicted to have increased significantly after long times, and remain unchanged as a function of pressure.

The secondary crystalline phase was discovered to be the most crucial microstructural parameter responsible for the fracture toughness. The chemistry and high degree of crystallinity of the secondary phase resulted in an intergranular fracture mode, which led to toughening by crack deflection, fiber pullout, and elastic bridging. The amount of secondary phase was found to decrease with increasing temperature and pressure, thereby reducing the amount of possible toughening, and causing a decrease in the fracture toughness.

The discoveries made in this study have resulted in the development of process optimization guidelines for the post sinter heat treatment of the current material.

ACKNOWLEDGEMENTS

Thanks to my wife, Sasha, who supported me emotionally and helped me get through the tough times of our being apart. Her love, caring, understanding, and the high value she places on education have been instrumental in my success as both a student and individual since we first met - with no exceptions to the past two years.

I am indebted to Dr. Wilkinson for all that I have learned under his excellent direction as a supervisor. I have learned by doing this thesis that the knowledge I strive to gain is not in a specific area; I strive to learn about the ways in which to gain knowledge about a subject that is new to me and others. Dr. Wilkinson is a steward of this ideology of higher education and I express my thanks for having me work under him.

My parents have been a great influence on my life. They were and always will be the first educators in my life. They prepared me for life, and still managed to remain interested in what I was doing, worry about my decisions, and dream of what I may become. They are amazing, and I hope that I will be as dedicated and attentive with my children.

I wish to thank Drs. Wilkinson, Henein, Corbin, and Apté for helping me with important decisions and questions about higher education. They have treated me as a friend and colleague throughout my university career, and their advice about graduate school, career paths, and life in general has been very rewarding and pragmatic.

Mr. Cal Tunney of MicroWear is very deserving of thanks, for his support during this project, and during the previous years that I have worked for him. His belief in me has opened a lot of doors, and what he has taught me from his vast technical business experience will help me tremendously. Special thanks to Rob Roy for all the useful planning and discussions we had, along with the sharing of knowledge. Our frequent discussions led to many breakthroughs in the understanding and improvements of the MicroWear material. And to Fraser McClure and Dave Allan who were full of good ideas and knowledge about the MicroWear process. Many others at MicroWear deserve mention for all their help during the fabrication process, but are too numerous to list. Thanks also to Glen Fitzpatrick of AMC for his contributions on the development and execution of plasma etching.

One word about the people that actually made things happen in practice: technicians. Without Dave Allan (MicroWear), Andy Duft, Chris Butcher, Fred Pearson, Klaus Schultes, and John Hudak (McMaster) none of this work would have been done as well, on time, or with as few problems as there were. Special thanks go to Fred for his *outstanding* electron microscopy abilities, and his patience and willingness to help. And to Andy, for keeping his cool when I would use the ultrasonic cutter for hours on end!

My peers have kept me focused, and allowed me to be defocused for short periods of time as well. I have had many useful and enlightening discussions with them about school, life, 'reading books', and 'modeling'. I have made friends for life here, as I

cannot see going to any conferences and escaping them! The A206 gang – many good times, I know that I won't find a better lab group.

Lest I be delinquent I must acknowledge my good friend from my alma mater, Virus – my cigar aficionado, they don't roll em' finer than you; Golden Boy – my Its buddy and 'lab safety' and 'photo-shop girl' co-writer and back up vocalist; Kev – my little Irish veggie, high five!; Gammer – da da da dah! the new and improved bad joke king (thank you, thank you very much); Tony – 'the recipe book' and fine microscopist; Jin – my Kung-Fu Novel Junkie; Denis – 'there is always a negative way of seeing things'; KTC without whom Chapter 4 never would have been written; Ben San and Boomer – my brothers in tough ceramics, 'if you want em'...talk to us'; and finally, Bubba, who proved me wrong many a time when I thought I didn't want to got out.

There are many others that made it an enjoyable and fruitful time – thanks to all, especially to the gals in the know: Betty and Veronika. I cannot leave out my friends from Germany, India, China, or Australia, as they have also made my stay at Mac rewarding.

Finally, I am grateful for the financial support supplied by MicroWear and NSERC over the course of this study. Special thanks to Ms. Nicole Viens at NSERC for her persistence and attention, which ensured that I had financial support from NSERC for this project.

TABLE OF CONTENTS

LIST OF TABLES

Chapter 3

Chapter 4

Chapter 5

Appendix B

Appendix C

Appendix D

LIST OF FIGURES

Chapter 2

Chapter 3

Chapter 4

Chapter 5

Appendix A

Appendix B

Appendix C

Appendix E

1. INTRODUCTION

Ceramics have been widely accepted as being useful engineering materials because of their high hot strength, high hardness, and good chemical resistance. With such properties, successful applications of structural ceramic materials include cutting tool inserts, wear parts, thermal barrier coatings, and turbine components. However, ceramics do not usually perform as well as desired because of their inherently brittle nature. For this reason the fracture behaviour of ceramics has been extensively studied, often times in the hope that variables associated with fracture behaviour can be controlled with processing techniques.

Materials known as silicon nitride ceramics exhibit particularly good mechanical and chemical properties when exposed to high temperature. However, as with many materials systems, the limits of silicon nitride ceramics lie in their thermo-mechanical processing history. The liquid phase sintering process commonly used to densify silicon nitrides presents a dilemma: the liquid left at the grain boundaries after densification, to a large extent, dictates the final properties of the ceramic. Thus, efforts have been made to develop processing conditions to try and eliminate the remnant liquid by transient liquid phase sintering or to try and alter the structure of the secondary phase by post-sinter heat treatments. The latter was the focus of this study.

The material used in this study was a microwave sintered silicon nitride produced at the MicroWear Corporation in Edmonton, Alberta. The composition used was MicroWear's own, which is used as a commercial cutting tool insert material in industry. In fact, the particular brand of cutting tool studied in this research has outperformed other silicon nitride based cutting tools in the high speed machining of gray cast iron. Thus, investigations of microstructural mechanisms that contribute to its excellent performance were of great interest to both the company and the field of silicon nitride research. Due to the link between microstructure and processing conditions, the effects of processing conditions on the microstructure were also of great interest.

As mentioned above, the investigation into post sinter heat treatments was the main thrust of this study. A better understanding of the behaviour of the secondary crystalline phases was sought, since these phases have great influence on the mechanical properties of the material. The post sinter heat treatment experiments performed in this study were based on the production conditions that were used when the research was executed. The main conditions that were varied independently were temperature and pressure, but some experiments were performed on the effects of time as well.

The main techniques used in the characterization of the microstructure were x-ray diffraction, and scanning and transmission electron microscopy. The x-ray diffraction analysis identified, and revealed trends in the amounts of the secondary crystalline phases as a function of the heat treatment conditions, along with the relative amounts of the α and β SiAlON phases. The secondary phases were also examined using HRTEM and

EDX analysis in order to determine their degree of crystallinity and chemistry. The β SiAlON grain size and distribution was quantified via SEM.

The results of the research have led to an understanding of how temperature, pressure, and time effect changes in the microstructure, and therefore properties. Thus, optimization of the material through adjustment of the processing conditions has been proposed. This research has resulted in changes in the processing conditions performed by MicroWear, and an improvement in the performance of the material has been realized.

2. LITERATURE SURVEY

The identification of unsolved problems in the literature is of particular importance when putting the current research into perspective. Obviously, it is meaningless to perform the same tests on the same material with the same techniques and find the same results! It is more meaningful to seek solutions to problems identified by others that have not been solved, while at the same time questioning the conclusions of others to determine whether or not they have merit, or hold true in a current work. Such a critical attitude is desirable for the sake of the advancement of knowledge.

In order to put the current work in context, and demonstrate why the research was performed, four general areas of the literature will be investigated: general history and definitions related to the field of silicon nitride ceramics, fabrication via liquid phase sintering including the effects of microwave heating, microstructural development as a function of thermo-mechanical treatment conditions, and finally, mechanical properties and their associated microstructural mechanisms in silicon nitride ceramics.

2.1 Brief History

Silicon nitride ceramics were first discovered near the end of the last century, as evident in a patent held by Mehner in 1895, but their use as engineering materials was not investigated until the 1960's [Messier and Croft, 1982]. The appeal of silicon nitride ceramics lies in their high thermal shock resistance, low density, high hardness, wear and chemical resistance, and good high temperature strength. Much research has been performed on this family of ceramic materials in order to optimize the properties, and processing routes.

The reason we call silicon nitride ceramics a family of materials is due to the fact that there are many variants. The manufacturing method most suited for producing silicon nitride ceramics involves the use of other ceramic additives, which form a eutectic liquid with the residual surface silica on the silicon nitride powder, thus allowing liquid phase sintering. The liquid phase has a tendency to react with the silicon nitride and form silicon nitride alloys by solid substitution. These alloys are termed SiAlONs when Al and O are in abundance in the liquid. The crystal structure of silicon nitride has two polytypes, the α and β phases, which can both substitute Al-O bonds in place of Si-N bonds and hence form a SiAlON. The β phase is limited to strictly Al and O substitution, whereas the α phase can also accommodate interstitial cations of radius up to 1.0Å [Ekström and Nygren, 1992].

Different degrees of substitution can be made in SiAlON ceramics depending on the initial starting composition of the powder. The ranges of room temperature substitution for the α and β SiAlONs are determined by the following chemical formulae:

$$\alpha\,\textit{SiAlON}\text{: } \mathbf{M_xSi_{12-(m+n)}Al_{(m+n)}O_nN_{16-n}}$$

where M is the interstitial cation, $0<x<2$, $1<m<2.4$, and $0<n<1.7$

βSiAlON: **$Si_{3-z}Al_zO_zN_{4-z}$**

where $0<z<2.1$

The α and β SiAlONs may also coexist in equilibrium, with some restrictions on their degrees of substitution. For instance, in order to have a mixed α/β SiAlON it is generally accepted that the value of x be less than 1/3 and z be less than 1 [Sun et al. 1991a and 1991b]. The reason for the constraints on the degrees of substitution is rooted in the α → β phase transformation that occurs above 1500°C via a dissolution-reprecipitation mechanism through the liquid phase [Messier et al., 1978; Clark and Thomas, 1987; Ordoñez et al., 1999]. For certain composition ranges (i.e. oustide of those listed above) it is possible to avoid, or fully complete the α → β phase transformation and obtain single phase α or β SiAlONs. The term 'single phase', however, does not take into account those phases formed from the liquid phase on cooling. The liquid phase cools and solidifies into an amorphous phase, or a refractory crystalline phase. Depending on the chemistry of this secondary phase different properties result.

The character of silicon nitride powder used can also affect the final phase composition and properties of the material. If for example a pure α phase silicon nitride powder is used, the α → β transformation produces rather elongated β grains with some residual α phase (SiAlONs or silicon nitride), the amounts of each depending on the time at temperature [Mitomo et al., 1995; Ukyo and Suda, 1996]. The elegant study of Lange (1979) demonstrated that the higher the initial α content of the starting powder, the higher the fracture toughness of the resultant material due to the higher aspect ratio of the elongated β phase. For high β content powders, relatively equiaxed β grains are produced since there is no transformation and little grain growth due to impingement [Lee et al., 1990; Wötting and Ziegler, 1986]. Alternatively, if a small amount of β phase is included with a balance of α phase powder a highly bimodal distribution of β phase results due to the seeding action of the β phase. Such seeding has been found to produce a small volume fraction of very large β grains and result in high toughness silicon nitride composites, as high as 11MPa√m [Li and Yamanis, 1989]. Typical values of very good toughness are in the range 8-9 MPa√m, so the promise of higher values is intriguing.

Although the α and β SiAlONs have similar properties, the α phase is harder than the β phase, so applications such as cutting tools and wear parts are more suited to higher α SiAlON content composites [Bartek et al., 1992; Ekström and Nygren, 1992]. However, the equiaxed α phase has a lower fracture toughness than the elongated β phase, so it is often common to have some β phase present in any applications requiring the high hardness of the α phase. Such is the case when considering mixed α/βcutting tool materials. The improved tool life and decreased wear rates of SiAlONs versus silicon nitrides has also been observed by Gnesin and Yaroshenko (1994) and Ekström and Nygren (1992). Thus, there is a driving force to developing mixed α/β SiAlONs for cutting tool applications, hence the impetus of the current study.

2.2 Liquid Phase Sintering

2.2.1 History

While the three main methods used to fabricate silicon nitride ceramics are reaction bonding, hot pressing and pressure/pressureless sintering, the current review will only deal with the latter. However, despite the differences between hot pressing and pressure/pressureless sintering, the process of densification is identical, namely liquid phase sintering. The fact remains that any applied pressure during hot pressing or pressure sintering contributes to some rearrangement of grains when a liquid phase is present.

Due to silicon nitride's covalent bonding attempts at achieving densification via solid state sintering have resulted in limited success [Messier and Croft, 1982; Ziegler et al., 1987; Šajgalik, 1991]. In fact, any densification observed in solid state sintering has been owed to a thin surface layer of SiO_2 present on the powder surface [Jack, 1978; Wötting and Ziegler, 1983]. This surface layer on the silicon nitride is a key factor in the success of liquid phase sintering, as it reacts with sintering additives to form a eutectic liquid at temperatures below the decomposition temperature of silicon nitride [Messier et al., 1978]. One of the first experiments to show that additives increased the amount of achievable densification via pressureless sintering was by Terwilliger and Lange (1975). Their study showed that pressureless sintering of silicon nitride powder (90vol%α and 10vol%β) with 5wt% MgO resulted in high sintered densities (90% theoretical) in the relatively short time frame of 15 minutes at 1650°C. They also found that increasing temperature and time were deleterious to the densification behaviour due to decomposition, which as they noted, went against the conventional wisdom regarding the sintering of powders.

Over time, different sintering additives have been investigated in the attempt to produce more dense materials, and more refractory grain boundary phases from the liquid of sintering. If one views recent literature, rare earth and aluminum oxides and nitrides seem to have resulted in the greatest success for both of the above problems, and fabrication of materials with these additives is receiving much attention of late [for example Huang et al., 1996; Huang and Chen, 1996; Haviar, 1994; Kleebe et al., 1999; Roseflanz and Chen, 1999]. These recent studies are also focussed more on mixed α/β SiAlONs as opposed to the earlier work on β SiAlON materials (when the existence of the α SiAlON phase was yet undiscovered). As mentioned in the previous section, the difference in the properties of α and β SiAlON phases results in a good combination of hardness and toughness, without hindering the ease of sintering. In addition to absorbing Al and O, α SiAlON can also absorb rare earth cations from the liquid phase, which makes it an attractive phase to exploit for transient liquid phase sintering, as well as altering the chemistry of the secondary phase during post sinter heat treatments.

However, the temperature stability of rare earth-doped α SiAlONs is of concern, thus prompting studies into other metal substitutes for the commonly used rare earths. Ca additives have been found to form Ca α SiAlONs, which interestingly, have been found to exhibit an elongated grain morphology [Wood et al., 1999]. This brand of α SiAlON opens even more doors for the exploration of sintering additives in the silicon nitride system.

The continuous investigations of different sintering additives over the few decades that silicon nitride ceramics have been explored has led to much insight regarding the phase compatibility, densification behaviour, and stability of the different secondary phases that may coexist with both α and β SiAlON over a fairly large range of compositions. The majority of the work done on mixed α/β SiAlONs has used conventional heating to perform liquid phase sintering. Post sintering heat treatments have also been limited to conventional heating methods, and have often used the application of pressure to further densify the ceramics, and to alter the secondary phase chemistry and crystallinity [for example Bartek et al., 1992]. This leads to the next topic of discussion, the effect of microwave heating on liquid phase sintering behaviour.

2.2.2 Microwave Sintering

When an alternative processing method is used in any well-established fabrication process one must always analyze its benefits, and its drawbacks. In the current study, an in depth review of the literature on microwave theory and sintering will not be presented, since the current study is more concerned with the effects of post sinter heat treatments using conventional heating methods. However, the fact that the current material was produced by microwave sintering necessitates some investigation regarding the effects of microwave heating on densification behaviour, grain size development, and mechanical properties.

The major driving forces behind the use of microwave heating in the sintering of ceramics have been its reduced energy consumption (cost savings), and different heating profile in comparison to electrical resistance heating. The selective nature of microwave-material interactions allows for volume heating of a ceramic body, circumventing the slow process of heat conduction from the surface of the part inwards [Sutton, 1993; Clark et al., 1993; Tiegs et al., 1991; Janney and Kimrey, 1988]. This direct heating is the source of the efficiency of microwave heating because the furnace itself is not required to be at the same temperature as ceramic load being fired [Janney et al., 1993].

Other results of microwave heating are the improved product uniformity and yields, improved or unique microstructures and properties, and the synthesis of new materials [Sutton, 1989]. However, in the comparison of the microwave heating to conventional heating, many factors need to be considered since claims of microwave enhanced diffusion, lowering of activation energies, and lowering of sintering temperatures have not been in good agreement between various researchers [Janney et al. 1993].

What has generally been accepted to be fact about microwave sintering is the faster rate of densification, and lower sintering temperatures when sintering ceramics via liquid phase sintering [Sutton, 1989; Janney and Kimrey, 1988; Varadan et al., 1988; Tiegs et al, 1993; Tinga, 1988; Binner, 1990]. However, the mechanisms responsible for these observations have received debate. Some claims discuss the possibility of enhanced grain boundary diffusion present due to a higher temperature at the grain boundaries [Tinga, 1993], whereas Johnson (1991) demonstrated that any such temperature difference between the bulk and the grain boundaries is negligible.

A report by Ahmad and Clark (1993) witnessed an enhancement of the diffusion and reaction zone of zinc oxide in polycrystalline and single crystal alumina. They proposed that lattice distortions, present only when microwave heating was used, was the mechanism responsible for the enhancement of reaction and diffusion. Freeman et al. (1993) also observed evidence of a microwave effect on ion transport in crystalline solids, but did not supply any possible mechanisms. They did however, show that there was no lowering of the activation energy of sintering, and suggested that inaccurate temperature measurement was to blame for earlier reports claiming microwave effects on activation energies [for example Janney and Kinmrey, 1990]. Of the reports on microwave enhanced diffusion during the microwave heating of ceramics considered here, the treatment of Katz et al. (1988) explored the fundamentals of diffusion, and how microwave interactions could, if at all, enhance diffusion. They proposed that any microwave effects would be smaller than an order of magnitude difference in the diffusivity. This is by no means a small effect, but is smaller than other researcher's claims of 2-3 orders of magnitude difference in the diffusivity. This result implies that earlier reported microwave enhanced diffusion may have had other variables contributing to the final observations. When one considers the differences in the experimental methods, temperature measurements, and raw material variations it is easy to see that such a wide spectrum of interpretations of the microwave heating of ceramics has been reported. It is therefore, very difficult to pinpoint the microwave effects on the sintering behaviour of ceramics. However, we can discuss the final results of the microwave effects on the microstructure, since there has not been much conflict in this area.

The presence of a reverse temperature profile across a bulk specimen being heated in a microwave field has been well established [Janney et al., 1993; Sutton, 1989; Clark et al., 1993; Johnson et al., 1993]. This temperature profile is a result of the penetration of microwaves into the body, and radiative losses from the surface. An interesting result of this temperature profile is the reverse porosity gradient observed as compared to conventionally fired ceramics [Plucknett and Wilkinson, 1994]. Another result of the temperature profile is the uniformity of heating, the uniformity in grain size, and a very fine grain size [ibid.; Varadan et al., 1988; Patterson et al., 1990]. However, one must realize that the fine grain size is merely an effect of the reduced sintering time required to achieve high density [ibid.; Tiegs et al., 1991].

Considering the present system, the short sintering time required by microwave heating is a direct result of the interaction of the microwaves with the sintering additives, and the furnace design. In order for densification to occur the sintering additives need to be liquid. The sintering additives used in the present study do not couple extremely well with microwaves at room temperature, (although do so more effectively than silicon nitride). Thus, an alternative method to microwave heating is required to raise the temperature of the ceramics to such a temperature where coupling becomes efficient. Hybrid heating is the solution to this problem. Hybrid heating employs either the use of electrical resistance elements or a susceptor (a material that couples well with microwaves at room temperature) to provide radiative heat to the ceramic load within the furnace. Both Oak Ridge National Laboratory and the University of Florida have done extensive research on these methods of hybrid heating. Such heating can result in the sintering additives melting in a very short time.

Since the microwaves penetrate the ceramic body the sintering aids are heated uniformly and the liquid forms simultaneously throughout the volume. The rapid formation of the liquid throughout the bulk causes particle rearrangement very early on in the sintering schedule. Since particle rearrangement offers the most significant percentage of total densification in liquid phase sintering [German, 1985] the observed densification rate using microwave heating is observed to be much higher than conventional heating. Observations that microwave heating could achieve comparable densities to conventional heating at lower temperatures were really just observations of faster liquid formation in the former, not that microwaves cause any great enhancement in diffusion. The liquid formation at any given point in time in conventional heating displays a radial dependence, as a time delay exists due to conductive heat transfer from the surface inwards.

With such rapid densification during hybrid heating sintering times can be as short as 30 minutes at temperature for some ceramics [Patterson et al., 1990]. The short time does not allow for significant grain growth to occur, so the final grain size is very fine (e.g. Plucknett and Wilkinson (1994) found the mean grain size to be 100nm in a microwave sintered β SiAlON ceramic). As already mentioned, another result of the rapid and uniform heating is that the variation in grain size is very limited.

The fine grain size present after microwave sintering has been found to be responsible for different final mechanical properties. While the hardness did not seem to be affected, Patterson et al. (1990) found that the toughness of microwave sintered aluminas were slightly higher than conventionally sintered aluminas processed at the same temperature. Their proposed explanation for this phenomenon was that microwave sintering caused differential heating rates between the grain boundaries and grain interiors, and resulted in their being higher residual thermal stresses, which contributed to toughening. This was proposed to counterbalance the fact that the grain size in the microwave sintered alumina was smaller (which should therefore have reduced the fracture toughness [Mussler et al., 1982]). The differential heating rate proposal seems reasonable when viewing the study of Tinga (1993) which discussed possible reasons why grain boundaries could be thought to have higher heating rates. However, Tinga did not make any conclusions as to the implications of the differential heating rates between grain boundaries and grain interiors.

While reports on the grain size of microwave sintered ceramics has been extensive, reports on the secondary phase chemistry and distribution have been minimal. Plucknett and Wilkinson (1994) found that the fine grain size of a microwave sintered β SiAlON was a major factor in there being proportionately more amorphous film present at two-grain junctions than in conventionally sintered materials with larger grain size. This was an important finding, which raised the question as to whether microwave sintered fine grained silicon nitride ceramics would perform well at high temperature.

The same study also investigated the effects of a conventional annealing treatment on the devitrification of the remnant amorphous phase from microwave sintering. However, no unusual behaviour in comparison to conventionally sintered material was observed, suggesting that microwave sintering is a viable processing method for achieving silicon nitride based ceramics with equal (or enhanced) properties compared to conventional process routes. It should be stated that early goal of microwave sintering was not to achieve superior properties, so much as it was to achieve similar properties at a reduce processing cost. The fact that some properties are enhanced by microwave heating is an added benefit worthy of investigation and exploitation.

2.3 Microstructural Development

The development of microstructure in silicon nitride ceramics has already been demonstrated to be dependent on the initial powder character, composition, and heating method during sintering. Other variables such as temperature, pressure, and time also have been found to affect the microstructure, so these will be reviewed next. In order to focus the review, the following will mainly discuss the microstructural development high α content powders with rare earth and aluminum containing additives.

2.3.1 Phase Equilibria

The first topic that must receive attention is the accepted phase equilibrium diagrams that are used in the study of silicon nitride ceramics. If one recalls, there are at least four ceramic compounds present in the prepared powder before sintering: silicon nitride, a residual layer of SiO_2 on the silicon nitride powder, a rare earth oxide or nitride, and an aluminum oxide or nitride. One can then infer that there are six potential components to be considered for the creation of a phase diagram: three elements, each existing as either a nitride or oxide (Si, Al, or R, where R is a rare earth metal; R=Y for the current study). Therefore, a complex problem exists for the two dimensional representation of such a multi-component system. Fortunately, a creative solution was proposed by Jänecke (1907) who realized that the R-SiAlON system could be represented graphically as a triangular prism, with the faces being pseudoquaternary diagrams, and the ends representing the nitrides and oxides of the three metallic elements (see Figure 2.1a). The necessary requirement of the Jänecke prism (as it is now termed) is that all edges of the prism are equal in length. This requirement is achieved by representing compositions in the prism in equivalents. To maintain electrical neutrality, each corner of the prism must have a valence balance of 12+ and 12- (e.g Si_3N_4: $3x4^+ + 4x3^- = 0$). Any section perpendicular to the major axis of the prism can then be thought of as a ternary with a fixed O/N ratio (the corners of which are the three metals of the system). The particular example in Figure 2.1 from Jack (1978) shows the point P with a valency composition of:

$$\mathbf{Mg^{6+}Si^{4+}Al^{2+}O^{6.6-}N^{5.4-}}$$

which corresponds to an atomic composition of:

$$\mathbf{Mg_{3.00}Si_{1.00}Al_{0.67}O_{3.30}N_{1.80}}$$

As one has most probably already presumed, a different prism needs to be constructed for each temperature that is of interest! Fortunately, the general phase equilibria for the

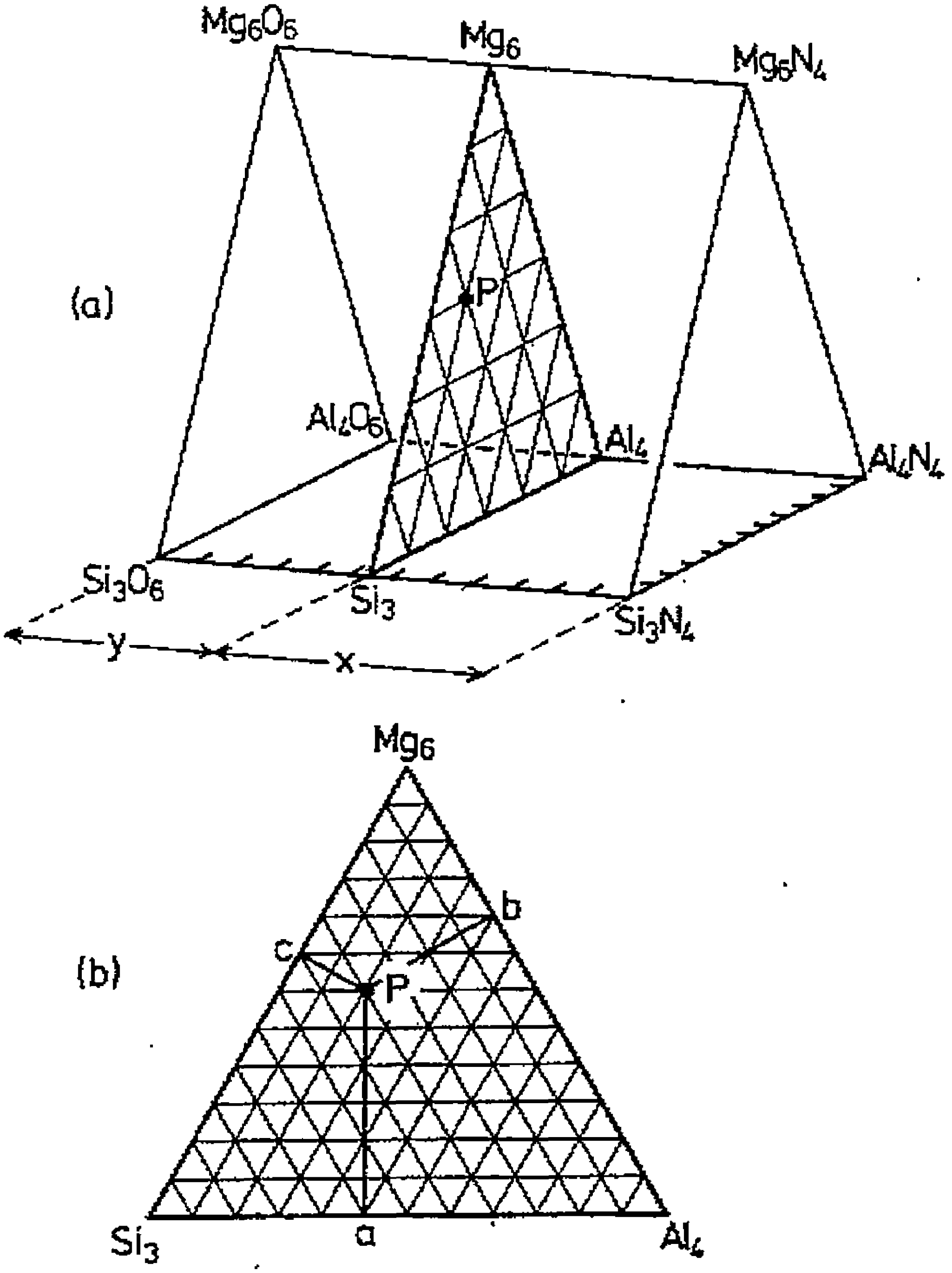

Figure 2.1: Illustrative example of representing a composition by a point P within the Jänecke prism of Mg-SiAlON [Jack (1978)]. See text for details.

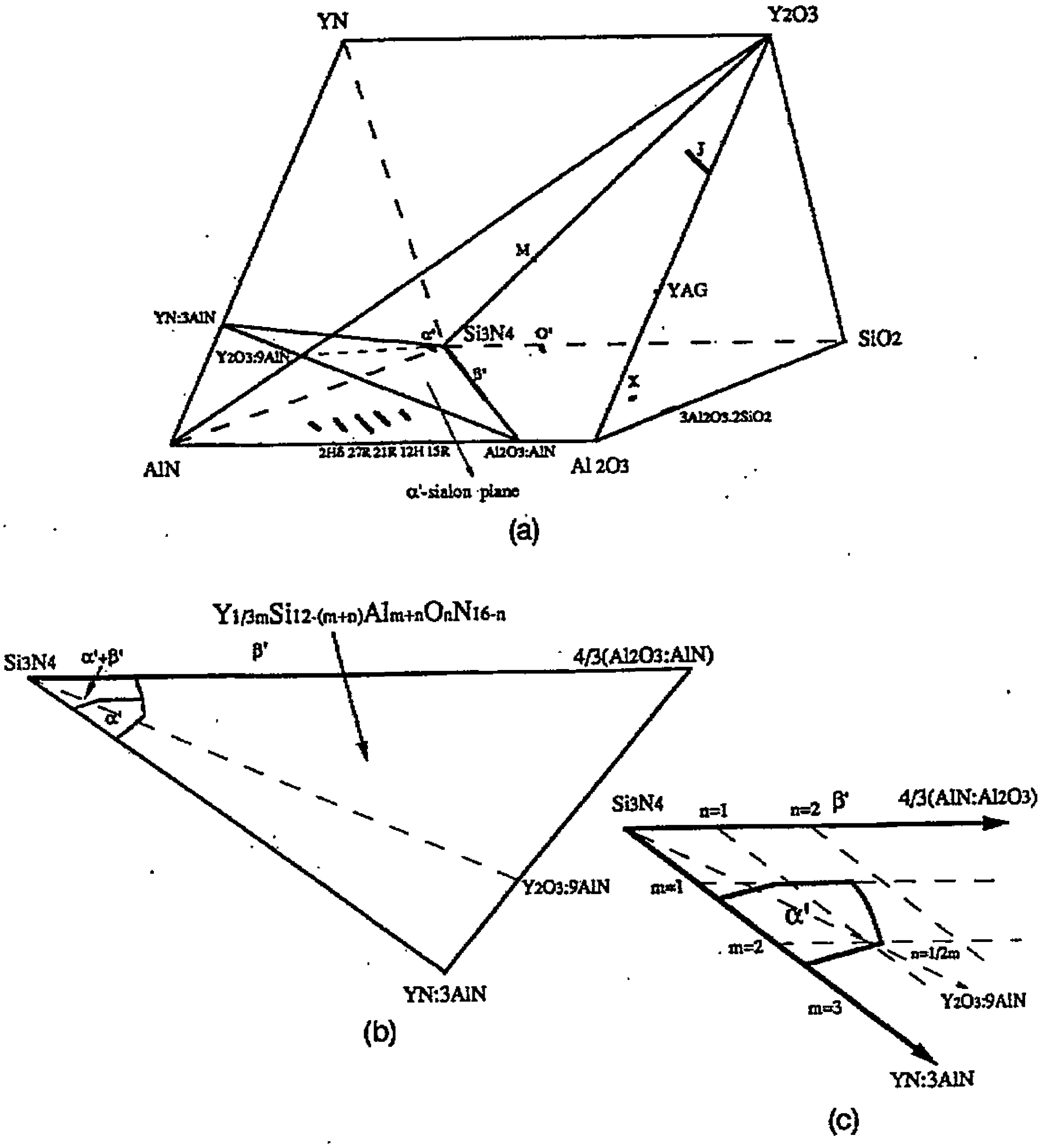

Figure 2.2. (a) Jänecke prism of Y-SiAlON system, (b) α SiAlON plane, and (c) enlarged corner of the α SiAlON plane.[Sun et al.(1991a)].

Y-SiAlON system has most commonly been represented at room temperature, and as Figure 2.2 illustrates, the system is usually plotted on one prism. Of course, with increased temperature some of the boundaries will shift, but it has generally been observed that the locations of the phases do not change drastically.

The region of the equilibrium diagram that is of interest to this study is the Si_3N_4 corner, and more precisely the α SiAlON plane. The composition for this study lies in the two phase α+β region near the corner in Figure 2.2. As one may imagine, this is a point in three-dimensional space, so the determination of phase compatibility also involves three dimensions. Compatibility tetrahedra have therefore been delimited to determine which phases are in equilibrium. The development of these tetrahedra is still fairly new (over the past decade) so there are many unanswered questions as to how the tetrahedra change with temperature. However, very recent research has been done on the high temperature phase stability of the α SiAlON phase with different rare earth metals [Rosenflanz and Chen, 1999]. This research has shown that the extent of the single phase α SiAlON region (as seen in Figure 2.2) enlarges with increased temperature, thus causing different phase assemblages at different temperatures. Such contributions to the field continue to be made, and the field of phase equilibria is still growing.

The effects of pressure on the phase equilibria have not been as well studied as those of temperature. Essentially, this is understandable, since the pressures usually used in the HIP'ing of silicon nitride ceramics do not exceed much more than 200MPa, and for the current study this is certainly true. However, the possibility does exist that high pressures may alter the equilibrium of the phase assemblage and cause resorption of particular phases, by a shift from congruent melting to incongruent melting behaviour of the secondary phases [Eitel, 1951]. Unfortunately, the complex nature of the phase equilibria does not allow for simple tests of this hypothesis.

2.3.2 The $\alpha \rightarrow \beta$ Transformation and β Grain Growth

As mentioned in section 2.1 the $\alpha \rightarrow \beta$ phase transformation is thought to occur via a dissolution reprecipitation mechanism. The rate-controlling step for the transformation has been debated due to observations by different researchers. The postulated rate-controlling mechanisms are either dissolution of the α phase, diffusion of Si and N through the liquid, or an interfacial reaction involving the β phase (i.e. the growth mechanism of the β phase). It appears that different researchers have obtained evidence that any of these rate-controlling mechanisms may be active depending on the slightly different experimental conditions, and the possibility that the rate-controlling step can change with varying conditions.

The recent work of Ordoñez et al. (1999) has shown the controlling step of the $\alpha \rightarrow \beta$ transformation in the system Si_3N_4-Y_2O_3-SiO_2 to be the dissolution of the α phase. This was inferred from the observed first order kinetics of α phase dissolution, and by the fact that the volume of liquid phase (intergranular phase) did not change with time. Explanation of the conclusions is rooted in the composition and amount of the liquid phase. The addition of Y_2O_3 to the system Si_3N_4-SiO_2 causes a decrease in viscosity of the liquid, and favours the precipitation of the β phase over Si_2N_2O. With the small amounts of liquid present in their study, Ordoñez et al. (1999) assumed that supersaturation of the liquid with Si and N occurred rapidly and therefore diffusion and nucleation of the β phase was not limiting. The constant volume of liquid was a necessary requirement to prove this; if diffusion or nucleation/precipitation of the β phase were rate limiting then there would be a period in time when the liquid volume would increase due to constant α dissolution. Another argument proposed was that a larger volume of liquid phase would result in different kinetics of the system, owing to a time lag in achieving supersaturation of the liquid phase. A potential drawback of comparing these findings to other studies is the requirement of the liquid phase composition to remain constant throughout the sintering process. In any system where the liquid composition changes, there is a greater probability to have a different rate-controlling step, such as an interfacial reaction, or diffusion.

Lee et al. (1988), and Kang and Han (1995) have shown that the β grain size is independent of the volume fraction of liquid phase, suggesting that an interfacial reaction controls the kinetics of the α → β transformation. The volumes of liquid studied were rather large at 20-50 and 10-30vol% respectively. Both research groups assumed that nucleation was not the limiting step since there were many nucleation sites available for the growth of β grains (either α or β Si_3N_4 particles within β SiAlON grains). By increasing the volume fraction of the liquid phase without altering its chemistry, it was found that the grain size of β SiAlON grains was unaffected. This observation was interpreted to mean that the growth of the faceted β grains was interface reaction controlled. If diffusion had been the rate-limiting step one can imagine that the grain size should have been smaller with an increase in liquid phase volume because of the longer diffusion path.

Considering the grain growth of faceted grains, Lai and Tien (1993) studied the kinetics of the anisotropic growth of β-Si_3N_4 which gives rise to its elongated morphology. These researchers found that the activation energies of grain growth along the c axis and the prism faces were different, the growth in the c axis being preferred. It was proposed that the growth on the prism faces required more energy due to their relative smoothness in comparison to the basal planes, which can exhibit screw dislocation and two-dimensional growth at lower driving forces. This finding also explains reports of the α → β transformation rate decreasing with time [Ordoñez et al., 1999; Krämer et al., 1993; Messier et al., 1978]. When the β grains grow along their c axis they will, at some point in time begin to impinge on each other, and become interlocked. Once a high percentage of the β grains exhibit this interlocking the growth along the c axis becomes extremely difficult, and the growth of prism planes becomes favoured. However, the activation energy is much higher for the prismatic growth, so the rate of growth decreases with increased time. A feature often seen in microstructures after long times at high temperature is the commencement of growth on the prism planes and a subsequent decrease in aspect ratio of the β grains with time [Ziegler et al., 1987].

From the arguments about liquid volume-independent grain growth and β grain growth mechanisms being crystallographic orientation dependent, it seems convincing that the rate-controlling step in the α → β transformation should be an interfacial reaction. However, reports by Krämer et al. (1993) and Kleebe et al. (1999) have proposed that the rate-liming step in the α → β transformation is dependent on the volume of liquid phase present. When the volume of liquid phase is small the liquid is no longer interconnected, and the diffusion path of Si and N is through the intergranular film between two-grain junctions. Diffusion is much slower through these partially ordered films, and so the grain growth is limited by diffusion [Krämer et al., 1993]. β grain growth is found to follow Ostwald ripening behaviour in materials with small volume fractions of liquid [ibid.; Kleebe et al., 1999].

2.4 Mechanical Properties

Rather than simply summarizing the values of the various mechanical properties that have been characterized throughout the literature, the scope of this section of the review will be on the specific properties of hardness and toughness, and their associated microstructural mechanisms. These properties are most responsible for the performance of a cutting tool material since the hardness correlates to the wear rate, and the toughness to the ability of the tool to withstand shock. Of course, the thermal shock resistance and high temperature hardness and strength are important properties as well, but the current study is focused on the room temperature property evaluation of materials, so these properties have not been included in this review. However, from room temperature investigations of the microstructure one can imagine that these high temperature properties can be predicted to a certain degree.

2.4.1 Hardness

Before identifying which microstructural characteristics have been found to affect the hardness of silicon nitride ceramics, it is useful to first discuss the general concept of hardness. As explained by Mott (1956), hardness is often thought of as a relative term; the hardest metal in the eyes of a metallurgist does not compare with the softest ceramic known to the ceramist. The ranges of hardness for metals and ceramics are rather different as well, because of their different structure.

The absolute hardness of materials can be directly compared when care is taken to follow a standardized method of hardness testing. For the case of engineering materials, the standardized test most common for the determination of hardness is the indentation hardness test.

Hardness is usually taken to be a material's resistance to permanent deformation or damage [ibid.]. With this in mind, the deformation and damage processes that occur in a given material will therefore directly contribute to its hardness. So, in fact, the hardness of a material cannot be thought of as being a distinct property, but rather a combination of other properties that exhibit mechanical responses. Properties that dictate the mechanical response of a material include, for example, the yield strength and elastic modulus. One must also consider that the hardness of a material can change as it is being tested [ibid.]. For the case of metals, strain hardening occurs as a result of hardness testing, and the hardness test itself changes the hardness of the metal examined [Tabor, 1951]. However, atomic bonding differences in the structure of ceramics do not usually allow for such strain hardening to be observed when testing the hardness of ceramics, and strain hardening can be assumed to be absent in silicon nitride ceramics.

While many more issues and examples could be found to demonstrate other general factors contributing to hardness, let us now turn to the specific material of study, namely silicon nitride based ceramic composites, and discuss their reported hardness behaviour. The two phases of silicon nitride (α and β) have been found to exhibit different hardness values, with the α phase being reported to be the hardest [Ekström and Persson, 1990; Jack, 1986; Ekström and Ingelström, 1986; Ekström and Olsson, 1989]. When considering only the α phase Reimanis et al. (1996) found that the hardness of single crystals of α silicon nitride (grown by chemical vapour deposition (CVD)) ranged from 26-36GPa, as measured by the Vicker's microindentation technique (crystallographic orientation was responsible for the range of hardness). Dense polycrystalline single-phase α and β silicon nitrides (also produced by CVD) have been measured to have hardness of 32-42GPa and 21-32GPa respectively at room temperature [Ekström and Persson, 1990]. These hardness' are similar to those of single crystals, but no explicit reasons for the variation in hardness of polycrystalline materials were found in this review. The possibility of preferred crystallographic orientation during deposition could cause some variation in hardness. Another variation in hardness could have been the loads at which the tests were done; when examining hardness data, one should always ascertain what load the tests were done at, as numerous reports have shown that increasing loads yield lower hardness values [ibid.; Mukhopadhyay et al., 1990].

For this review we must also consider the fact that secondary phases may be present in the microstructure, and that the major phase composition of interest is a mixed α/β SiAlON composite, not a polycrystalline single phase ceramic as described above. Reported cases for the hardness of polycrystalline α or β SiAlON ceramics containing an intergranular glassy phase, were found by the author to be ~70% of the polycrystalline single-phase values. The hardness of α/β SiAlON composites has been found to be a function of the α/α+β phase ratio [Ekström and Persson, 1990] with the hardness increasing approximately linearly with increasing α/α+β ratio from about 1500-2000Hv (16-21GPa) for α/α+β = 0–1 respectively [Ekström and Nygren, 1992]. Notice that this range of hardness is extremely small. Also of note is that all the hardness data reported in the literature was from materials manufactured by either hot pressing, or HIP'ing, and no microwave sintered data was found.

Although the most significant factor for explaining the hardness differences between high and low content α SiAlONs, the α/α+β ratio is not the sole microstructural characteristic responsible for hardness. As already mentioned the additional presence of an intergranular glassy phase caused a reduction in the hardness of polycrystalline α or β silicon nitrides. Presumably, the decrease in hardness was observed because the strength of the grain boundaries was lower with the presence of the intergranular glassy phase. Similarly, the presence of another crystalline phase at multigrain pockets could be hypothesized to affect the hardness by the same argument.

From a different perspective, Bartek et al. (1992) and Ekström and Persson (1990) discovered that factors such as increasing grain size and degree of subsitution of β

SiAlONs caused decreases in the hardness. It should be mentioned, that these two effects are inseparable, since higher degrees of substitution in β SiAlONs also cause increased grain growth during sintering [ibid.; Lee et al., 1988; Kang and Han, 1995].

Thus, when considering all these microstructural factors one can infer that the microstructural characteristics of importance regarding the hardness of α/β SiAlONs are the α/α+β ratio, the grain size (of both α and β SiAlON), the degree of substitution of the β SiAlON phase, the presence and potentially the thickness of an intergranular film, and the presence, distribution, and amount of a multigrain junction pocket phase. The areas of interest regarding microwave sintered silicon nitrides are therefore seen to be the effect of small grain size on the hardness, and the nature of the secondary phases.

2.4.2 Toughness

The general fracture behaviour of ceramic materials has been well studied, with no exception to silicon nitride ceramics. Many researchers have investigated silicon nitride based ceramics to determine the apparent fracture mechanisms, and toughening mechanisms present as functions of the processing conditions [Lange, 1973; Himsolt and Knoch, 1979; Li and Yamanis, 1989; Beals and Bar-on, 1990; Becher et al., 1995; and Kleebe et al., 1999]. The results of most of the fracture investigations cited here were obtained from high content low substitution β SiAlONs with minimal amounts of grain boundary phases (amorphous as opposed to crystalline). These studies declared that the size and morphology of the β phase was the critical parameter that dictated the final fracture toughness of the material. High aspect ratio and large diameter β grains were found to yield the highest fracture toughness values for these silicon nitride ceramics. The mode of fracture found in most cases was intergranular fracture. The observed toughening mechanisms were crack deflection by large elongated β grains, grain debonding, elastic bridging and pullout, and fiber rupture. For all of these mechanisms a larger grain size was found to enhance their toughening effects (assuming no large differences in thermal residual stresses due to a larger grain size). The reader is referred to treatments by Mussler et al., 1982; Rice et al., 1981; Rice and Freiman, 1981; Becher, 1991; Nair, 1990, Becher et al., 1991; and Becher et al., 1988 for detailed descriptions of the effect of grain size on fracture toughness for the above mentioned microstructural toughening mechanisms.

Most investigations concerned with the fracture of fiber reinforced ceramics (in situ or otherwise) have simply mentioned that the composition of the intergranular phase was thought to be important for determining the bebonding and pullout behaviour of the elongated phase. Some treatments on this subject have given more attention to the nature of the intergranular phase [Becher et al., 1995 in particular]. However, the recent study of Kleebe et al. (1999) took an in depth approach to the fracture behaviour of silicon nitride ceramics with the intergranular phase character in mind. While Kleebe et al. (1999) realized that the grain size and morphology of the β phase were important in determining a certain level of toughening, their study focused more on the evolution of the microstructure as a function of secondary phase composition to ultimately show that the limiting variable on the fracture toughness was rooted in the secondary phase chemistry.

The conclusions made by Kleebe et al (1999) were similar to other studies in that the grain morphology was found to influence the toughness. However, they demonstrated that the chemistry of the secondary phase affected the morphology of the grains, the degree of crystallization of the secondary phase at triple pockets, the development of residual stresses in the glassy intergranular phase, and altered the chemistry of the amorphous intergranular phase. Thus, as was proposed by Becher et al. (1995) the nature of the intergranular phase needs to be well characterized when attempting to describe the fracture behaviour of in situ fiber reinforced composites such as the silicon nitride ceramics.

2.5 Summary

The research done on the sintering of silicon nitride in the past thirty or so years has discovered much in the areas of densification, additive chemistry, secondary phase compatibility, microstructural development, and mechanical properties. It is well known that in order to achieve highly dense, high performance silicon nitrides that oxide and nitride ceramic additives of rare earths, aluminum and calcium can be used. However, the proportions of these additives are still being explored at present to determine optimal powder compositions, which will lead to better overall processing behaviour and mechanical response. Therefore, the area of composition development is one that offers investigation.

The study of the processing methods of silicon nitride ceramics will always be present, partly due to the fact that the final phase composition of the microstructure is process-path dependent and because more efficient, effective, and less costly ways of fabrication are sought in any manufacturing process. Particular areas that have been identified as being important are the time, temperature, and pressure at which processing is carried out. Of these areas, time and temperature have received the most attention, allowing the variable of pressure to be explored further.

While the microwave sintering of ceramics has been studied extensively, there are many questions about it that remain to be answered. For instance, the possible enhancement of diffusion due to microwaves is still disputed. The microstructural evolution of microwave sintered silicon nitride ceramics has been well characterized in terms of the grain size and porosity for β SiAlONs. However, less numerous investigations of mixed α/β SiAlONs via microwave sintering allow for some advancement of knowledge to be made on these materials. Not many commercially microwave sintered silicon nitride ceramic cutting tools exist at present, but the higher hardness of microwave sintered α/β SiAlONs warrants some investigation into the mechanisms of hardness in these materials.

The uncertainties in the mechanisms of β grain growth as a function of volume of liquid phase, and chemistry of the liquid phase reveal an area where progress could be made in the study of silicon nitride ceramics. Essentially, studies, that are more specific, need to be performed to elucidate the volume fraction at which there is a shift in the rate-controlling step in the $\alpha \rightarrow \beta$ phase transformation, or to determine the effects of the chemistry on the rates of transformation along with differing volumes of liquid phase.

The mechanical properties of hardness and toughness are key issues to the success of ceramics in the future. The microstructural mechanisms that account for these properties are of extreme interest to the field of silicon nitride ceramics as well. Although there are generally accepted theories on the mechanisms responsible for the hardness of mixed α/β SiAlONs, there is always the potential that certain systems behave slightly differently due to the complex interaction of other properties and hardness. The toughness of silicon nitride ceramics has been well studied, and the toughening mechanisms identified. This is not to say that everything is known concerning the effect of secondary phase character on the toughness. Similar microstructures may have the same aspect ratio, volume fraction of β phase, and same amount of secondary phase, but the fracture toughness can be drastically different due to the chemistry of the secondary phase. Thus, more investigation into alternate grain boundary phases must be researched along with processing methods required to optimize their toughening effects.

The current work involves investigation into some of the unsolved problems in silicon nitride ceramics highlighted above. In particular, the current study is an investigation of a microwave sintered mixed α/β SiAlON, known to have a higher hardness than predicted by current theory. Therefore, discovery of the mechanism that creates this outstanding hardness behaviour is of great interest to the field.

The effect of post sinter heat treatment conditions on the microstructure and properties of a microwave silicon nitride is of interest in order to determine the response of the material, and compare it to conventionally prepared materials. This evaluation of microwave sintered materials is necessary to determine whether microwave heating is a superior processing route, or simply an alternative route. In addition, the characterization of microwave sintered materials will allow potentially different applications to be developed to capitalize on their unique properties.

3. EXPERIMENTAL

This chapter deals with the experimental design and procedures undertaken during the course of the thesis research. While many techniques and processes were employed during the research five main sections are presented in this chapter: experimental design, specimen fabrication, property evaluation, materials characterization, and error analysis.

All of the specimen fabrication and bulk of the property evaluation was done at The MicroWear Corporation's facilities in Fort Saskatchewan and Edmonton, Alberta. The remainder of the work (unless otherwise mentioned) was done at McMaster University in Hamilton, Ontario. Any work the author commissioned, or had assistance with is noted where appropriate.

3.1 Experimental Design

As was previously mentioned, the primary goals of this work was to learn how the post sinter heat treatment conditions affect the microstructure and mechanical properties of a microwave sintered silicon nitride based ceramic. In order to fulfill this goal HIP experiments had to be performed that would allow for independent classification of the results of pressure, temperature, and time. Time was chosen to be a control leaving pressure and temperature as variables. However, neither the temperature or pressure were varied simultaneously; HIP tests were done under either isochronal and isobaric, or isochronal and isothermal conditions.

3.1.1 Selection of HIP Conditions

There were six primary conditions selected for this study: one sintered condition and five HIP treatments. At the time of the testing the standard production parameters were 120 minutes at 1800°C under 30000psi (207MPa) Argon (from a cryogenic source). This condition was chosen to be one of the heat treatment conditions, and the time of 120 minutes was maintained throughout the remainder of the tests. Temperatures above and below the sintering temperature were chosen, whereas all pressures chosen were above ambient pressure (i.e. the sintering pressure). Figure 3.1 shows the HIP conditions (sample sets 2-6) along with the sinter conditions (sample set 1 (SS1)). Note that the time at temperature is 120 minutes for all HIP conditions and only 15 minutes for the sintered samples.

The HIP temperatures were chosen in part due to equipment constraints, literature reports of the silicon nitride decomposition temperature, and α/β phase transformation temperature. The maximum temperature that the HIP equipment could safely and consistently reach was 1800°C, so this was chosen as the maximum (25°C above the sintering temperature). This maximum is less than the silicon nitride decomposition temperature of around 1900°C [Messier and Croft, 1982; Jack, 1976].

In an attempt to isolate the α/β phase ratio as a contributor to the properties of the material the minimum HIP temperature was chosen to be 1500°C. Since the α/β phase transformation proceeds at temperatures in excess of 1500°C [ibid., Messier et al., 1978], it was thought that at the low temperature condition (SS 5, Figure 3.1) little or no phase transformation would occur. Without little of the α/β phase transition occurring at this temperature any changes in the microstructure would be most likely limited to secondary phases, thus any differences in the properties would not be associated with a drastic change in the ratio of α to β phases.

It should also be mentioned that MicroWear was conducting some similar research at the same time as this study. In addition to the conditions mentioned above MicroWear was also interested in conditions that varied the time, and temperature and pressure simultaneously. As a manner of curiosity and completeness for this work some smaller sample sets (microstructural samples (MS)) were included in these additional conditions, seen in Figure 3.2.

3.1.2 Selection of Sample Type

Being that MicroWear produces cutting tool inserts the natural choice for the specimen geometry was a cutting tool insert. The geometry of the cutting tool insert chosen for study was essentially a rectangular prism, (termed LNU in the cutting tool industry). The standard LNU thickness was halved for this study. The thickness was changed for two reasons: the parts would not be mistaken for production parts, and if future flexure bars were to be made the thinner parts would require significantly less machining and grinding. A modified LNU is seen in Figure 3.3.

The basis behind the selection of the LNU was the fact that it was the largest possible insert MicroWear could press (longest and widest, with variable thickness). The large size of the insert afforded the possibility of sectioning the specimen into different pieces for independent chemical and physical analyses, while leaving enough material for the possibility of making flexure bars. However, as it turned out, no flexure bars were made in this study.

3.1.3 Population Size

The most critical factors determining the number of samples to be prepared for this project were the need to have all samples from a single sinter run, to have all samples fabricated from a single batch of raw material, and to have more than enough samples than was thought to be necessary.

Initial estimates on the number of samples needed were based on indentation, or single edged-notched beam (SENB) fracture testing of flexure bars. Going by the tests of Lawn [Lawn, 1975], it was decided 40 or so samples were needed to characterize the material using indentation toughness testing: 15 samples under no indentation load, plus 5 samples each at 5 different indent loads. Since six conditions were decided upon (as sintered and 5 HIP'd), this meant that a minimum of 240 bars would be needed. Adding 10% for possible specimen breakage prior to testing, a total of 260 bars would be needed. At 3 bars per LNU this meant that 90 bars would be needed. Thus, 15 LNU's per heat treatment condition would satisfy the requirements for statistically necessary sample size.

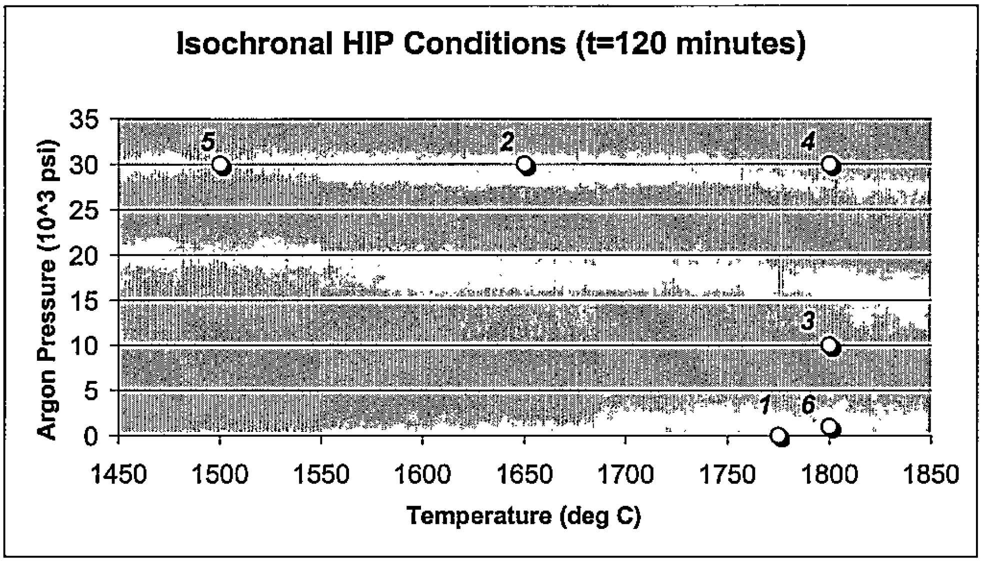

Figure 3.1. Isochronal HIP conditions, showing isothermal and isobaric nature of the sample sets. The sintered condition (sample set 1) is also indicated.

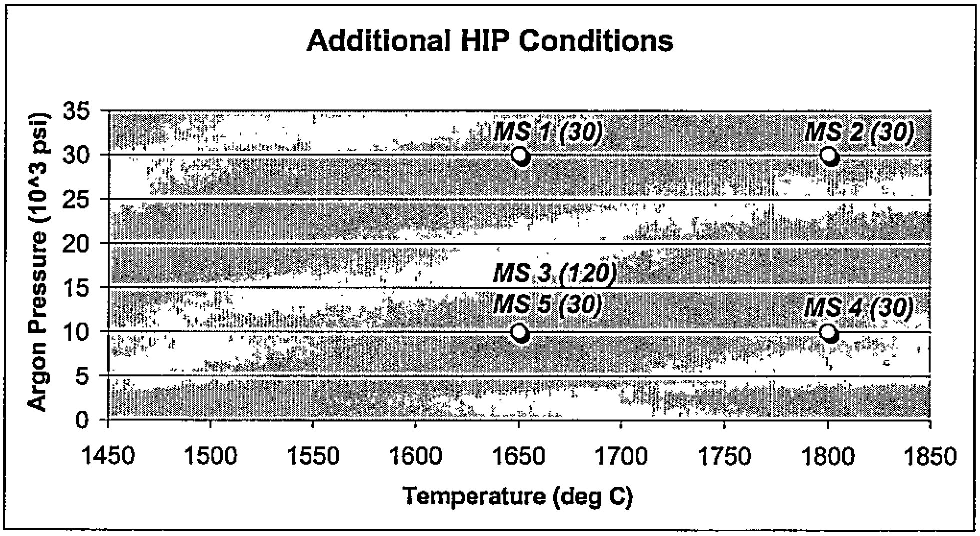

Figure 3.2. Additional Isochronal HIP conditions (time at temperature in parentheses).

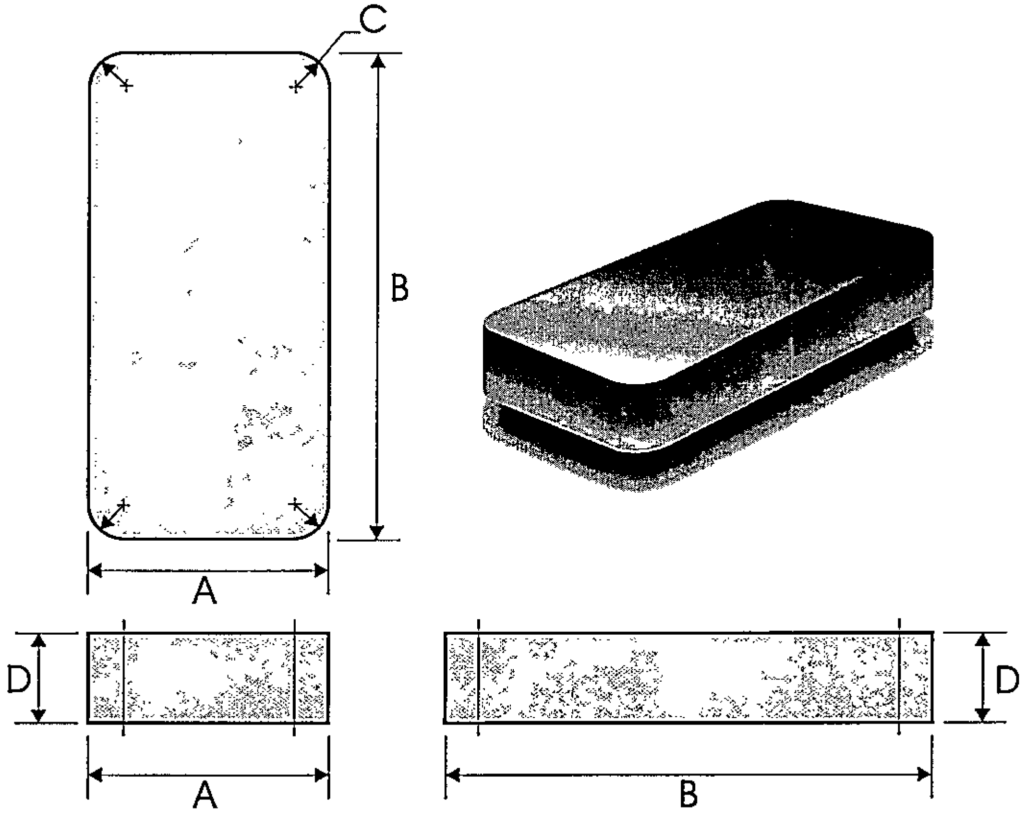

Dimension	Pressed Value (mm)	HIP'd Value (mm)
A	25.63 ± 0.10	20.07 ± 0.08
B	49.91 ± 0.10	39.12 ± 0.08
C	4.66 ± 0.10*	3.64 ± 0.08**
D	9.10 ± 0.20	7.10 ± 0.16

* Not measured, taken from die drawings

** Calculated based on 22% linear shrinkage from pressing

Figure 3.3. Schematic of the LNU specimen geometry with approximate dimensions after pressing, and after HIP'ing. The approximate linear shrinkage from pressing through to HIP'ing is 22%.

In practice however, there were other constraints on the number of samples to be prepared: the size of the microwave sintering furnace, and the attempt to maintain typical production run parameters. Based on production sinter schedules the size of the furnaces at the time of the fabrication allowed for approximately 3kg of pressed parts to be sintered successfully. At approximately 19g each, 153 LNU's could fit in a single sinter-run. This more than satisfied the statistical requirements for the number of samples, and allowed for extra samples in the case of unexpected circumstances. As a further precaution, two sinter runs were decided upon – albeit they would have to be treated as independent experiments if the second were to be used.

3.2 Specimen Fabrication

This section is a general chronological description of the methods practiced by MicroWear in the fabrication of silicon nitride based ceramic cutting tool inserts. The following procedures were followed for the synthesis of the materials studied in the present work. A flowchart of the process can be seen in Figure 3.4.

Standard procedures, such as milling and powder pressing, are summarized with the minimum information required to duplicate the specimens. Intellectual property issues concerning the powder composition and the microwave furnace design do not allow for detailed description in this thesis.

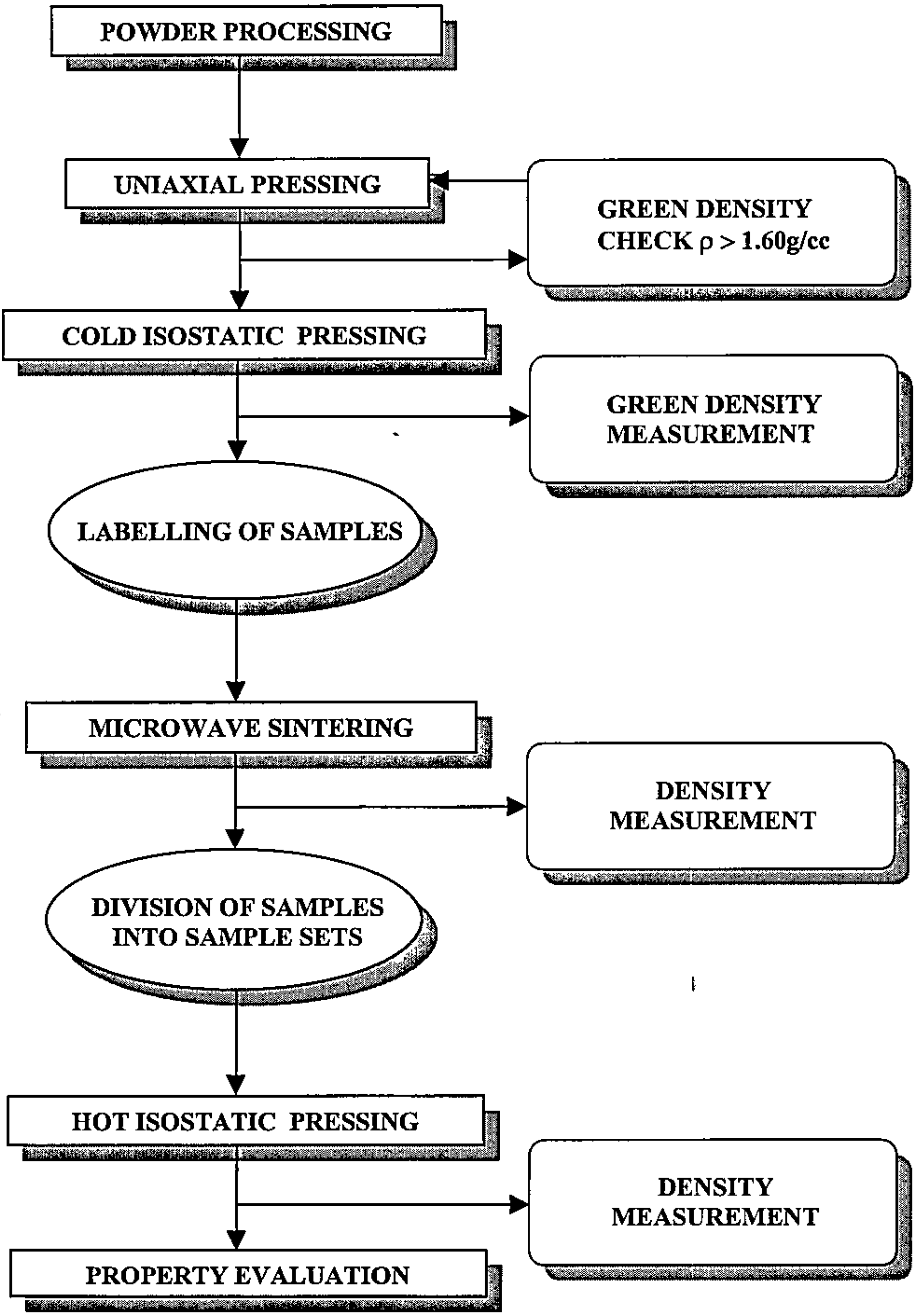

Figure 3.4. Flowchart of the fabrication process up until Property Evaluation. Note the points in the process where the density is taken to ensure quality control.

3.2.1 Powder Preparation

The author did not participate at all in the preparation of the ceramic powder used in the fabrication of the material studied. The powder used in this study was made by MircoWear staff with their established wet powder preparation procedure. This procedure involved the milling of silicon nitride powder (UBE SN-E10) with approximately 10 total wt% ceramic additives (high purity Y_2O_3 and an aluminum containing compound) plus polymeric lubricants and binders in hexane for 48 hours. The solvent was evaporated and the powder screened.

As mentioned above, 3kg of inserts could be successfully sintered in one run. The batches of powder that MicroWear produced at the time were on the order of 5kg. This meant, considering some powder was needed to set up the press, that only one batch of powder could be used per sinter run. Since two sinter runs were carried out, two random powder batches were selected, one for each sinter run: powder #746 and powder #753. However, all results, discussion, and conclusions presented hereafter are centered on samples made from a *single* batch of powder (powder #746). The samples made with powder #753 were not used in any form in the present work and will not be mentioned again, but information about their fabrication can be found in Appendix A.

3.2.2 Pressing

A uniaxial 30-ton Hydramet Press equipped with tungsten carbide die faces was used in the manufacture of the modified LNU inserts. Pressing was carried out with the assistance of MicroWear staff.

From production experience, the necessary pressed density had to be greater than 1.60g/cc. The 160 LNU's produced had a pressed density of 1.61g/cc, determined by the following equation:

$$\rho = \frac{m}{[(l * w) - 0.17] * t} \tag{3.1}$$

where m is the mass [g], and l,w, t are the length, width, and thickness of the LNU [cm] as measured with digital calipers. The compaction pressure was 128 MPa.

3.2.3 Cold Isostatic Pressing

Following uniaxial pressing the LNU's were cold isotsatically pressed (CIP'd) in an ABB Autoclave Isopress to affect a green density increase that cannot be achieved by uniaxial pressing. CIP'ing increases the value of the density, but more importantly it reduces the density gradients created in uniaxial pressing so that sintering will not create any warpage. The CIP process is essentially an immersion of green ceramic pieces in an incompressible fluid (water) that is pressurized, resulting in a uniform compaction and subsequent densification. This process was done with the assistance of MicroWear staff.

Green inserts were placed in watertight latex tubes and immersed in water, which was then pressurized to 345MPa. Using Equation 3.1, the CIP'd density for the LNU's was 1.84g/cc, a 12.5% increase over uniaxial pressing.

Following CIP'ing the LNU's were placed in a dessicator until microwave sintering occurred approximately 18 hours later.

3.2.4 Specimen Labelling

After investigating how the LNU's were going to fit into the furnace, a labelling system was devised so that every LNU's position would be known. The samples were labelled by scribing each end with an identification number so that sectioning would not result in misidentification.

The identification number included four pieces of information: the sinter run (A or B, A for powder #746), the furnace level (bottom = 1, top = 2), the column number (1 through 7 for the bottom and 1 through 10 (0) for the top), and the row, or layer number (1 though 9 for both bottom and top). For example, the identification number **A25-6** correlates to a specific LNU made from powder #746, on the top level, in column 5, sixth from the bottom. This information is more meaningful with the aid of a visual map, seen in Figures 3.5 and 3.6.

Note that there are 90 parts on the top level and 63 on the bottom, equaling 153 parts. It was known that the sinter density of the bottom level was slightly higher than

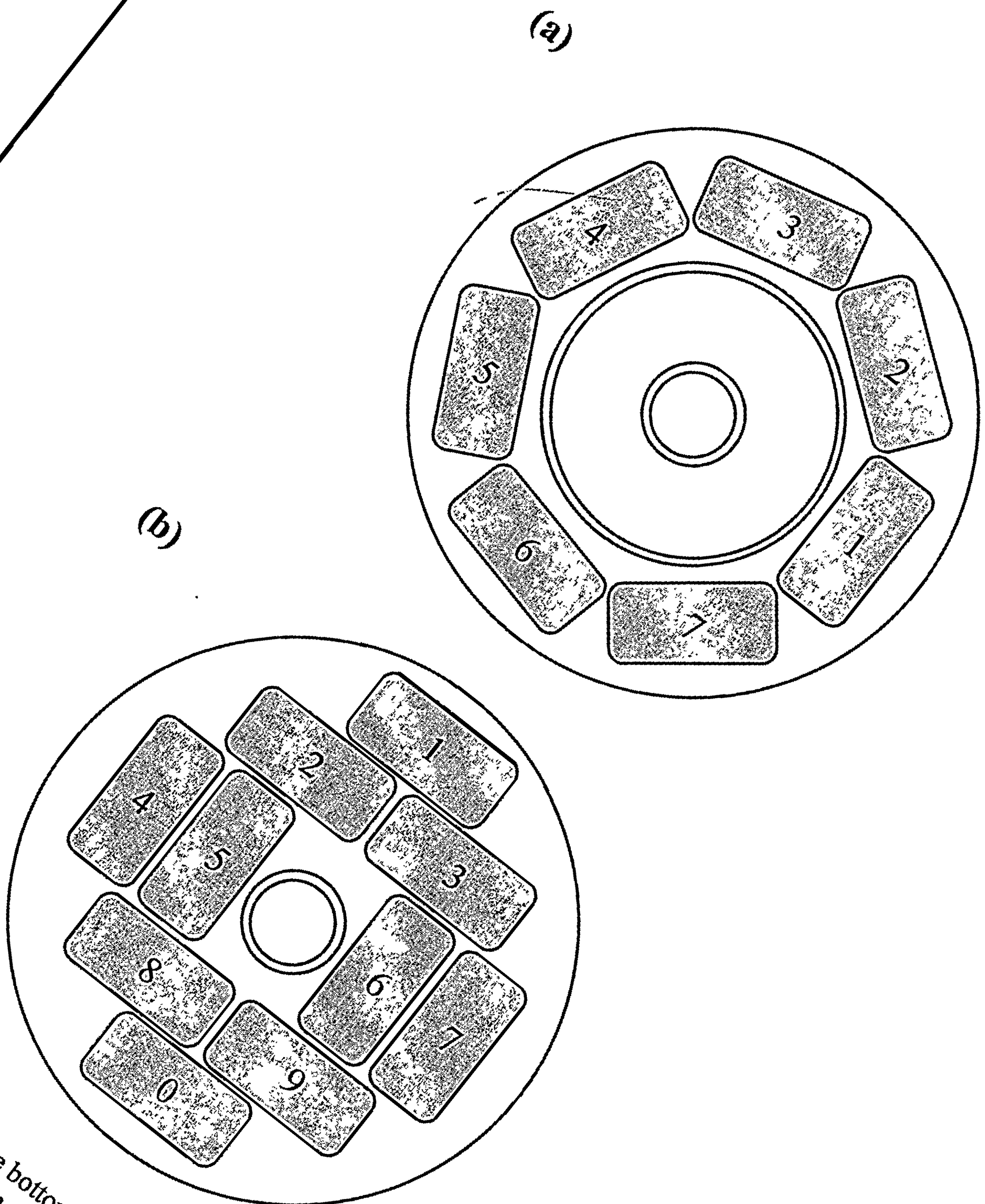

Figure 3.5. Plan views of the bottom (a) and top (b) levels of the furnace, showing the LNU column configuration, and column numbers.

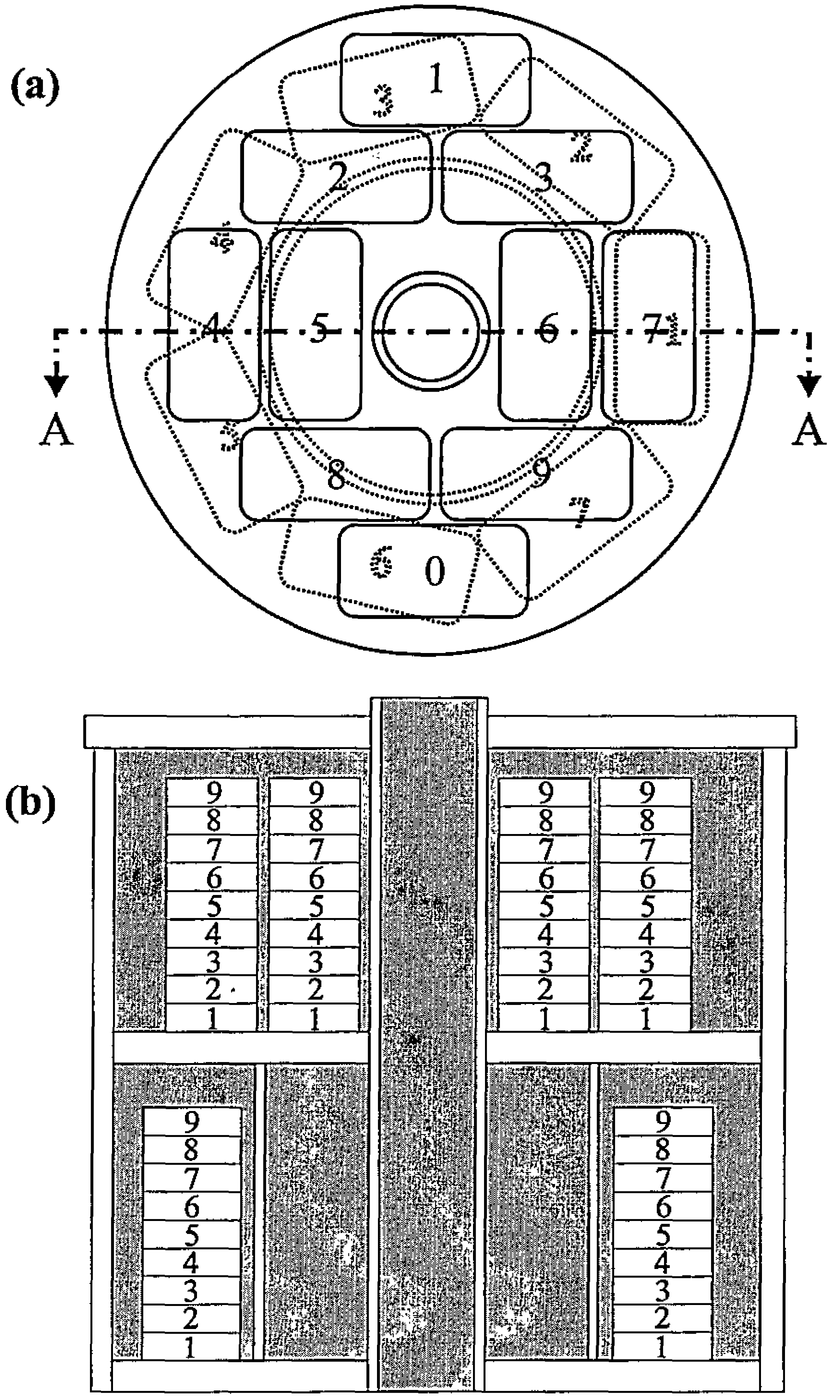

Figure 3.6. Plan view of the bottom and top levels of the furnace superimposed (a), and the section through A-A showing the configuration of the layers on the LNU's (b).

that of the top level, so the top was made to contain 90 parts - the number of statistically necessary samples for the six heat treatments.

3.2.5 Microwave Sintering

Not a lot can be said about the furnace design and operation of the MicroWear microwave sintering furnace, and these details are not crucial to understanding the results of this study. Microwaves (2.45GHz) were produced from two 5kW magnetrons, which created a multi-mode cavity inside the furnace. The temperature of the furnace could be measured in the microwave field to give an estimate of the ambient temperature near the parts (within 25°C [McClure, 1998a]). However, the actual temperature of the parts or microconstituents was not well known, so any reference to microwave sintering temperatures should taken as a rough estimate.

Hybrid heating was employed in the furnace, as silicon nitride does not couple well with microwaves at room temperature. As mentioned in Chapter 2, hybrid heating utilizes dielectric heating of, and radiation from susceptors to raise the temperature of the ceramic load in the furnace. Once the ceramics reach the temperature at which microwave heating becomes significant, all other forms of heating become negligible.

Due to the positive feedback nature of microwave heating the sintering process had to be carefully controlled. In order to control the temperature of the load the power input was regulated. Unlike conventional microwave ovens, where the power is turned on or off for different periods of time, the sintering furnace adjusted the magnitude of the power input. Figure 3.7 shows the temperature and power input profiles of the sintering run used to produce the specimens used in this research. Most of the process was in feedforward control with a small amount of feedback control near the end before the power was shut off. Notice that the time at sintering temperature was only around 15 minutes, and that the process took about 6 hours from power on to power off. Cooling took an additional 12 hours.

A slight nitrogen overpressure (constant flowrate of 90L/min.) was introduced into the sintering furnace throughout the process to prevent the possibility of oxidation of the silicon nitride and sintering additives, however the furnace was under atmospheric pressure. Also of note, the columns of parts were placed on previously sintered parts so that the green parts were not in direct contact with the susceptor material.

The author followed standard sintering procedures with some assistance from staff. Following sintering and cool down, the parts were marked with their position relative to the center of the furnace as they were removed: a black line was drawn down the center of the columns on the surface facing the center of the furnace. As is common in the MicroWear Process some samples were stuck together after sintering. These samples were split apart by a slight impact on a metal plate.

Interestingly, scales formed on the surfaces of the samples that were not in contact with other sample surfaces (i.e. the perimeter of the LNU's). This scale had different colours and adherent properties in different radial positions relative to the center of the

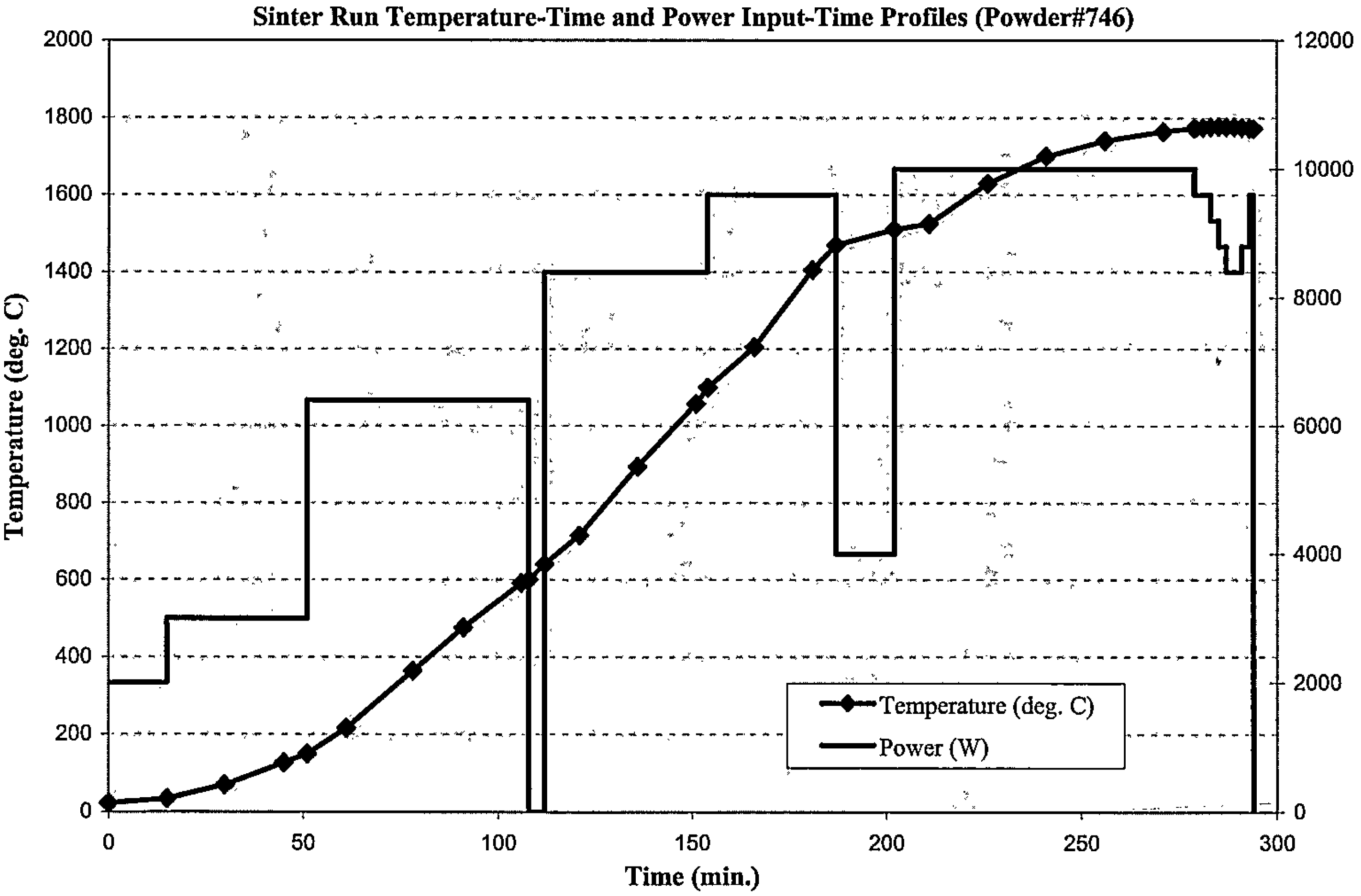

Figure 3.7. Microwave sintering profile showing the power input from both magnetrons, and the resulting temperature inside the furnace.

furnace. The scale was chipped off and collected for x-ray diffraction analysis. There was also scale formation on the lining of the furnace, but no samples from these surfaces were collected.

3.2.6 Division of Sintered Samples into Sample Sets

The basis behind the selection of samples for sample sets was the attempt to include as many 3-dimensional locations as possible in each set so that all the sample sets would be similar. This manner of selection, and similarity in sample sets would also allow for the detection and characterization of any positional dependence on properties.

Each sample set was to contain 15 LNU's, but recalling that the columns contained only 9 LNU's, a systematic approach was required. The top level was divided vertically into two sets of five columns (Figure 3.8). Each of these five columns could yield three sets of three samples. Table 3.1 shows the specific part numbers that were chosen to make the sample sets. Notice that the part numbers for sample sets 1 and 4, 2 and 5, and 3 and 6 are identical but the column number varies. Figure 3.9 demonstrates the pattern in which the three sets of three samples were taken from each column. Again note the pattern of selection was identical for sample sets 4-6 except that the column numbers were different. In any given column there were always two parts separating the previously chosen part. This pattern resulted in every sample set having at least one sample from each layer; six of the nine rows had 2 LNU's per row, and the remainder had only 1 LNU per row.

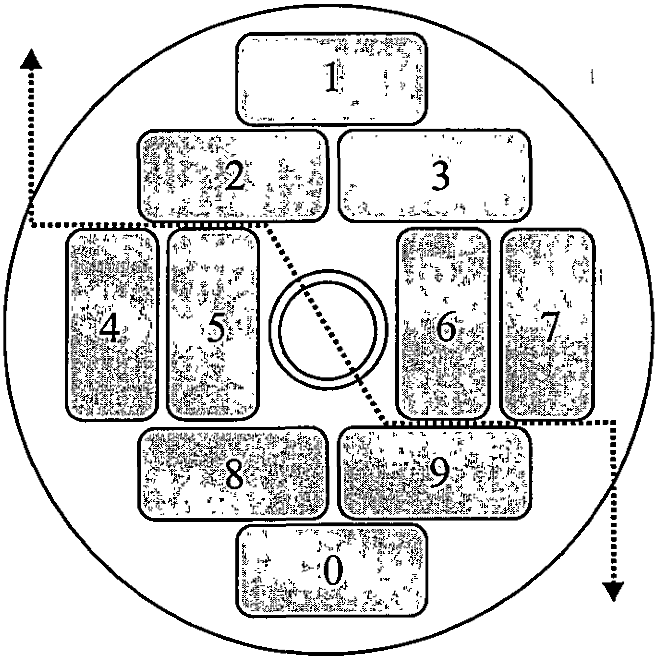

Figure 3.8. Plan view of the top level of the furnace, showing the division line for the separation of columns in order to make sample sets.

Sample Set	Column #	Part #'s	Sample Set	Column #	Part #'s
1	A22	9,6,3	4	A29	9,6,3
	A21	8,5,2		A20	8,5,2
	A23	7,4,1		A28	7,4,1
	A26	8,5,2		A25	8,5,2
	A27	9,6,3		A24	9,6,3
2	A22	8,5,2	5	A29	8,5,2
	A21	7,4,1		A20	7,4,1
	A23	9,6,3		A28	9,6,3
	A26	7,4,1		A25	7,4,1
	A27	8,5,2		A24	8,5,2
3	A22	7,4,1	6	A29	7,4,1
	A21	9,6,3		A20	9,6,3
	A23	8,5,2		A28	8,5,2
	A26	9,6,3		A25	9,6,3
	A27	7,4,1		A24	7,4,1

Table 3.1. Selection of LNU parts for the sample sets used in HIP experiments.

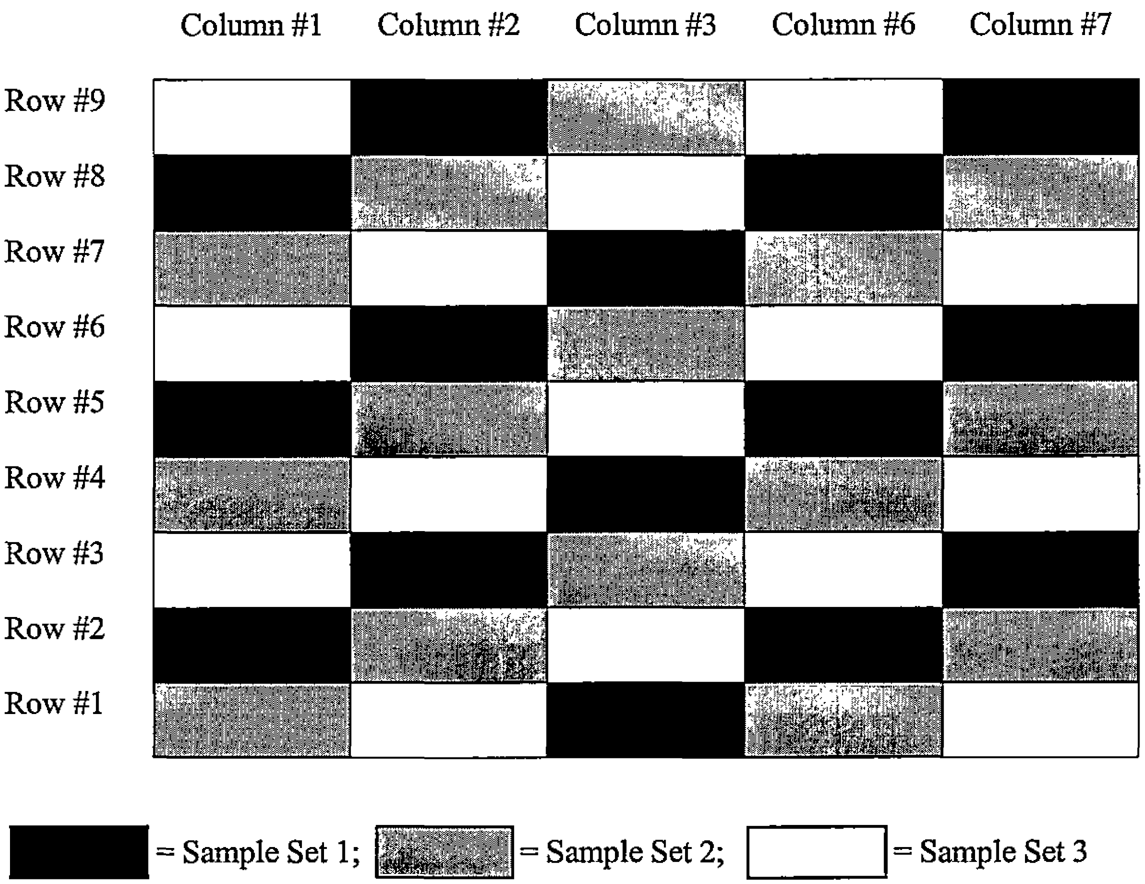

	Column #1	Column #2	Column #3	Column #6	Column #7
Row #9	□	■	▨	□	■
Row #8	■	▨	□	■	▨
Row #7	▨	□	■	▨	□
Row #6	□	■	▨	□	■
Row #5	■	▨	□	■	▨
Row #4	▨	□	■	▨	□
Row #3	□	■	▨	□	■
Row #2	■	▨	□	■	▨
Row #1	▨	□	■	▨	□

■ = Sample Set 1; ▨ = Sample Set 2; □ = Sample Set 3

Figure 3.9. Schematic of the pattern used to create the sample sets from the five columns after the vertical division of the top level.

Each of the smaller microstructural sample sets (mentioned in Section 3.1.1) contained only 3 LNU's taken from the bottom level of the furnace. A similar pattern to the sample set selection was used in the MS selection, except no vertical division was made. Table 3.2 shows the part identification numbers selected for the MS sets.

Sample Set	Column #	Part #'s
MS 1	A11	9,6,3
MS 2	A12	8,5,2
MS 3	A13	7,4,1
MS 4	A14	8,5,2
MS 5	A15	9,6,3

Table 3.2. Microstructural sample set selection.

3.2.7 Hot Isostatic Pressing

All except one of the HIP experiments were performed in an ABB Autoclave QP-15 HIP at MicroWear by the author with some help from the staff. The exception was a HIP experiment performed in an IPS Eagle I HIP at McMaster University by Ms. Connie Barry. These two pieces of equipment had small differences, and thus resulted in some different observations to be outlined in Chapter 4. Regardless of the equipment, all HIP tests were carried out in an argon atmosphere with graphite furnace furniture.

The HIP conditions from Figures 3.1 and 3.2 were all carried out with previously HIP'd parts as the "dummy" thermal load (i.e. the LNU's plus some other MicroWear research samples were the only parts in the HIP that had not previously been HIP'd). There were three enclosed levels to the HIP and the LNU's were always placed in the middle level, with the top and bottom levels containing the dummy load. This is mentioned because there were three C-type thermocouples present in the HIP: one each at the top, bottom, and middle. These thermocouples were all in close agreement (± 6°C) at the desired temperatures for the HIP conditions being tested, however they varied more (up to 100°C between the top and middle thermocouples) during the ramp up in pressure and temperature. An example of the differences between the thermocouple readings can be seen in Figure 3.10. The condition portrayed in Figure 3.10 is the most severe condition in terms of temperature and pressure, so the variation in the thermocouple readings should be the highest. One can see that the temperature set point of 1800°C is adhered to with good accuracy, within ± 2°C for all thermocouples. The temperature of the HIP conditions should then be taken to be the temperature at which the samples were heat treated.

A general HIP profile for the above mentioned condition is seen in Figure 3.11. No significant differences existed in the operation of the various HIP conditions except in the set-points of pressure, and temperature. In the case of some of the MS conditions the time was also different. The average length of time for all 120 minute soak conditions was about 6.5 hours, and 5 hours for the 30 minute soak conditions.

The samples had no noticeable scale formation after HIP treatment so scale samples were collected.

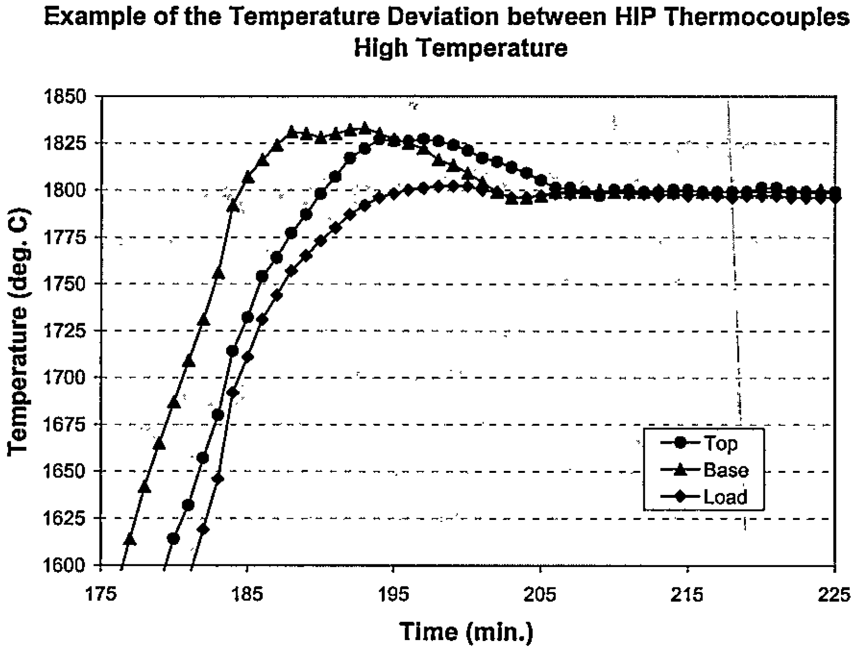

Figure 3.10. Example of the different HIP thermocouple readings at high temperature. SS4 (1800/30/120).

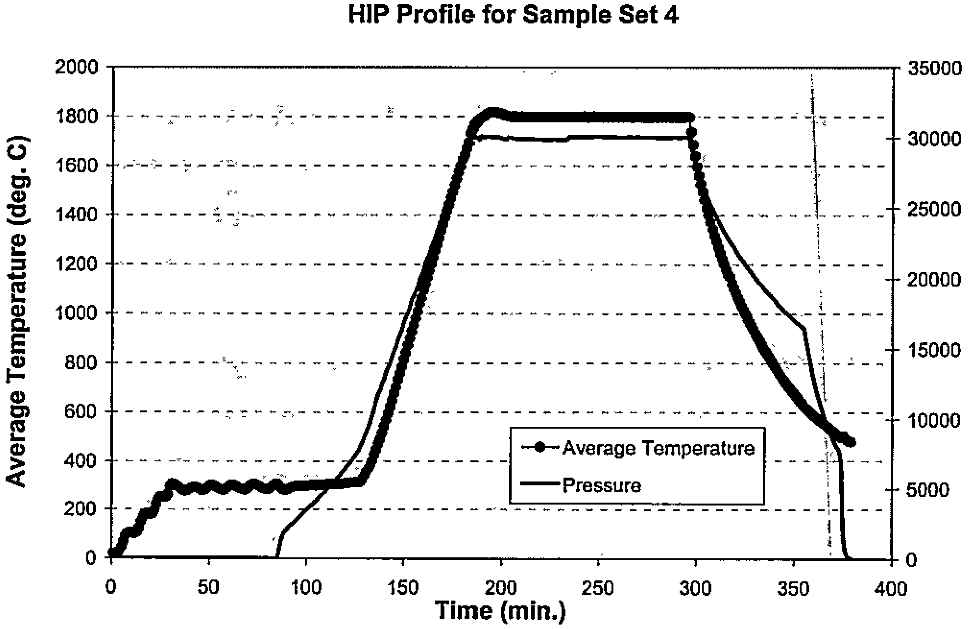

Figure 3.11. An example of a HIP profile in the ABB QIP-15 HIP. SS 4 (1800/30/120).

An additional HIP treatment was performed at McMaster University. This treatment was an annealing treatment done on certain sample sets for reasons that will be explained later. The conditions were as follows: 450 minutes at 1800°C under a 0.103-0.200 MPa argon atmosphere. The annealed samples were only the ends of the LNU's, about 1.5cm long. Samples were placed on a graphite disc, rather than in a graphite boat as in the MicroWear tests. Significant amounts of silica "hair" (whiskers) were discovered at the end of the test, along with a very thick layer of scale, both of which were removed from the samples and collected.

3.3 Property Evaluation

This section will describe how the LNU's were prepared for property evaluation, and explain the parameters and procedures used in the property measurements. The properties of interest were the density, indentation hardness, and indentation toughness.

3.3.1 Density Measurement

Density was of interest as a means of determining the amount of densification, or efficiency of sintering and HIP'ing. The standard MicroWear sinter density was approximately 98% theoretical, and >99% theoretical for the HIP'd density. Recall from Chapter 2 that the small density change achieved by HIP'ing (~2%) is believed to be caused by the closure of closed pores in the bulk of the sample. The method of density measurement used is reliable for the detection of closed porosity, but not for open porosity. No investigation was made into the types of porosity present for two major reasons. Firstly, any porosity present was most likely to be in the form of closed pores, located in the center of the samples [Plucknett and Wilkinson, 1994]. Secondly, any open porosity present at the surface was of little interest since cutting tools are designed to have a grind stock, which would effectively remove any porous layer from the inserts.

Referring back to the process flowchart (Figure 3.4) one can see the stages at which the density was measured. For the case of green density, Equation 3.1 was used. The Archimedes' immersion technique was used to measure the density of sintered and HIP'd LNU's. This technique used the measurement of mass in air and in water (to the nearest ten thousandth of a gram) to determine the density of the material according to Equation 3.2. The density of water used in all calculations was 1.0g/cc. After immersion in water the samples were moved around to remove surface bubbles and the readings of mass were not taken until 30s had elapsed. Samples were then left to dry in air.

$$\rho_{smpl} = \rho_{H_2O}\left(\frac{m_{air}}{m_{air} - m_{H_2O}}\right) \tag{3.2}$$

The density of all 153 LNU's was measured after sintering. In addition, all of the samples used in subsequent HIP treatments (90) were measured for density after HIP'ing. In the case of the HIP anneal treatment, which displayed significant scale formation, the density of the sectioned LNU's was measured before and after surface grinding. Recall that all scale that could be removed was removed before any density measurement, and that this pre and post grinding density measurement was an attempt to detect how invasive the scale formation was into the bulk of sample. Mr. Dave Allan of MicroWear carried out the density measurements done on the annealed samples.

The theoretical density of the material being studied was determined to be 3.2755g/cc [MacDonald, 1998]. This was based on a simple rule of mixtures approach, where the densities of the ceramic components were multiplied by their representative mass.

3.3.2 Indentation Hardness Testing

One of the most important properties of a cutting tool is its wear rate. It is known that the hardness of a material can affect its abrasive wear rate [Kuriakose et al., 1993]. Therefore, of particular interest for the cutting tool industry is the hardness of the inserts being used.

Two types of indentation hardness tests were performed: Rockwell A, and Vicker's Microhardness. The Rockwell tests were performed at MicroWear on a Mitutoyo ATK-F3000 Digital Rockwell A Hardness Tester by the author (with the exception of samples from the annealing HIP treatment). The Vicker's tests were performed on a LECO M-400-H2 Digital Microhardness Indenter. Test parameters are seen in Table 3.3.

Test Type	Indenter Type	Load (kg)	Application of Load (s)
Rockwell A	120° Diamond Cone	60	10
Vicker's	136° Diamond Pyramid	0.3	20

Table 3.3. Indentation hardness test parameters.

Some preparation of samples preceded hardness tests of either type. Samples had to have parallel surfaces to insure accuracy of the results in both test methods. Vicker's testing required that the test surface be highly polished, whereas Rockwell testing only required a ground surface.

In most instances a test block was cut from the LNU for all indentation testing. The geometry of the test block can be seen in Figure 3.12. None of the MS samples were cut to produce test blocks, whereas all 15 of the LNU's from the six sample sets were sectioned. Sectioning was done with a Buehler 20 LC metal bonded diamond blade in a Buehler Isomet 2000 saw operating at 4000rpm with an 800g load.

Following sectioning, 3 randomly chosen test blocks from each sample set (and one LNU from each MS set) were surface ground on a Harig Step Grinder using a resin bonded 320 grit diamond wheel. Each surface normal to the pressing direction had approximately 1-1.25mm of material removed to be sure that the bulk of the material was reached.

Rockwell testing was performed on the top surface of the ground test blocks and MS LNU's. Three indents were performed on each test block from each sample set, totaling 9 HRA indents per sample set. MS sets had only one sample to test so only 3 indents were performed. Position of the indents was similar on all test blocks, as shown in Figure 3.13. Hardness calibration was done on a MicroWear silicon nitride LNU of 94.7 HRA.

The HIP anneal samples were all test blocks. There were 3 test blocks in each of the three sample sets tested in this condition. Grinding was done in the same manner for these samples, but the HRA tests were performed on polished surfaces. The HIP anneal

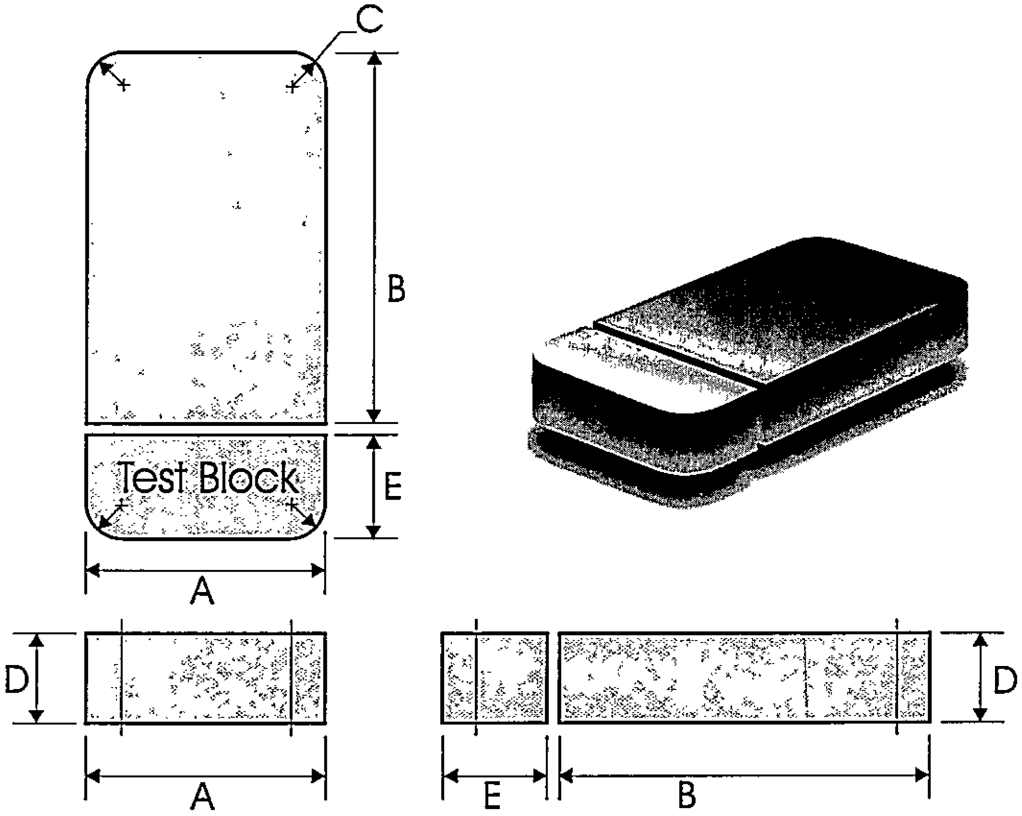

Dimension	HIP'd Value (mm)
A	20.07 ± 0.08
B	28 ± 2
C	3.64 ± 0.08**
D	7.10 ± 0.16
E	11 ± 2

** Calculated based on 22% linear shrinkage from pressing

Figure 3.12. Schematic of the sectioned LNU, showing the geometry of the test block.

HRA testing was treated identical to that of the sample sets in terms of the number and location of the indents.

After HRA testing the top surfaces of the test blocks and MS LNU's were polished using 30, 6 and 1 μm diamond slurries using a Buehler Autopolisher. Unfortunately, the polishing stage eliminated any possibility of further examination of the Rockwell indents.

Vicker's microhardness indents were positioned according to the map in Figure 3.13. Because of their small size, the indent diagonals were measured at 400X magnification [ASTM E 384-89]. Four indents per test block meant that 12 indents per sample set were made. Both the MS sets and HIP anneal samples had only one sample tested for Vicker's hardness; only 4 indents were made for these conditions.

Vicker's hardness was calculated using Equation 3.3 [Mott, 1957]:

$$H_v = \frac{2 \cdot L \sin(68^\circ)}{d^2} \tag{3.3}$$

where H_v was in units of kg/mm^2, the load L was 0.3kg (2.94N), and d was the average diagonal length in mm.

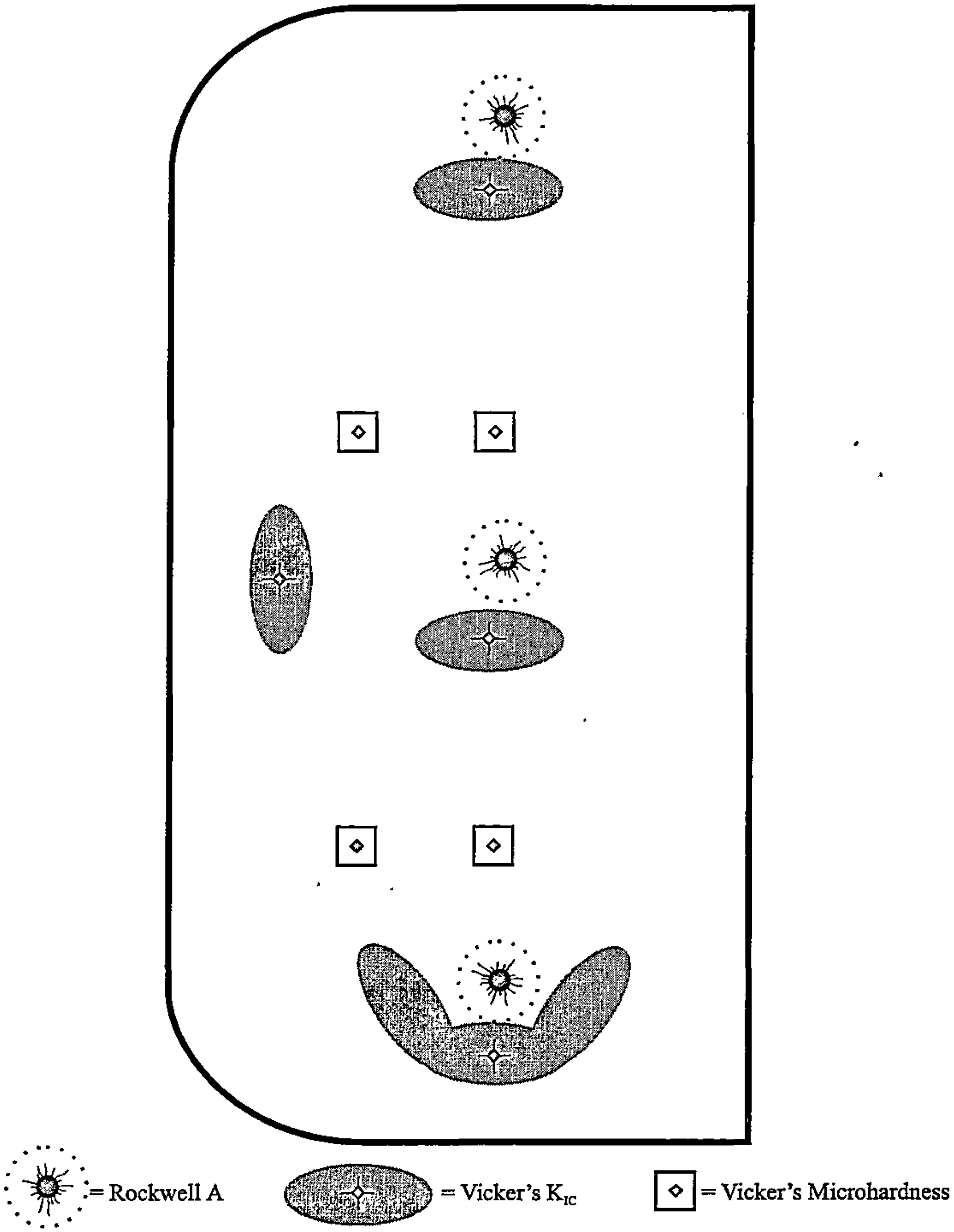

Figure 3.13. Schematic of indent locations on the top surface of the test block. The positions varied slightly, as depicted by the areas for each indent type.

3.3.3 Indentation Toughness Testing

The toughness of cutting tools is an important property when considering shock caused by interrupted cuts, and the initial impact of the insert with the work-piece when the cut is first initiated. Microstructural characteristics and mechanisms ultimately determine the toughness of a material, so having toughness data to accompany microstructural observations is paramount in the investigation and evaluation of different processing parameters.

While there are many methods available to test the toughness of material, the indentation toughness test has been adopted as being the most common for ceramics, and has received much study [Lawn, 1993]. Part of the test's attractiveness is due to the fact that minimal testing equipment is required (one needs only a hardness indenter equipped with a sharp indenter) and that minimal specimen preparation is necessary (samples need only be polished and have parallel surfaces). Another attractive feature of the method is that stable cracks are propagated, and inspection of them to determine fracture mechanisms is very easy and informative.

The toughness itself is determined by measuring the length of radial cracks, which result after the indentation has been made. Of course, the crack length measurement itself can introduce some error into the calculation of the toughness, but if all samples are measured in the same manner then comparable data can be collected.

Indentation toughness testing was performed on a Mitutoyo AVK-C2 Vicker's Hardness Tester. A load of 30kg was for applied for 10s. Samples were indented according to the map shown in Figure 3.13. Indentation toughness testing was done on the exact same samples as the HRA and Hv testing with no additional surface preparation.

Crack length measurement was done using image analysis (Image Pro) of images taken with a CCD camera at 100X magnification. Spatial calibration was done on a stage micrometer having 10μm divisions. Some crack length measurements were done on the Vicker's Testing machine as a means of comparison against the image analysis technique. This will be discussed in further detail in Chapter 4. For consistency all the crack length measurements were taken in one afternoon, except for the HIP anneal samples, which were measured on a different day since the anneal treatment was done one year later.

Crack lengths were then substituted into the Equation 3.4 [McClure, 1998b] for indentation fracture toughness determination:

$$K_{IC} = \left[\frac{0.095 \cdot 9.8 \cdot (2 \cdot 1000)^{1.5} \cdot P}{\left(\frac{L_1 + L_2}{2 \cdot 1000} \right)^{1.5} \cdot 10^6} \right] \tag{3.4}$$

where K_{IC} was in units of MPa√m, the load P was 30kg, and L_1 and L_2 were the crack lengths of the indent in μm.

3.4 Materials Characterization

This section explains the procedures used to prepare and analyze specimens for microstructural investigations. The various techniques used in the analysis of the microstructure were scanning electron microscopy (SEM), environmental scanning electron microscopy (ESEM), x-ray diffractometry (XRD), transmission electron microscopy (TEM) including conventional (CTEM), scanning (STEM), high resolution transmission electron microscopy (HRTEM), and energy dispersive x-ray analysis (EDX).

3.4.1 Scanning Electron Microscopy

The impetus behind SEM investigations was to discover the phase distribution, general grain morphology, and grain size distribution of the different heat treatment conditions. While the former two investigations were highly qualitative, the latter was quantitative. Both back scattered (BSE) and secondary electron (SE) imaging techniques were used in the SEM analysis. Mr. John Hudak of McMaster University operated the Phillips SEM 515 for the qualitative SEM studies and set up the SEM for the grain size measurements.

Sample preparation consisted of grinding and polishing (see section 3.3.2) the side face (normal to the pressing direction) of the selected test blocks. Reactive Ion Plasma Etching was then done on the polished surfaces to reveal grain structure. The Alberta Microelectronics Corporation (AMC) performed the plasma etching. However, AMC's initial Si_3N_4 etching procedure was too aggressive, so the author and Mr. Glen Fitzpatrick of AMC adjusted it accordingly. Additional information supplied by Dr. Paul Becher of Oak Ridge National Laboratory was helpful in determining the etching parameters. The final plasma etching parameters were: CF_4 gas with 5vol% O_2 gas at 12mTorr for 45-60s with a bias voltage of around 200V. These parameters resulted in an etching rate on the order of 25nm/min for β SiAlON relative to the grain boundary phase(s) and <25nm/min for the α SiAlON. Preferential etching rates existed due to differences in the concentration of Si-N, or Al-O bonds in the different phases [Walls and Ueki]. The larger the number of Si-N bonds (i.e. lesser the number of Al-O bonds) the faster the etching rate [ibid.]. Therefore, the relative etching rates of the different phases were thought to be:

$$\mathbf{Si_3N_4 \gg \beta\ SiAlON > \alpha\ SiAlON > Yttrium\ Rich\ Boundary\ Phase(s)} \qquad (3.5)$$

The confirmation of this hypothesis will be discussed in Chapter 4.

Finally, the polished and etched test blocks were gold coated by John Hudak to make them conductive in the SEM. The gold coating was assumed to be of uniform thickness.

The basis for phase determination by BSE imaging was atomic number contrast. Atomic number contrast reveals phases made of heavy atoms as light areas and dark areas as light element based phases. Of all atoms present, yttrium was the heaviest and nitrogen the lightest, therefore any yttrium rich phases showed up as white, and nitrogen rich phases showed up as black. α SiAlON grains showed up as gray because of the yttrium present in them. Since β SiAlON contains no yttrium α and β SiAlONs could be easily distinguished. Other researchers have also used this contrast difference technique to qualitatively identify, and distinguish between, α and β SiAlON phases [Ekström and Nygren, 1992; Bartek et al. 1992]. The technique is certainly not limited to these ceramics, and can be applied to any material that has some type of chemical gradient present within its microstructure.

Atomic number contrast is one way of distinguishing α and β, but two others were also utilized: grain morphology and preferential etching rates. The α and β based Si_3N_4 crystal structures both appear as hexagonal prisms. However, the β phase experiences anisotropic grain growth [Hwang and Tien, 1989; Krämer et al. 1993] and so becomes elongated. Based on the extremely high starting α Si_3N_4 content of the powder (>96%) elongated β phase grains were expected [Lange, 1979; Lee et al., 1990; Mitomo et al., 1995; Lee et al., 1998]. Therefore, β SiAlON grains were identified by their elongated hexagonal morphology, and the equiaxed hexagonal grains were identified as α SiAlON grains. This grain morphology difference between the two phases was observable in BSE and SE modes. Since SE mode offers topographical information (with very little atomic number contrast) it was more successful in detecting the preferential plasma etching rates of the phases (Equation 3.5).

Grain size measurements were only done on the β SiAlON phase; the small grain size and lack of good delineation of the α-α and α-secondary phase grain boundaries made it too difficult to accurately measure the size of individual α SiAlON grains. A stereo mixer was used to combine the signals of the BSE and SE detectors so that both topographical and atomic number contrast could be used to detect individual β grains. The signal was approximately 50/50 BSE/SE, but was varied to accurately see the outlines and extent of individual grains. Instead of taking photographs, grain size measurements were done by overlaying acetate sheets onto the display screen and tracing the β grains in the field of view with a fine tipped pen (0.25mm diameter nib). The sample was then moved, and the new grains traced. No predetermined areas were analyzed, and the sample was moved randomly each time to cover as much area of the sample as possible. Samples were typically moved 4 times at each magnification.

In a two dimensional section of a three dimensional matrix of randomly dispersed hexagonal prisms there were many 2D shapes observed. Various shapes from triangles to octagons can be produced when taking a cross section of a hexagonal prism [Hwang and Tien, 1989]. Therefore, measuring the grain diameter of hexagonal crystals from a two dimensional section must be done with care. The term grain diameter should be taken to mean the distance between parallel facet planes of the β phase crystals (i.e. {210} habit planes) [ibid.]. Following Hwang and Tien (1989) there are six useful shapes that can be observed when sectioning a hexagonal prism, as seen in Figure 3.14. Notice the arrows indicating the minimum grain diameter, or minimum grain width. Hwang and Tien (1989) showed that the minimum distance between parallel faces of an imperfectly shaped hexagonal grain on a 2D section varied less than 0.26% of the actual diameter of the grain (diameter of a perfect hexagon).

All of the projected shapes shown in Figure 3.14 were observed in this study, but only hexagonal grains were traced for the measurement of grain diameter. Some length and aspect ratio measurements were attempted on the rectangular shaped grains. However, the errors associated with aspect ratio measurement are much greater than the 0.26% deviation of grain diameter on a sectioned grain (see last section of this Chapter), so more emphasis was placed on grain diameter measurements.

The tracings of the grains had their minimum diameter measured with digital calipers to the nearest 0.01mm. Measurement of the minimum grain diameter was done from center to center of the traced lines of parallel faces. A conversion from the measured value to the actual diameter was then made based on the magnification at which the grains were traced.

The magnification, at which the grains were traced, played a role in the accuracy of the measurements. The highest magnification lead to the largest tracings and therefore the pen thickness was a small percentage of the dimension recorded. Thus, more grains were traced at high magnification to minimize measurement errors. The magnifications are listed in Table 3.4.

GRAIN SIZE MEASUREMENT

WIDTH: average of the minimum width of all the hexagonal grains on the cross-sectioned plane.

LENGTH: average of the length of all the rectangular grains on the cross-sectioned plane.

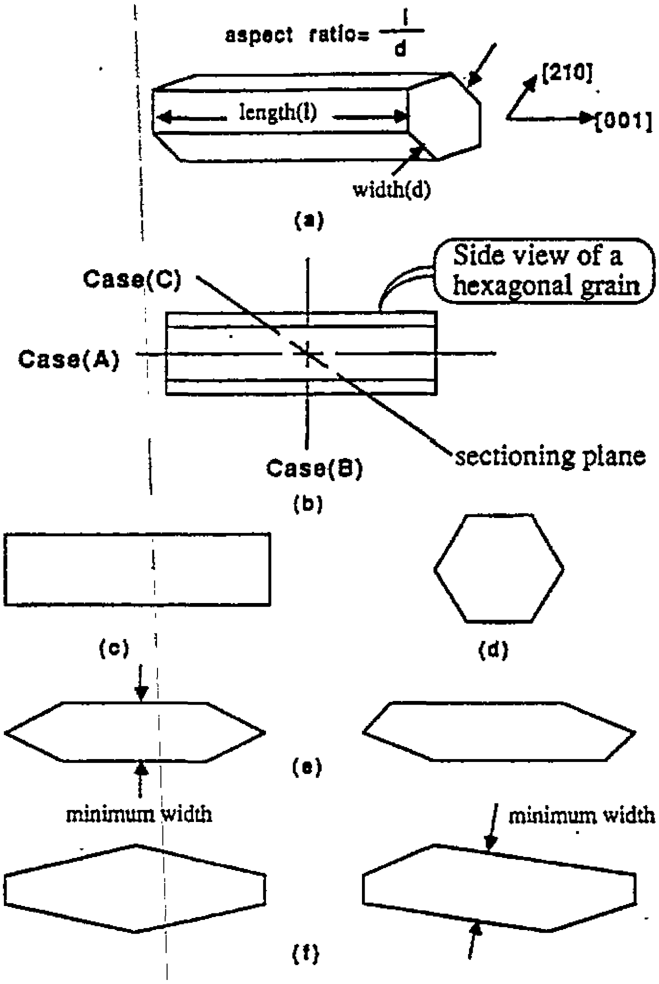

Figure 3.14. Schematics of a β grain (a), its relationship with the sectioning plane (b), and the projected grain shapes in case A (c), case B (d), case C.1 (e), and case C.2 (f). [Hwang and Tien (1989)].

Magnification Designation	Power	Population Size
High (HM)	21800X or 22800X	N > 240
Intermediate (IM)	11400X	N > 120
Low (LM)	2720X	N > 90

Table 3.4. Description of magnifications and number of grain measured in β grain size measurement.

Three sample sets (one test block from each sample set) were measured for β grain size: SS1, SS2, and SS4 (recall Figure 3.1 for heat treatment conditions). All of these except SS4 were investigated at all magnifications.

Curve fitting to the minimum grain diameter distributions was done with Origin™ V4.0 software (Microcal™ Software Inc., Northhampton MA.) using a log-normal curve fit equation similar to Equation 3.6a [Gerdan, 1960]. Both forms of the equations were tried. The differences between the two forms of the equation were negligible, so Equation 3.6b was used exclusively.

$$f(d)=\frac{1}{\sqrt{2\pi}\ln\sigma_g}\exp^{\left[\frac{-(\ln d-\ln d_g)^2}{2\ln^2\sigma_g}\right]} \tag{3.6a}$$

where f(d) was the frequency of the random variable d (minimum diameter), while d_g and σ_g were the apparent geometric mean and standard deviation respectively. The geometric standard deviation is the standard deviation of the distribution of ratios around the geometric mean, and whose logarithm is the standard deviation of the logarithm of the random variable [ibid.]. The log-normal distribution describes ratios of equal amounts in excess or defeat from a mean value instead of differences from a mean value [ibid.]. The large range of grain diameters was well suited for the use of a log-normal distribution.

$$f(d) = f_o + A \cdot \exp\left(\frac{-\ln^2\left(\frac{d}{d_g}\right)}{2w^2} \right) \tag{3.6b}$$

where f_o can be thought of as an intercept on the frequency axis, A is the maximum frequency at the mean of the data being fitted, and $w = \ln\sigma_g$.

3.4.2 Environmental Scanning Electron Microscopy

The ESEM (Phillips Electro Scan ESEM) was used to investigate the crack paths at the corners of the indentation fracture toughness indents. Sample preparation consisted of gluing the specimens onto aluminum stubs with colloidal graphite and polyvinyl acetate and drying. No preparation of the surface of investigation was made – precisely the reason for using the ESEM. The operating pressure was 3-6Torr $H_2O_{(g)}$ and the beam voltage ranged from 20-28kV.

3.4.3 X-Ray Diffractometry

Initial tests were done on bulk samples as a quick check for any secondary crystalline phases, and to determine the α/β phase ratios of the six different heat treatment conditions (Batch 1 of XRD tests). Based on the results of the first XRD tests the HIP anneal test was designed and performed. Samples from the HIP anneal heat treatment, and one of the samples from Batch 1 were then tested (Batch 2). Because of inconsistencies between the results of Batches 1 and 2 for the resubmitted sample a third XRD test was done on that sample (Batch 3).A fourth set of XRD tests (Batch 4) was done on more samples from Batch 1. Finally, a set of samples was done (Batch 5) to check the results from another diffractometer, the effects of surface preparation, and any sample orientation effects. See Appendix B for the details of the Batch 5 procedure. See Table 3.5 for the test parameters and details.

X-ray diffraction Batches 1-4 were performed on a Nicolet I2 Powder Diffractometer by Mr. Wen He Gong of McMaster University, whereas Batch 5 was performed on a Siemens Diffract 5000 instrument by Mr. Ryan Husagen of UMEX Incorporated (Fort Saskatchewan, Alberta). Cu $K\alpha$ radiation was used with a Ni filter, for all tests, and scan rates were 0.056° 2θ/min. for Batches 1-4 (18hours long), and 5.8° 2θ/min. for Batch 5 (12 minutes long). For the type of material used in this study, it was found that the scan rate did not yield different results in the amount of α/β, or in the presence of secondary peaks [Roy, 1999].

The surfaces scanned were the opposite faces of the indented test block samples. Recall that these surfaces were diamond ground well into the bulk of the samples. An area of approximately 20 mm^2 maximum (at low 2θ values) was scanned by the diffractometer. In the case of Batch 4, samples were ground on a 45 µm diamond platen

Batch #	Samples Tested	Time Period
1	SS1: A27-3 SS2: A23-9 SS3: A21-6 SS4: A28-4 SS5: A24-2 SS6: A20-6	12/15/98-01/28/99
2	SS1: A22-6 (Annealed) SS3: A27-4 (Annealed) SS4: A29-3 (Annealed) SS5: A24-2	07/05/99-07/08/99
3	SS5: A24-2	07/23/99
4	SS1: A27-3 SS2: A23-9 SS4: A28-4	08/10/99-08/12/99
5	SS5: A24-2 SS3: A21-6 SS6: A20-6	08/20/99

Table 3.5. Sample list for the different XRD Test Batches, including time schedule.

to remove all visible marks from step grinding. This additional grinding stage was carried out to remove any reaction layers that may have built up over time. All other XRD test parameters were maintained except for this extra grinding.

Phase identification involved comparison of the experimental scans with JCPDS/ICCD PDF cards (found in Appendix C). It should be noted that these cards were usually data from, or calculations of pure materials, not from polyphase ceramics.

The α/β phase ratios for the different samples were calculated according to methods outlined in Gazzara and Messier (1977), except for the measurement of the $\alpha_{(301)}$ peak. α and β peak heights were measured to the nearest 0.1mm. The background was not subtracted. The method of Devlin and Amin (1990) was also used for comparison. These methods assumed that α and β phases were the only phases present, so the amounts of the phases were interpreted as a ratio.

3.4.4 Transmission Electron Microscopy

The transmission electron microscope was used to investigate the morphology and distribution of the secondary phases within the microstructure, and to do identification of the SiAlONs and other phases. Two different TEMs were used: a Phillips CM-12 (120kV) microscope equipped with a LaB_6 filament, and a JEOL JEM 2010 F Field Emission Electron Microscope (200kV). Mr. Fred Pearson and Mr. Andy Duft were vast resources of knowledge, and offered much information and many ideas on sample preparation techniques, and equipment operation. Fred performed all of the TEM work on the JEOL with the author present, whereas the author performed the work on the CM-12 with the help of colleague Mr. Tony Quan.

Sample preparation was essentially a three-stage process involving sectioning, thinning to electron transparency, and coating. Test blocks were cut parallel to the pressing direction with a Micro-Matic Precision Wafering Machine using a 220 grit diamond blade (2700 rpm) to produce two smaller test blocks. One of these blocks then had a thin slice (300-500μm) cut from it using a low speed Buehler Isomet 11-1180 saw equipped with a Buehler 15 LC diamond blade. A 3mm-diameter disc was then ultrasonically cut from the thin slice using a slurry of 9μm diamond grit as the cutting medium (SiC grits were also tried, but lacked efficiency). The thin sections were mounted on a glass slide with a thermal glue (Crystallbond™) to make the ultrasonic cutting easier.

Once a 3mm disc was obtained it was thinned by diamond polishing. A TEM thinning jig was designed and fabricated using a MicroWear silicon nitride cutting tool with a micrometer inserted into it. The disc was thinned so that it had parallel surfaces; each side of the disc was thinned separately by mounting it to the micrometer head using Crystallbond™. Grinding the first side with 9μm diamond slurry was done until the disc was approximately 200μm thick. Polishing was then performed with 3, 1, and 0.1μm diamond slurries, which removed a total of around 5μm maximum. After flipping the disc over, and remounting it to the jig, the disc was thinned to a thickness of 70-100μm using 9μm diamond slurry. Final polishing was done with 3 and 1μm diamond slurries.

Dimpling was carried out using a Gatan Dimpler Grinder, Model 656. Two grinding stages were done (9 and ¼ μm diamond paste) to thin the disc so that the crater had a minimum thickness of 10-20μm. Different dimpling wheel diameters were used, and it was found that the 20mm wheel was best for coarse grinding and the small 16mm wheel (felt surface) was best for the fine grinding. The dimpling was performed on the rougher surface (from thinning) to eliminate back thinning.

Ion milling was accomplished using a Gatan Precision Ion Polishing System (PIPS), Model 691 (*not* a cold stage ion mill). Dimpled specimens were thinned in the PIPS until they just started to show a perforation. The argon beam energy was 5keV (at 15-20μA) and was directed at the thinnest portion of the foil at 5-7° tilt on both the top and bottom guns. Ion milling typically took approximately 1 hour for every 5-6μm to be removed up to 20μm.

A conductive coating of carbon was sputtered onto the dimpled and milled surfaces of the foils using a Balzers Kleinbedampfungsunlage Mikro BA 3 device. The thickness of the carbon coating was not determined, but a fair amount (as far as carbon coatings go) was needed to prevent charging in the TEM.

Conventional TEM techniques employed were bright field imaging (BF), and convergent beam diffraction (CBD). STEM was used to locate areas to analyze with EDX, and HRTEM was performed to produce lattice imaging in regions containing grain boundaries and grain boundary phases.

Since the TEM images through the thickness of the foil, areas for EDX analysis were chosen near the edge of the perforation (the thinnest portion of the foil) to reduce the possibility of material being either above or below the region of interest. EDX analysis was done in STEM mode with a spot size of approximately 8-10 Angstroms. Typical collection rates of ~ 400-500 cps were achieved and collected for 100s. At high magnifications (e.g.1 MX) there was beam damage induced in the specimens and some mass loss undoubtedly occurred, as there were holes "drilled" in the specimen. LINK ISIS Rev. 3 (Oxford Instruments) software was used to determine semi-quantitative chemical composition ranges for the areas studied. No additional standards to those supplied with the software were prepared or analyzed; default Cliff-Lorimer factors and mass absorption coefficients were used. Some element mapping was also performed using the same program, but with a larger scanning area. Approximately 40 frames (18s of collection time each) were collected for the element maps.

In HRTEM Fast Fourier Transforms (FFT), as computed in real time by Pentacle Software, were referenced as the analysis spot was moved over grain boundaries. The FFT gave information about the crystallinity of the material within the area of the spot on the sample via diffuse rings; small rings indicated presence of little to no amorphous material, whereas larger, more diffuse rings indicated presence of comparatively more amorphous material. Due to the presence of the amorphous carbon coating there was always a signal indicative of a small amount of amorphous material.

3.5 Error Analysis

This section deals with the possible sources of error present, and their magnitudes, for the procedures listed in the previous sections of this chapter. Explanations about the manner in which errors were calculated are listed when required.

3.5.1 Density Measurement Error

Root mean square error analysis was done on Equation 3.2. Two different errors for the mass measurement were used for comparison: ±0.0005g and ±0.001g. The error in the density of water was constant at ±0.002g/cc due to temperature fluctuations. The values of the errors in density are shown in Table 3.6.

Δmass (g)	$\Delta\varepsilon_{rms,\rho}$ (g/cc)
± 0.0005	± 0.0020
± 0.001	± 0.012

Table 3.6. Comparison of the Root Mean Square Errors of Density for different uncertainty values of mass.

These errors in density did not account for any effects of adhesion of air bubbles to the surface of the samples, or for any regions of less dense surface scales. However, since all the samples were tested in the same manner these environmental errors should have been constant for all density measurements, and would therefore only affect the magnitude of the final value as compared to the theoretical density.

3.5.2 Indentation Hardness Error

Due to the small indent size produced when testing hard materials, such as silicon nitride, the measurement of either the depth of the indent or its dimensions must be made to a high degree of accuracy. Without the use of extremely high powered optical, or electron optical devices the measurement of the depth of penetration on the indenter is easier [Tabor, 1986]. Depth measurements can be made with great accuracy and can be digitized, automated and reported to high precision, but the geometry of the indenter, zero position, elastic recovery, and the piling up or sinking in of material around the indentation all lead to uncertainty in the measure of the true pressure over the indentation [ibid.]. For these reasons care has to be taken when analyzing the results obtained from the depth of penetration tests.

Rockwell indentation measured the depth of penetration of the indenter into the sample. Therefore, the accuracy to which the depth measurement could be made had a direct effect of the error associated with the HRA number. The testing machine used measured the depth of penetration automatically, i.e. without any human interpretation.

The accuracy of the measurement was not known so the discussion of the error associated with HRA measurements was based on statistical arguments.

The 95% and 98% confidence intervals of the mean HRA value (y_{HRA}) for each of the different HIP conditions were determined using the student t-test [Mendenhall and Sincich, 1992]. The student t-test was used due to the small sample size (n<30), and it was assumed that the HRA data followed a normal distribution. Results of this analysis are shown below in Table 3.7. s* was the standard deviation based on (n-1) samples. The error on the HRA data was determined to be ±0.1HRA of the mean HRA for each sample set. This value was very close to the standard deviation of the data for sample sets 1-6, but not for the MS sets and annealed samples.

Sample Set	n	s*	95% CI	98% CI
SS1	9	0.148	y ± 0.11	y ± 0.14
SS2	9	0.093	y ± 0.07	y ± 0.09
SS3	9	0.083	y ± 0.06	y ± 0.08
SS4	9	0.127	y ± 0.10	y ± 0.12
SS5	9	0.112	y ± 0.09	y ± 0.11
SS6	9	0.109	y ± 0.08	y ± 0.11
SS1 annealed	9	0.112	y ± 0.09	y ± 0.11
SS3 annealed	9	0.220	y ± 0.17	y ± 0.21
SS4 annealed	9	0.150	y ± 0.12	y ± 0.14
MS1	3	0	y ± 0.0	N/A
MS2	3	0.058	y ± 0.14	N/A
MS3	3	0.058	y ± 0.14	N/A
MS4	3	0.1	y ± 0.25	N/A
MS5	3	0.1	y ± 0.25	N/A

Table 3.7. Confidence intervals of the mean HRA value for the different HIP Conditions. Magnitudes of the mean values ranges from 94.1 to 95.1HRA.

Further statistical analysis was done to determine the number of indents required to give this ±0.1HRA error of the mean HRA (for SS1-6 only). This calculation was done using

Equation 3.7 [ibid.]. In order to ensure all the conditions were represented, a maximum standard deviation ($\sigma = 0.15$) for the data was used:

$$n = \frac{(z_{\alpha/2})^2(\sigma)^2}{(H)^2} \tag{3.7}$$

where n is the sample size required to give sample statistics with a standard deviation σ, with an associated 95% confidence interval of the mean equal to ± H. $z_{\alpha/2}$ is the z score value for a 95% confidence interval: $z_{0.025} = 1.96$ for this study. The number of required samples predicted by Equation 3.7 was 9. This was in agreement with the number of tests performed, also 9.

As mentioned, the Vicker's microindentation tests determined the hardness by measuring the diagonals of the impression, and substituting them into Equation 3.3. Although the author repeated the measurements as consistently as possible there was certainly some subjectivity and human error introduced into the measurement due to the small size of the indents. Even though the minimum magnification [ASTM E384-89] was used to measure the indents, a higher magnification would certainly have decreased the measurement error. The measurement error was not determined for the diagonal measurements, but it was most likely on the order of ±0.05μm. Statistical analysis was done following the same procedure outlined for the HRA analysis. Table 3.8 shows the 95% confidence intervals of the mean Hv hardness. From the values in Table 3.8

Sample Set	n	s*	95% CI
SS1	12	83	y ± 53
SS2	12	127	y ± 81
SS3	12	99	y ± 63
SS4	12	129	y ± 82
SS5	12	107	y ± 68
SS6	12	103	y ± 65
SS1 annealed	12	123	y ± 78
SS3 annealed	12	86	y ± 55
SS4 annealed	12	74	y ± 47
MS1	4	49	y ± 78
MS2	4	16	y ± 25
MS3	4	116	y ± 185
MS4	4	88	y ± 140
MS5	4	83	y ± 132

Table 3.8. Confidence intervals of the mean Hv value for the different HIP Conditions. Magnitudes of the mean values ranged from 1810 to 2149Hv.

it can be seen that the error on the mean Hv values is on the order of ±80Hv for SS1-6 including annealed samples, but is higher for MS samples. For the sake of including some measurement error, the error on mean of the Hv values was set at ±100Hv (closer to the standard deviation of the data as well). Similar errors on Hv numbers these types of materials have been reported elsewhere [Ekström and Nygren, 1992]

Equation 3.7 predicted that 7 samples were necessary to yield an error of ±100Hv on the mean HV values. The standard deviation used for this calculation was set to 130Hv. Since 12 indents were performed for all except the MS samples, the Hv experiments had a sufficient number of samples to give statistically meaningful results.

3.5.3 Indentation Toughness Error

Indentation toughness experiments had some measurement error associated with them, but it was difficult to quantify because of the nature of the crack tip. Depending on the magnification that one looks under to measure the distance from crack tip to crack tip one could get seemingly different results. Of course, there should exist some optimum magnification, beyond which no statistically significant difference in crack dimensions is noticed. Comparing identical indents at 100X magnification and at 170X approximately ±8μm difference in crack length was observed, or ~2% difference in total crack length. This difference correlates to a 2% difference in K_{IC} value as well: about ±0.15MPa√m for the toughness values observed for the materials studied. This error was most likely accommodated into the actual measurements of the crack lengths, so on average the statistical treatment of the fracture toughness data should give a good overall indication about the magnitude of the error on the K_{IC} determination.

The methods of Section 3.5.2 were employed for the statistical analysis of the K_{IC} data. Table 3.9 summarizes the results of the analysis. An error of approximately ±0.35MPa√m seems an appropriate value based on the standard deviation values, and considering any measurement errors, and it follows most of the 95% confidence values for *all* sample sets. It was found, using Equation 3.7, that 12 samples were needed to get statistically acceptable data (95% confident) for a standard deviation of 0.5MPa√m with an error of ±0.35MPa√m. This number correlated to the sample size collected.

3.5.4 Grain Size Measurement Error

There were thought to be two major sources of error in the measurement of the grain diameters, both related to the thickness of the pen. Firstly, the placement of the line with respect to the actual grain boundaries on the screen, and secondly the measurement error associated with using the calipers to measure to the half-width of the lines.

Sample Set	n	s*	95% CI	98% CI
SS1	12	0.25	y ± 0.16	y ± 0.21
SS2	12	0.31	y ± 0.20	y ± 0.26
SS3	12	0.52	y ± 0.33	y ± 0.44
SS4	12	0.43	y ± 0.27	y ± 0.36
SS5	12	0.21	y ± 0.13	y ± 0.18
SS6	12	0.40	y ± 0.25	y ± 0.33
SS1 annealed	12	0.58	y ± 0.37	y ± 0.48
SS3 annealed	12	0.42	y ± 0.27	y ± 0.35
SS4 annealed	12	0.47	y ± 0.30	y ± 0.39
MS1	4	0.22	y ± 0.36	N/A
MS2	4	0.19	y ± 0.31	N/A
MS3	4	0.23	y ± 0.37	N/A
MS4	4	0.20	y ± 0.32	N/A
MS5	4	0.21	y ± 0.34	N/A

Table 3.9. Confidence intervals of the mean K_{IC} value for the different HIP Conditions. Magnitudes of the mean values ranged from 6.24 to 7.99MPa√m.

The line placement error was obviously more pronounced at low magnifications, since as the line was drawn the boundary was hidden. At low magnification any deviation from the grain boundary was difficult to detect. The magnitude of this error will be hypothesized in Chapter 4.

The error associated with the measurement of the diameter (distance to the half-width of the lines) was estimated at ±0.15mm. Based on this measurement error the grain diameter values, due to pen thickness alone, had an error of ±7nm at 22800 and 21800X, ±13nm at 11400X, and ±55nm at 2720X.

Obtaining accurate data from aspect ratio measurements presents more difficulty when dealing with 2D sections. Using geometrical considerations (Figure 3.15) a shallow section of a grain can result in an almost infinite overestimation of the aspect ratio, while the maximum underestimation of the aspect ratio is ~15%. Both of these estimations are valid for a known length, but as the length increases the probability of achieving a section along the longitudinal axis reduces significantly, so the 2D method for determining aspect ratio can be ambiguous. Deep chemical etching and grain extraction is a much better method to accurately determine aspect ratios of β grains, but it is also more time consuming [Lai and Tien, 1993]. However some authors have used statistical arguments to predict the true dimensional parameters of grains based on 2D sections [Plucknett and Wilkinson, 1994].

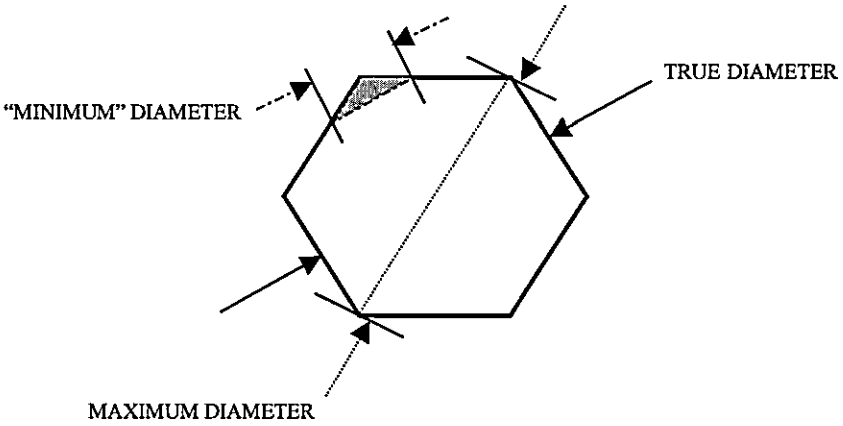

Figure 3.15. Geometrical considerations for the limits on projected grain diameters for longitudinal sections of hexagonal grains. The shaded region is the portion of the grain left in the matrix upon surface preparation for the estimation of minimum diameter.

3.5.5 XRD Error

Inconsistent relative intensities of some peaks (in particular those of $\alpha_{(210)}$ and $\alpha_{(102)}$) in comparison to the α Si_3N_4 PDF card used (41-360) most likely caused some error in the α/β phase ratios. The magnitude of the error for the α/β phase ratio was thought to be

± 3 wt% β. Since the different methods are not entirely independent (the Devlin and Amin method (1990) uses the corrected intensities as calculated by the Gazzara and Messier method (1977)) the errors for the two methods were similar. The value of ± 3 wt % β was based on readings as taken from the calibration curve used in the Gazzara and Messier method (1977), and peak height measurement error.

Some peak shifting for candidate phases was most likely present due to defects, substitutional or interstitial ions, or residual thermal or mechanical stresses. Since no internal standard was included, and the samples were blocks of material instead of powders it was impossible to determine any magnitudes of peak shifting that may have occurred. Indeed, some peak shifting to lower 2θ values should have occurred for the α and β SiAlONs since there is a lattice expansion in both crystal structures as Al and O are substituted into the structure [Sun et al., 1991a]. However, due to the low additive content, and predicted low substitution levels of the SiAlON phases the peak shifts may not have been larger than the detectable limits of the equipment [Roy, 1999]. Therefore, no attempts were made to quantify the degrees of substitution for the SiAlONs phases.

3.5.6 EDX Error

There were thought to be four possible sources of error in the EDX analysis. Firstly, the EDX analysis was performed with a small probe size, which caused some mass loss during the collection of the spectra. To compensate for beam damage the beam was moved slightly within the region of interest during the scan.

Secondly, software defaults were used in the calculation of compositions. Ideally, it would have been best to prepare standards of the compounds thought to be present, and calibrate the software accordingly. The data presented in Chapter 4 should then be taken to be semi-quantitative at best, but useful for comparative purposes.

The nature of through thickness contrast in the TEM was another source of possible error. All attempts were made to only analyze areas where there was thought to be no variation in phase through the thickness of the foil, but it might have been possible that there were some underlying regions of different composition. To keep this error at a minimum HRTEM mode was first used to identify regions of single phase (regions where the lattice contrast revealed no overlapping phases). STEM was then used to do the EDX analysis on the previously identified single-phase regions.

Lastly, it was noticed that there was a film around the edges of the perforation made in ion milling. This film was thought to be either C from coating, or SiO_2 as a product of oxidation of the SiAlON grains. The latter argument seems less likely, as SiAlONs are known to be fairly oxidation resistant, especially at room temperature [Jack, 1976; Ekström and Nyrgren, 1992].

The determination of the amounts of the light elements was difficult due to peak overlaps of C, N and O. For these light elements (and heavier ones as well) electron energy loss spectroscopy (EELS) could have been used [Chadwick, 1990]. EELS would have given more accurate results on the composition, but again the use of EELS would have required standards to be made.

The exact chemical composition of the phases was not a major goal of this study, so it was determined that the errors associated with EDX were acceptable when considering the qualitative information that EDX gave. In the future however, if more analysis were to be done on this material, the use of EELS with properly prepared standards would be paramount.

4. RESULTS

This chapter is a presentation of the results obtained from the various techniques of experimentation as described in Chapter 3. The main purpose of this chapter is to alert the reader to the trends observed in the data, and to determine whether the observed trends were true or spurious. In some cases it will be shown that the errors calculated in Chapter 3 may have been overestimated, and new errors based on the data will be assigned.

4.1 Results of Property Evaluation

Raw data, in the form of property measurements of individual specimens (density, hardness values, crack lengths etc.) is found in Appendix C. However, the results displayed in the text forthwith are mean values and standard deviations of the mean.

4.1.1 Density

The density values presented in this section are reported to the third decimal place in order to show that the error estimation from 3.5.1 was most likely overestimated. The sintered and HIP'd densities are discussed in terms of both the predicted error, and the standard deviations of the data. It was found that a more reasonable error estimation of ±0.003g/cc be used when analyzing the data, rather than the previous calculation of

TOP LEVEL Average Density (g/cc)				BOTTOM LEVEL Average Density (g/cc)			
Column		Layer		Column		Layer	
1	3.241 ± 0.002	**1**	3.238 ± 0.004	**1**	3.246 ± 0.003	**1**	3.248 ± 0.002
2	3.240 ± 0.002	**2**	3.239 ± 0.004	**2**	3.247 ± 0.002	**2**	3.248 ± 0.003
3	3.242 ± 0.002	**3**	3.241 ± 0.006	**3**	3.244 ± 0.002	**3**	3.247 ± 0.002
4	3.237 ± 0.003	**4**	3.240 ± 0.003	**4**	3.245 ± 0.003	**4**	3.245 ± 0.002
5	3.243 ± 0.002	**5**	3.240 ± 0.003	**5**	3.247 ± 0.001	**5**	3.245 ± 0.003
6	3.244 ± 0.003	**6**	3.240 ± 0.003	**6**	3.249 ± 0.001	**6**	3.246 ± 0.003
7	3.238 ± 0.002	**7**	3.240 ± 0.002	**7**	3.249 ± 0.001	**7**	3.246 ± 0.003
8	3.236 ± 0.001	**8**	3.241 ± 0.003			**8**	3.247 ± 0.003
9	3.239 ± 0.001	**9**	3.240 ± 0.002			**9**	3.248 ± 0.002
10	3.238 ± 0.002						

Table 4.1. Average sintered densities of the top and bottom levels by column and by layer. Error is one standard deviation of the mean.

±0.01g/cc. The smaller error allowed for better detection of certain trends in the data, but did not change the nature of the trends observed.

The as sintered density of all LNU's is presented in Table 4.1. The data has been averaged by column and layer, and shown with the standard deviation of the average. Any variations in density were only detected in the third decimal place, and since these variations were within the error limits any concerns of position-dependent density in the sintering furnace are ruled out. The sintered density was determined to be uniform, at approximately 99% theoretical.

However, it appeared as thought the bottom level sintered to a slightly higher density than the top. Recall that the only samples taken from the bottom level were the MS samples, so these samples should be thought of as having a slightly higher density than those taken from the top level.

Average sintered and HIP'd density values for the various heat treatment conditions are shown in Table 4.2. Notice again that the MS samples (bottom level) had a slightly higher sintered density than the other sample sets, but the HIP'd density was the same for all sample sets. Annealed samples (SS3 and SS4) were the exception, and had the highest HIP'd density because of their multiple heat treatments.

The sintered density was typically 0.018-0.023g/cc less than the HIP'd densities of the SS and MS conditions, and 0.021-0.029g/cc less than the annealed conditions. These differences suggest that HIP'ing increased the density slightly from 99% theoretical to >99% theoretical.

Sample Set	Average Sintered Density (g/cc)	Average HIP'd Density (g/cc)
SS1	3.241 ± 0.003	
SS2	3.241 ± 0.002	3.256 ± 0.002
SS3	3.242 ± 0.004	3.257 ± 0.002
SS4	3.239 ± 0.003	3.261 ± 0.001
SS5	3.239 ± 0.003	3.260 ± 0.002
SS6	3.238 ± 0.003	3.257 ± 0.004
SS1 annealed	3.241 ± 0.005	3.259 ± 0.001
SS3 annealed	3.241 ± 0.003	3.266 ± 0.002
SS4 annealed	3.241 ± 0.003	3.267 ± 0.002
MS1	3.246 ± 0.003	3.256 ± 0.006
MS2	3.248 ± 0.003	3.258 ± 0.001
MS3	3.244 ± 0.003	3.259 ± 0.003
MS4	3.245 ± 0.004	3.254 ± 0.004
MS5	3.247 ± 0.001	3.259 ± 0.003

Table 4.2. Average Sintered and HIP'd densities for the different sample sets. Error is one standard deviation of the mean.

4.1.2 Indentation Hardness Testing Results

Indentation hardness data is shown in Table 4.3. Figure 4.1 illustrated the hardness of the 120 minute soak conditions plotted as a function of HIP pressure and temperature.

Sample Set	Average HRA ± σ	Average Hv ± σ
SS1	94.92 ± 0.15	2128 ± 83
SS2	95.00 ± 0.09	2090 ± 127
SS3	94.72 ± 0.08	1969 ± 99
SS4	94.69 ± 0.13	1891 ± 129
SS5	95.10 ± 0.11	2149 ± 107
SS6	94.58 ± 0.11	1936 ± 103
SS1 annealed	94.33 ± 0.11	1944 ± 123
SS3 annealed	94.09 ± 0.22	1810 ± 86
SS4 annealed	94.07 ± 0.15	1849 ± 129
MS1	95.10 ± 0.00	2073 ± 49
MS2	94.77 ± 0.06	1983 ± 16
MS3	95.03 ± 0.06	1979 ± 116
MS4	94.90 ± 0.10	1858 ± 88
MS5	94.90 ± 0.10	1928 ± 83
Estimated Error	**± 0.1**	**± 100**

Table 4.3. Average Rockwell A hardness (HRA) and Vicker's Microhardness (Hv).

From this figure the HRA hardness decreased with increasing temperature: a 0.2 HRA difference (outside error limits) existed between the lowest, and highest temperature conditions (SS5 vs. SS4). There seemed to be a limiting temperature for the decrease in HRA, and this threshold was estimated to be close to 1650°C.

Pressure was seen to have no effect on the HRA hardness, evident in the small range of values between the different pressure conditions at 1800 and 1650°C: 94.6-94.7HRA, and 95.0-95.1HRA respectively.

Figure 4.2 shows the effect of time on HRA. It seemed as though most conditions experienced a slight decrease in hardness with increasing time. This vertical shift was only about +0.1HRA so it cannot be said for certain if the shift actually existed or not.

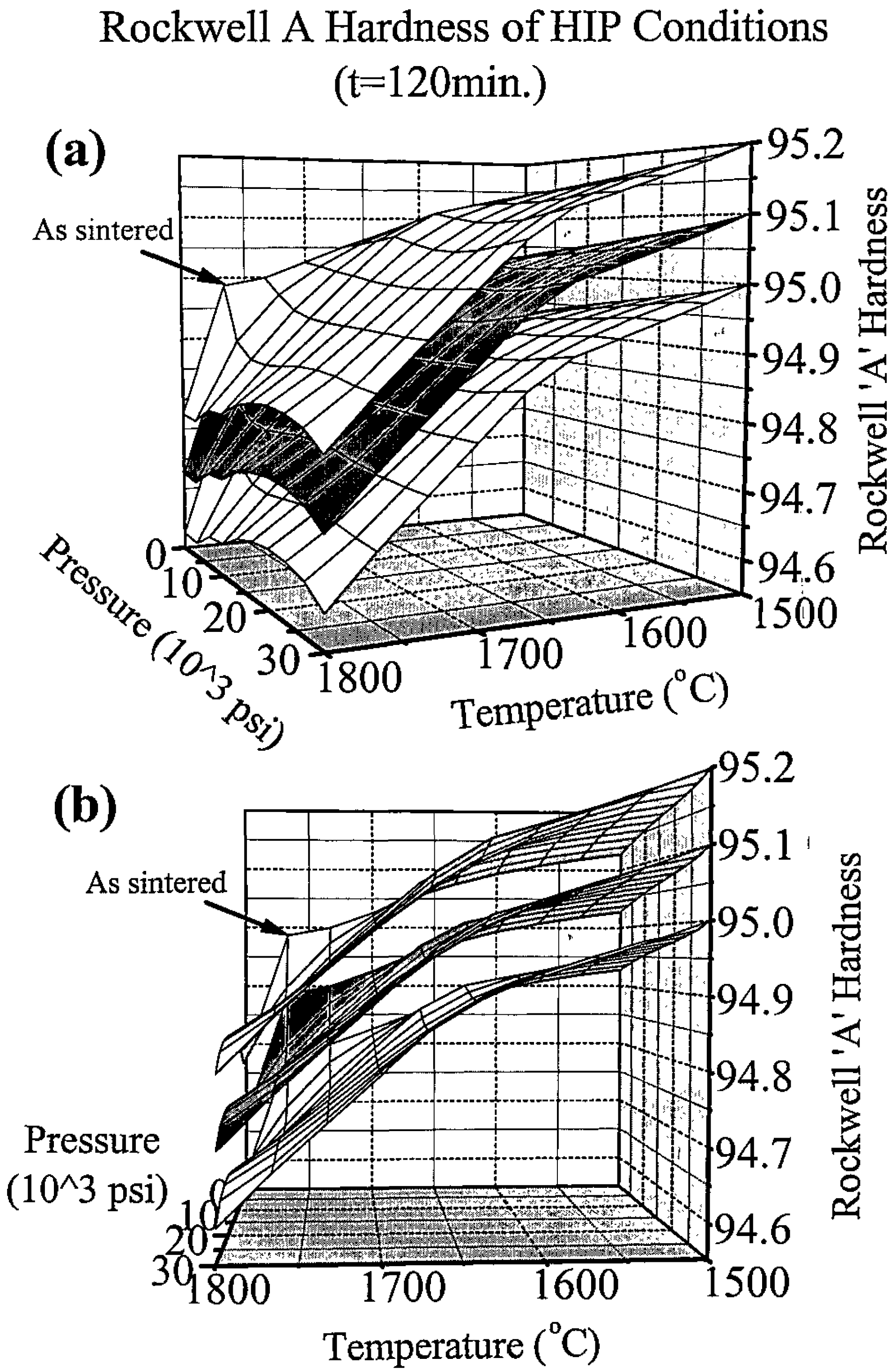

Figure 4.1. Rockwell A Hardness of the various HIP conditions for a soak time of 120 minutes. Upper and lower surfaces are error boundaries (error=0.1 HRA). (a) and (b) are different rotations of the same surfaces.

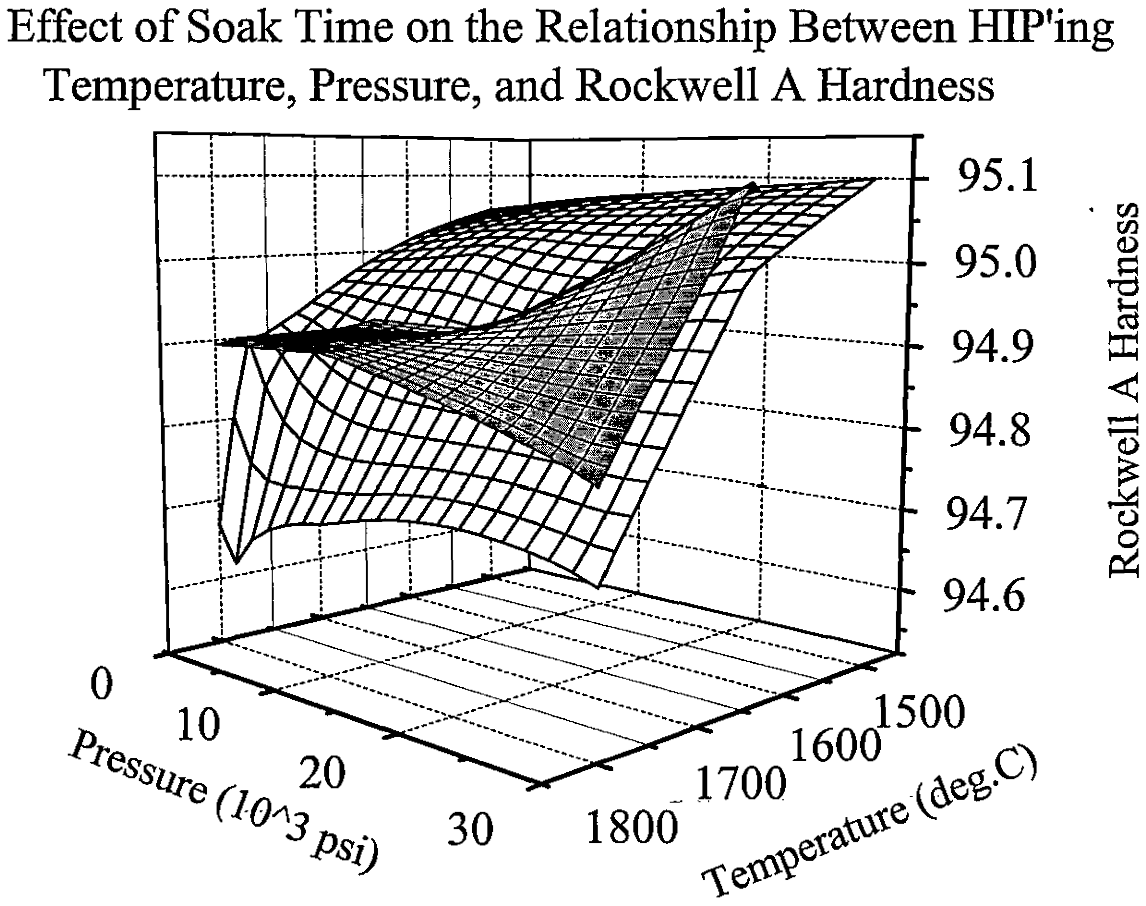

Figure 4.2. HRA as a function of HIP time. Dark and light surfaces are the 30 and 120 minute soak times repsectively. Surfaces intersect in the region of 1650° C and 10000psi.

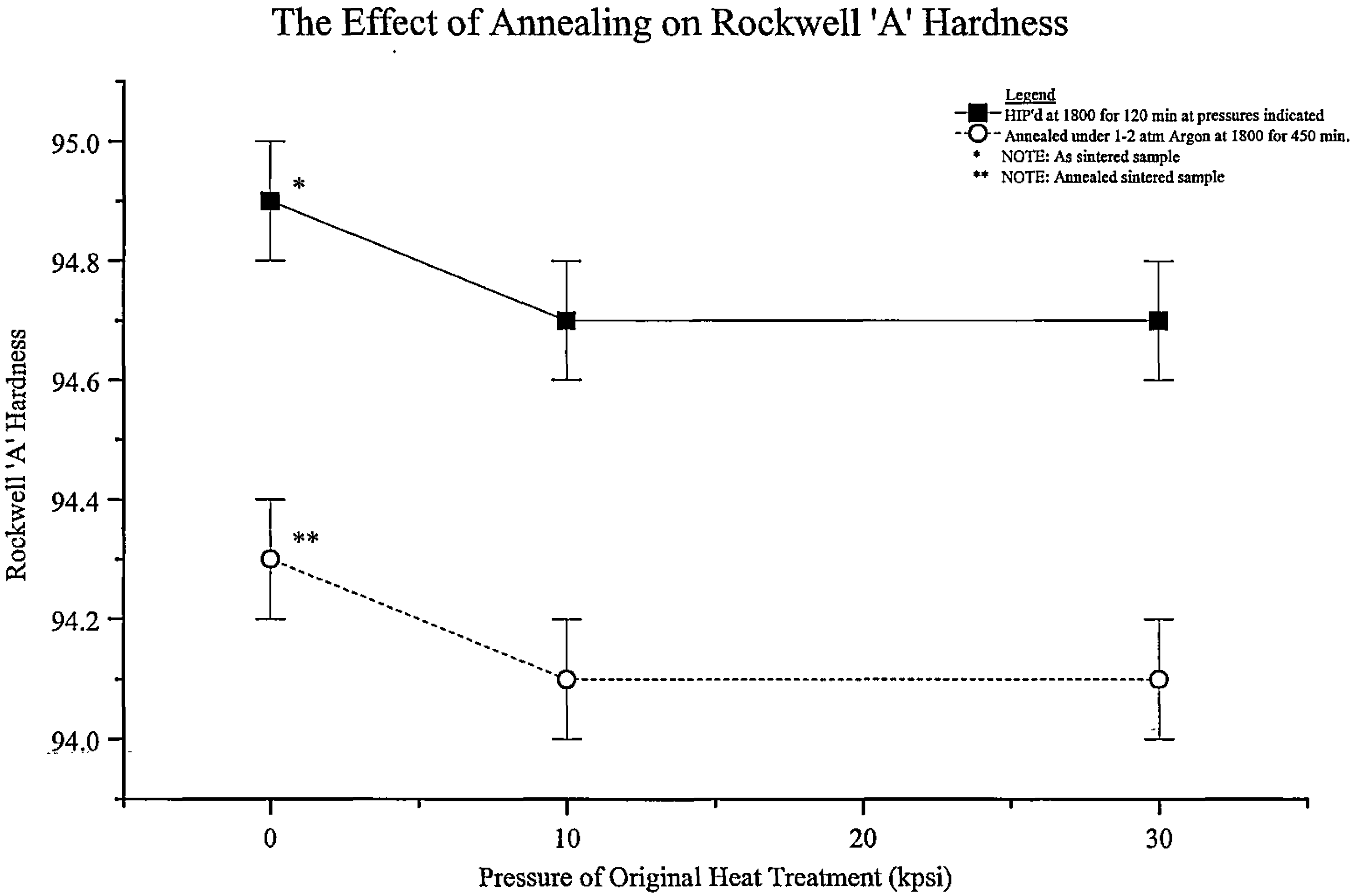

Figure 4.3. HRA before and after annealing. Errors bars are 0.1 HRA.

The final trend seen in the HRA data concerned the annealed hardness. Annealing caused a uniform decrease in HRA of 0.6HRA (0.4 outside of the error limits) for SS1, 3 and 4. See Figure 4.3 for a graphical representation. This trend was certainly real due to its shear magnitude.

The trends in the Vicker's hardness data were not found to be significantly different from those observed for Rockwell hardness. One can compare Figures 4.4-4.6 with 4.1-4.3 to see the same general shapes of the hardness surfaces as a function of the HIP conditions. However, no conclusions about the effect of time on Hv (between the 30 and 120 minute soaks) could be made due to scatter.

Although the trends from the HRA and Hv tests seem similar, the magnitude of the error for each method was different, so one has to question if trends were really there. Assuming a real trend existed, wouldn't both tests have shown it? The answer to this question depends heavily on the magnitude of the difference for the property in question. If the difference in the property being measured were small, then only the most accurate test would have detected it (if the most accurate test used could detect it!). For this study, the Rockwell hardness measurements were determined to be the most accurate, as they produced a smaller standard deviation of the mean (HRA: 1% error on hardness; Hv 5% error on hardness).

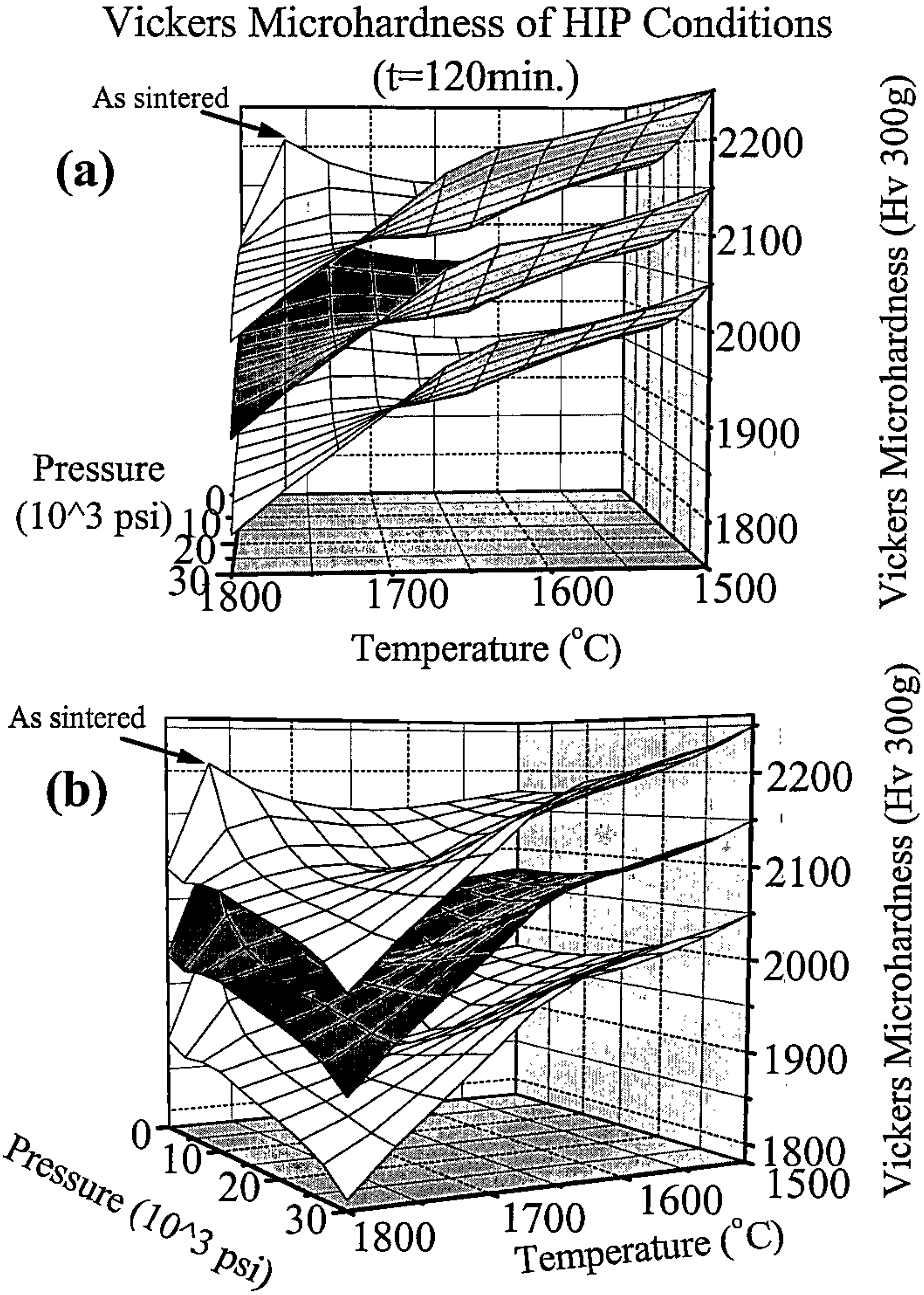

Figure 4.4. Vickers Microhardness of the various HIP conditions for a soak time of 120 minutes. Upper and lower surfaces are error boundaries (error=100Hv). (a) and (b) are rotations of the same surfaces.

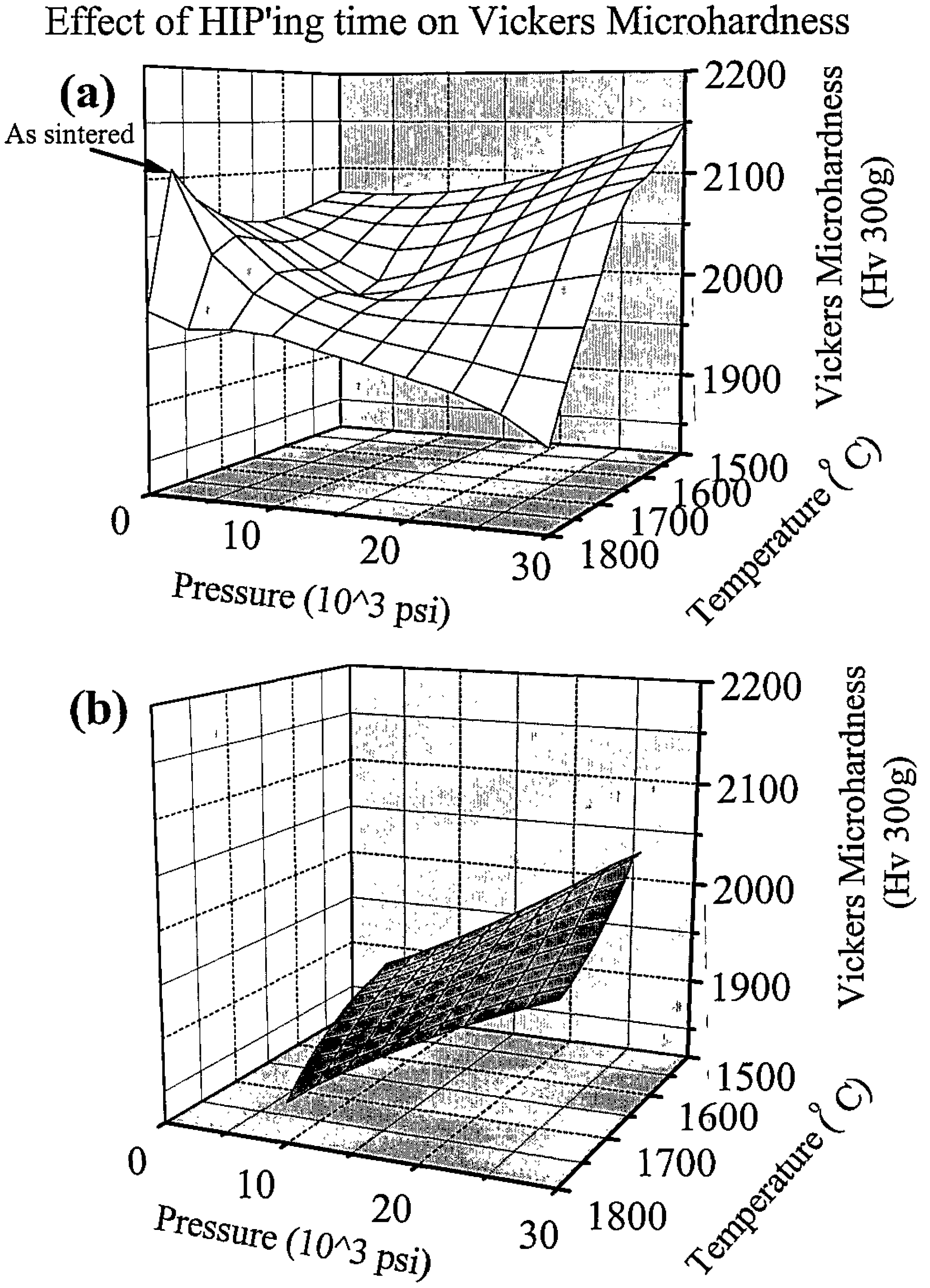

Figure 4.5. Vickers Microhardness at the various HIP conditions for a soak time of (a) 120 minutes and (b) 30 minutes.

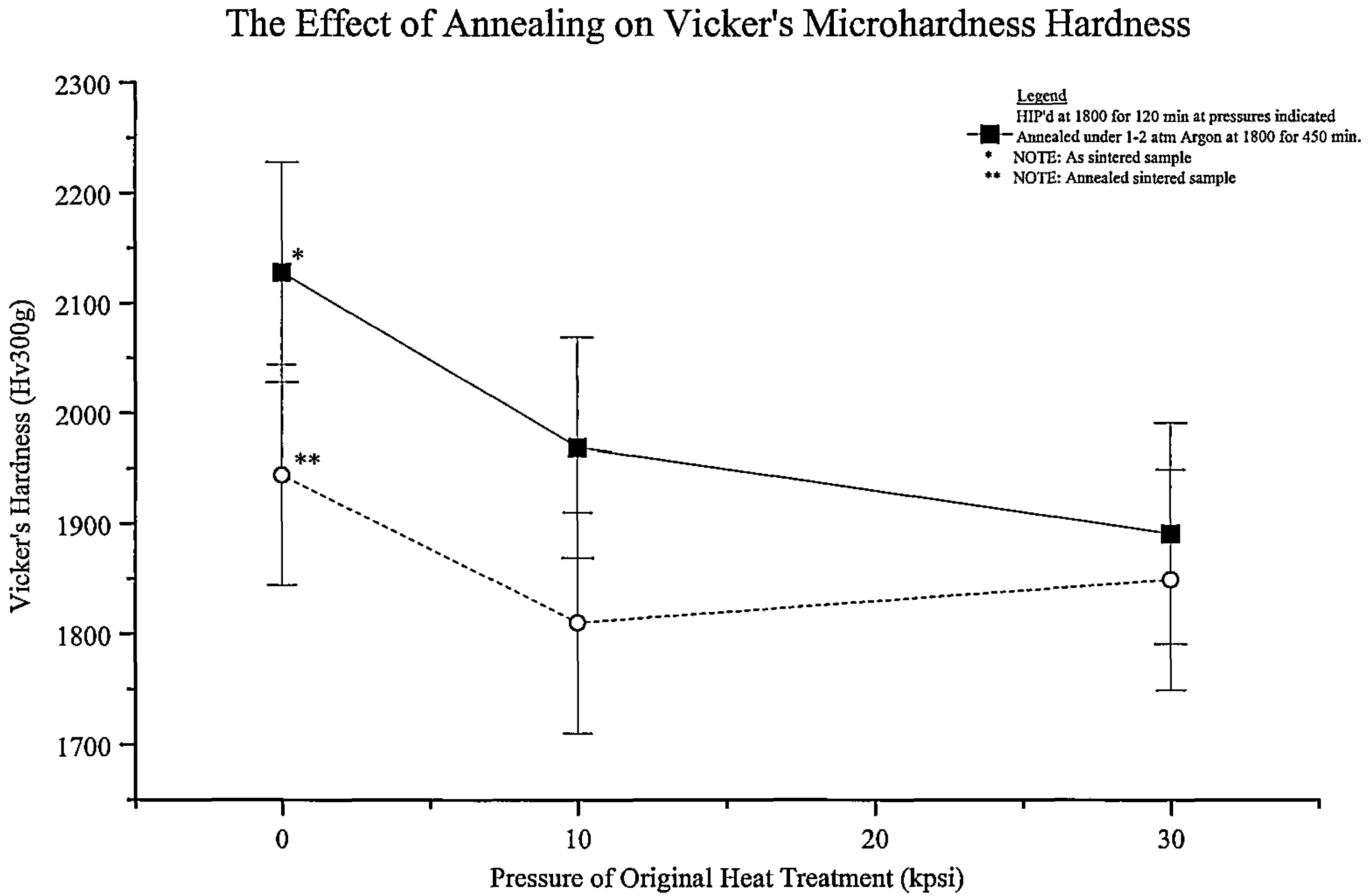

Figure 4.6. Hv before and after annealing. Errors bars are 100 Hv.

4.1.3 Indentation Toughness Results

The results of the indentation fracture toughness experiments are shown in Table 4.4. From this table the differences in K_{IC} values as a function of the HIP conditions appeared to be small, but showed trends with the temperature, pressure, and time. These trends are more easily seen with the aid of Figures 4.7 and 4.8. From these figures, the toughness can be seen to decrease with increasing temperature and pressure, but to increase slightly when HIP time was increased from 30 to 120 minutes.

Sample Set	**$K_{IC} \pm \sigma$ (MPa$\sqrt{m}$)**
SS1	7.54 ± 0.25
SS2	7.54 ± 0.31
SS3	7.45 ± 0.52
SS4	6.74 ± 0.43
SS5	7.28 ± 0.21
SS6	7.99 ± 0.40
SS1 annealed	6.42 ± 0.58
SS3 annealed	6.84 ± 0.42
SS4 annealed	6.63 ± 0.47
MS1	7.42 ± 0.22
MS2	6.23 ± 0.19
MS3	7.43 ± 0.23
MS4	7.08 ± 0.20
MS5	7.30 ± 0.21
Estimated Error	**± 0.35**

Table 4.4 Average indentation fracture toughness for all heat treatment conditions.

The question as to whether the trends observed were real or not can be settled by the results of multiple tests. Notice that the shapes of the surfaces for different HIP times (Figure 4.8) are extremely similar. With this repeatability, it is next to impossible that

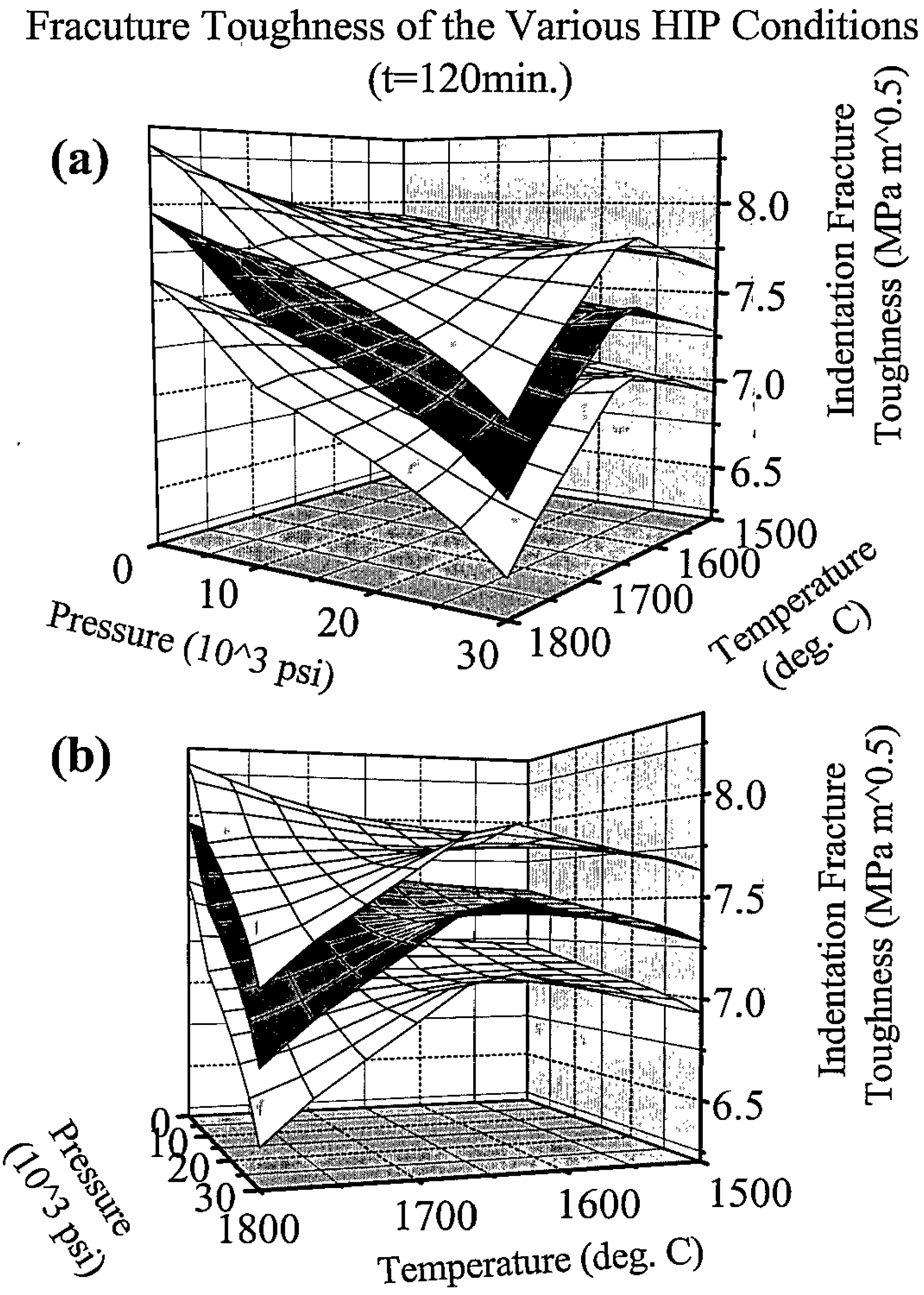

Figure 4.7. K_{IC} of the various HIP conditions for a soak time of 120 minutes. Sintered data point not present. Upper and lower surfaces are error boundaries (error=0.35MPa m^0.5). (a) and (b) and different rotations of the same surfaces.

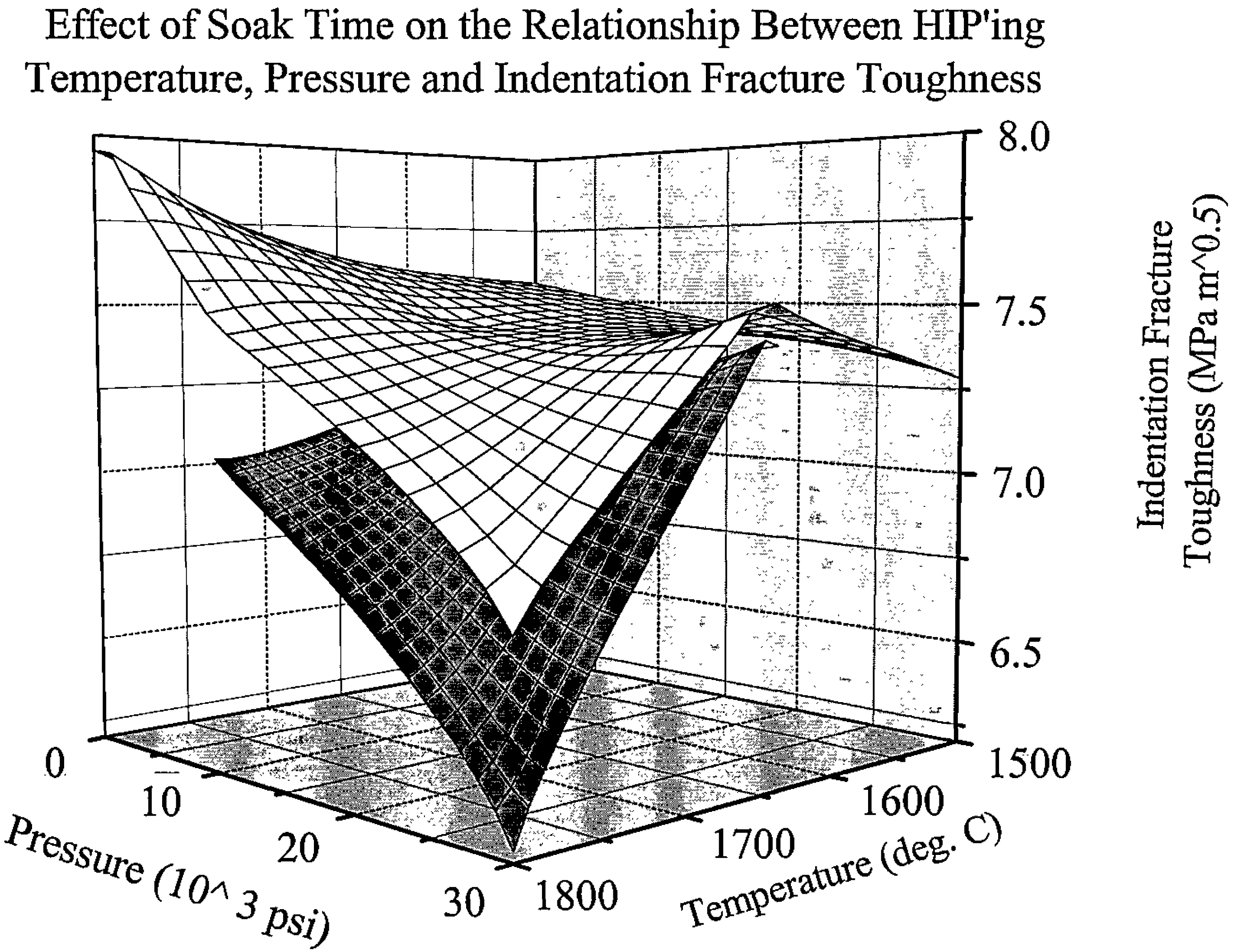

Figure 4.8. K_{IC} as a function of HIP time. Dark and light surfaces are the 30 and 120 minute soak times respectively. Sintered data point not present.

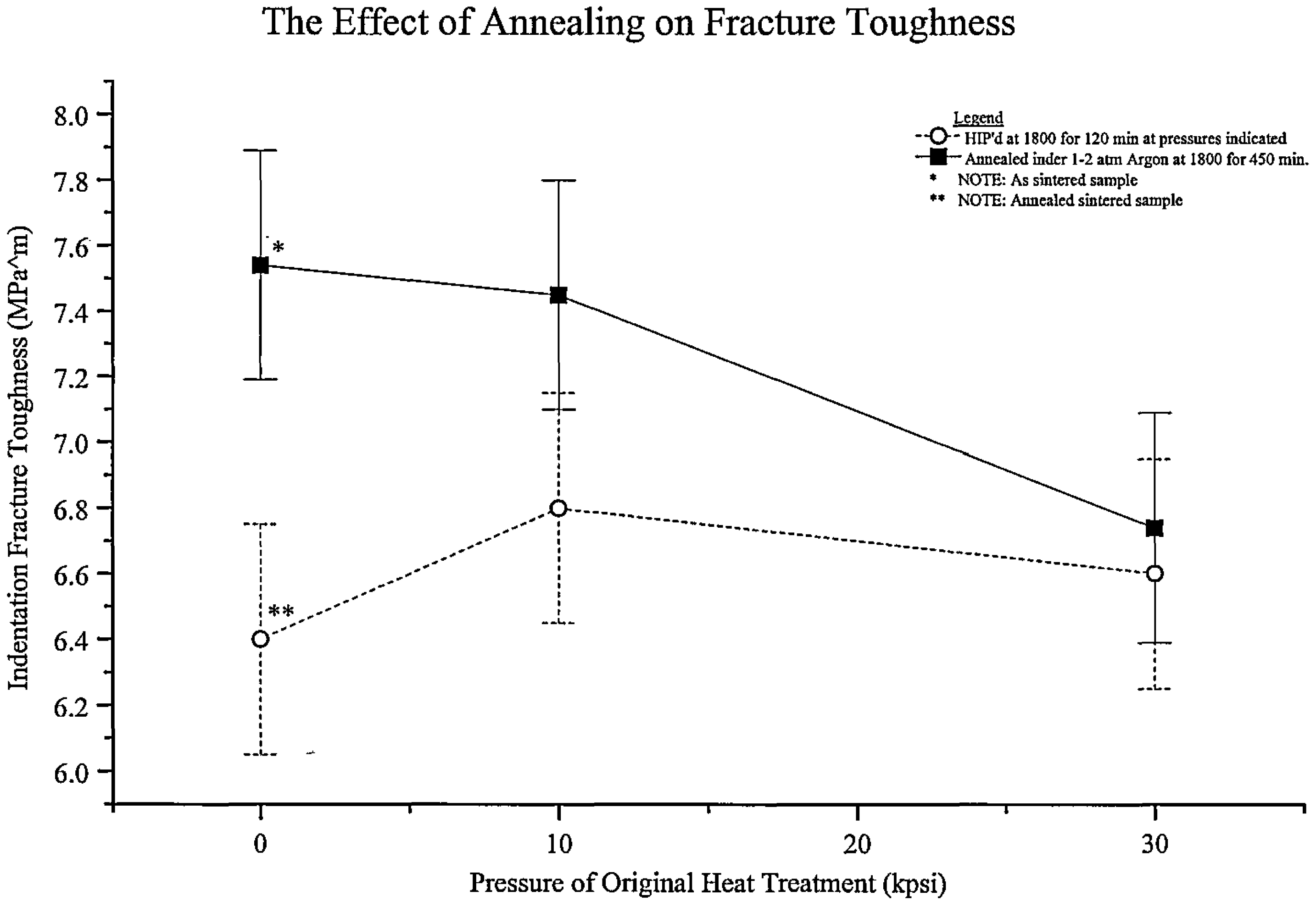

Figure 4.9. K_{IC} before and after annealing. Errors bars are 0.35 MPa^m.

scatter could have produced such similar curves on completely different batches of samples. Therefore the observed trends were thought to be true.

The effects of the annealing heat treatment on toughness are seen in Figure 4.9. While the as sintered material (SS1) undoubtedly experienced a decrease in toughness with the long annealing time at 1800°C, the other HIP conditions experienced less of a loss in toughness. It could be said that there was no detectable decrease in toughness for SS4 due to the error overlap, whereas there was likely a small decrease in the toughness of SS3.

* * * * * * * * * * *

In any analysis of only two or three data points it is difficult to say for certain that trends are present and real. However, when those results are repeatable, as seen in the hardness and toughness data of this study, the trends, however small, can be assumed to be real. Hence, investigation into microstructural phenomena becomes warranted.

The important trends extracted from the hardness and toughness testing are as follows:

1. Both HRA and Hv *decrease* with *increasing* HIP temperature, regardless of pressure or time.
2. HRA *decreases* with *increasing* HIP time at constant temperature and pressure (Hv did not have such a pronounced response to time).
3. K_{IC} *decreases* with *increasing* temperature and *increasing* pressure, regardless of time.
4. Annealing at high temperature results in a *decrease* in HRA, Hv, and K_{IC}.

For the processing conditions studied, the condition dependent effects did not seem to be very pronounced, and so there must either be competing mechanisms governing the final behaviour of the materials, or there is simply not much change in the microstructure. Chapter 5 will deal with these hypotheses.

Of potential interest for the reader are the results of tandem MicroWear tests of material fabricated using the same process as the current study, and HIP'd simultaneously with the present material. The results of Rockwell hardness and indentation fracture toughness testing are shown graphically in Figures 4.10 and 4.11. Notice that the MicroWear data supports the trends reported for the current study, thus eliminating any doubt that measurement errors were too large to detect changes in mechanical properties.

4.2 Results of Materials Characterization

4.2.1 Scanning Electron Microscopy

This section is a presentation of the observations of microstructural investigations performed in the SEM, and the results of grain size measurements. The qualitative portion will focus on findings regarding porosity, grain morphology, distribution, and relative size, and the distribution of secondary phases. Temperature was found to have affected the microstructure, but no conclusions about the effects of pressure could be made.

Four of the six HIP conditions were investigated in the SEM: SS1(A21-8), SS2 (A26-1), SS4(A29-1) and SS6(A29-6). Figures 4.12 through 4.15 show typical microstructures for each of the investigated HIP conditions after plasma etching. Very little porosity was found in any of the samples, and as seen by the micrographs in Figures

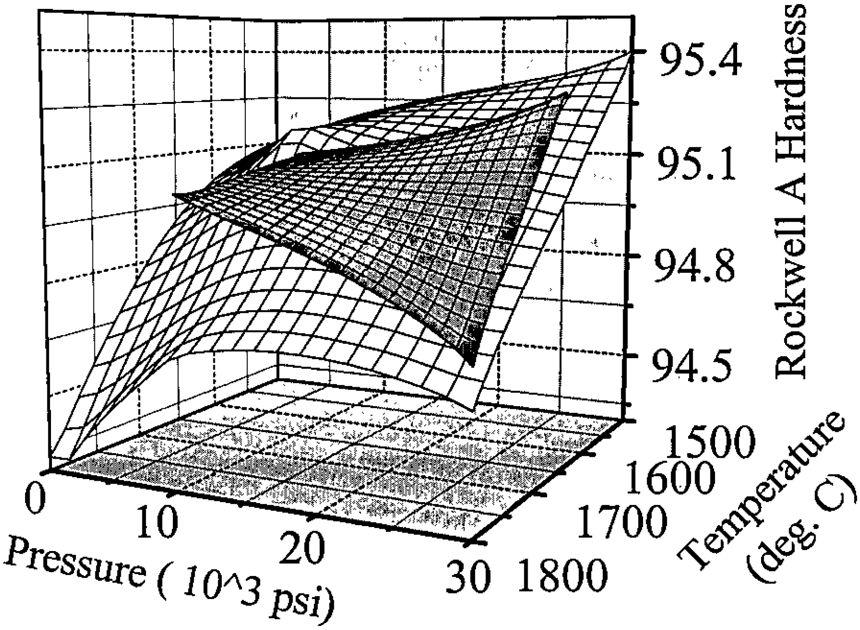

Figure 4.10. HRA as a function of HIP conditions for MicroWear Tests. Dark surface is 30 minute soak, and light surface is 120 minute soak.

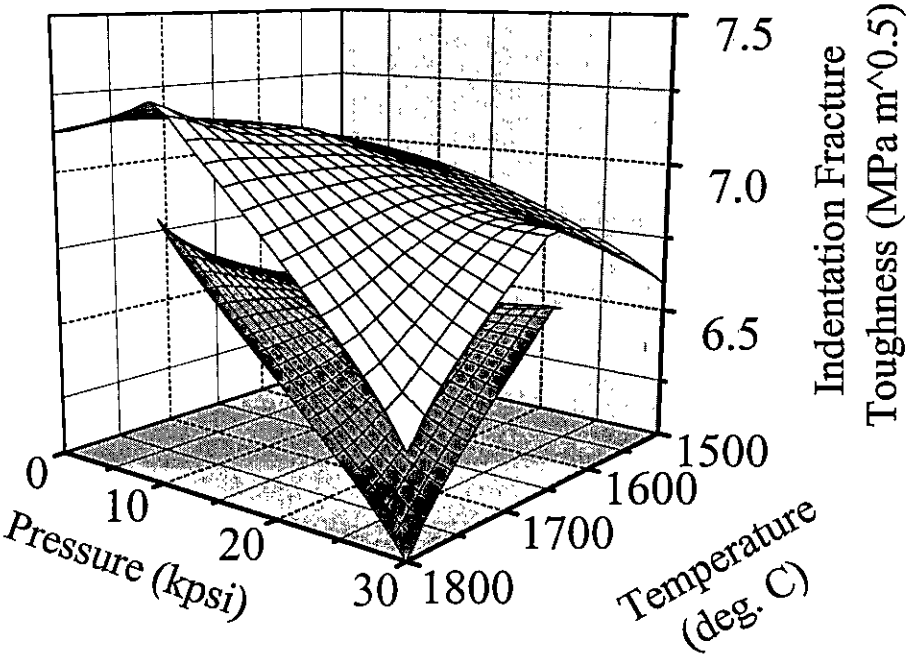

Figure 4.11. K_{IC} as a function of HIP conditions for MicroWear Tests. Dark surface is 30 minute soak, and light surface is 120 minute soak.

4.12 to 4.15. The size of any areas that were thought to be pores (blackest organically shaped holes) was extremely small (e.g.$<<1\mu m$). The bottom right hand corner of Figure 4.12a contains a pore, which is the blackest, therefore deepest, region in the field of view. The region is also at a multigrain junction, which are the only location that pores would remain stable in such materials. Recall that the topographical contrast was produced by preferentially etching rates. That being said, it was difficult to identify black areas as porosity, pullout or very small β grains. Based on the density, one would have expected there to be greater amounts of porosity in the as sintered condition, but this was not quantified nor verified by SEM investigations. The optical micrographs of the toughness indents seen in Figures E1-11 of Appendix E show the result of pullout, and pitting as a direct result of polishing, and perhaps some porosity, but it was difficult to distinguish porosity from polishing artifacts.

The α and β SiAlON phases could be easily distinguished from each other based on the depth of the etch in each phase: the β grains were elongated and more deeply etched than the α grains, whereas the α grains are not etched much past the level of the secondary phase. The most deeply etched grains, that are not necessarily elongated, can be seen within the boundaries of β SiAlON grains. These were β silicon nitride grains that were nucleation sites for the precipitation and growth of β SiAlON grains [Krämer et al., 1993; Kang and Han, 1995]. These β silicon nitride cores were present in all conditions (see Figures 4.12-4.15). It appeared that the number of β Si_3N_4 cores decreases with increasing temperature of the condition ($N_{\beta\ cores}$: SS1>SS2>SS4, SS6). However, no difference between the two pressure conditions (SS4 and SS6) could be detected. From

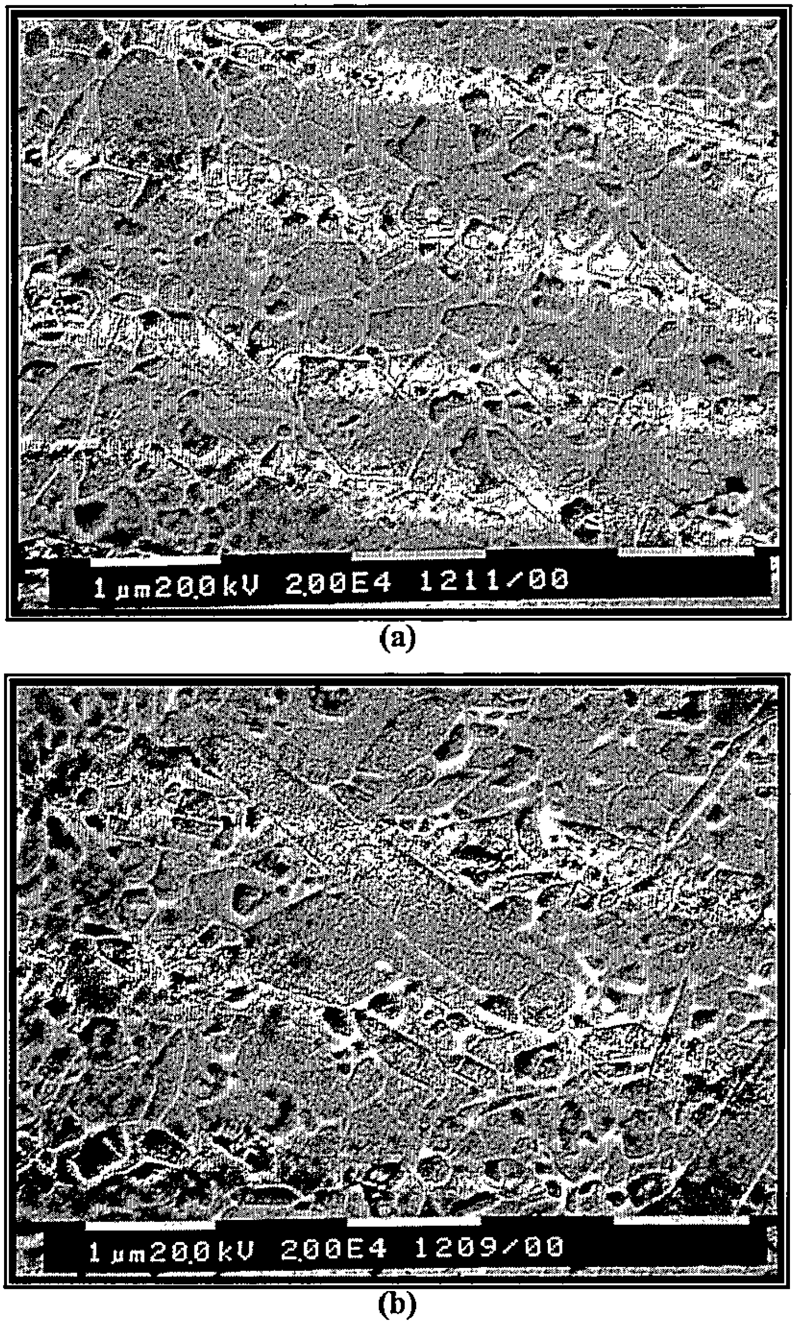

Figure 4.12. Secondary Electron SEM micrographs of as sintered (SS1) condition: **(a)** and **(b)** are different random areas in the bulk of the specimen.

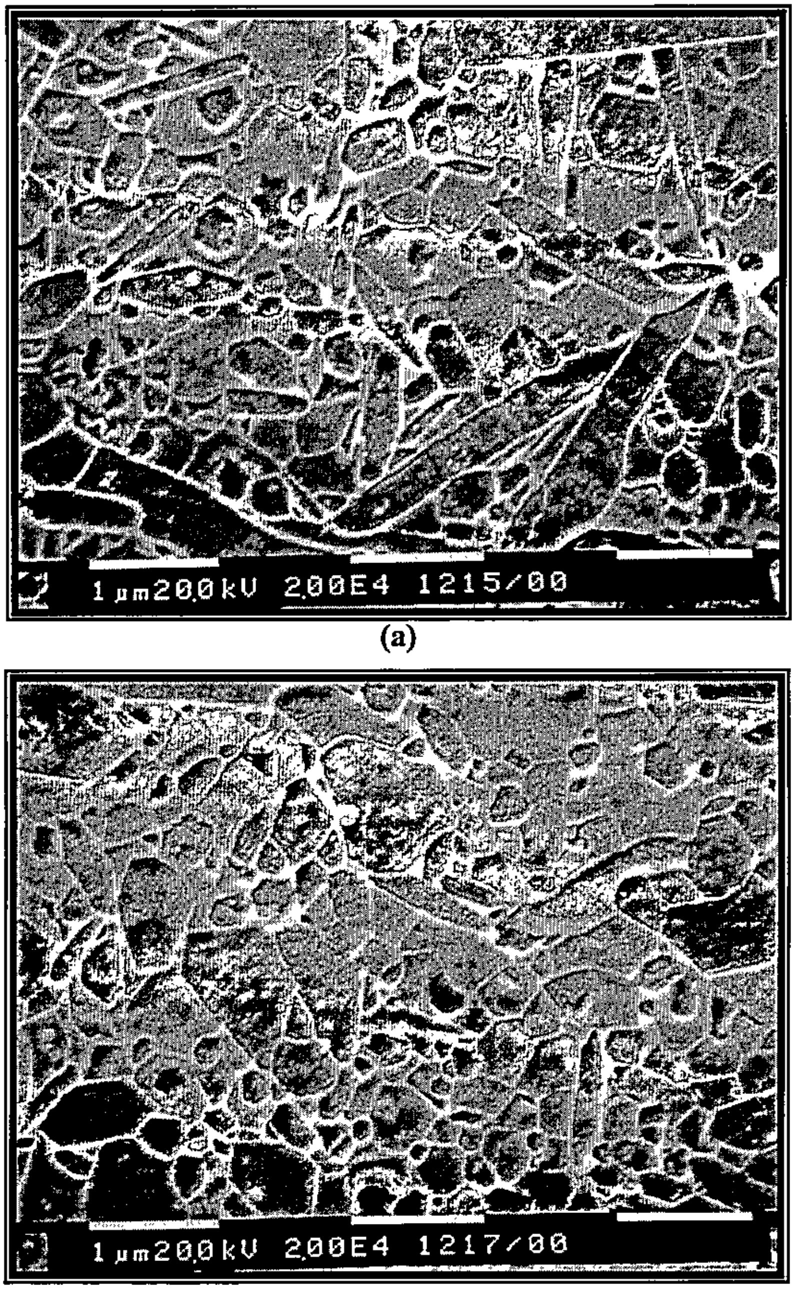

(a)

(b)

Figure 4.13. Secondary Electron SEM micrographs of 1650°C at 30000psi for 120min. (SS2): **(a)** and **(b)** are different random areas in the bulk of the specimen.

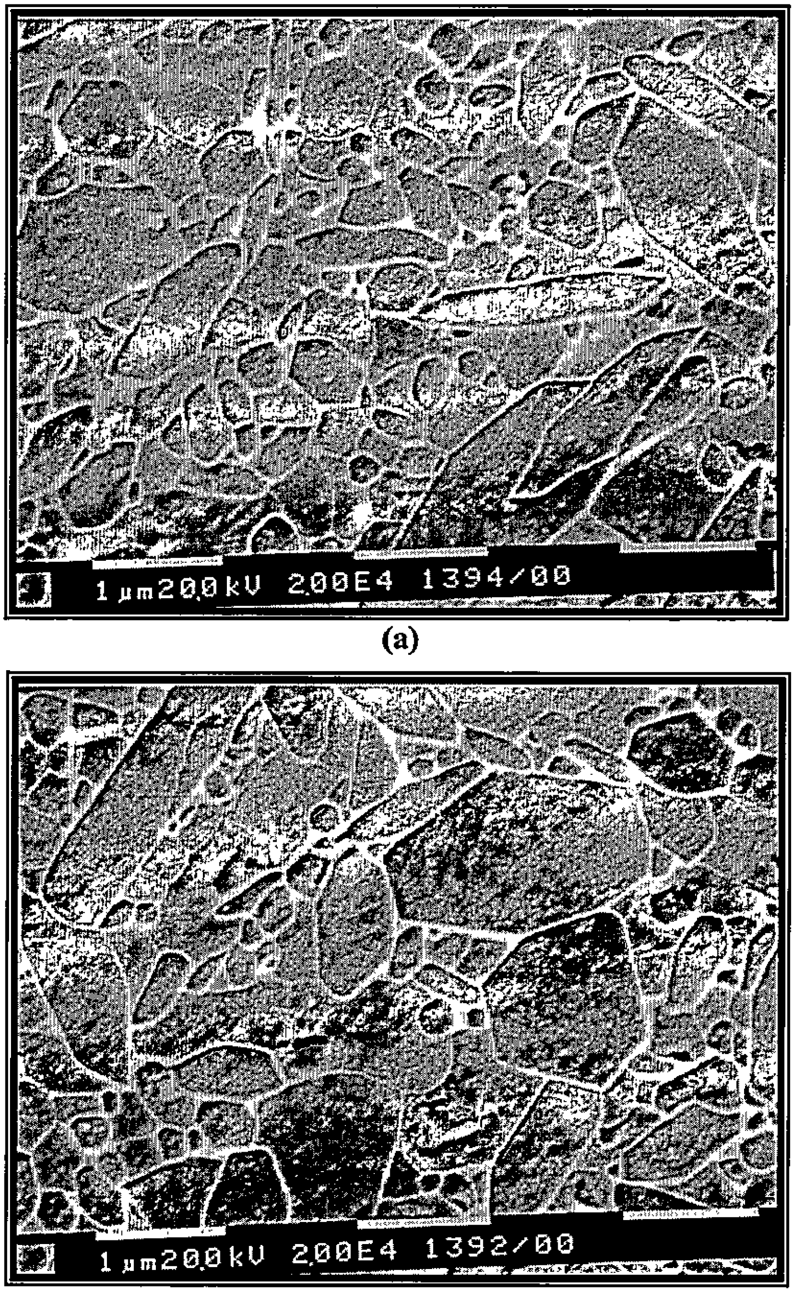

(a)

(b)

Figure 4.14. Secondary Electron SEM micrographs of 1800°C at 30000psi for 120min. (SS4): **(a)** and **(b)** are different random areas in the bulk of the specimen.

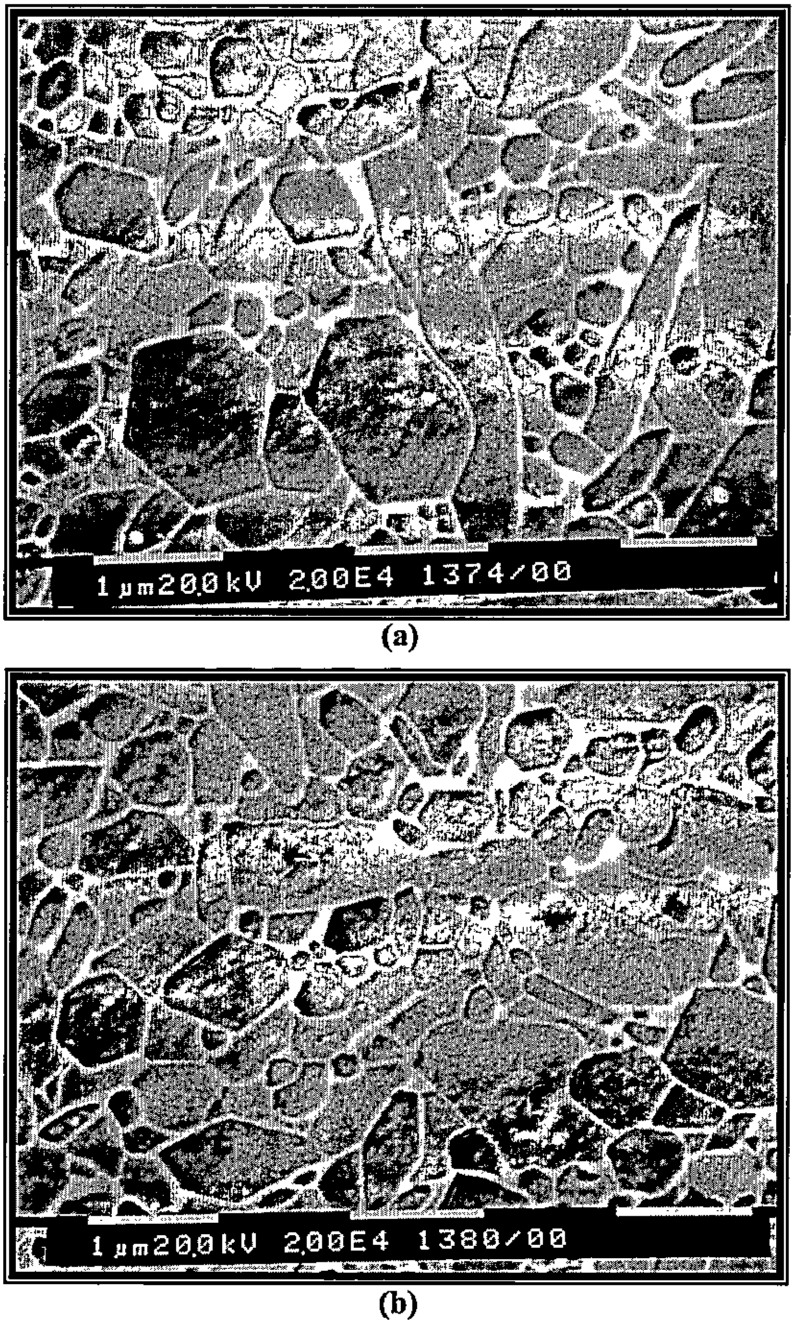

Figure 4.15. Secondary Electron SEM micrographs of 1800°C at 1000psi for 120min. (SS6): **(a)** and **(b)** are different random areas in the bulk of the specimen.

here forward, any discussion of α and β grains (or phases) will be in reference to SiAlON phases, not Si_3N_4 phases unless explicitly stated.

The size of the α and β grains was observed to be different. From the micrographs, the β grains had various minimum diameters ranging from ~100nm to >1μm, whereas the α grains ranged from ~200nm to 600nm. Fewer of the smaller β grains were observed as the temperature was increased ($N_{small\ \beta}$: SS1>SS2>SS4, SS6). This apparent reduction in the number of small β grains could be seen easily when comparing Figure 4.12 with either Figure 4.14 or 4.15.

Another obvious difference between the specimens was the apparent increase in the average β grain diameter with increasing temperature (D_β:SS4,SS6>SS2>SS1). Concomitant with the apparent increase in β grain diameter was a slight reduction in the maximum (not mean) α grain diameter. The decrease in the α grain diameter was only observed between SS2 and SS4 or SS6. It was difficult to see any trends in the α/α+β ratio, but it appeared as though there was a decrease in α content ratio with increasing temperature above 1650°C.

The aspect ratios of the grains appeared to be on the order of 5-10 for all samples with the length usually being 1-3μm. In some cases the length was found to be over 10μm (Figures 4.16 through 4.18). It was difficult to discern any large differences in aspect ratio between the samples examined, so no trends are reported here.

Figures 4.16 through 4.18 show the results of collecting backscattered electrons, and hence have atomic number contrast. The identification of the α and β phases was much easier in this mode, but delineation of the grain boundaries was poor, especially at α-α grain boundaries (Figure 4.18). Since α contained yttrium it was seen as the equiaxed gray phase, and β as the dark elongated phase.

Secondary phase regions were seen as flat bright regions located at multigrain junctions (see Figures 4.12 to 4.15). These regions were etched the least, so appear as the highest regions on the sample surface. Another secondary grain boundary phase was visible as white lines surrounding α and β SiAlON grains. It was difficult to tell whether or not the composition was different between the multigrain and two-grain junctions due to the small thickness of the two-grain boundary layer. However, the two-grain boundaries did not appear to be as white as the multigrain junction regions, suggesting that there was less (or no) yttrium present. An alternative explanation could be that the two-grain boundaries were simply too thin to produce enough contrast. Due to the small grain size no EDX was done on the samples, as the spatial resolution was not adequate.

The different modes of operation in the SEM revealed trends in the size and distribution of the secondary phases as functions of both the HIP temperature and pressure. SS2 contained some areas with heterogeneity in the secondary phase distribution at multigrain junction pockets. The heterogeneity is seen well in Figures 4.19-4.21[1]. Notice that SS2 had much larger, and well-defined regions of secondary phase as compared with SS1 (Figure 4.16). It was not determined if the total area of secondary phase differed between these conditions, but the number of secondary phase

---

[1] The samples examined at UMEX (as noted in Figures 4.19 and 4.20) were Cr coated.

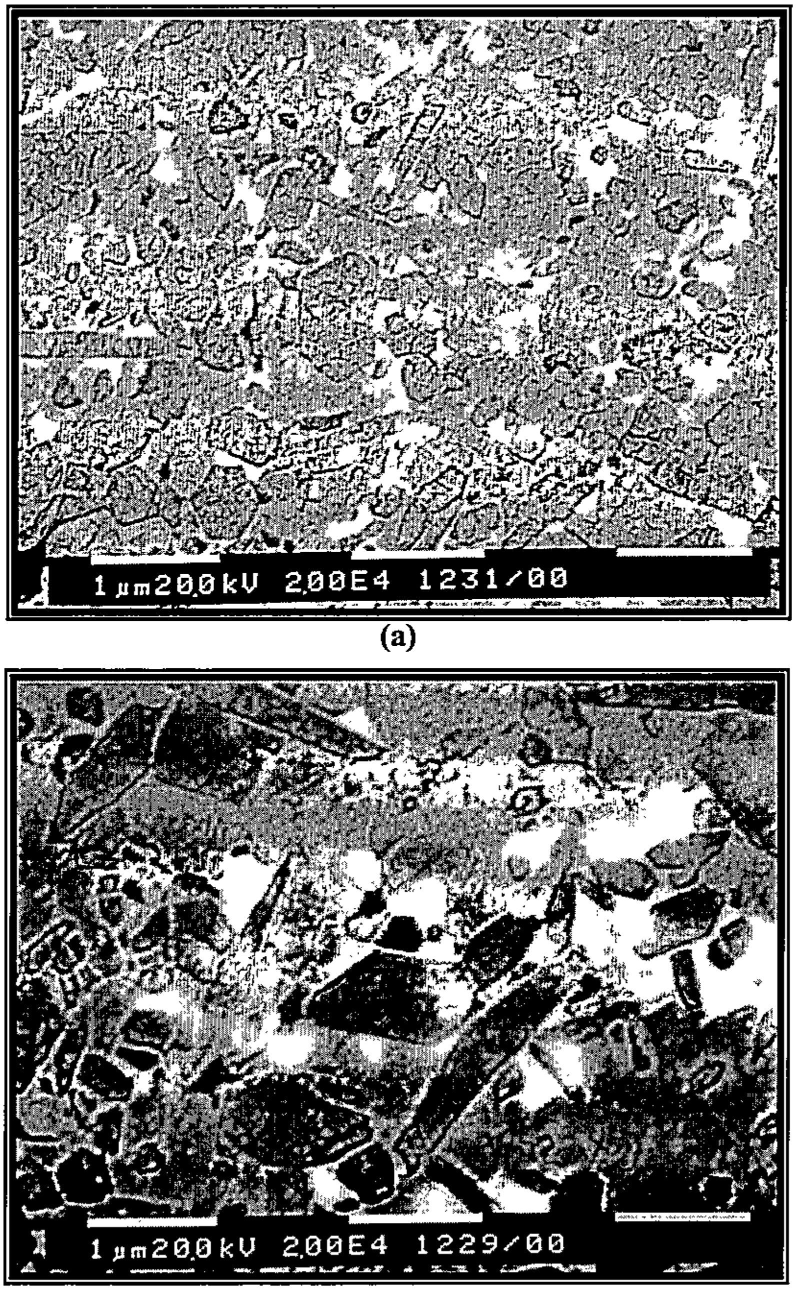

Figure 4.16. Backscattered Electron SEM micrographs of **(a)** SS1 and **(b)** SS2.

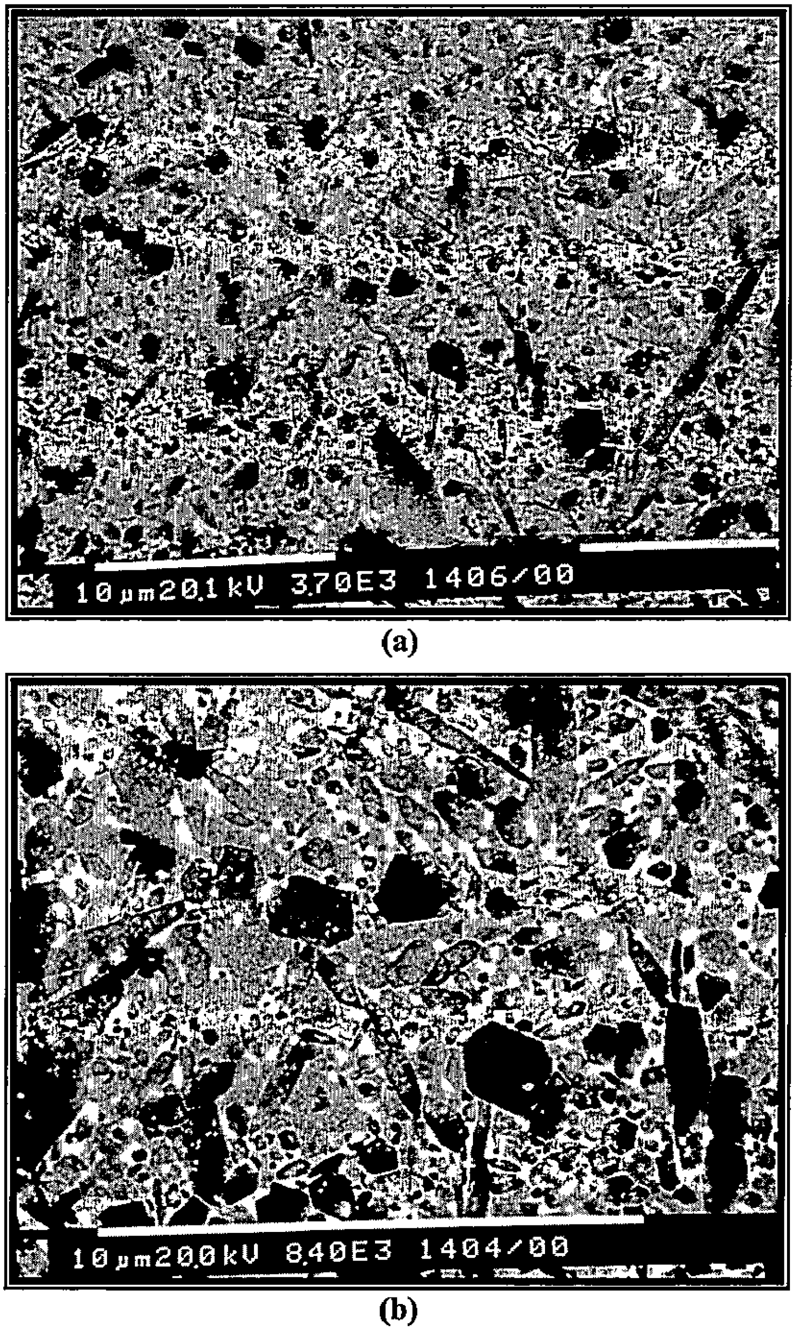

(a)

(b)

Figure 4.17. Backscattered Electron SEM micrographs of SS6: **(a)** and **(b)** are different magnifications of the same area.

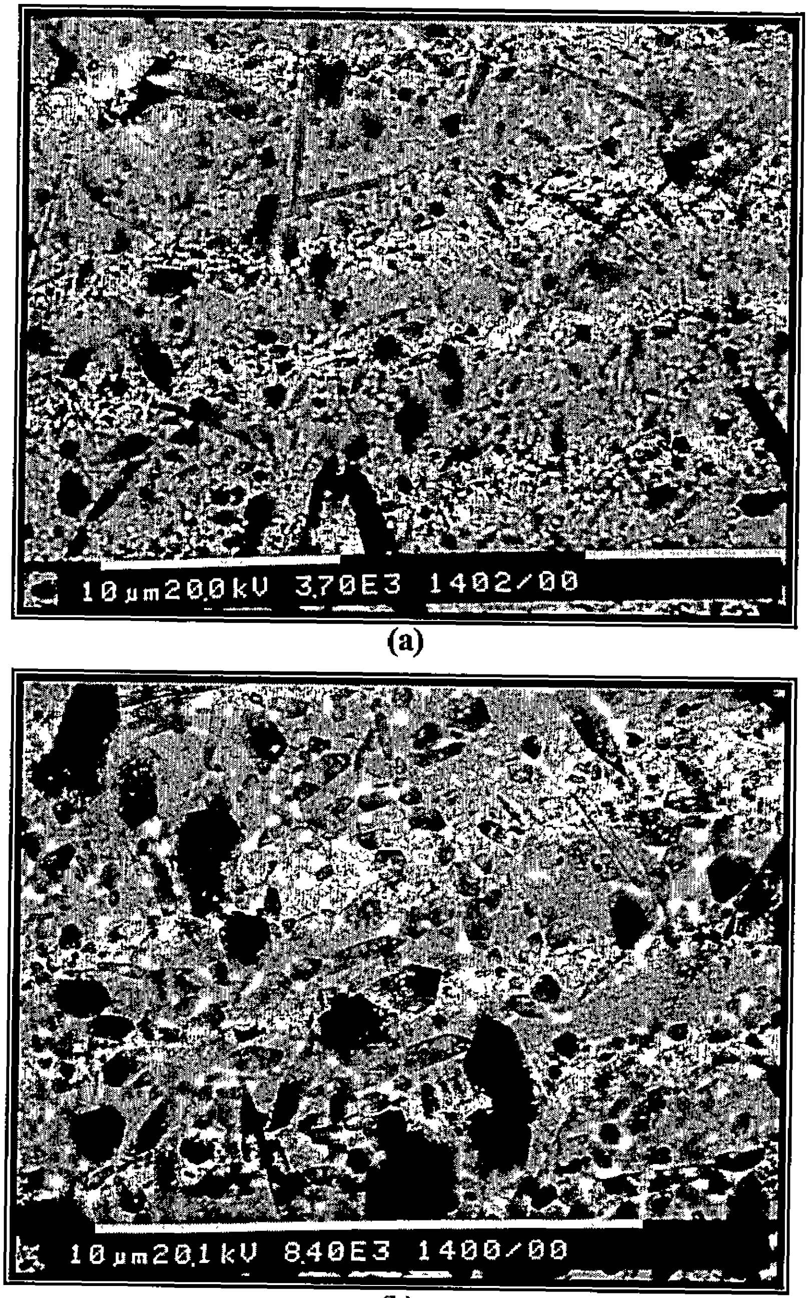

(a)

(b)

Figure 4.18. Backscattered Electron SEM micrographs of SS4: **(a)** and **(b)** are different magnifications of the same area.

regions was thought to be different. The heterogeneity was believed to be heat treatment condition related phenomenon rather than a sampling effect because more than one sample in SS2 showed the same behaviour. No other conditions showed similar heterogeneity.

In summary, qualitative SEM investigations revealed that the microstructure contained at least three discrete phases: α and β SiAlON with an yttrium rich multigrain junction phase. A fourth phase distributed along two-grain junctions was unconfirmed, but appeared to be chemically different from the multigrain junction phase

The distribution of the secondary phases experienced changes as a function of temperature, and to a lesser extent pressure. SS2 was found to have a heterogeneous distribution of multigrain junction phase, whereas all other conditions had fairly uniform distributions. On average, the regions of multigrain junction phase were much larger in area in SS1 and SS2 than in the high temperature conditions, and there appeared to be more secondary phase present. A slight decrease in the number of large multigrain junction pocket areas was detected as the pressure was increased (at high temperature).

Increasing the HIP temperature resulted in a slightly greater amount of β phase. The β phase also appeared to have experienced grain coarsening with increasing temperature. Lastly, the number of β SiAlON grains with β Si_3N_4 cores decreased with increasing temperature. No differences whatsoever, were observed in grain size as a function of pressure.

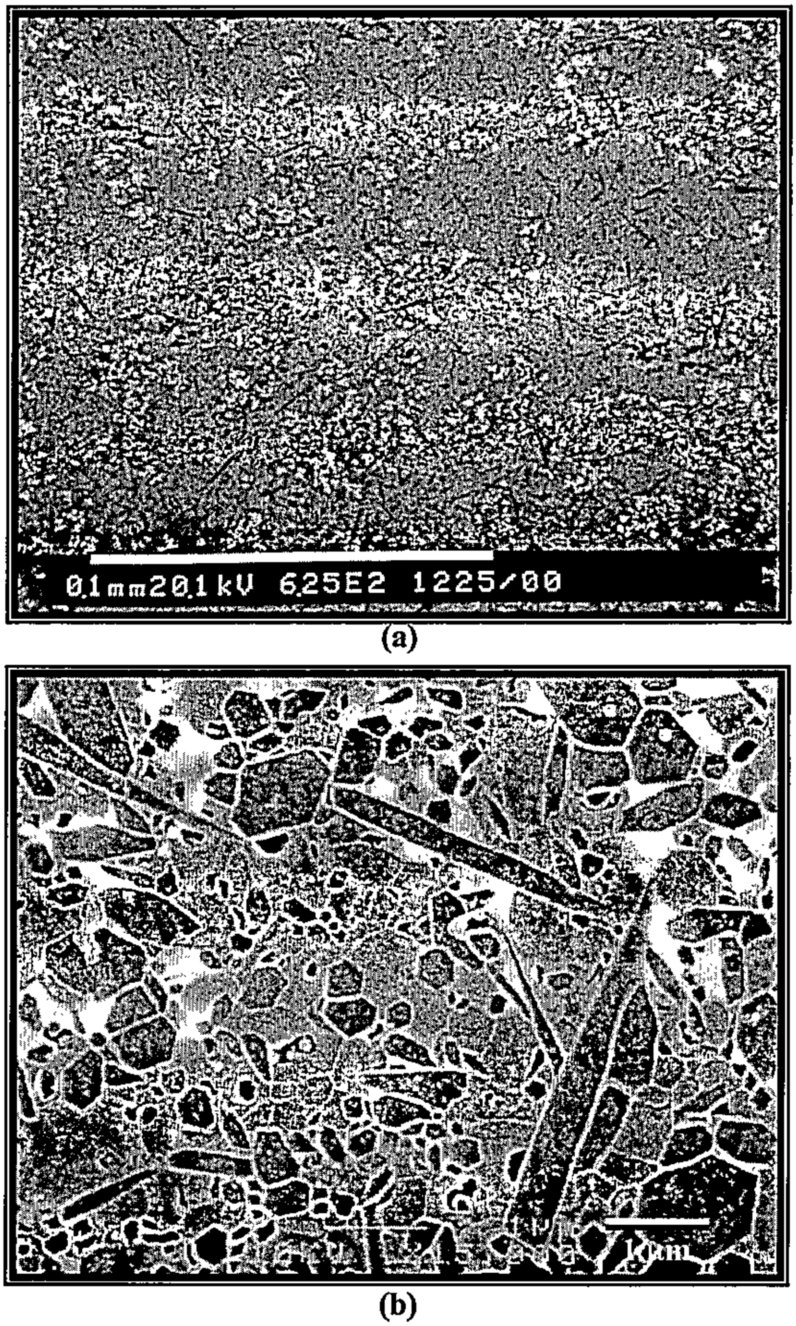

Figure 4.19. SEM micrographs of SS2 (A26-1) showing the heterogeneity of the yttrium rich secondary phase at multigrain junctions: **(a)** backscattered electron image, and **(b)** secondary electron image (UMEX).

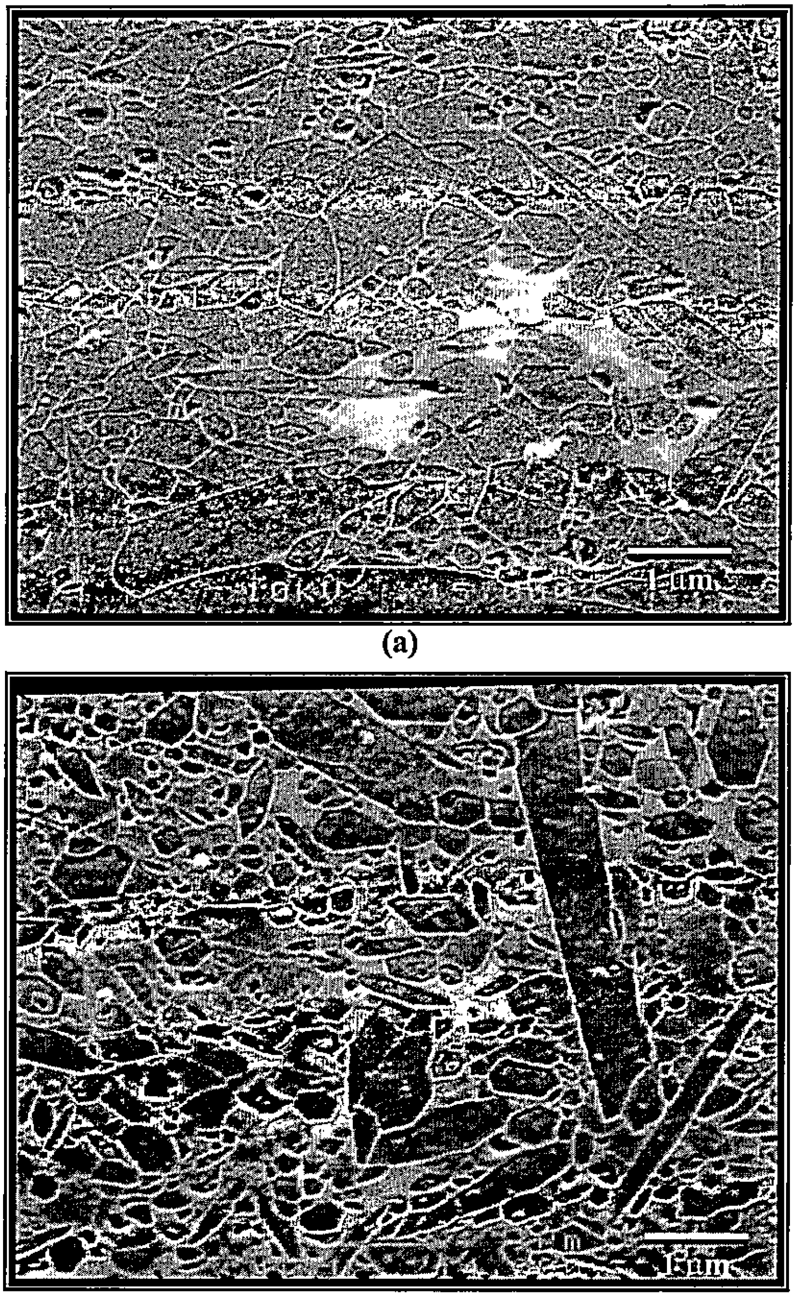

(a)

(b)

Figure 4.20. SEM micrographs of SS2 showing the heterogeneity of the yttrium rich secondary phase at multigrain junctions: **(a)** secondary electron image (A27-2) at 45° tilt, and **(b)** secondary electron image (A26-1) at 45° tilt. Both (a) and (b) taken at UMEX.

Figure 4.21. ESEM micrograph of SS2 (A27-2) showing the heterogeneity of the yttrium rich secondary phase at multigrain junctions. ESEM secondary electron mode.

The measurement of grain diameter in the SEM was performed on SS1(A21-8), SS2 (A26-1), and SS4(A29-1). The reason so few samples were chosen was based on the observations from the qualitative SEM work. The difference between the lowest pressure and highest pressure condition was not very significant, so only the high pressure condition was examined. There was no great difference between the as sintered and mid-temperature condition, so the low temperature condition was left out of the characterization.

As was alluded to in section 3.5.4, the magnification at which the grain diameters were measured resulted in different errors on the grain size. Figures 4.22 and 4.23 show the raw frequency plots of the minimum grain diameters for SS1 and SS2 (SS4 had only high and intermediate magnification measurements done). A bin size of 0.1μm was used in all frequency plots. The distributions seem to be log-normal except at low magnification, which appeared to be more Gaussian. The low magnification measurements were thought to contain a high degree of measurement error, and therefore cause a spurious shift in distribution to higher average grain diameter. The low magnification data was therefore deemed inaccurate, and was not used in any further analysis.

The high and intermediate data had similar distributions, and were therefore grouped into one data set for each condition so that an overall grain diameter distribution could be determined (see Figures 4.24 to 4.26). Regression analysis resulted in the determination of the parameters in Equation 3.6b. The results of the analysis are shown in Figure 4.27 and Table 4.5.

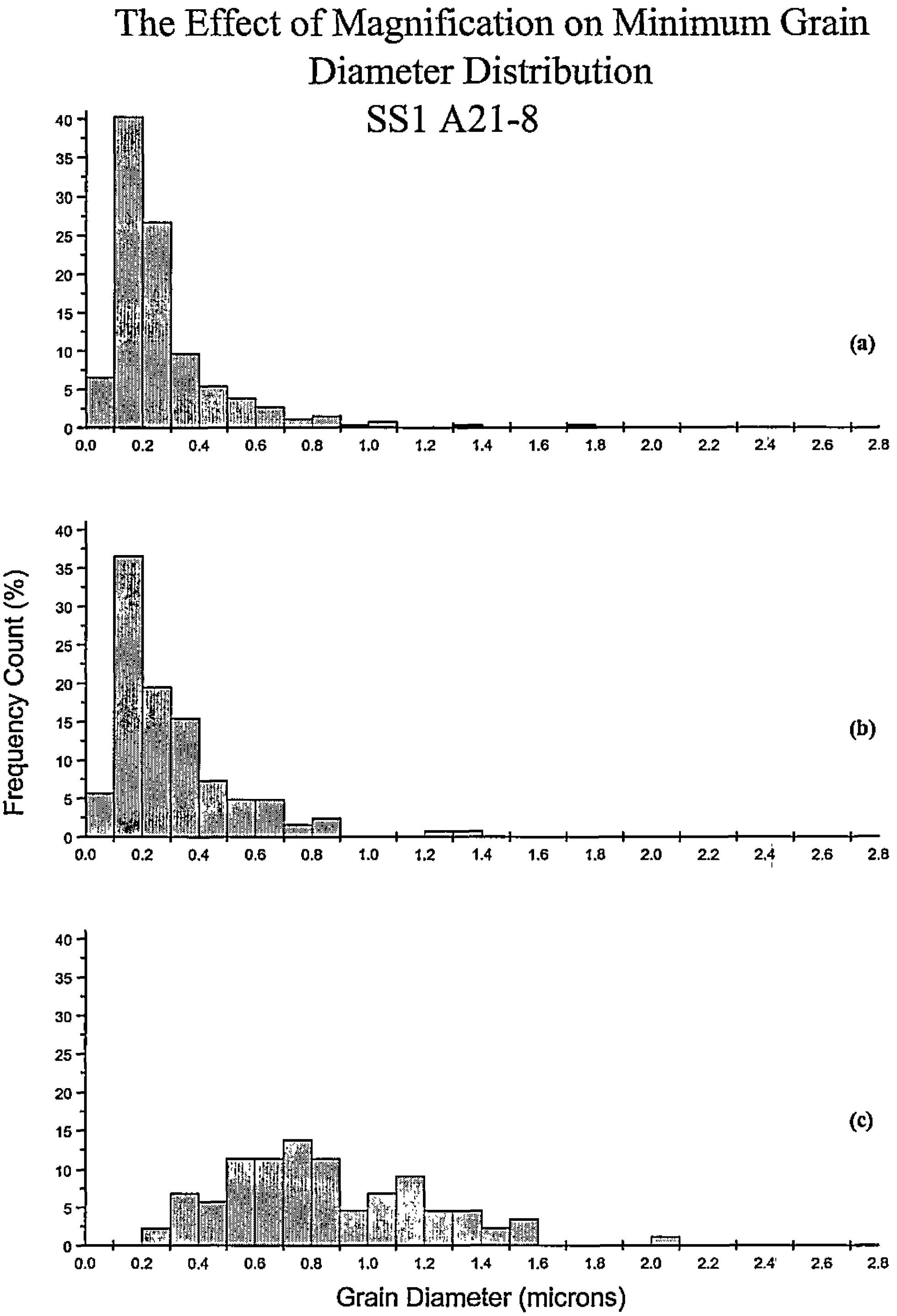

Figure 4.22. Comparison of minimum grain diameter as a function of magnification. Sample A21-8 (1775/00/15). (a) 21800X, N=258; (b) 11400X, N=123; (c) 2720X, N=87.

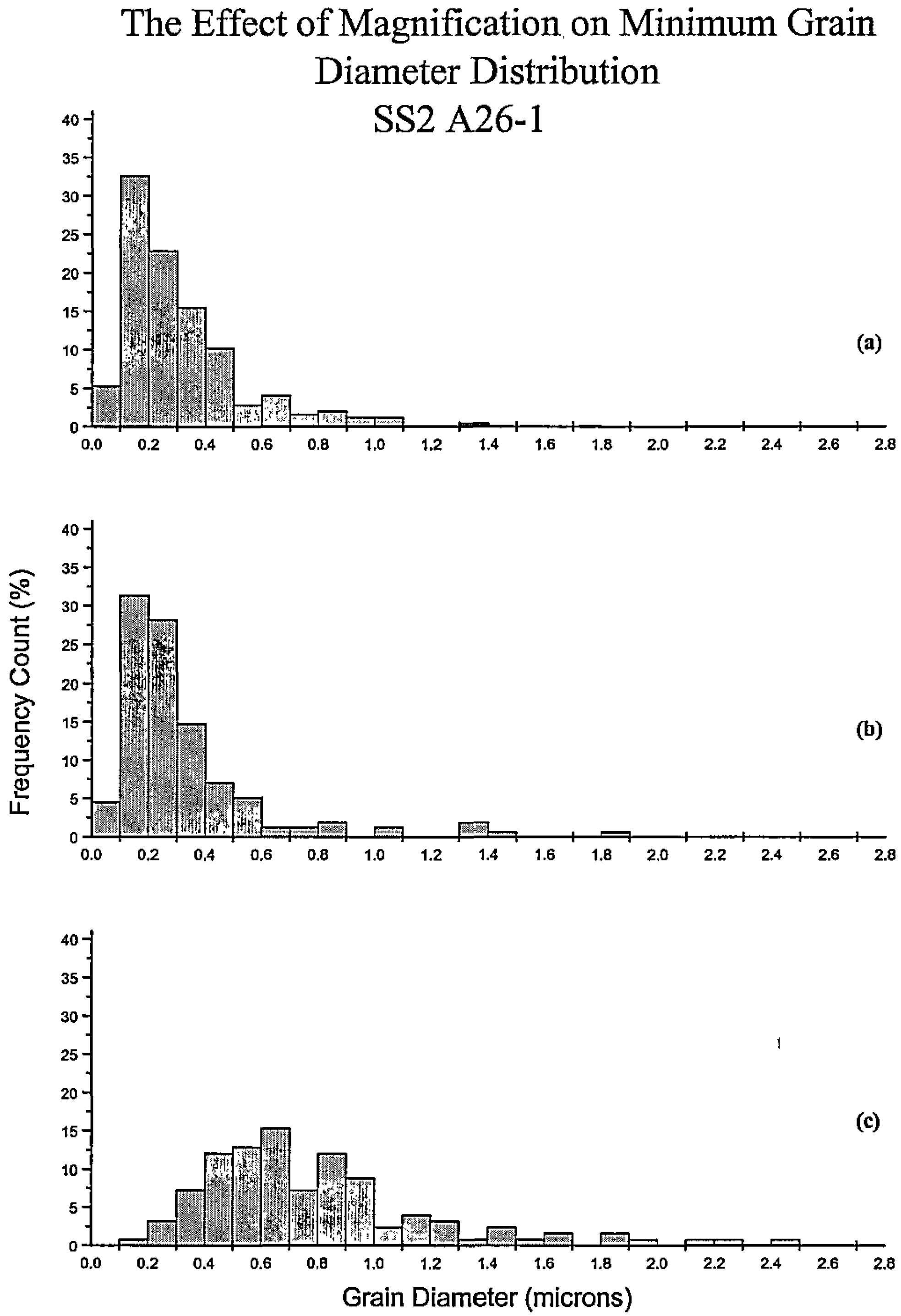

Figure 4.23. Comparison of minimum grain diameter as a function of magnification. Sample A26-1 (1650/30/120). (a) 21800X, N=245; (b) 11400X, N=156; (c) 2720X, N=124.

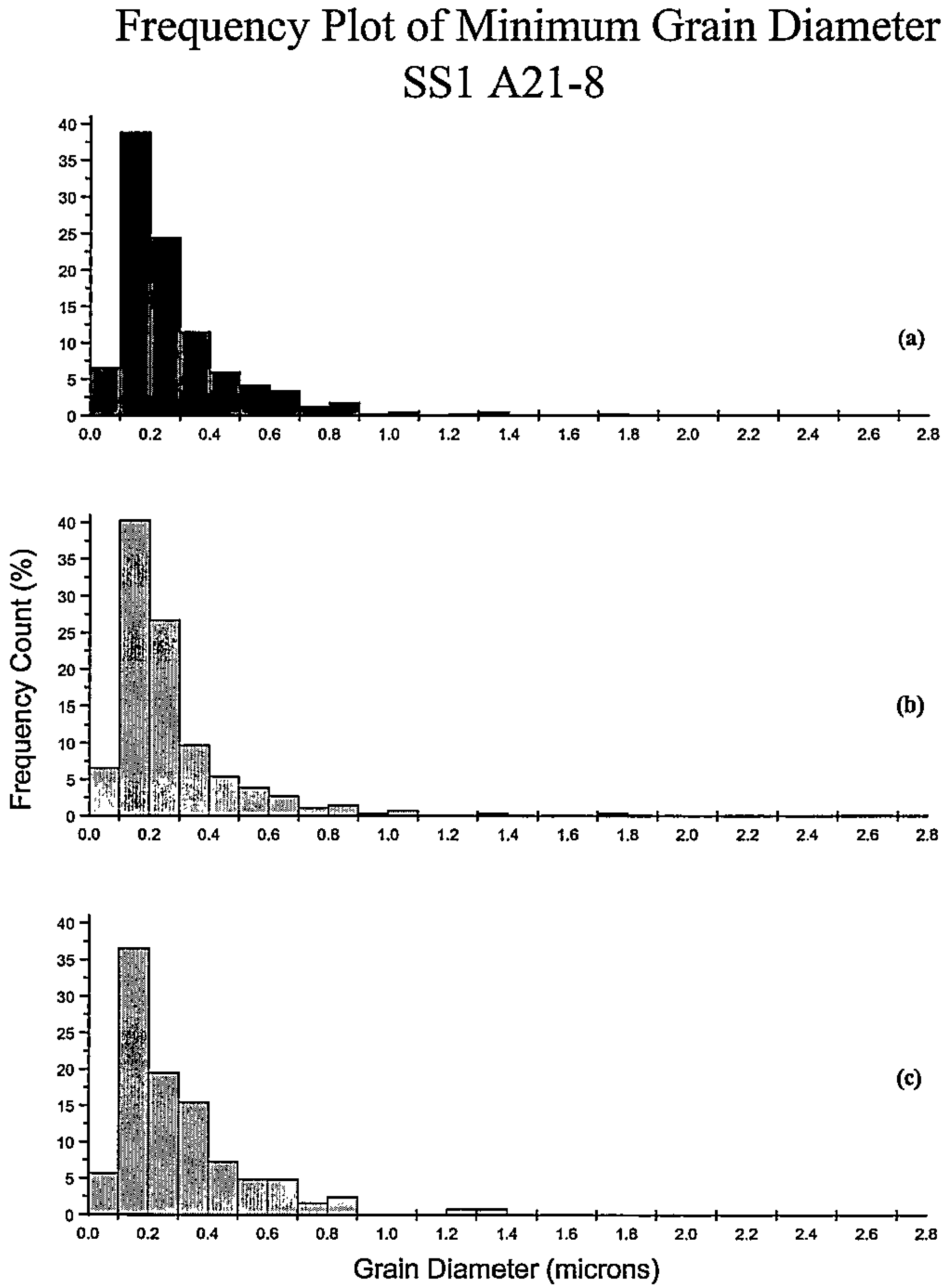

Figure 4.24. Minimum grain diameter at high and intermediate magnification. Sample A21-8 (1775/00/15). (a) Summation of (b) and (c), N=381; (b) 21800X, N=258; (c) 11400X, N=123.

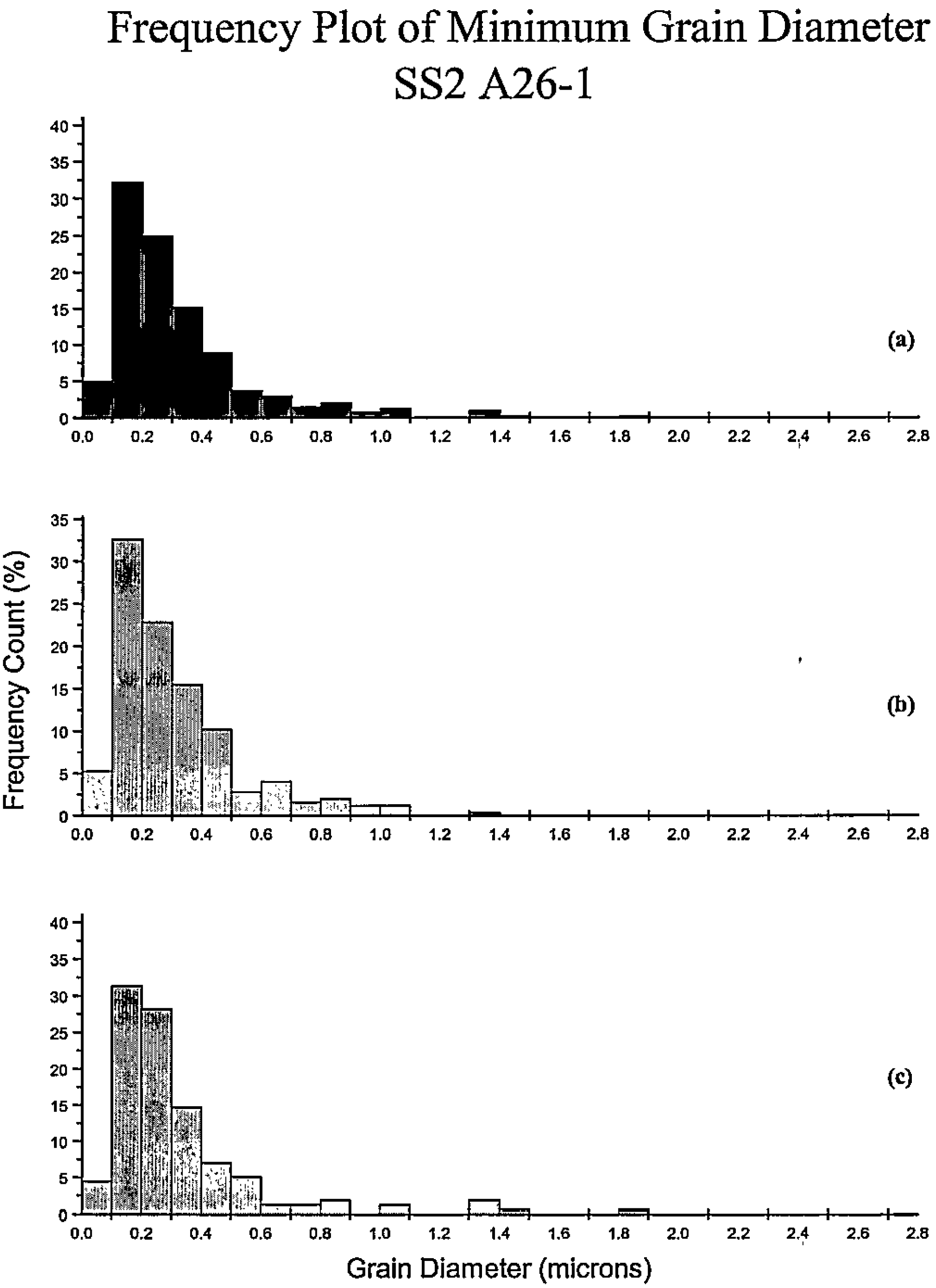

Figure 4.25. Minimum grain diameter at high and intermediate magnification. Sample A26-1 (1650/30/120). (a) Summation of (b) and (c), N=401; (b) 21800X, N=245; (c) 11400X, N=156.

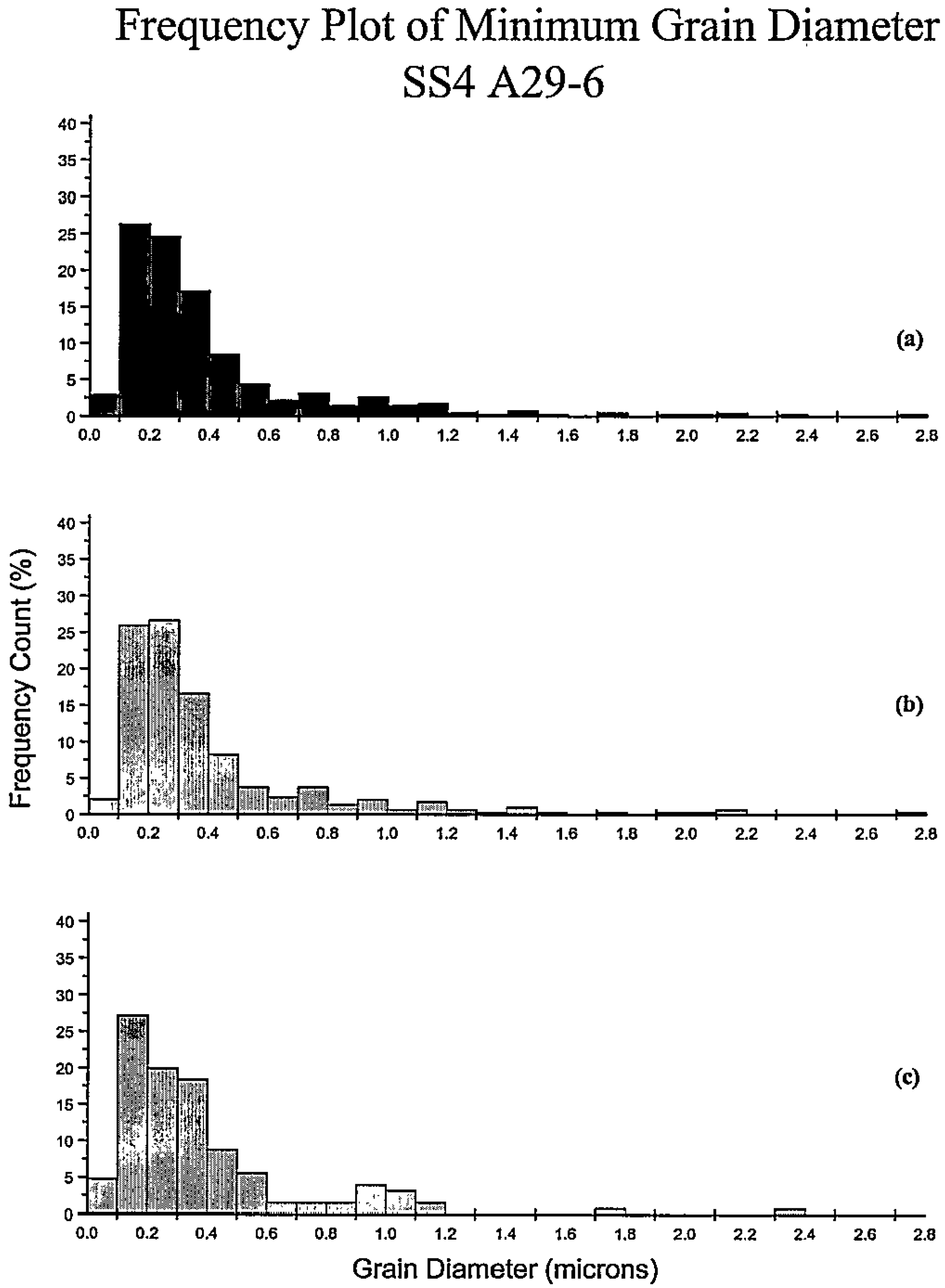

Frequency Plot of Minimum Grain Diameter
SS4 A29-6

Figure 4.26. Minimum grain diameter at high and intermediate magnification. Sample A29-6 (1800/30/120). (a) Summation of (b) and (c), N=414; (b) 22800X, N=289; (c) 11400X, N=125.

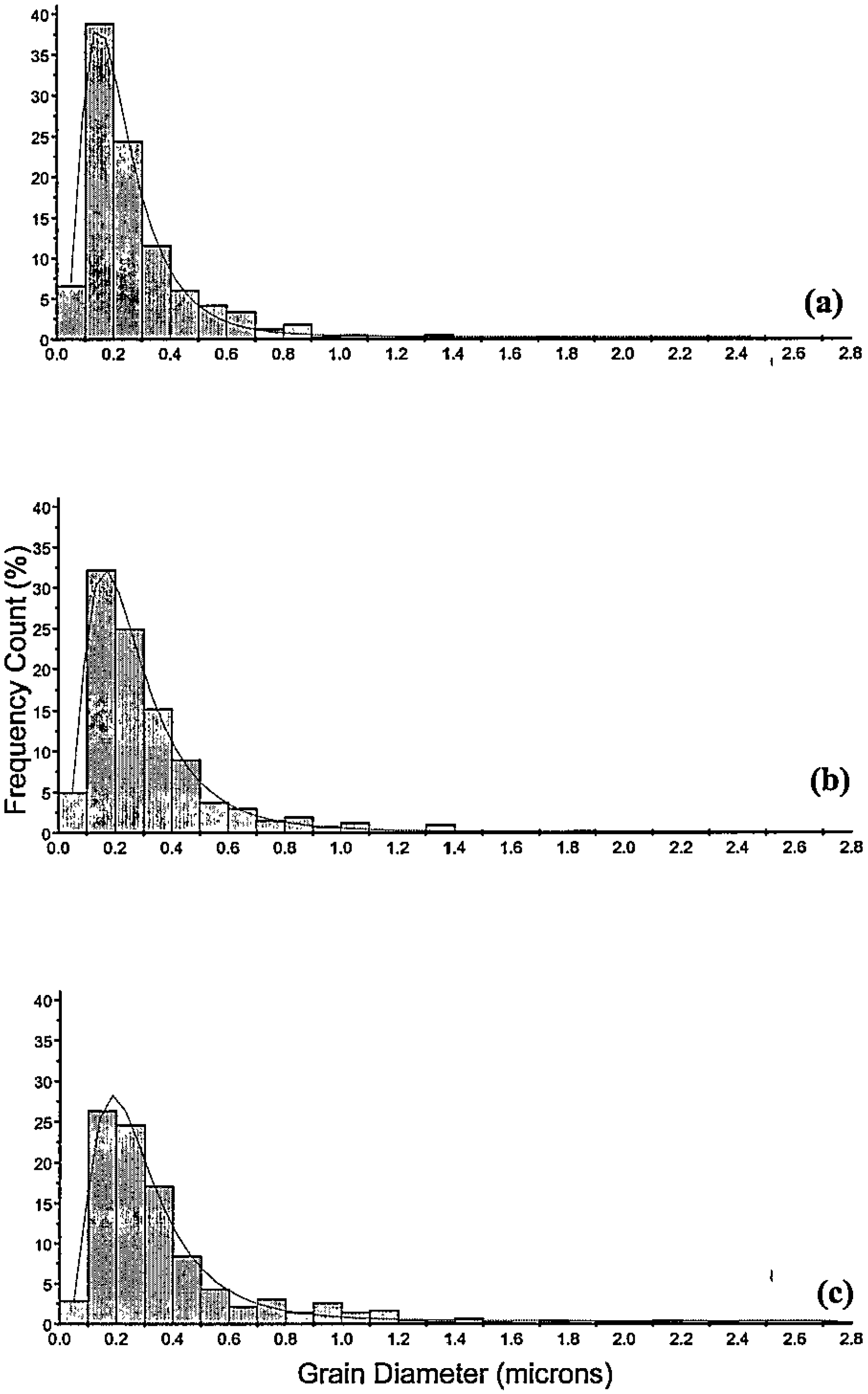

Figure 4.27. Results of curve fitting the minimum grain size data with a log-normal equation. (a) SS1, (b) SS2, and (c) SS4.

Sample Set	Magnification.	d_g	σ_g	w	y_o	A	χ^2
1	HM+IM	0.146 ± 0.002	1.78 ± 1.01	0.575 ± 0.010	0.305 ± 0.153	38.15 ± 0.63	0.415
	HM	0.146 ± 0.003	1.73 ± 1.01	0.549 ± 0.015	0.466 ± 0.272	40.20 ± 0.91	0.825
	IM	0.148 ± 0.008	1.82 ± 1.04	0.596 ± 0.044	0.921 ± 0.841	33.66 ± 2.06	4.39
	LM	0.658 ± 0.026	1.62 ± 1.05	0.483 ± 0.051	-0.321 ± 0.003	12.24 ± 0.88	2.43
2	HM+IM	0.163 ± 0.002	1.85 ± 1.01	0.616 ± 0.010	0.151 ± 0.114	32.07 ± 0.40	0.204
	HM	0.159 ± 0.003	1.89 ± 1.02	0.638 ± 0.017	0.085 ± 0.193	31.64 ± 0.73	0.683
	IM	0.172 ± 0.003	1.76 ± 1.02	0.567 ± 0.017	0.235 ± 0.171	32.93 ± 0.65	0.561
	LM	0.567 ± 0.019	1.55 ± 1.04	0.436 ± 0.038	0.305 ± 0.430	13.43 ± 0.86	2.051
4	HM+IM	0.186 ± 0.004	1.79 ± 1.02	0.584 ± 0.019	0.396 ± 0.164	27.85 ± 0.58	0.483
	HM	0.195 ± 0.003	1.70 ± 1.02	0.532 ± 0.018	0.501 ± 0.158	28.93 ± 0.61	0.480
	IM	0.169 ± 0.007	1.95 ± 1.04	0.670 ± 0.037	0.270 ± 0.380	26.45 ± 1.17	1.973
	LM	N/A	N/A	N/A	N/A	N/A	N/A

Table 4.5. Results of Regression Analysis on Minimum Grain Diameter Measurements.

The differences between the conditions were seen more easily when the fitted curves were regenerated and plotted on the same axes, as seen in Figure 4.28. As one can see, the sintered material had the highest frequency of counts at the lowest mean grain diameter, and the distribution was the narrowest. As the HIP temperature increased the mean grain diameter was seen to increase, while the frequency at the mean diameter was seen to decrease. Accompanying the reduction in number of grains at the mean diameter was the overall increase in frequency of larger grains as the HIP temperature increased. This behaviour suggested classical grain coarsening.

The differences in grain size were not extreme, but when considering the fact that some grain size differences were detectable by eye in the SEM, the trends were believed to be real. At the very least, it could be said that the sintered condition (SS1) had a different grain diameter distribution from the high temperature and pressure condition (SS4).

4.2.2 Environmental Scanning Electron Microscopy

The ESEM investigations were concerned with the examination of cracks introduced by fracture toughness testing. This section, since it mostly deals with a crack characterization, will also reference optical micrographs of the toughness indents, found in Figures E1-11 of Appendix E. It was difficult to identify extreme differences between the conditions examined, however, some differences were observed between the samples.

Multiple cracks forming at only on of the corners of some indents were detected.

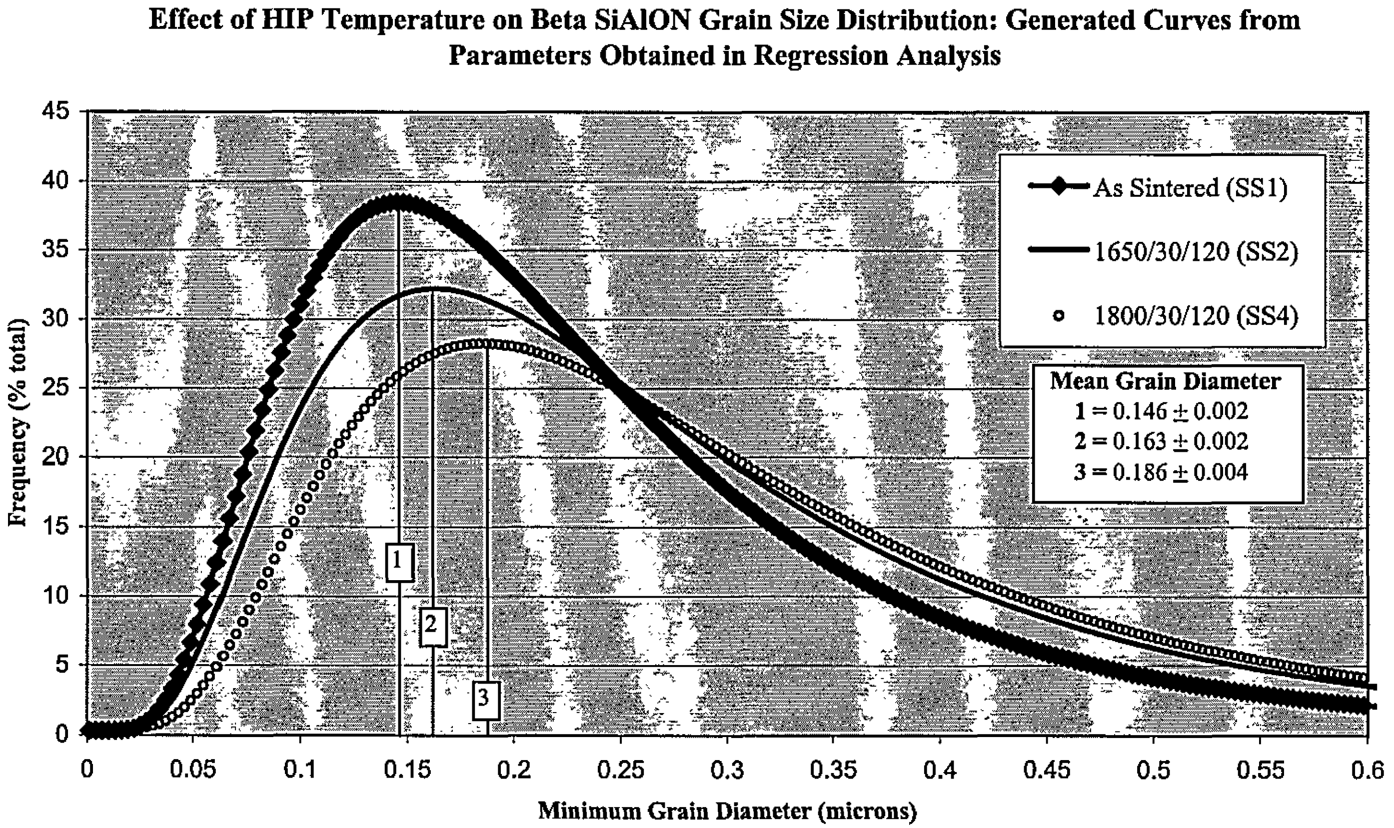

Figure 4.28. Grain size distributions generated from regression analysis for SS1, SS2 and SS4. The width of the lines vertical lines labeled 1, 2 and 3 is the regression error assosciated with the mean values of grain diameter.

These multiple cracks did not seem to follow any trends in terms of where they were located, except in SS6, where it was always the top corner. The only other set of samples that exhibited multiple cracking more than ~10% of the time was SS4, but no trends were found for these samples.

Some cases were observed where the cracks lengths were very different (i.e. the difference was much greater than 50μm). These cases were seen only in the annealed samples, and differences of up to 130μm were found.

Similar observations made from the optical micrographs were also seen in the ESEM. The ESEM afforded higher magnification to view the crack paths, and also gave some contrast based on atomic number. Samples investigated in the ESEM were SS1: A27-2, SS2: A23-9, and SS4: A28-4 (i.e the same sample sets as for the SEM work).

Figure 4.29 shows an indent on SS1 in which the mentioned multiple cracking can be seen at the top corner. It is not extremely clear, but one can see regions of crack deflection and grain bridging along the radial median cracks emanating from the corners (e.g. bottom crack half way down).

Figure 4.30 shows an indent in SS2, and the similar features of cracking on the impression surface, polishing artifacts, and generally straight emanation of cracks from the indent corners as seen in Figure 4.29. The distribution of the yttrium rich secondary phase was also seen to be rather coarse (similar to SEM investigations). A large zoom of the bottom crack, near the tip, is seen in Figure 4.31. This micrograph demonstrates the torturous path of the crack (relatively speaking of course) and a region where the crack did not completely break the plane of the specimen surface. The crack propagated in an intergranular fashion between both β and α grains. β grains that de-cohered and possibly experienced pullout were either ruptured, or remained in tact (see Figure 4.31).

The mechanisms observed, as well illustrated by Figure 4.31, were seen in all of the investigated specimens. It was difficult to determine any differences in the crack paths of the three specimens examined, since all the same toughening mechanisms seemed to be present for all conditions. As Figures 4.32 to 4.34 show, SS4 (a less tough material than SS1 or SS2) behaved in much the same manner as SS1 and SS2. It appeared that perhaps more fiber rupture (in place of bridging) occurred in SS4 than in SS1 or SS2, as evidenced by the greater number of large β grains that were seen to have fractured in the crack tip wake (Figure 4.34).

In summary, ESEM investigations revealed that crack propagation followed an intergranular fracture mode in all samples. The presence of crack deflection, elastic bridging, de-bonding, pullout and rupture, and possibly friction sliding were all observed as common toughening mechanisms [see Lawn, 1993]. The high temperature HIP condition (SS4) was observed to have had less fiber decohesion / debonding and more fiber rupture in comparison to the as sintered (SS1) and mid temperature condition (SS2).

The coarse heterogeneity seen in the SEM for SS2 was also detected in the ESEM study. In comparison, the microstructure of SS4 had a more uniform distribution of secondary phase, with smaller amounts present. The larger grain size of SS4 was also observed, and these larger grains were often debonded, or ruptured after minimal deflection of the crack.

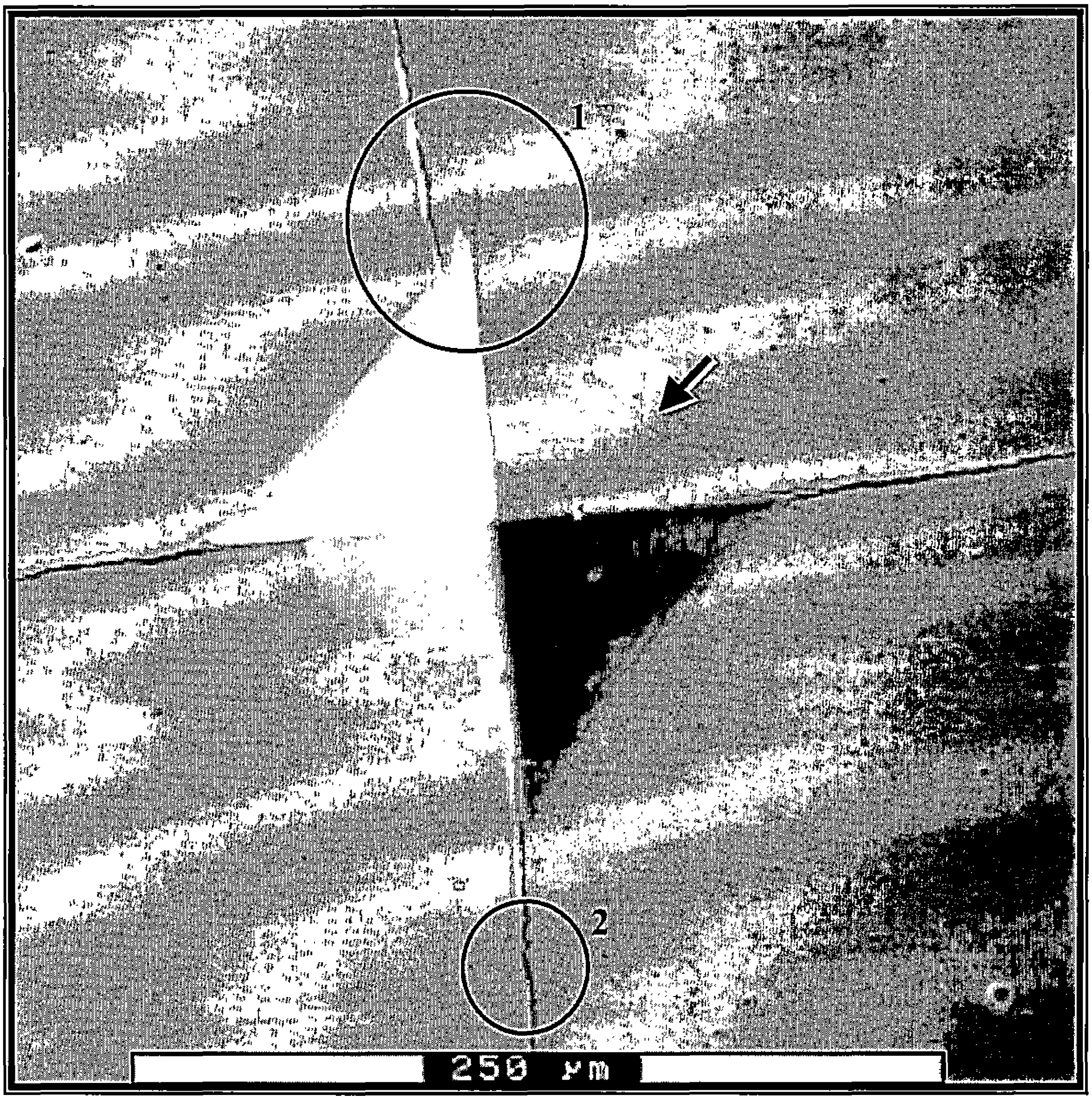

Figure 4.29. ESEM secondary electron micrograph of SS1. (A27-3 indent 3). Notice the small cracks at the top corner of the indent (1), along with the lateral cracking on the surfaces of the impression (arrow). Some crack deflection and grain bridging is also visible (2).

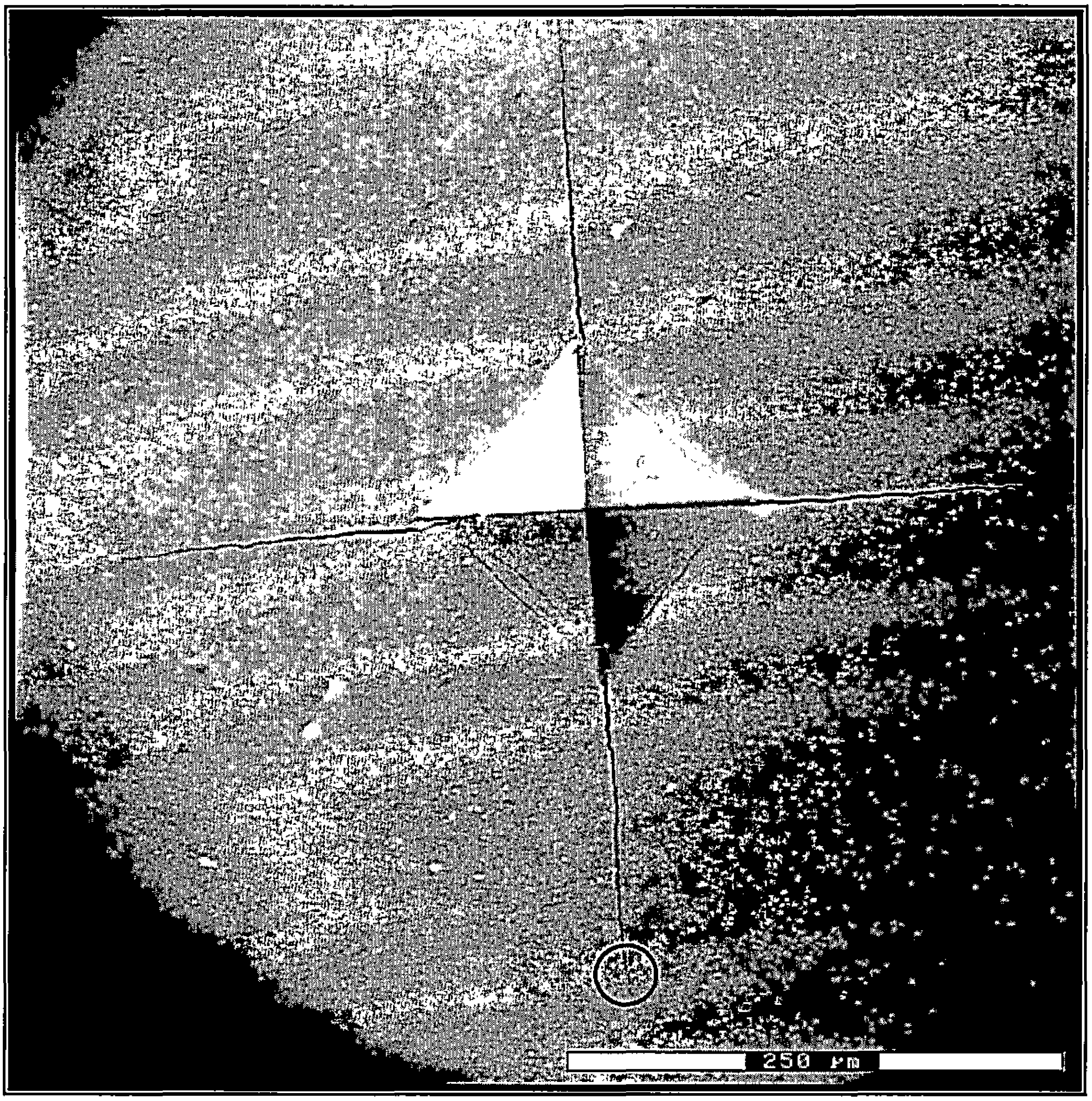

Figure 4.30. ESEM secondary electron micrograph of SS2. (A23-9 indent 1). Notice similar features to SS1, but with a lack of porosity. The atomic number contrast shows that the distribution of the secondary phase is rather coarse. Marked region is area shown in Figure 4.31.

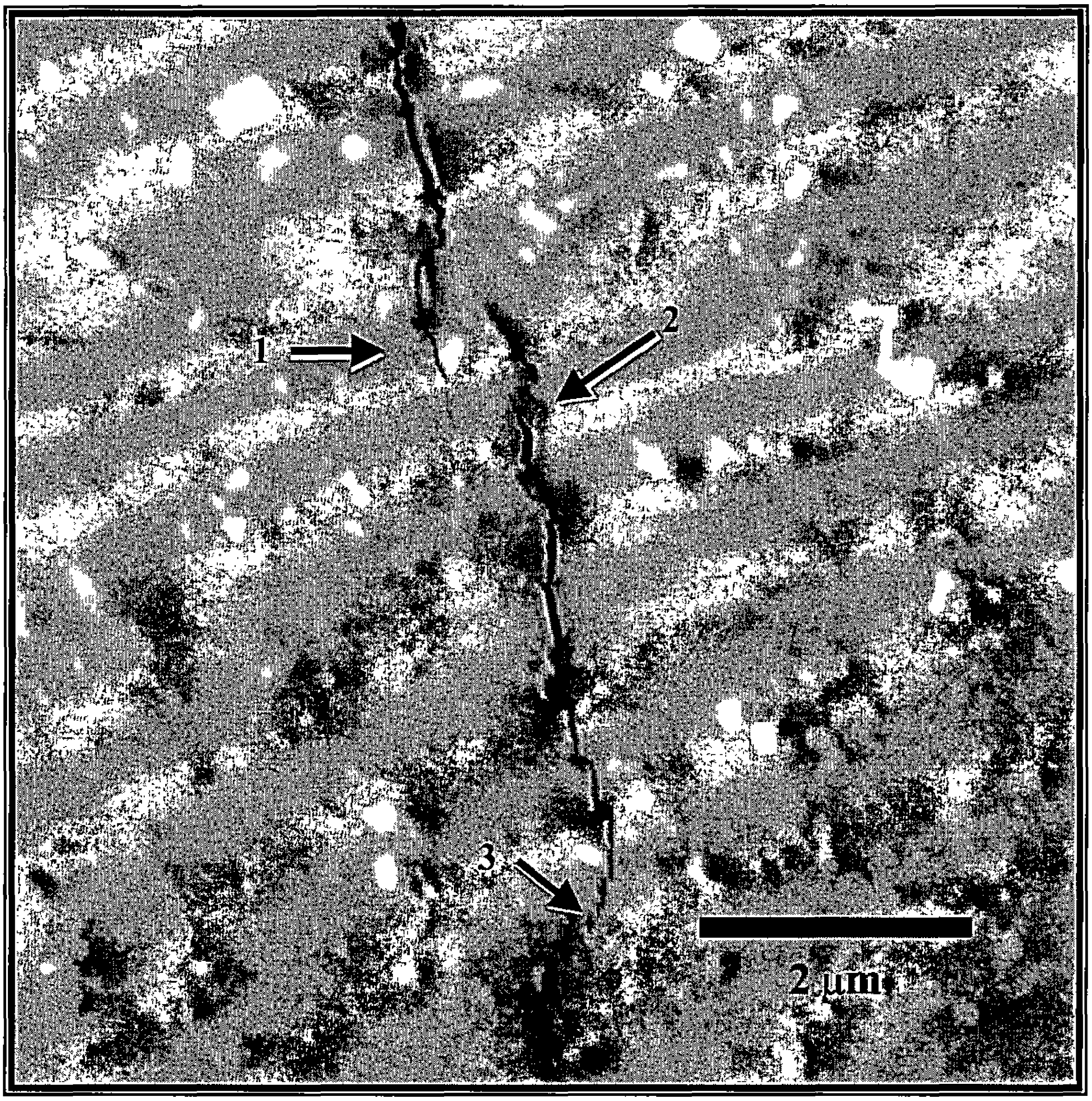

Figure 4.31. ESEM secondary electron micrograph of SS2 (A23-9 indent 1) near the crack tip (marked region in Figure 4.30). Crack deflection, fiber pullout and rupture, and possibly frictional sliding were all present as mechanisms of toughening. Of particular note is the region where the crack did not break the plane of the specimen (1) until after a large deflection. (2) and (3) mark regions near large deflections where β grains appear to be bridging the crack wake.

Figure 4.32. ESEM secondary electron micrograph of SS4 (A28-4 indent 2). Multiple cracks were seen emanating from the corner. Crack deflection, pullout and fiber fracture are prominent along the crack. Light region in center is beam damage. Marked region is area shown in Figure 4.33.

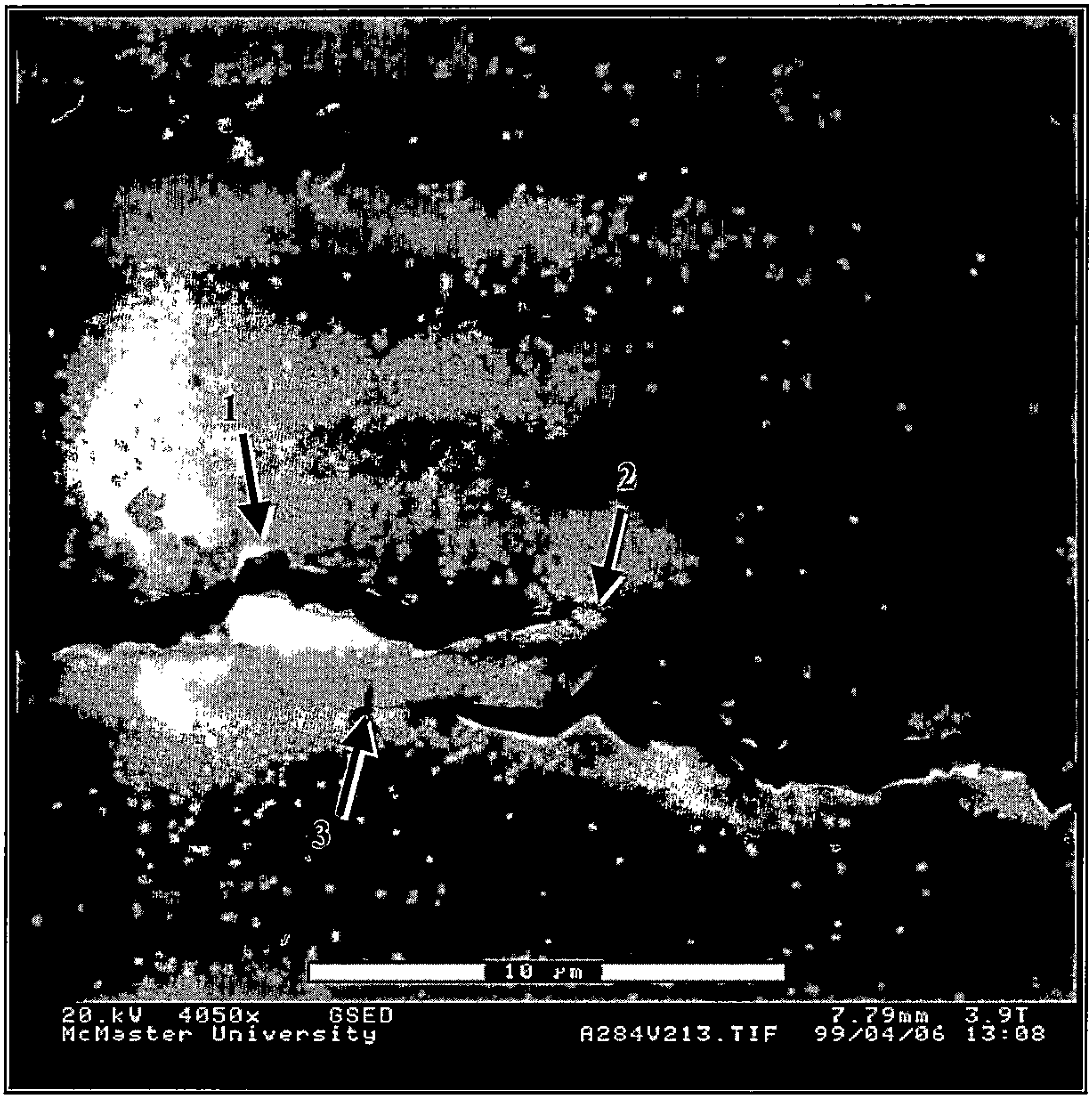

Figure 4.33. ESEM secondary electron micrograph of SS4 (A28-4 indent 2) showing the region marked in Figure 4.32. Regions of intergranular fracture around large β grains were seen at (1) and (2). A partially de-bonded β grain was seen to have undergone rupture (3) while one end remained embedded in the matrix. Notice the fine dispersion of the secondary phase. Beam damage above the crack appeared as a lighter tone of gray.

Figure 4.34. ESEM secondary electron micrograph of SS4 (A28-4 indent 2) showing a region containing moderate crack deflections around large β grains (1) and β grain rupture in the crack wake (2). Crack propagation was from left to right.

4.2.3 X-Ray Diffractometry

The results of the five batches of x-ray diffraction (XRD) tests are presented in this section, including the identification of crystalline phases and the determination of the $\alpha/\alpha+\beta$ ratios. The presence of secondary crystalline phases (phases other than α or β) was detected, and observed to follow trends with respect to the heat treatment temperature, pressure, and time. Appendix C includes individual plots of intensity versus 2θ, JCPDS Powder Diffraction File standards used in phase identification, and calculations of the $\alpha/\alpha+\beta$ ratios.

The analysis of the XRD data proved difficult, as evident in the number of different batches of tests. The first batch of results differed enough from the other tests to suspect that some unknown variables were present. However, all the tests identified the same secondary phases, with Batch 1 indicating that perhaps some additional phases were present. The trends seen in the data of *every* batch were similar, so the inconsistencies in Batch 1, although puzzling, were not found to affect the interpretation of the results.

According to Gazzara and Messier (1977) and Devlin and Amin (1990) the region 20-40° 2θ contains all of the necessary α and β peaks required to perform phase analysis, so this region was enlarged to make peak height measurement more accurate. The highest peak intensities of the secondary phases also fell into this domain.

The results of Batch 1 are seen in Figures 4.35 and 4.36. The α and β SiAlON phases are solid substitutions based on the structure of their respective Si_3N_4 phases, so their diffraction behaviour was very similar to the standards, and they were identified easily. The fact that internal standards were not included in the tests did not affect the identification of the α and β phases, but failed to allow for the determination of the substitution levels of the SiAlON phases.

In comparing the Batch 1 scans with the α and β Si_3N_4 cards it was noticed that some samples did not have the proper relative intensities between the $\alpha_{(102)}$ and $\alpha_{(210)}$ peaks (34.6° and 35.3° 2θ respectively), nor between the $\beta_{(200)}$, $\beta_{(101)}$ and $\beta_{(210)}$ peaks (27.1°, 33.7°, and 36.1° respectively). These improper relative intensities seemed to have been a function of the amount of secondary phase, which was in turn a function of the heat treatment conditions. The presence of peak overlaps could have caused the relative intensity ratios anomalies, but no conclusions about this were made.

One can see, in Figure 4.35 that as the pressure was increased (under constant temperature of 1800°C for 120 minutes) the amount of secondary phase decreased. Notice that the anomalous relative intensity ratios in the low pressure condition (SS6) were corrected once the high pressure condition was reached. It appeared that there was a direct correlation in the amount of crystalline secondary phase and the relative intensity of the aforementioned peaks. This was further supported by the fact that SS6 had the largest amount of secondary phase, and had the most anomalous relative intensity ratios.

When comparing only the (210) peaks for both the α and β phases the ratio of α to β seemed constant regardless of the increase in pressure. However, it can be seen from these peaks that there was a decrease in α content after HIP'ing.

The effect of temperature (at 30000psi for 120 minutes) can be seen in Figure 4.36. Again there is the anomaly of the improper α and β relative intensity ratios, and an overall decrease in the amount of secondary crystalline phase with increasing temperature. However, it was seen that the amount of secondary crystalline phase (SCP) did not decrease at 1500°C. It was not until 1650°C that a noticeable decrease in the amount of SCP was detected. This implied that there was an activation temperature for whatever phenomenon was responsible for causing the reduction of SCP (between 1500 and 1650 °C). The $\alpha/\alpha+\beta$ ratio was also observed to decrease with increasing temperature, but only above 1500-1650°C.

There was difficulty in trying to identify the SCP due to the strange relative intensity anomalies, and numerous secondary peaks present in Batch 1. There were many possible candidate phases, and many different combinations of phases that would match some, but not all of the SCP at once. The results of the phase identification for all batches are seen in Table 4.6. Polytypoids of AlN (listed in Table 4.6) may have been present in small amounts, but their identification was not distinctly made. The polytypoids listed were those which have been reported to be compatible with mixed α/β SiAlONs along with the M and J phases [see Huang et al, 1996; Huang and Chen, 1996; Sun et al., 1991a; 1991b].

Batches 2-4 were performed approximately six months after Batch 1 on the same diffractometer, and Batch 5 was performed at UMEX around the same time as Batches 2-4. XRD pressure and temperature series are shown in Figures 4.37 and 4.38. The slightly different appearance in some of the scans was due to the different machine that was used for Batch 5 (and possibly the faster scan rate). Consult Table 4.6 for the results of the phase identification.

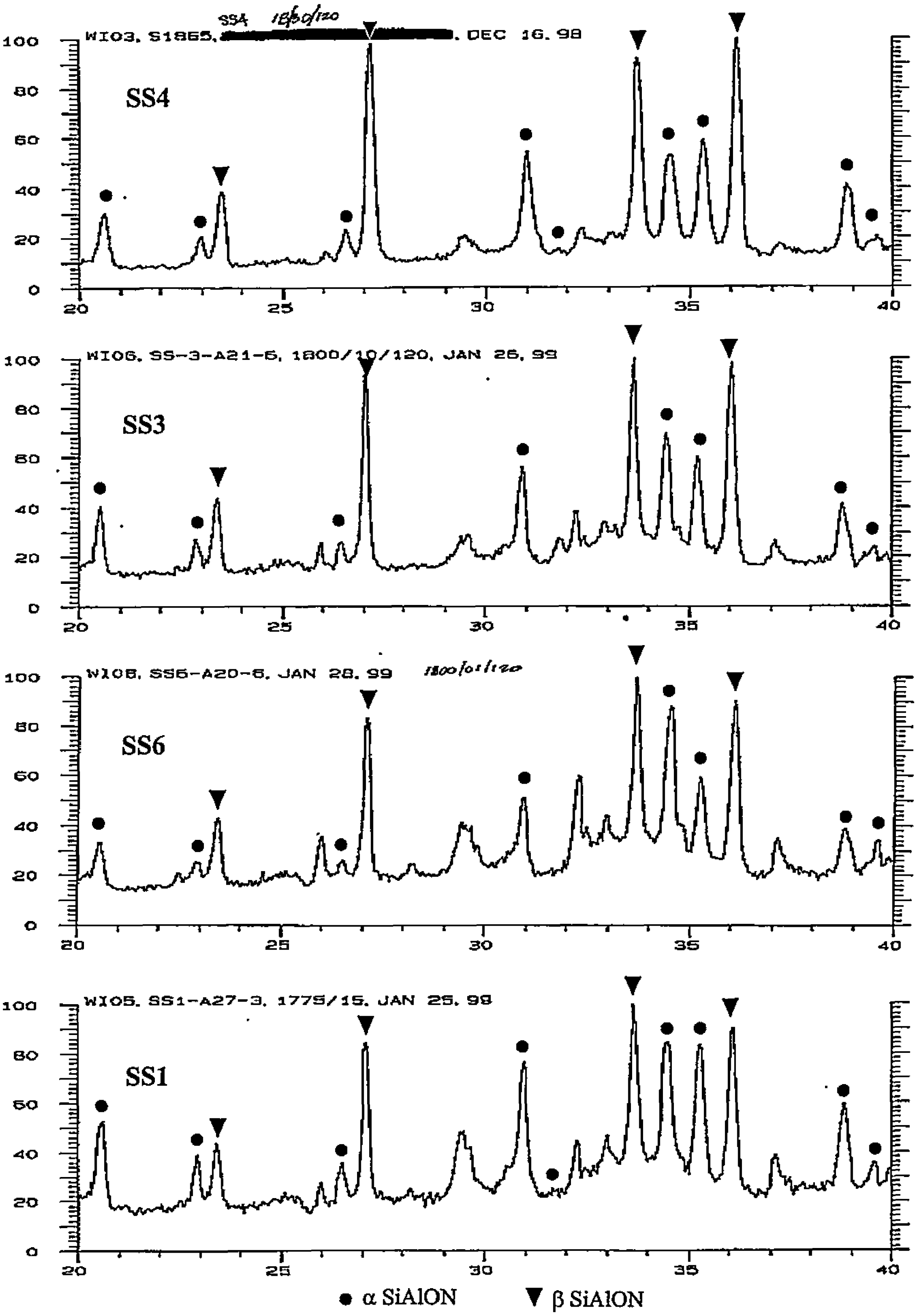

Figure 4.35. Batch 1 XRD scans showing the evolution of the phase composition as a function of increasing pressure at 1800° C. Pressure increases from bottom to top.

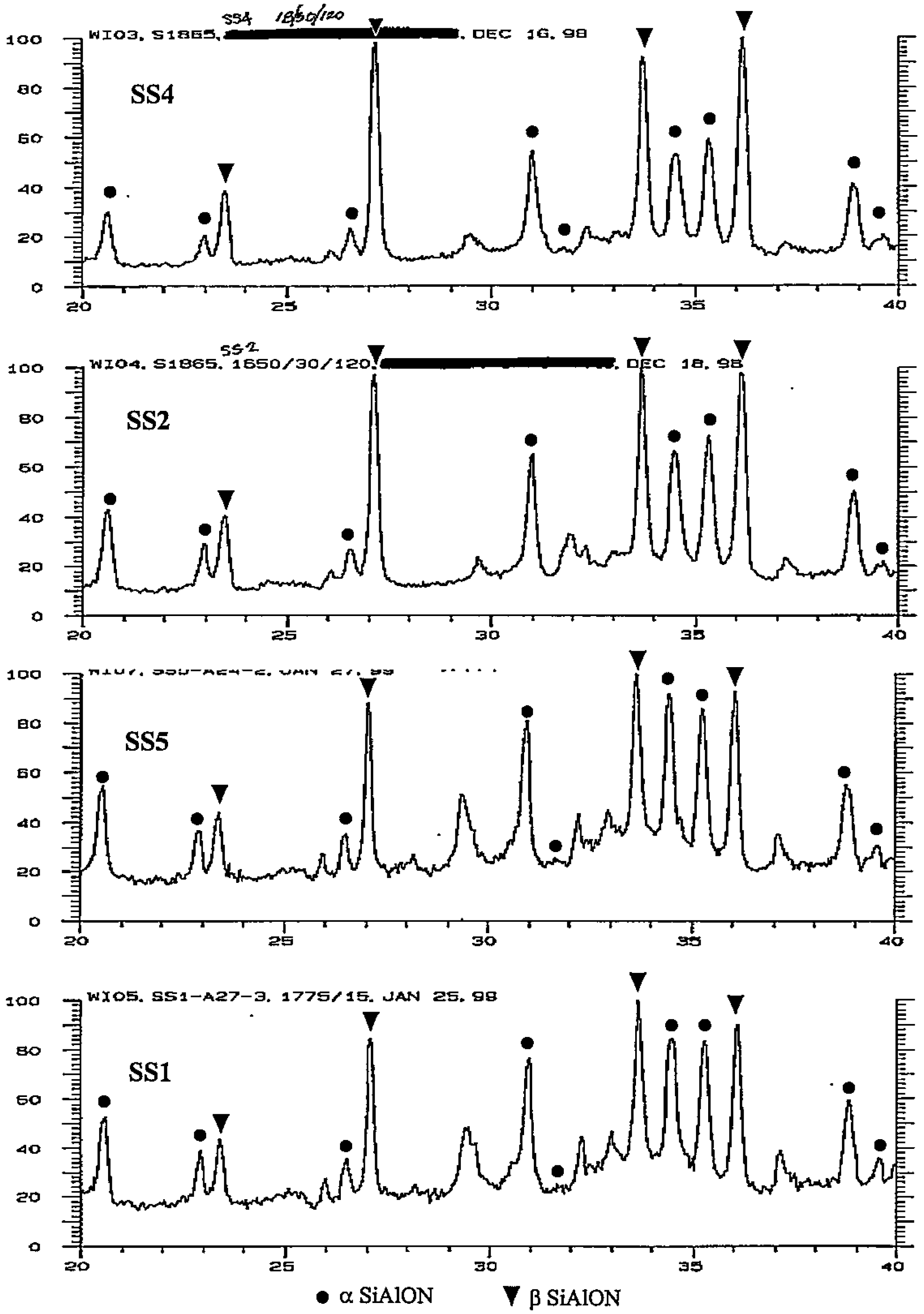

Figure 4.36. Batch 1 XRD scans showing the evolution of the phase composition as a function of increasing temperature at 30000psi. Temperature increases from bottom to top.

The apparent trends seen in all the batches regarding the SCP relative intensities and amounts were very similar. However, Batch 1 appeared to have some additional phases. Some of these unidentified peaks of these phases were rather intense, seen for example in SS6 at 22.5°, 26°, 28.2°, 32.25°, and 32.35° (see Figure 4.35). No phases were found that matched these peaks.

After annealing very weak SCP were detected (see Figure 4.39). Upon first inspection, one might argue that the peaks claimed to be present were simply background noise. However, the phases that were reported had many of the peaks present in the proper proportion, and the fact that shoulders on the α and β phases were still present indicated that the secondary phases were present, but in very small amounts. The background was also lower for the annealed samples than for the preannealed scans. Notice that SS3 still had a fair amount of M phase after annealing.

Results of the $\alpha/\alpha+\beta$ ratio calculations are seen in Table 4.7.Trends in the $\alpha/\alpha+\beta$ ratio were difficult to discern between the batches of tests because of intensity anomalies in Batches 1 and 5, and the fact that Batch 5 was done on a different diffractometer. These factors did not allow for direct comparison of the data to be made, but the trends seen in each data set appeared to be similar.

The difference in the amount of β phase between the as sintered state (SS1) and the highest temperature (and highest pressure) condition (SS4) was about 12wt%. Considering that the error on the quantification of the β fraction was ± 3wt% the difference in amounts was not pronounced, but was real. SS1 and SS5 seemed to have the same $\alpha/\alpha+\beta$ ratio, as did SS3 and SS6. SS4 had the highest amount of β. It appeared as

XRD Batch	Sample	SCP Present
1	SS1: A27-3	j(s), J(m), S(m), M(w), A(w), P:?(w)
	SS2: A23-9	M(m), J(w), A(vw), S(w)
	SS3: A21-6	M and or M'$_{ss}$ (m), J(m), j(m), S(m), A(w)
	SS4: A28-4	j(m), J(m), M(w), A(w), P:?(w)
	SS5: A24-2	j(s), J(m), S(m), M(w), A(w), P:?(w)
	SS6: A20-6	j(s), J(m), M(w), A(w), P:?(w)
2	SS1: A22-6 (Annealed)	j(vvw), J(vvw), M(vvw)
	SS3: A27-4 (Annealed)	M(w), j(vvw), J(vvw)
	SS4: A29-3 (Annealed)	J(vvw), j(vvw)
	SS5: A24-2	j(s), J(m), M(vvw)
3	SS5: A24-2	j(s), J(m), M(vw), A(vvw), P:?(vvw)
4	SS1: A27-3	j(s), J(m), M(vw), A(vw), P:?(vvw)
	SS2: A23-9*	M(m), A(m), J(m), j(w)
	SS4: A28-4	j(m), J(w), A(vw), M(vw), P:?(vvw)
5	SS3: A21-6	j(m), M'$_{ss}$(m), J(w), A(vw), P:?(vw)
	SS5: A24-2	j(s), J(m), M(vvw), A(vvw), P:?(vvw)
	SS6: A20-6	j(m), J(w), M(vvw), A(vvw), P:?(vvw)

*Unusually high background present.

(s)>(m)>(w)>(vw)>(vvw), ? indicates that some peaks may have been present for P phases, but were not indexed.

Legend

Symbol	Compound	Variants/Comments
J	$Y_4Si_2O_7N_4$	$Y_4Si_2O_7N_4$ and $Y_4Al_2O_9$: J'$_{ss}$ = $Y_4Si_{2-x}Al_xO_{7+x}N_{2-x}$
M	$Y_2Si_3O_3N_4$	M'$_{ss}$ = $Y_2Si_{3-x}Al_x O_xN_{4-x}$
j	$Y_{10}Al_2Si_3O_{18}N_4$	This phase is similar to J'$_{ss}$ with x~0.8 containing slightly less O and slightly more N, and therefore could actually be J'$_{ss}$
Y	Y_2O_3	Present as unreacted powder, or oxidation product
S	Si_2N_2O	Only thought to be present in Batch 1
A	$Y_{4.67}O(SiO_4)_3$	Possible to have some Al present
P	AlN Polytypoids	12H: $SiAl_5O_2N_5$
		21R: $SiAl_6O_2N_6$
		27R: $SiAl_8O_2N_8$

Table 4.6. XRD phase analysis and descriptions of the various secondary phases.

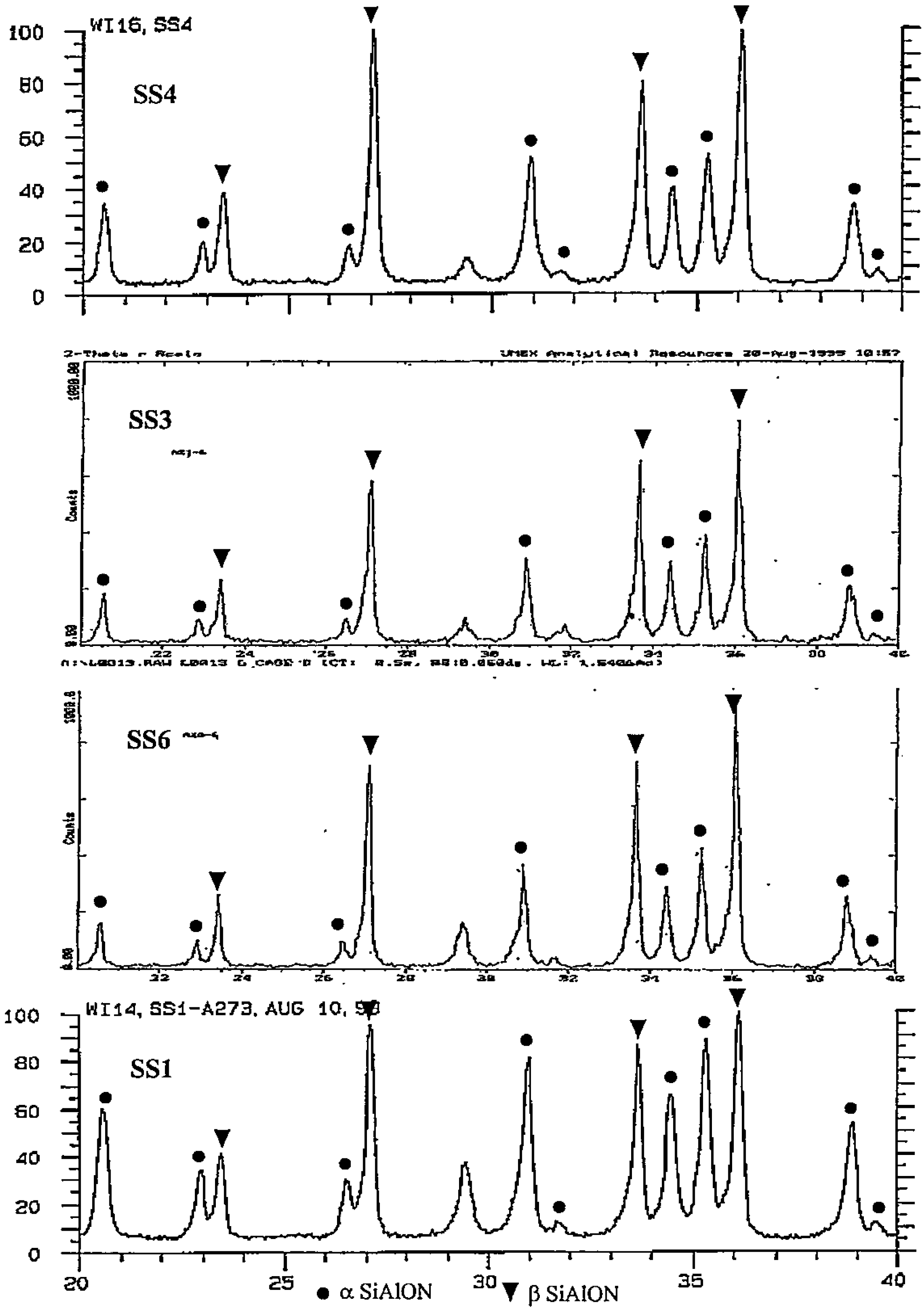

Figure 4.37. Batches 4 and 5 XRD scans showing the evolution of the phase composition as a function of increasing Pressure at 1800 C. Pressure increases from bottom to top.

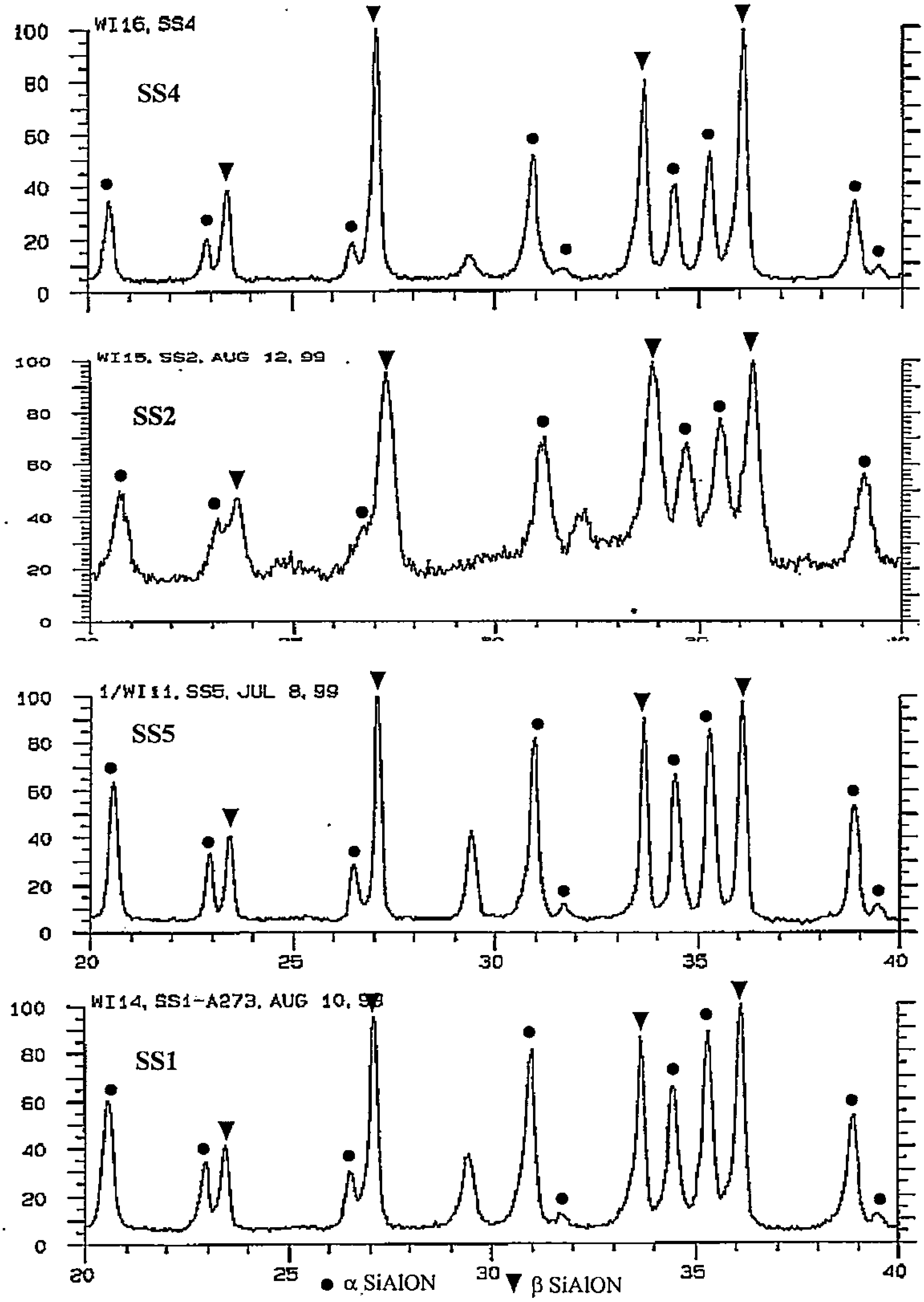

Figure 4.38. Batches 2 and 4 XRD scans showing the evolution of the phase composition as a function of increasing Temperature at 30000psi. Temperature increases from bottom to top.

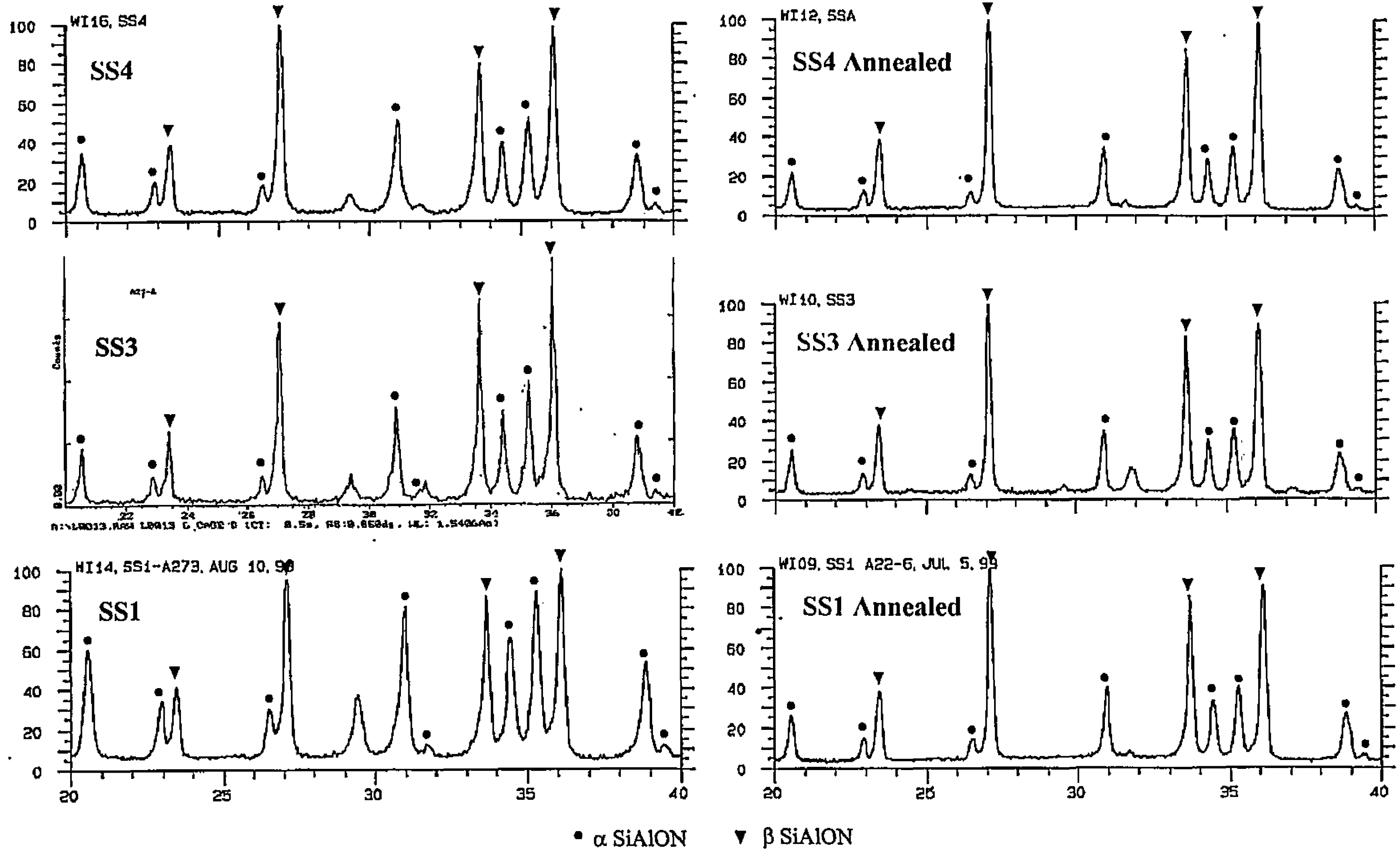

Figure 4.39. Batches 2, 4 and 5 XRD scans showing the change in the phase composition after annealing. Pre-annealed scans are on the left, and increasing pressure of original HIP pressure increases from bottom to top. Notice that SS3 still contains some M phase peaks in the annealed state .

though the amount of β increased with increasing temperature at 30000psi, and that there was no significant change in β fraction with pressure at 1800°C.

It was thought that the amount of relative intensity deviation from normal caused inaccurate values in the $\alpha/\alpha+\beta$ ratio determination, since some peaks were affected more than others (presumably because of peak overlap). After further investigation it was discovered that Batch 1 tests with anomalous relative intensities overestimated the $\alpha/\alpha+\beta$ ratio because the anomalous α peak was always proportionately higher than the

XRD Batch	Sample	Wt% β (Gazzara)	Wt% β (Devlin)	$\alpha/\alpha+\beta$ Ratio
1	SS1: A27-3	39	41	0.59
	SS2: A23-9	46	47	0.53
	SS3: A21-6	49	49	0.51
	SS4: A28-4	52	53	0.47
	SS5: A24-2	40	41	0.59
	SS6: A20-6	47	48	0.52
2	SS1: A22-6 (Annealed)	59	60	0.40
	SS3: A27-4 (Annealed)	62	63	0.37
	SS4: A29-3 (Annealed)	65	65	0.35
	SS5: A24-2	42	43	0.57
3	SS5: A24-2	43	44	0.56
4	SS1: A27-3	43	43	0.57
	SS2: A23-9	43	44	0.56
	SS4: A28-4	53	55	0.45
5	SS3: A21-6 Case D	57	58	0.42
	SS5: A24-2 Case A	47	49	0.51
	SS5: A24-2 Case B	47	48	0.52
	SS5: A24-2 Case C	44	45	0.55
	SS5: A24-2 Case D	44	45	0.55
	SS6: A20-6 Case D	59	61	0.39

(see Appendix B for test case parameters concerning Batch 5).

Table 4.7. XRD phase analysis, showing the weight percent β phase (relative to the α phase) at the different heat treatments as calculated by the methods of Gazzara and Messier (1977) and Devlin and Amin (1990).

anomalous β peak. Batch 5 was found to underestimate the α/α+β ratio because of the larger anomalous β peaks. This discovery explained the slight variations in α/α+β ratio between Batches 1 and 5 and Batches 2-4 for identical samples. Since no differences in α/α+β ratios were detected between the samples in Batches 2-4, and there were no anomalous intensities in these batches, it was concluded that the presence of anomalous intensity ratios was the cause of α/α+β ratio variation between the batches.

There was a trend found in the Batch 5 data (SS5 A24-2) that suggested surface preparation had an influence on the amount of β content (refer to Appendix B). Polished surfaces were found to have contained more β than ground surfaces. For this study, only ground surfaces were compared when considering any trends between data sets.

The effect of annealing on the α/α+β ratio is seen in Figure 4.40. Notice that the anomalous β peaks for Batch 5 caused a lower α/α+β ratio as compared to Batch 1. The annealed values of the α/α+β ratio (Batch 2) are seen to be lower than preannealed values, indicating a progression of the α → β transformation over long times.

One can see, with the aid of Figure 4.41, that the α/α+β ratio decreased with increasing temperature (at high pressure). For Batches 2-4 the α/α+β ratio was observed to remain constant until 1650°C, after which it decreased significantly. The change in the α/α+β with temperature appeared to be approximately linear with temperature for Batch 1 and there seemed to be a temperature lag for Batches 2-4.

The difference in the absolute values of the α content between Batches 1 and 5 were due to the aforementioned intensity anomalies, and did not affect the interpretation of the effects of pressure; no major change in the $\alpha/\alpha+\beta$ ratio was observed as a function of pressure.

In summary, the XRD results showed pressure, temperature and time effects on the crystalline phase composition of the material. The amount of secondary crystalline phase was found to decrease with increasing temperature at constant high pressure (30000psi), and a decrease with increasing pressure at constant high temperature (1800°C).

The effect of long times at high temperature (1800°C) and ambient pressure resulted in almost entire elimination of secondary crystalline phases for the as sintered sample (SS1) and the high temperature-high pressure condition (SS4). Presence of the M phase was detected after annealing SS3.

The identity of the secondary crystalline phase was found to change from the j phase to the M phase when going from 1500°C to 1650°C (under 30000psi) then back to the j phase at 1800°C. This change was also observed in the isothermal conditions of 1800°C as pressure was varied from 1000 to 10000 to 30000psi. Error in the identification of the major phases was not thought to be present, as all peaks across the 10-70° 2θ region were indexed. Although the results of Batch 1 seemed to be extremely different than the other tests it was found that the results of Batch 1 gave the same conclusions regarding SCP identification for the phases that were possible to index. Nevertheless, the results of Batch 1 should be viewed with some reservation, since there were inconsistencies that could not be explained.

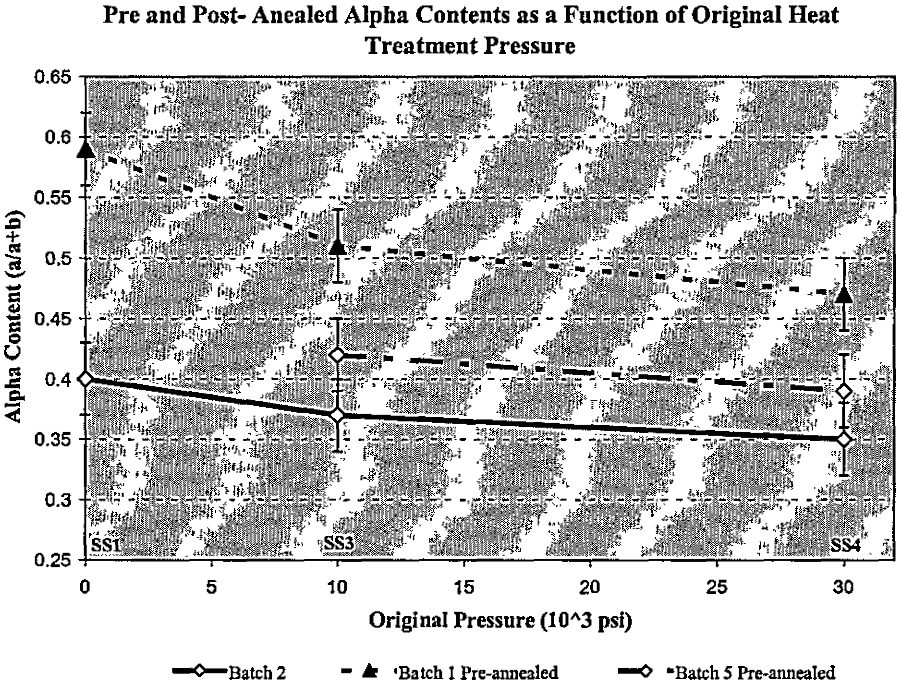

Figure 4.40. Pre and Post-annealed α/α+β ratio for Batches 1&2 (pressure series samples).

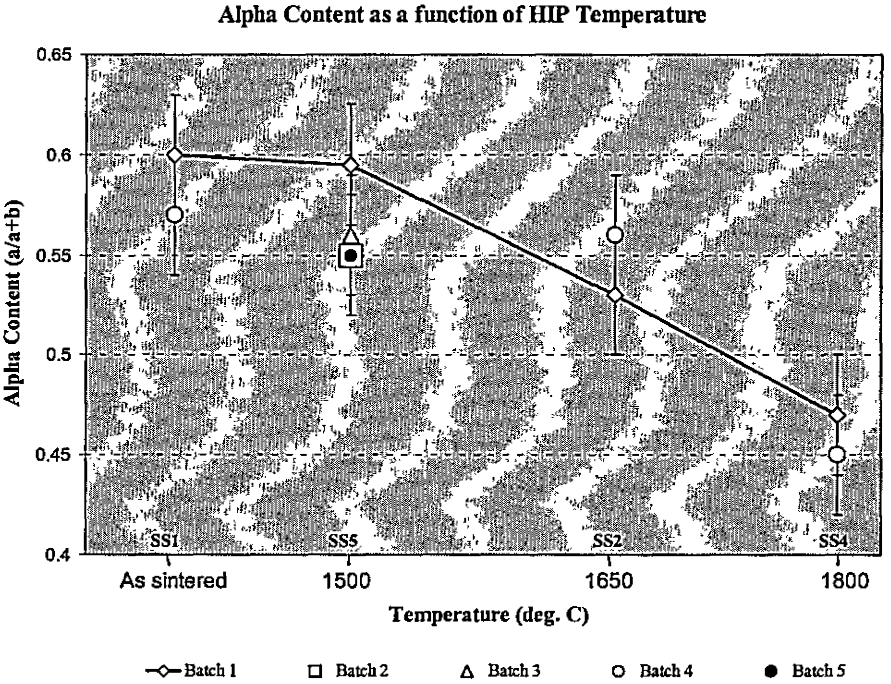

Figure 4.41. The α/α+β ratios for the different XRD Batches as a function of HIP Temperature.

Increasing the temperature of the HIP conditions was found to reduce the $\alpha/\alpha+\beta$ ratio above 1500-1650°C. Long annealing time also reduced the $\alpha/\alpha+\beta$ ratio. However, the $\alpha/\alpha+\beta$ ratio remained unchanged with increasing pressure.

Caution had to be taken when trying to compare all the XRD data that was collected from the different machines under possibly different conditions. Although there were some different parameters involved in the XRD testing, the results showed that some trends in the data seemed to be real, and any significant differences had explanations based on legitimate principles. For instance, since the $\alpha/\alpha+\beta$ ratio was calculated from peak height measurements, any large deviations in relative intensity with respect to the standard intensities caused some miscalculation of the ratio, regardless of any normalization performed. In support of this claim, the absence of anomalous relative intensity ratios resulted in identical $\alpha/\alpha+\beta$ ratios for identical samples tested more than once.

4.2.4 Transmission Electron Microscopy Results

TEM investigations were largely qualitative, but some attempts to quantitatively analyze multigrain junction pocket phases will be summarized here. TEM studies verified the presence of crystalline multigrain junction phases in all of the three samples examined: SS1, SS2 and SS4 (i.e. as sintered and mid and high temperature conditions at high pressure). The EDX analysis was found to be very sensitive to the region of the foil analyzed, and it was difficult to accurately determine the identity of the multigrain junction pocket phases.

Recall from the XRD and SEM analyses that both temperature and pressure were found to alter the amount and distribution of the grain boundary phases. Similar trends were found from TEM investigations. The most different conditions, both in temperature and pressure (i.e. SS1 and SS4) were investigated first to see if any similar differences, reported from SEM investigations, were detectable in the TEM. A larger β grain size was detected in SS4, along with a different distribution of the secondary phase (see Figures 4.42 and 4.43).

Although no quantitative methods (in the TEM) were employed to characterize the size distribution of the secondary phase it was apparent that the sintered material (SS1) had a relatively normal distribution of pocket size, whereas the highest temperature HIP'd material (SS4) had more of a log-normal distribution. This was inferred from a few observations. Firstly, the size of the largest sized pocket phase regions did not seem to change between the samples, but the frequency of them decreased with HIP'ing. Secondly, the frequency of mid-size pockets decreased significantly with HIP'ing along with their size. Lastly, there was a higher frequency of small pockets in the HIP'd material, which were also smaller in comparison to the smallest pockets found in the as sintered material. One can see these trends in Figures 4.42 and 4.43 Also apparent was the increase in frequency of three-grain junctions in the HIP'd material, which did not contain any secondary phase pockets visible at the magnification viewed. Based on all these observations it was concluded that there was less total amount of pocket phase present after HIP'ing at high temperature, and that the size distribution of the pocket phase had also shifted from a normal to a log-normal distribution.

The other high pressure, but mid-temperature, sample that was investigated (SS2) was not well characterized at low magnification, so few observations can be reported here with direct evidence. Any differences in the microstructure with respect to the grain size and secondary phase distribution were difficult to discern, and were certainly not as apparent as the differences between SS4 and SS1. More investigation in HRTEM mode was done on this sample to detect the presence of crystalline pocket phases.

As mentioned, all three samples were found to have crystalline pocket phases. There were a few different methods used to determine if the pocket phases were crystalline or not. Firstly, the fact that contrast variations were seen in the pocket phases when the specimen was tilted indicated that there was some type of atomic ordering present in the pocket phase [see Clarke, 1983]. Convergent beam diffraction was attempted on some of the pocket phases. The small regions of the pocket phases did not allow for good diffraction patterns with the pocket phase on a zone axis, but the presence of diffraction spots also indicated some regular atomic arrangement (i.e. spots instead of rings were observed). When the through beam and a diffraction spot from one of the pocket phases was selected in the objective aperture the contrast much improved, and the extent of the pocket phase was observed more clearly. An example of this technique was already seen in Figure 4.43. The unvarying contrast of the pocket phase in this bright field image indicated that the pocket phase regions in the field of view had the same orientation,

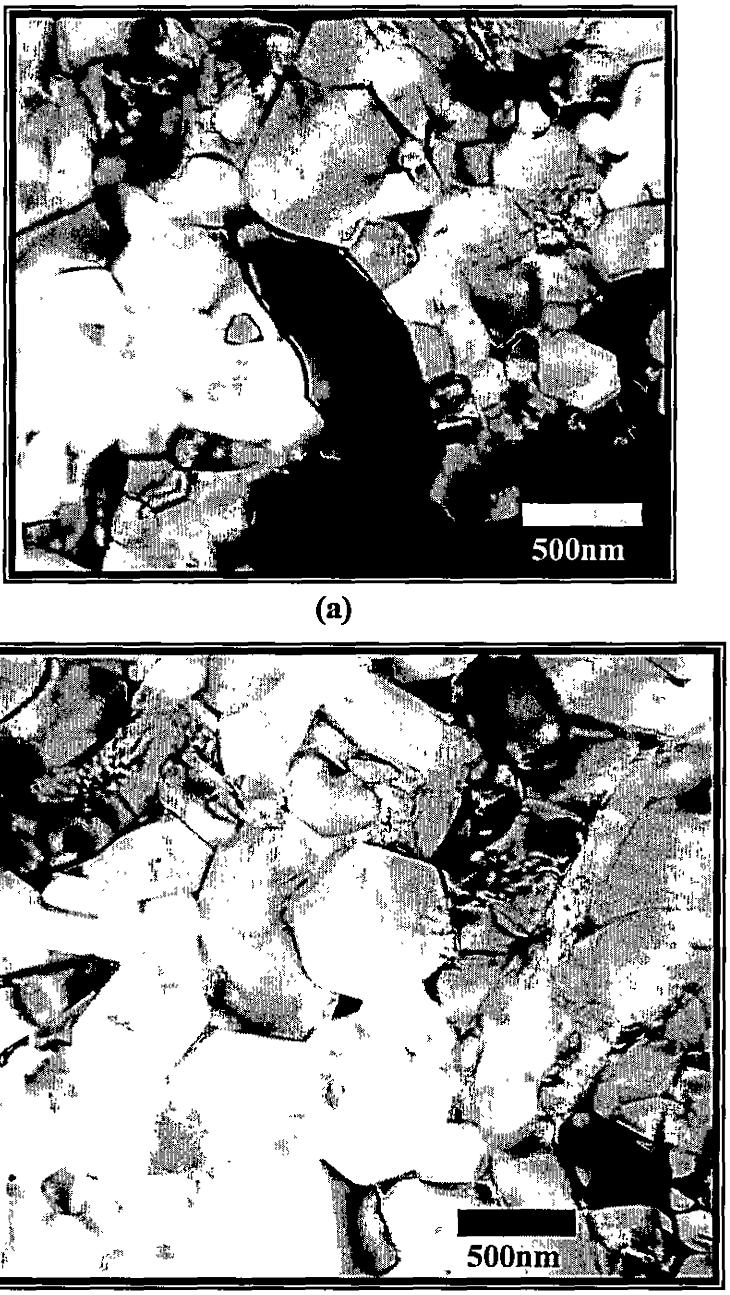

(a)

(b)

Figure 4.42. General TEM bright field micrographs of **(a)** SS1 (A27-6), and **(b)** SS4 (A28-1). Notice that fewer grains of the smallest size in (a) are present in (b), and that average grain size is slightly larger in (b). Also notice the number of secondary phase pockets to be smaller in (b). The grains in (b) also appear to be arranged in a more compact structure in certain areas when compared with (a).

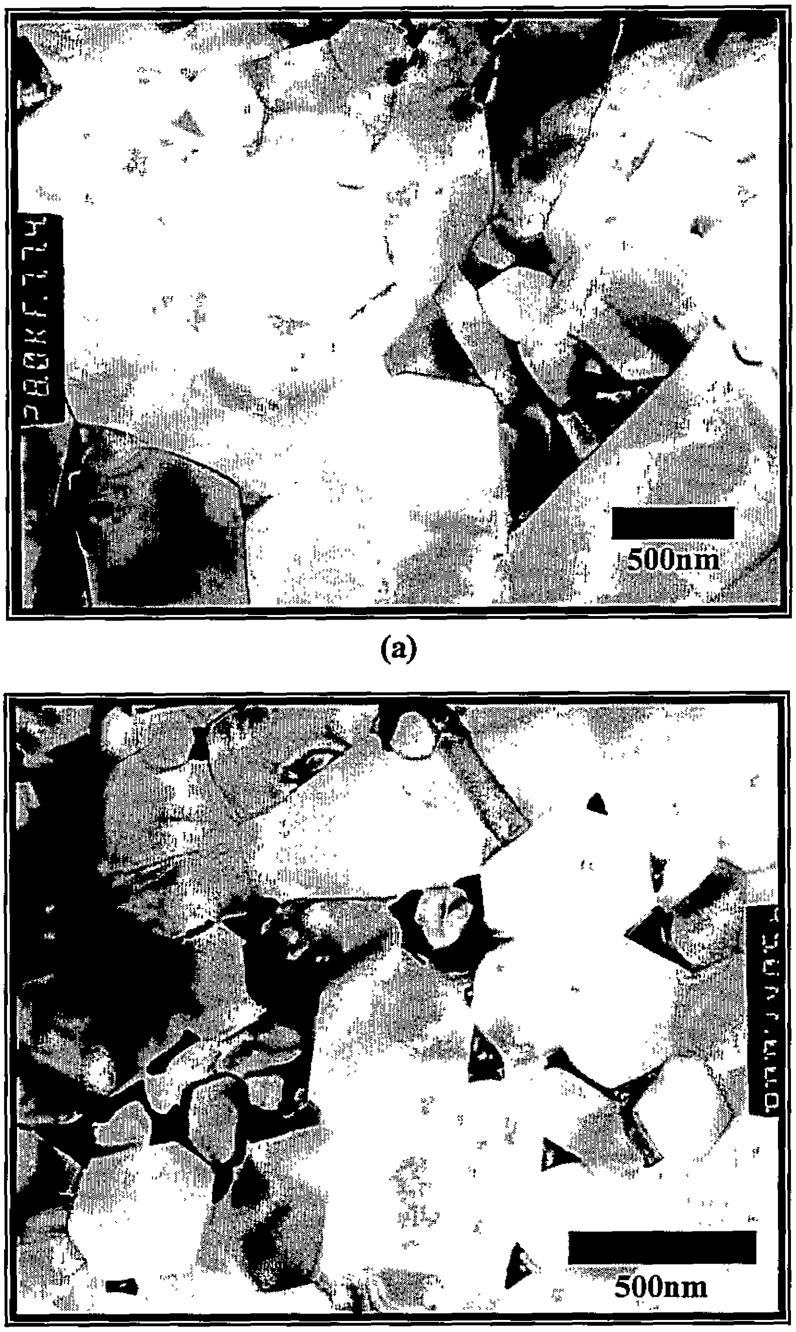

(a)

(b)

Figure 4.43. Bright field TEM micrographs of **(a)** SS4 (A28-1) and **(b)** SS1 (A27-6), in which (b) had the through beam and a diffraction spot from the pocket phase selected to give better contrast. The difference in grain size between the two conditions is much more apparent here than in Figure 4.42.

which meant that they were most likely crystalline. Lattice imaging was also performed using HRTEM, which confirmed that the pocket phases present in the materials studied were indeed crystalline.

Lattice imaging also made it possible to detect discontinuities across the boundaries between the pocket phase and adjoining SiAlON grains. Based on numerous reports of these types of discontinuities, they were thought to be amorphous, or have some limited periodic atomic arrangement [see ibid.; Clarke and Thomas, 1978; Pezzotti et al, 1996; Pan et al, 1996]. One particularly good example of a discontinuity was found in the SS2 foil (see Figure 4.44). This micrograph clearly shows the different SiAlON and pocket phase grains, along with a rather thick perimeter of discontinuity (amorphous material). An enlargement of the lower left hand portion of the pocket phase is shown in Figure 4.45. This enlargement shows the blunt edges of the SiAlON grains, and the region of amorphous material between them. Notice that the thickness of the amorphous material decreases as it penetrates the two-grain SiAlON boundary. The other samples did not show such a thick perimeter of amorphous material, but there were some smaller less pronounced regions observed in corners at the junctions between the pocket phase and the two-grain SiAlON boundaries in SS4 (see Figure 4.46). It was not determined from TEM investigations if there were any trends in the amount of amorphous material present between the pocket phases and the SiAlON grains. Attempts to analyze the chemistry of the thick perimeter of amorphous material found in SS2 (Figures 4.44 and 4.45) were not taken to be accurate due to reasons explained below, so are not presented here.

The EDX analysis was done largely to detect the levels of aluminum in the SiAlON grains, so that a rough estimate on the level of substitution could be made. Typical EDX plots of the highest and lowest level substitution β SiAlON grains are shown in Figure 4.47. Notice that there is little aluminum present, which indicates that the SiAlONs had a low degree of substitution. The x values of substitution were determined from the atomic Si/Al ratio as calculated by LINK ISIS software. Assuming that the stoichiometry of the β SiAlON followed the formula:

$$\mathbf{Si_{3-x}Al_xO_xN_{4-x}}$$

the value of x was solved for using the relation $(3-x)/x = Si/Al$. Of the grains analyzed the x values were not found to vary significantly between samples, or even in the same sample. The approximate range of x was ~0.1 to 0.2 for the three conditions that were investigated. It appeared that the larger grains had slightly higher x values but not enough grains were analyzed to determine if this trend was real or not. One must remember that the defaults of the analysis software were used and that more accurate results could have been obtained had a more thorough analytical technique been employed. However, on the other side of the coin, an exact determination of the degree of substitution would really be a moot point, as SiAlONs, like classical solid solutions, have been reported to exhibit coring and compositional gradients from adjacent glassy, or grain boundary phases [see Kang et al, 1995; Bonnell et al, 1986]. Considering this point, one may realize that the particular regions of the grains analyzed in this study could have been different from a region slightly closer to the center of the same grain. However, this is not to say that the analysis was useless, because it did give an estimate on the magnitude of the average

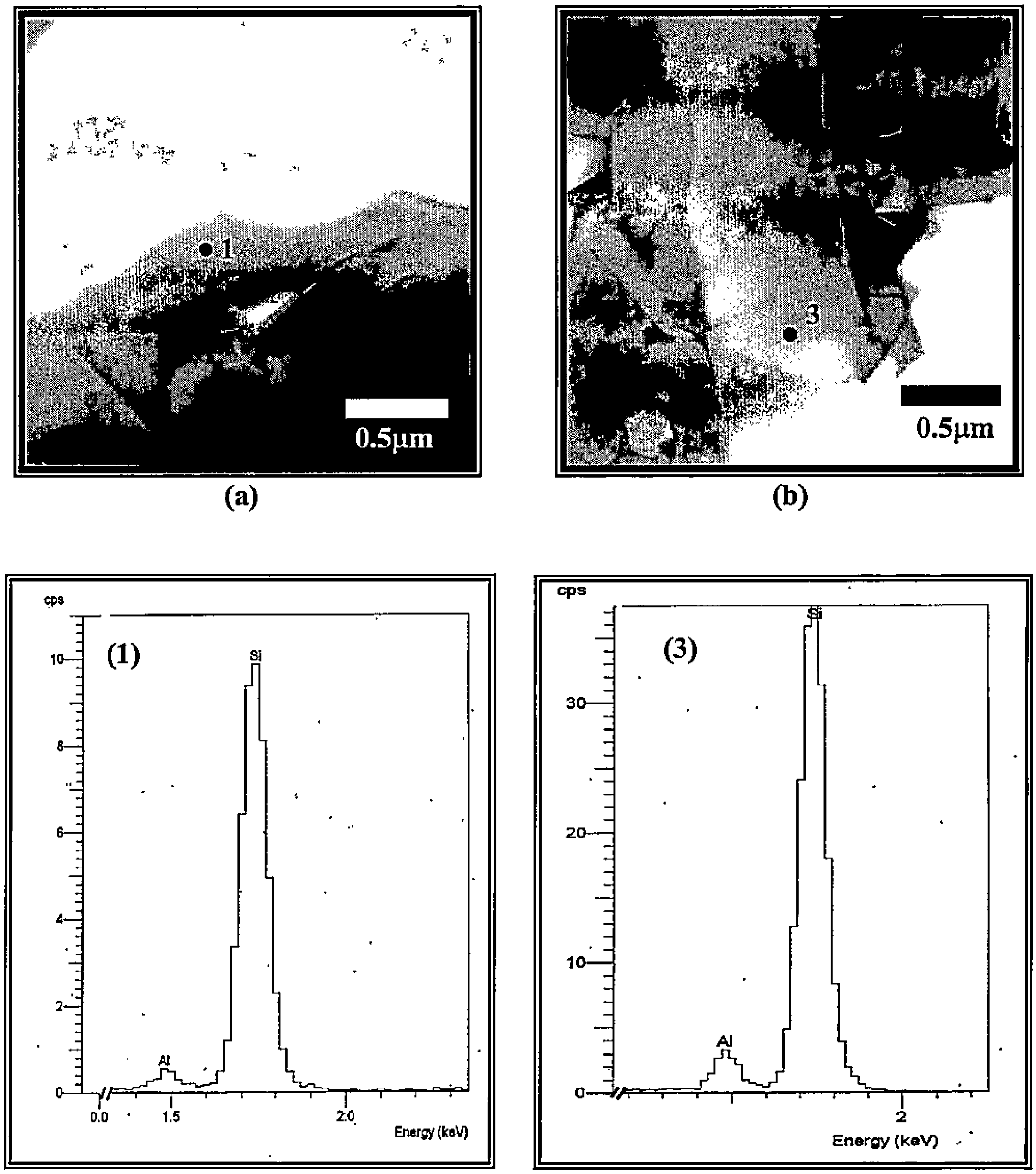

(a) (b)

Figure 4.47. EDX spectra (1) and (3) collected from marked regions in (a) and (b) respectively. Both were β SiAlONs with x=0.1 and x=0.2 for 1 and 3 respectively. Both STEM images areas are from SS1 A27-6.

degree of substitution for the SiAlON grains. When considering x values, one must interpret the value to be an average of all grains, and an average of the gradient in each of those grains.

The amount of Al and O substitution in α SiAlON grains was higher than for the β SiAlON grains, and resulted in lower Si/Al ratios. A typical EDX spectrum of what was determined to be an α SiAlON grain is seen in Figure 4.48. The determination of the degree of substitution for the α SiAlON phase was more complicated than for the β phase as seen in the stoichiometry of the α phase:

$$\mathbf{Y_xSi_{12-m+n}Al_{m+n}O_nN_{16-n}}$$

Based to the published work of Sun et al (1991a, 1991b) it was assumed for this study that the value of m was fixed at 1, and n could vary from 0.5 to 1.7 (m+n=1.5-2.7). Solving for (m+n) using $Si/Al = [12-(m+n)]/(m+n)$ it was determined that (m+n) was around 1.5. For this material, one would expect the value of n to be slightly higher ($n>0.6$), due to the O content present in the form of surface oxides on the Si_3N_4 powder and sintering aids [see Haviar, 1994]. However, one must realize that the estimation of m and n are again averages and dependent on the region of the grain that is anlayzed. Thus, assuming the values of m and n to be plausible, the value of x (amount of Y) was determined to be 0.23-0.28 (depending on the atomic ratio that was used to determine x). This result was consistent with the reports of Haviar (1994) and Sun et al (1991a, 1991b) who reported that the x values of α SiAlONs in a mixed α/β SiAlON have to be less than x=0.33.

From the EDX analysis, estimates on the range of compositions of the α and β SiAlON phases were thought to be:

$$\boldsymbol{\alpha}\mathbf{:}\ \mathbf{Y_{0.23\text{-}0.25}Si_{10.5\text{-}10.7}Al_{1.5\text{-}1.7}O_{0.5\text{-}0.7}N_{15.5\text{-}15.3}}$$

$$\boldsymbol{\beta}\mathbf{:}\ \mathbf{Si_{2.9\text{-}2.8}Al_{0.1\text{-}0.2}O_{0.1\text{-}0.2}N_{3.9\text{-}3.8}}$$

No trends in the degree of substitution were found between the heat treatment conditions, but then again only a small number of grains were analyzed on each of the three foils (about 10 per foil).

The EDX analysis of the pocket phases was less successful. Only one region on one of the foils had seemingly identifiable atomic ratios with minimal doubt. This fact was rather disconcerting, but unsurprising considering that a semi-quantitative approach had been taken from the start of the EDX investigations. The geometry constraints necessary to isolate the pocket phases were much less forgiving in comparison to the analysis of α and β grains, so the fact that difficulties were experienced was understandable. In order to ensure an accurate analysis a *very* thin region of the foil had to be found where there was a minimal occurrence of inclined grain boundaries between the pocket phase and the α or β SiAlON grains. While the small grain size resulted in there being many possible pockets present, the incidence of suitable pockets for analysis was extremely low. Also, the small grain size, and log-normal distribution of the grain size resulted in the pocket phases being very small. The largest pockets that were found were usually no greater than 80-100nm across. While this dimension was not really that small, one must also realize that the largest dimension observed was usually not the dimension of the region that

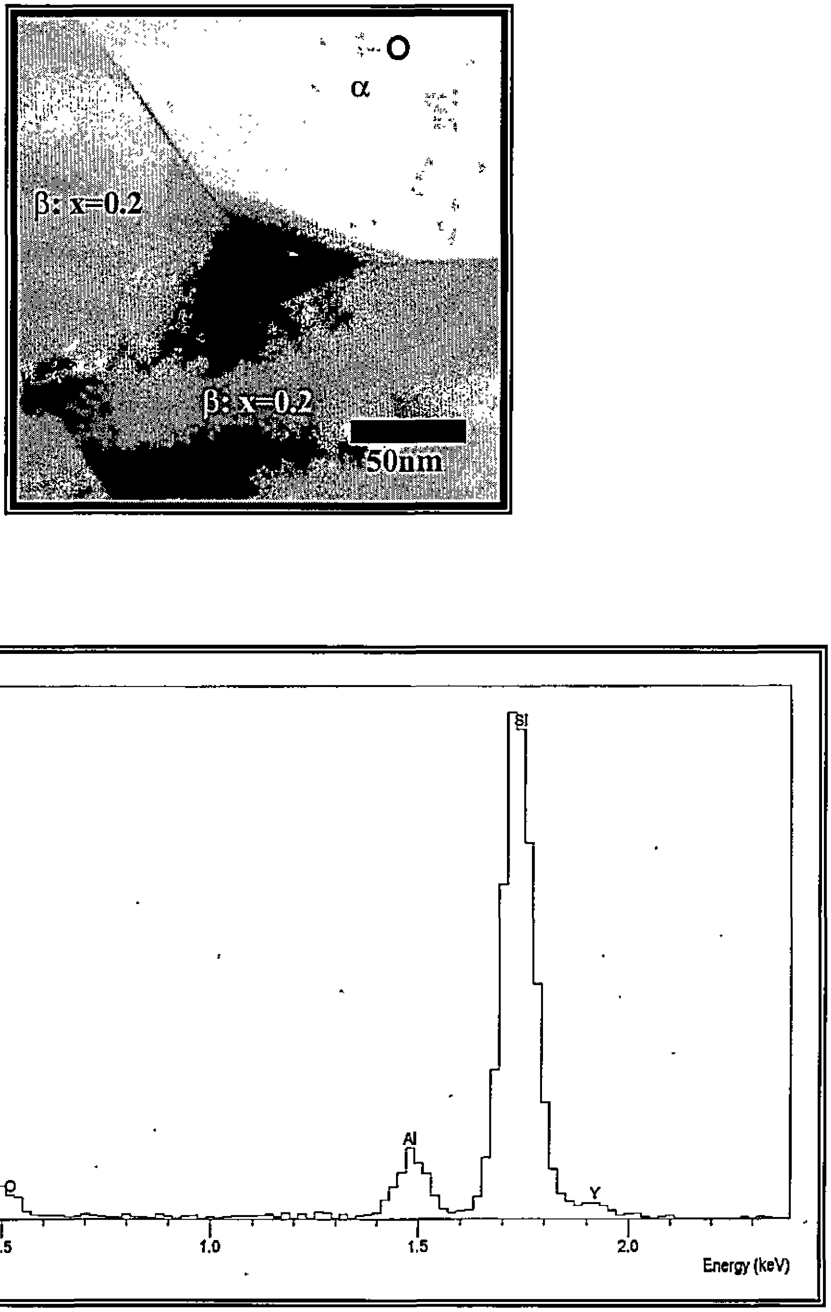

Figure 4.48. Typical EDX spectrum of an α SiAlON grain collected from the marked region in the STEM micrograph. The adjunct grains in the field of view were β SiAlON grains with the substitution levels indicated on the image. SS1 A27-6.

could be analyzed (i.e. pure pocket phase running through the thickness of the foil without intersection of an inclined boundary or underlying grain). Tilting of the specimen was attempted, but with tilting the cross section usually decreased making it more difficult to ensure that only the pocket phase would be analyzed.

Essentially, the small size of the regions that were of interest had to be analyzed with a very small probe size (~8Å). Because of the small probe size the pocket phase experienced damage and mass loss with increased time of x-ray collection. Some attempts were made to move the probe, but undoubtedly there was error due to mass loss. The thinner the region of the foil the more significant the error due to mass loss, since thin sections experienced damage almost instantaneously. Figure 4.49 shows evidence of holes that were drilled through the pocket phase and neighboring SiAlON grains after EDX analysis.

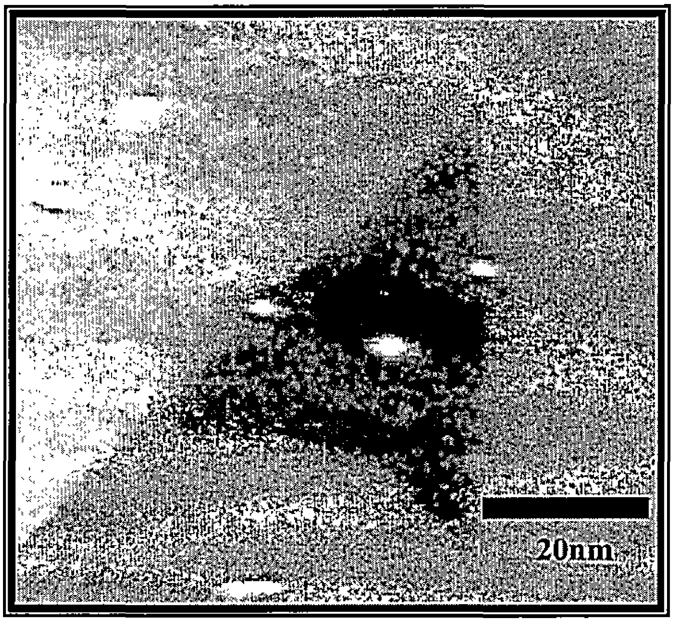

Figure 4.49. Example of beam damage causing mass loss in regions of EDX spectrum collection. All regions appearing as white spots were areas of analysis and resultant damage. STEM image, SS2 A23-6.

Drifting of the sample caused problems as well, so beam tracking was employed in some cases. One can see the regions of the thick amorphous region of SS2 (Figure 4.49) where the EDX analysis was sought, but it can clearly be seen that there was drift and damage across the boundary, so those spectra were not thought to be accurate.

Unfortunately, the situation was such that the thinnest regions of the foil necessary to ensure that only the pocket phase was being analyzed resulted in their being a large degree of mass loss and uncertainty in the measurement. Certainly electron diffraction should be explored as an alternative route to characterizing the chemistry of the pocket phases. Some attempts were made to do just that, but no results from them are presented here.

Despite all the difficulties in obtaining accurate spectra of pocket phases, there was one pocket phase region of SS2 that was analyzed in different places with similar results (shown in Figure 4.50). The atomic ratios for this region, along with those of the adjoining grains are shown in Table 4.8. The pocket phase was determined to be M'_{ss}. Comparison of the spectra collected in this study with analysis done by Ahn and Thomas (1983) showed good agreement in terms of the relative intensity of the peaks for N-melilite (M phase). A slight variation in the peak intensities of Y and Si, along with the presence of an Al peak would be expected for M'_{ss}. The HRTEM image of the region showed the β grain lattice contrast well, and also showed that the area from which spectra 22 and 26 were collected was also crystalline (see Figure 4.50). The structure of the secondary phase and its orientation on either side of the point of contact between the β grains appeared to be the same based on the lattice fringes.

Spectrum #	Si/Al	Si/Y	Si/O	Candidate Phase
23	31.12	*	10.77†	β SiAlON, x=0.09
24	38.32	*	20.73†	β SiAlON, x=0.08
22	4.04	1.32	0.65	M'ss x=0.5-0.6
26	3.51	1.17	0.72	M'ss x=0.6-0.7

* Y peak had negligible area. † not used in calculation of x value.

Table 4.8. Atomic ratios for the spectra collected as depicted from Figure 4.50. The presumed identities of the phases are also shown. SS2 A23-6.

It was not determined if the contrast difference between the pocket phase and the region where the two β grains met was an inclined boundary or a region of amorphous material.

The analysis of the pocket phases seemed to always indicate that Y, O, Si, Al, Ar, and N were present. Therefore, it was thought that these pockets were based on yttrium aliminum silicate nitride compounds. The only trend that could be found between the samples was that secondary phases in SS2, for the most part, contained less Y (relative to the Si peak) than either SS1 or SS4. The O and Al levels were not found to follow any trends.

The amount of argon detected in the secondary phase regions in all samples was seen to be present in larger amounts in the HIP'd conditions. The source of the argon was thought to be from ion milling in the case of the as sintered sample (SS1) and from the atmosphere of the HIP for the other samples. In one case (SS2) argon was calculated by the EDX software to be present at 16 atomic % of the compound.

The TEM investigations presented here revealed how the effect of pressure at high temperature changed the microstructure. From a geometrical standpoint, it was found that the amount of the secondary phase decreased in amount after high pressure (30000psi) was applied at high temperature (1800°C), as was evident in the reduced size and frequency of secondary phase pockets in SS4 compared with SS1. It should be clarified that the largest pocket phase regions were not found to change much in dimension, but reduced only in their frequency after HIP'ing at high temperature. The medium and smallest sized secondary phase pocket regions appeared to have decreased both in size and number. Accompanying this decrease in the amount of secondary phase was an increase in β grain size (and α grain size), and the rearrangement of all grains to produce a higher percentage of three-grain junctions (with no secondary phase pockets at the intersection) in the HIP'd material.

The medium temperature heat treatment of 1650°C at 30000psi (SS2) was not as well characterized as the as sintered or high temperature (high pressure) conditions, but it was thought to have only undergone a slight change in grain size, and minimal decrease in pocket phase amount.

The pocket phases were found to be crystalline in nature after all heat treatment conditions, with some instances of a perimeter of amorphous phase isolating them from the SiAlON grains. The thickness of the amorphous phase was found to decrease as it penetrated two-grain SiAlON junctions grain boundaries. No trends were found to exist for the amount of the amorphous material associated with the different processing conditions, but few regions were examined.

No trends in the degree of substitution of the α and β SiAlON phases were found to exist as a function of the heat treatment conditions. As alluded to, the actual determination of these degrees of substitution does not give much insight other than the average chemical composition of the grains, as the substitution levels depend on position in the grains. The substitution values were found to be x=0.1-0.2 for the β SiAlONs, and m+n=1.5, x=0.23-0.25 for the α SiAlONs.

Chemical analysis of pocket phases using EDX was found to be very difficult. As a whole, the analyses were thought to be inconclusive, but one large thin area in SS2 was determined to be M'_{ss} (x=0.5-0.7). This pocket phase, analyzed in two separate locations, gave repeatable results, so it was thought to have been identified correctly. Other spectra, while potentially correct, could not be matched with any of the compounds thought to be present from XRD analysis, or with any compounds for the system of study. It might have been possible that the regions analyzed were not detected in the XRD tests because they had too small a volume fraction.

5. DISCUSSION

This chapter contains the discussion of the trends observed in Chapter 4, and will present the scientific bases upon which the trends can be explained. The ensuing discussion will first identify the specific microstructural characteristics and mechanisms thought to dictate the mechanical properties of hardness and toughness determined in this study. Secondly, the relationships between the changes in the processing conditions and the changes in the property-specific microstructural characteristics will be made, which will in turn lead to a demonstration of how the trends in the mechanical properties were effected by the changes in processing conditions.

5.1 Microstructural Mechanisms Responsible for Properties

The results of the electron microscopy and XRD investigations gave the most insight as to which microstructural mechanisms were present, and responsible for the observed trends in indentation hardness and toughness. In Chapter 4 it was found that hardness and toughness exhibited some similar trends as a function of the processing conditions, but as will be shown, these trends were largely governed by different microstructural mechanisms. As will be discussed, one must consider that the hardness of a material is dependent on a combination of other intrinsic properties of the material, so certain microstructural mechanisms cannot solely be responsible for the hardness of a material.

5.1.1 Hardness

Recall from Chapter 2 that the microstructural characteristics of importance regarding the hardness of mixed α/β SiAlONs are the $\alpha/\alpha+\beta$ ratio, the grain size (of both α and β SiAlON), the degree of substitution of the β SiAlON phase, the presence and thickness of the intergranular film, and the presence, distribution, and amount of secondary phase. With these factors in mind, let us examine the results of this study.

The $\alpha/\alpha+\beta$ ratio will be addressed first. The different XRD Batches gave slightly different values for the $\alpha/\alpha+\beta$ ratio, as was mentioned in Chapter 4. The errors in the technique were thought to account for some of the scatter, but the relative intensity anomalies in Batches 1 and 5 were thought to be more likely an explanation. An investigation of the data was made in order to determine whether the differences in results were significant or not.

The temperature series at high pressure was analyzed first (SS1, SS5, SS2, SS4). The $\alpha/\alpha+\beta$ ratios for identical samples (done in the different Batches) were plotted against each other to produce Figure 5.1.Since Batch 1 was the only complete data set, it was plotted as the abscissa. The alpha contents of SS1, SS5 and SS2 all seem to overlap in the region of $\alpha/\alpha+\beta = 0.6$, with the exception of the value of SS2 = 0.53 for Batch 1. The alpha contents of SS4 determined from Batches 1 and 4 were very similar. From

Figure 5.1 one can see that the $\alpha/\alpha+\beta$ ratio did not change significantly until after 1650°C; there was only a negligible decrease in alpha content with increasing temperature from the as sintered state (SS1) through the low temperature condition (SS5) to the mid temperature condition (SS2) (when ignoring the result of Batch 1 for SS2). The trend-line shown on the figure indicates that a near linear fit was obtained (slope=0.8, R^2=0.75). This result made it possible to conclude that there was not a significant variation between the different XRD Batches for the $\alpha/\alpha+\beta$ ratios of samples SS1,2,4 and 5.

When the $\alpha/\alpha+\beta$ ratios and hardness are plotted against the HIP temperature of the corresponding conditions it can clearly be seen that there is a strong correlation between the hardness and the $\alpha/\alpha+\beta$ ratio, see Figure 5.2. Both HRA and Hv decrease with decreasing $\alpha/\alpha+\beta$ ratio, which itself does not start to decrease until between 1500 and 1650°C.

The effect of pressure on the hardness can be seen to be negligible (Figure 5.3). The scatter in the data aside, there does not seem to be much change in either the Rockwell or Vicker's hardness with pressure. The $\alpha/\alpha+\beta$ ratio does not seem to vary with pressure either. The scatter in the $\alpha/\alpha+\beta$ ratio as a function of pressure is much higher than was seen for the effect of temperature, but the lower pressure values for Batch 1 and 5 (although different in magnitude) do not seem to vary significantly with pressure. Therefore, the relatively constant value of $\alpha/\alpha+\beta$ ratio over the pressure range seems to explain the constant hardness observed with increasing pressure.

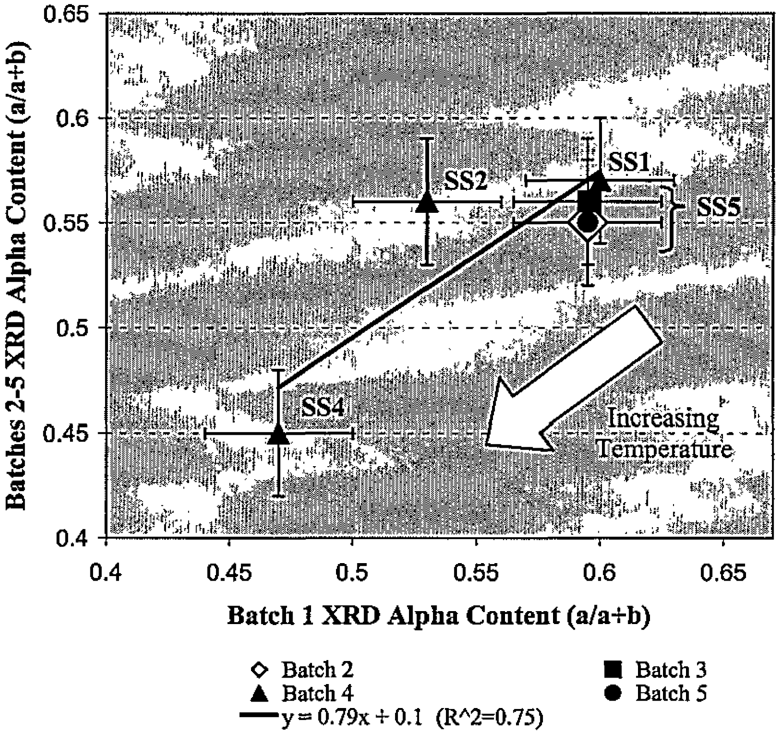

Alpha Content of XRD Batches 2-5 vs. Batch 1 Values (Temperature series at high pressure: SS1, SS5, SS2 and SS4)

Figure 5.1. $\alpha/\alpha+\beta$ ratio values for samples of Batches 2-5 plotted against Batch 1 results. Notice that the slope of the regression line is near 1, indicating that the data from the different Batches was not extremely different. Error bars are ± 0.03.

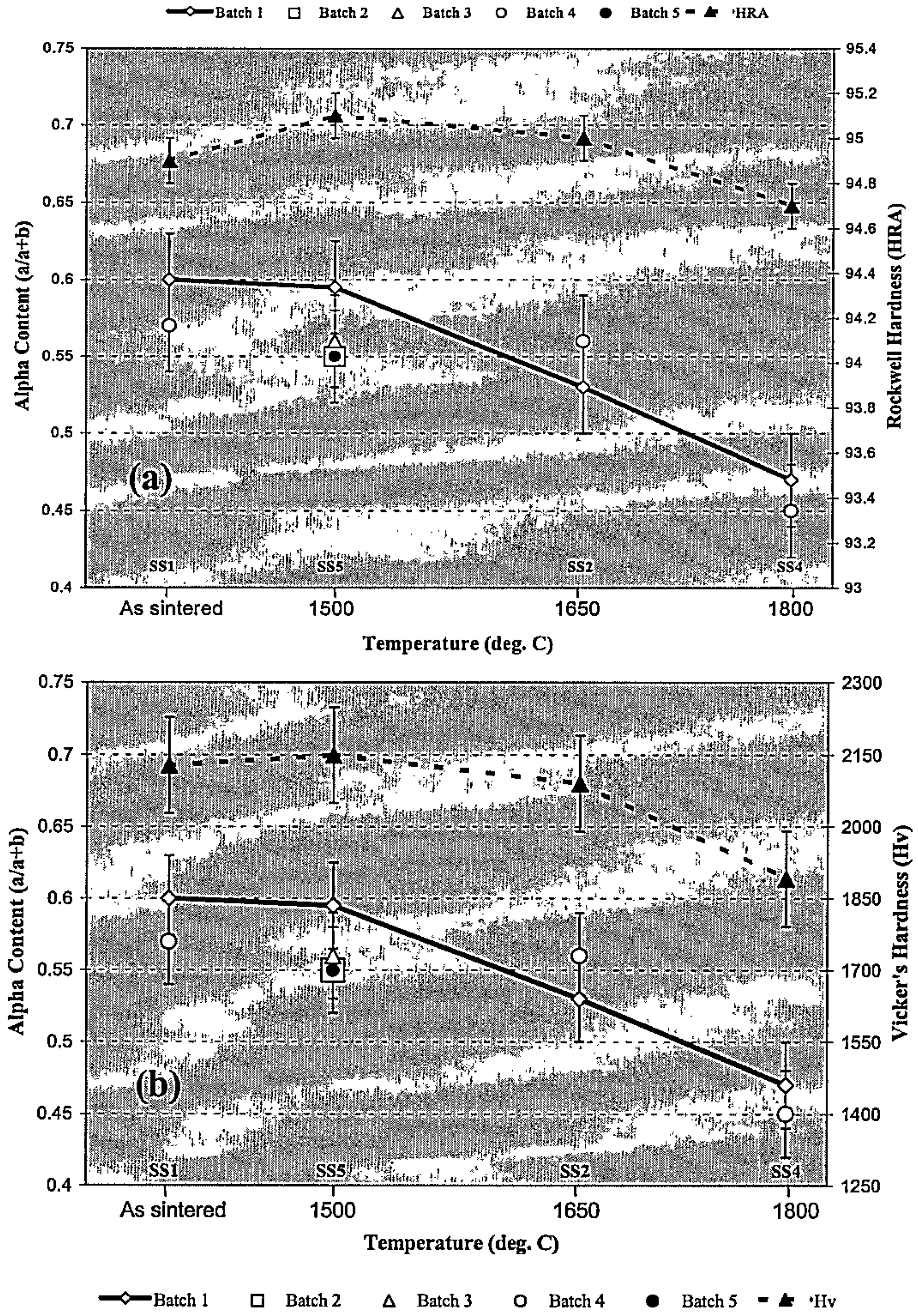

Figure 5.2. The effect of HIP Temperature (at high pressure) on α/α+β ratio and (a) Rockwell hardness and (b) Vicker's hardness. Notice the strong correlation between hardness and α/α+β ratio.

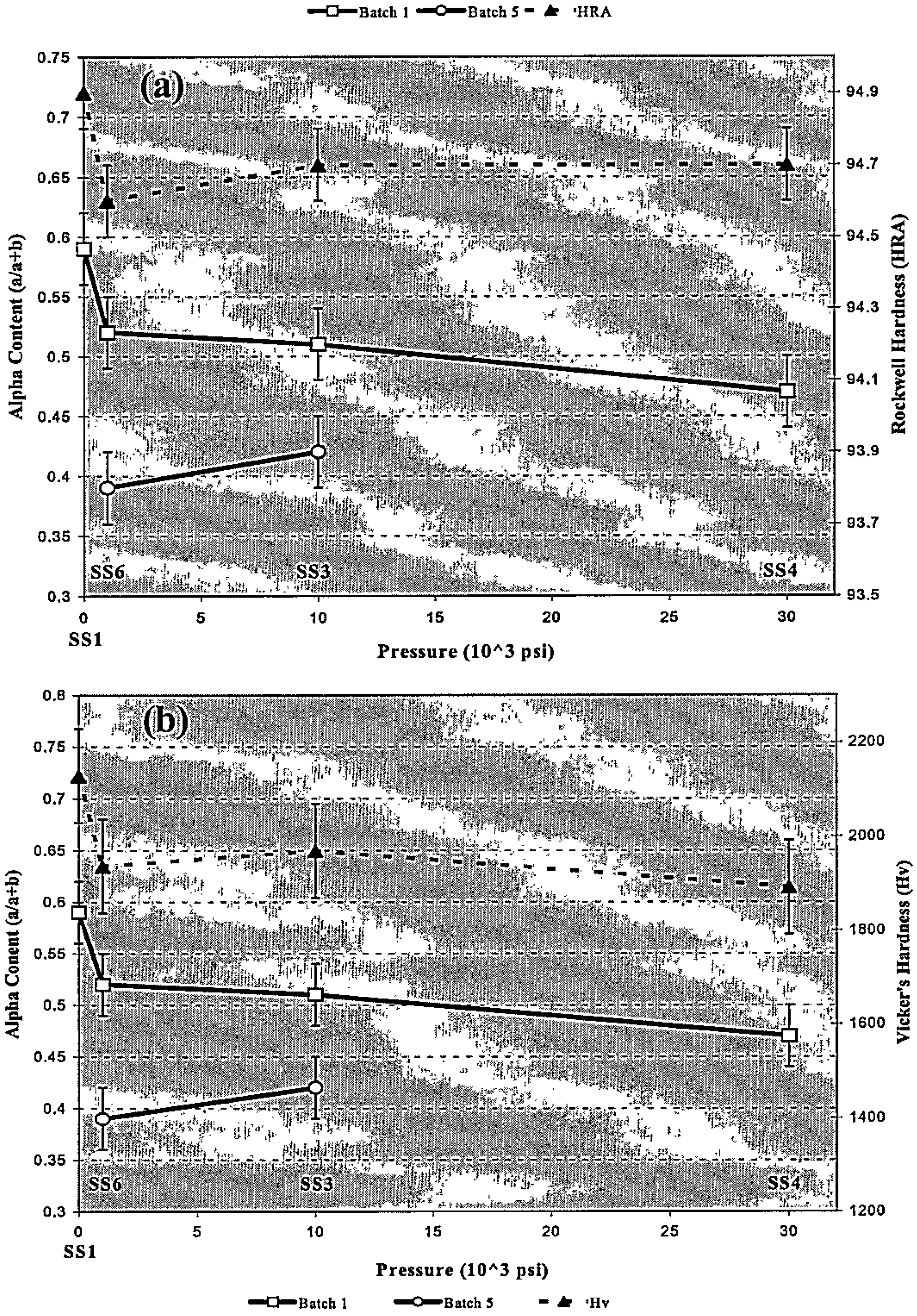

Figure 5.3. The effect of HIP pressure (at high temperature) on α/α+β ratio and (a) Rockwell hardness and (b) Vicker's hardness. Notice that there seems to be little effect of pressure on hardness or α/α+β ratio.

The changes in $\alpha/\alpha+\beta$ ratio we are considering are only 0.13 from the as sintered state to the highest temperature and pressure conditions, so one can appreciate that the magnitude of the hardness change is small, but very real. From the range of hardness of α/β SiAlONs reported by Ekström and Nygren (1992), the approximate change in hardness should be 500Hv from $\alpha/\alpha+\beta=0-1$. When we analyze the results from this study we find that the change in Vicker's hardness for $\alpha/\alpha+\beta$ going from 0.47 to 0.60 is 250Hv, which is roughly 4 times the change that Ekström and Nygren (1992) predicted for the same incremental change in $\alpha/\alpha+\beta$ ratio. It seems apparent that the change in the $\alpha/\alpha+\beta$ ratio of the present material does not follow the hardness behaviour described by others. However, recall that the $\alpha/\alpha+\beta$ ratio was only one mechanism found to control the hardness of α/β SiAlONs, so it could be that the present material is influenced more by other factors.

The absolute values of the hardness of the materials in this study were also higher than those reported in literature for similar applied loads. One must remember that all the data compared to the current study was from conventionally prepared materials, not microwave sintered materials. The question then arises: why are the materials in this study so much harder than those reported for α/β SiAlONs with similar $\alpha/\alpha+\beta$ ratios? The answer could be linked with the method of processing, or that the magnitude of the $\alpha/\alpha+\beta$ ratio is not as important as other mechanisms that are responsible for the hardness in these materials.

Aside from the $\alpha/\alpha+\beta$ ratio, two other mechanisms could be responsible for the high hardness of this material: the small grain size, and the character and distribution of the secondary phase. Of these, the grain size will be considered first.

The grain size of microwave sintered silicon nitrides has been found to be much smaller than their conventionally produced counterparts [Plucknett and Wilkinson, 1994]. The present material's grain size was found to follow the same trend. The fast sintering time did not permit much grain growth to occur after the transformation of $\alpha \rightarrow \beta$ had begun, and after cooling the remnant grain structure contained a distribution of small α and small β SiAlON grains.

The change in the grain size with increasing HIP temperature (at high pressure) was quantified in Chapter 4. There appeared to be no change in grain size as a function of pressure, but this was a qualitative observation. In discussing the change in grain size as a function of the temperature (at high pressure) it should be emphasized that the $\alpha/\alpha+\beta$ ratio and the grain size are directly related. As the grain size of β was found to increase with increasing temperature, the amount of β was also found to increase (i.e. the $\alpha/\alpha+\beta$ ratio decreased; see Figure 5.4). This was due to the fact that α was consumed in the phase transformation, and the β grains underwent coarsening. It follows that the alpha grain size distribution would also change during the transformation: based on the higher interfacial free energy of the smaller α grains, they would dissolve first, resulting in the average grain size of the α phase increasing as the $\alpha \rightarrow \beta$ transformation progressed. Thus, by knowing how the β grain size evolved, we can predict how the α grain size changed.

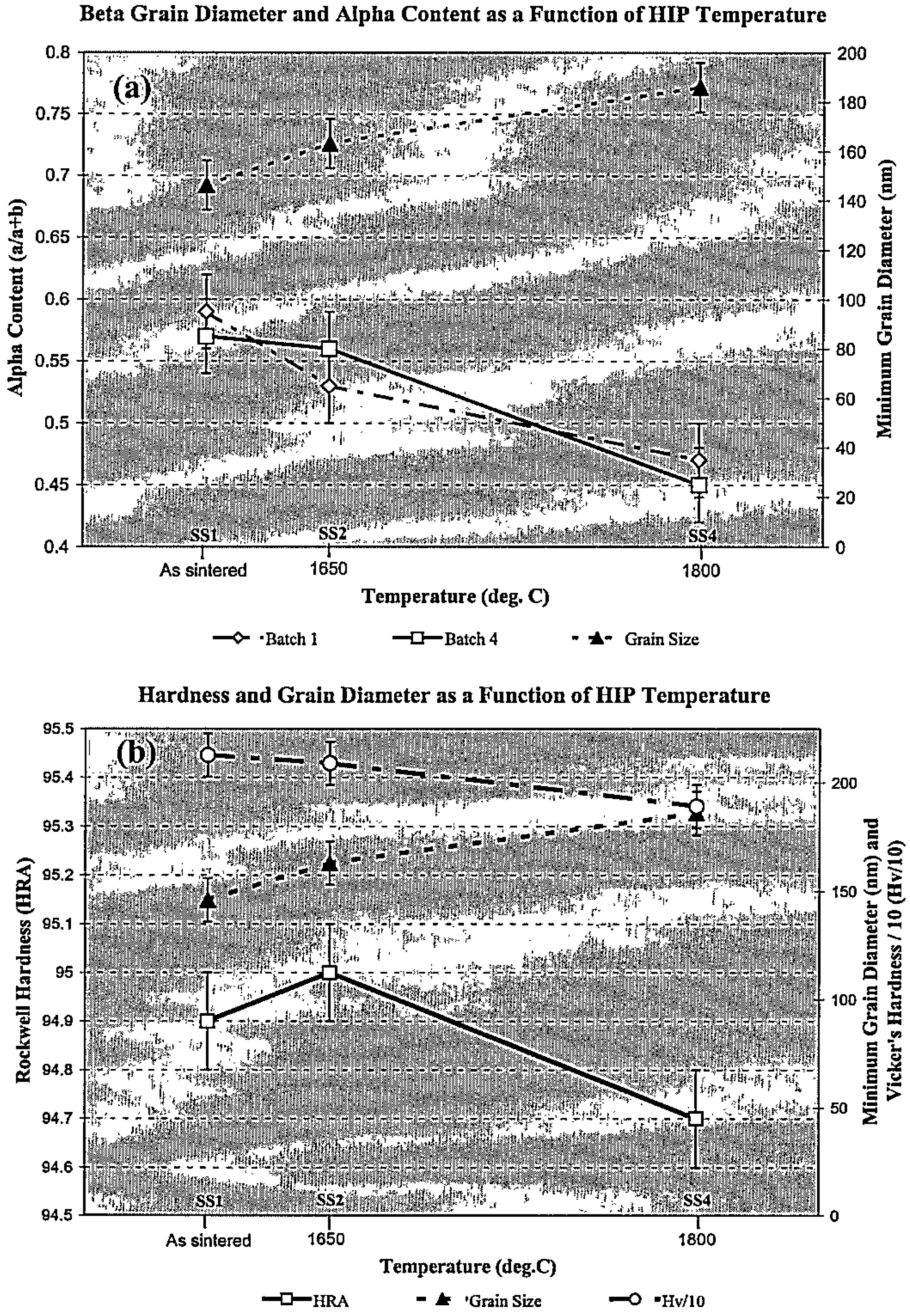

Figure 5.4. The effect of HIP Temperature on (a) the $\alpha/\alpha+\beta$ ratio and β Grain diameter, and (b) the Rockwell and normalized Vicker's hardness (and grain diameter).

For the above case we have assumed that there is a relatively large increase in β content and a significant amount of coarsening and dissolution of the α phase. One can imagine that the supersaturated liquid phase of sintering could supply the necessary Si, N, Al, and O required by β grain coarsening without any further dissolution of the α phase. However, the changes in the α/α+β ratio would not be significant, nor would the degree of coarsening when considering the small amount of liquid phase present in the studied material. We must also realize that this phenomenon would only occur during sintering for the present material, as refractory crystalline secondary phases were formed from the liquid phase upon cooling. This will be discussed in more detail below.

When hardness and grain size are plotted against HIP temperature one sees that an increase in grain size has accompanied a decrease in both HRA and normalized Hv (Hv/10 for ease of showing all values on the same plot). From this plot it seems unequivocal that the α/α+β ratio, β grain size, and hardness are all inter-related. In further support of this idea it was discovered that neither the α/α+β ratio, grain size, or hardness were affected by HIP pressure.

More evidence in favour of the presumed inter-relatedness of α/α+β ratio, grain size and hardness is found in the annealed heat treatment data. Recall that the hardness decreased after the long time annealing heat treatment. When we plot the hardness and α/α+β ratio together versus the original heat treatment pressure of the annealed samples, we find that annealing caused a relatively constant decrease in both α/α+β ratio and hardness (see Figure 5.5), with no effect of pressure on the pre or post annealed hardness or α/α+β ratio (compare Figure 5.5 to Figure 5.3). While no grain size measurements

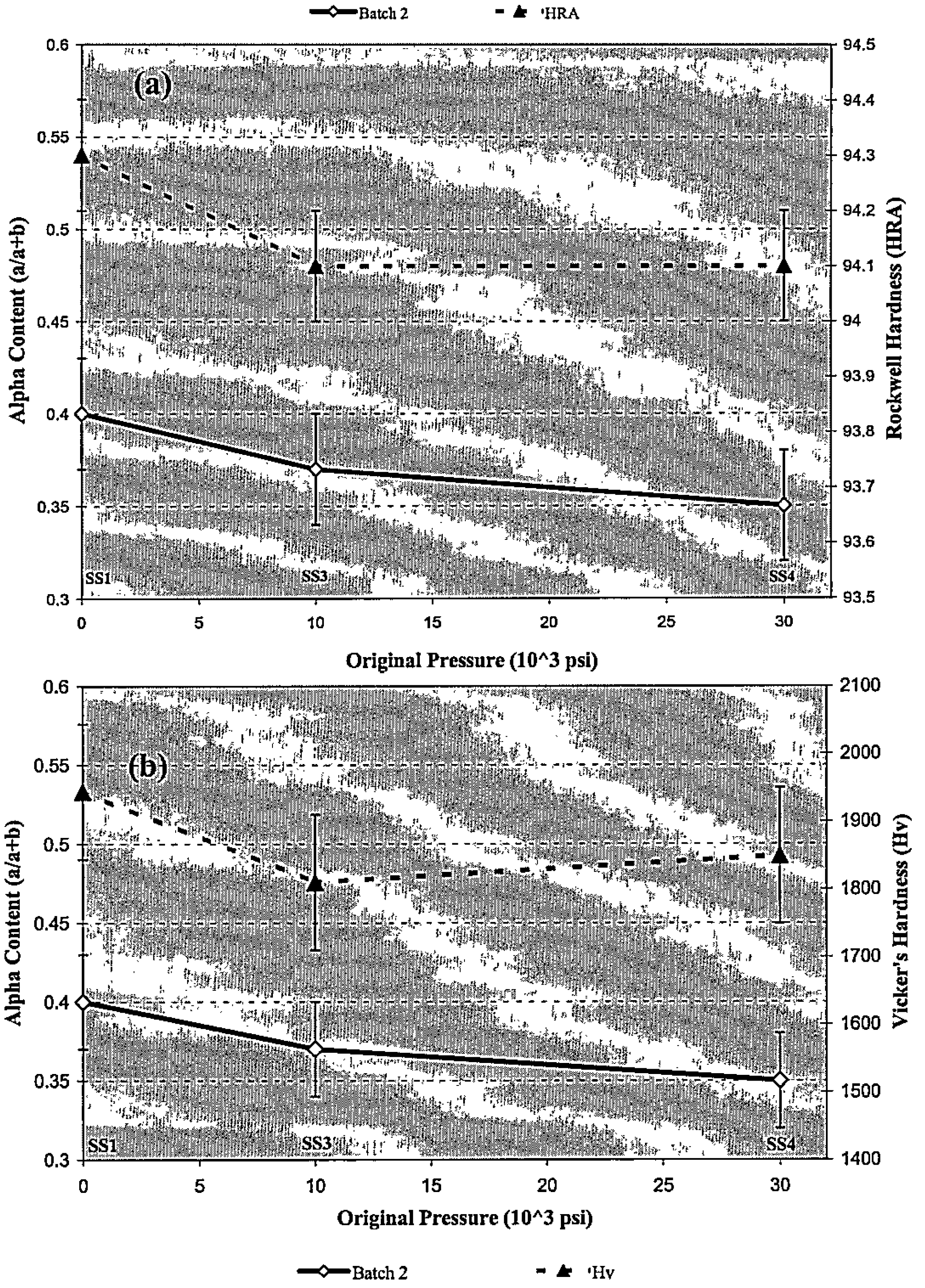

Figure 5.5. Annealed $\alpha/\alpha{+}\beta$ ratio and (a) Rockwell hardness and (b) Vicker's hardness plotted as a function of pre-annealed heat treatment pressure.

were done on any of the annealed samples, we can assume that substantial grain growth most likely occurred (reports from grain size in literature for long time heat treatments are the basis for this presumption [e.g. see Lee et al., 1988]). With these facts in mind, we almost have a complete understanding of the microstructural mechanisms responsible for the hardness.

To complete the discussion of the microstructural mechanisms found to be responsible for hardness, let us examine the observed trends regarding the secondary phase. When the trends in the amount of secondary phase are referenced, the reader should be reminded that secondary phase amount is the amount of *crystalline* secondary phase present at the multigrain grain junction pockets. From the TEM investigations of this study we also assume that there is an amorphous film between two-grain junctions. The analysis of the amorphous grain boundary film will be discussed in the next section concerning fracture toughness.

Firstly, the amount of secondary crystalline phase was found to decrease with increasing temperature (at high pressure) and also to decrease with increasing pressure (at high temperature). If high hardness were dependent on a large amount of secondary phase present in the microstructure we would have expected a decrease in hardness with increasing pressure and temperature. From the data it was found that there was only a decrease in hardness with increasing temperature, and no significant changes in hardness with pressure. Therefore, the trends in the hardness and secondary phase amount do not match very well, and it seems very unlikely that hardness is related to the amount of secondary phase. This conclusion also seems valid if we assume that hardness of the material is simply related to the amount of energy required to move dislocations in the different phases. The volume fraction of the phases then becomes an important point to consider, along with the relative hardness of each of the phases. When we consider the present material, the small amounts of secondary phase present (10-15 volume % maximum), and their small size and isolation from one another we conclude that not enough secondary phase was present in the microstructure to have had an impact on the hardness. Therefore, the microstructural parameters of importance to this study were discovered to be the $\alpha/\alpha+\beta$ ratio and the grain size.

The hardest materials of this study were those produced as sintered and at a low temperature heat treatment. We found that these conditions also had the highest fraction of the α phase, so as already reported there was a link between the hardness and the amount of α phase. A possible reason why α is the harder of the two silicon nitride phases can be inferred form the facts that the α c-axis is twice as large as the β phase, and the stacking of α basal layers is not as symmetric as the β phase [Reimanis et al., 1996]. These two features could be thought of to make the movement of dislocations more difficult in the α phase as compared to the β phase, because the Burger's vector would be larger. So, if more of the harder α phase was present in the microstructure then by a simple rule of mixtures approach the hardness of the material would also be higher.

The grain size of the material in this study was not seen to change independently of the $\alpha/\alpha+\beta$ ratio. Therefore, although we detected a decrease in the hardness with increasing grain size, we cannot neglect the fact that increasing grain size was accompanied by a decrease in α content. As a result, the changes in grain size and $\alpha/\alpha+\beta$

ratio cannot be separated into independent mechanisms for hardness. However, we can, as a rough approximation, compare the hardness of the materials of this study with the results of other studies on similar materials with the same $\alpha/\alpha+\beta$ ratio, similar x value of α SiAlON, and a larger grain size. When this comparison is made, we find that the hardness of the present study was higher than those of other studies [Ekström and Nygren, 1992; Bartek et al., 1992]. There is some doubt in the comparison as to how much harder the current material is because lower indentation loads were used in this study, and we have already been alerted to the fact that lower loads usually produce higher hardness values. Nonetheless, the hardness of the microwave sintered material seems to be higher, if only slightly, indicating that perhaps the small grain size of the material contributes to its hardness. However, the most prominent mechanism responsible for the hardness of mixed α and β SiAlONs appears to be the $\alpha/\alpha+\beta$ ratio.

5.1.2 Toughness

Again referring to Chapter 2, the prominent microstructural mechanisms responsible for toughness in *in situ* reinforced composites, such as the current material, have been identified to be the elongated phase phase's morphology and grain size, and the character of the secondary phase. The present study found that the nature of the secondary phase was mostly responsible for the fracture behaviour observed. Therefore, the discussion of the fracture behaviour of the material in this study will primarily focus on the trends observed in the secondary phase instead of on the grain size and morphology of the α and β phases. While the latter mechanisms cannot be ignored, they were thought not to have had considerable effect on the toughness of the material.

Two initial arguments can be made to support the claims of negligible grain size and morphology effects on the toughness. Firstly, let us consider the grain morphology issue. The grain size of the material was found to increase with increasing temperature, and the amount of β also increased (these two phenomena are directly related). Assuming that the defect concentration in the grains did not increase as they grew, we can assume that their strength did not change [Brenner, 1957]. The assumption of unchanging strength of the β grains is paramount to demonstrate that an increase in grain diameter should have caused toughening. As Brenner (ibid.) found, the tensile strength of whiskers was inversely proportional to their diameter due to the increased presence and probability of defects in large grains. For the current study the increases in grain size were small, and therefore the strength of individual grains should not have been significantly different between the smallest and largest grains. Thus, the ability for elongated grains to exist as bridges across the crack tip wake, once debonding and crack deflection occurred, was not strength dependent, and therefore not size dependent. And, any instances of fiber rupture that were observed would therefore have been related to the strength of the interface between the elongated grains and the secondary phase.

The results of this study show that the toughness decreased with increasing grain size, at high pressure (see Figure 5.6). This result implies that either the grain size increase was so large that the defect concentration of the grains was higher (and the strength therefore lower) or that a completely different mechanism was operating. From the above argument, the small changes in grain diameter were most likely not responsible for a strength decrease of the β phase, therefore, a more influential mechanism must be present. The results of Kleebe et al. (1999) show that the change in grain diameter observed in this study should have had no effect whatsoever on the toughness of the material, and if anything, there should have been a slight increase in toughness, not the observed decrease.

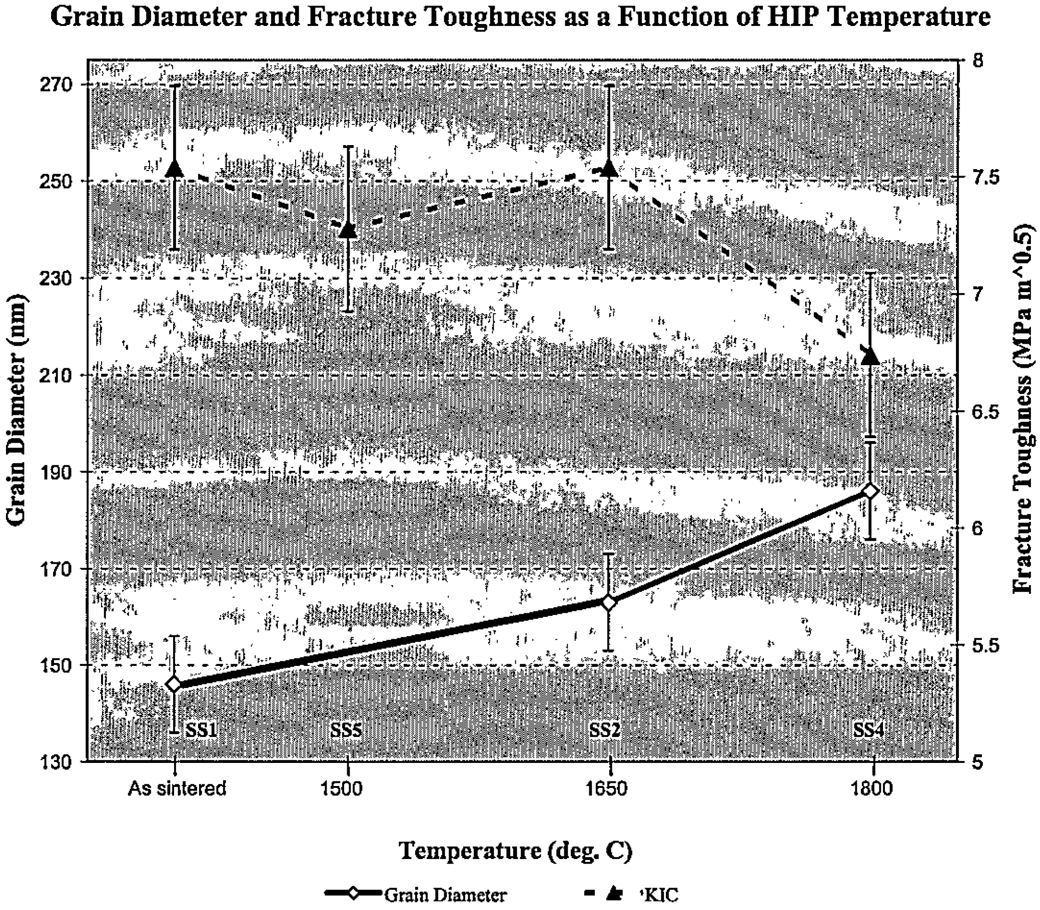

Figure 5.6. The effect of HIP Temperature on the grain diameter and fracture toughness of heat treatments done at high pressure.

This brings up the second point about the α and β grain morphologies. It was found that there was a decrease in the toughness as the pressure was increased, and that no change in grain size was thought to have occurred as a function of pressure. If the fracture behaviour of the current material was linked to the grain size alone, then the decrease in fracture toughness with increasing pressure should not have been observed.

When pondering this interpretation of the results, the lack of toughening observed with increasing grain size outlined so far has been for the case of high-pressure conditions only. When we compare the fracture toughness at the mid pressure conditions (MS3 and SS3) it was found that the fracture toughness did not change at all with increasing temperature. When the low-pressure condition (SS6) is analyzed we actually find that an increase in toughness occurred above the sintered condition (SS1). Could it be possible that at mid and low pressure the small grain size increase contributed to toughening, and that at high pressure there was another overriding mechanism responsible for the toughness decrease? Let us investigate possible answers to this question.

Let us assume first that the answer to the above question is yes, and try to find supporting evidence. Let us also neglect, for the moment, changes in the secondary phase, as those will be discussed in the next section. Recall that a pressure effect on the grain size was not observed. If this observation was correct, it would not seem possible that samples heat treated at the same temperature would exhibit such large differences in toughness when their grain size was equivalent. Furthermore, it would not be expected that long time annealing treatments, at the same temperature, would cause a decrease in toughness because more grain coarsening (hence toughening) would have occurred (we again make the assumption that the increase in grain diameter was not large enough to have reduced the strength of the elongated grains, which seems reasonable). From these arguments, we find it difficult to support any possibility that the grain size increase due to increased temperature had any effects of the toughness of the conditions studied, regardless of the pressure.

To complete the treatment of grain size effects on the toughness we have one variable left to consider: time. The observation of lower toughness at shorter HIP times will be explained here. When we compare the XRD analysis of the long time annealing heat treatment and the 120 minute HIP conditions discussed above we find that longer times caused increases in the amount of β phase. Although no grain size measurements were done on the annealed samples we can be certain that an increase in β grain size occurred because some α phase was consumed. That being said, we can extrapolate back in time to the shorter HIP times and predict that not as much α had transformed to β as compared with the 120 minute conditions. Due to the fact that the same trends were seen in the toughness data at shorter times we can conclude that there must have been a slight grain size increase from 30 to 120 minutes, which caused a very slight increase in the toughness. Naturally, this prediction assumes that no changes in the secondary phase occurred between the 30 and 120 minute conditions. The fact that the toughness did not continue to increase as the grain size increased can be explained by a competing microstructural mechanism, namely the evolution of the secondary phase.

The fact that the amount of crystalline phase was found to decrease with increasing temperature and pressure seems to fit well with the observed trends in fracture toughness. However, let us first analyze the results obtained regarding the secondary phase, and its response to the changing processing conditions before we come to any conclusions about how the fracture toughness was affected by the secondary phase characteristics.

It was found that increasing the pressure at high temperature caused a decrease in the amount of crystalline secondary phase, which was also assumed to be tantamount to a decrease in the total amount of secondary phase. Likewise, an increase in temperature caused a decrease in the total amount of crystalline phase (again found to be a decrease in the total amount of secondary phase). In order to understand these findings a few different approaches will be presented here: discussion of the distribution of the secondary phase, the degree of crystallinity of the secondary phase pockets, the thermodynamic equilibrium of the system, and an investigation into how much amorphous phase film should be present in the different materials.

In addition to the amount of secondary phase, it was also found that the distribution of the secondary phase changed as a function of both pressure and temperature. However, we must keep in mind that when we discuss the effects of pressure and temperature that any effects of pressure were seen at high temperature, and vice versa. The change in the size and distribution of the secondary phase can be summarized as follows: there was a decrease in the size and number of small and medium regions of secondary phase, and little to no change in the size of the large regions, but a decrease in their frequency. This can be explained by how the distribution was produced to begin with. In sintering, large regions of secondary phase were created when interlocking of long (or large) grains prevented rearrangement of the local grains around the pocket. By the opposing argument, the smaller and medium sized pockets were created when significantly more rearrangement could take place. HIP'ing at high pressure and high temperature caused further rearrangement to occur, resulting in a reduction in the size of the pockets neighbouring the rearranged grains. Presumably, the large pockets that remained had already undergone the maximum local rearrangement possible during sintering, so the application of pressure did not alter their size. This particle rearrangement also produced more three-grain junctions with very small amounts of secondary phase at the point of intersection.

When considering this microstructural development, one question remains: where did all the liquid medium go if the size and number of all pockets decreased after rearrangement? In order to answer this question we need to consider two possibilities: could the liquid have been absorbed, or could it have been redistributed as an amorphous film along grain boundaries. It was found that the total amount of crystalline secondary phase decreased as the pockets got smaller and disappeared, and that no difference in glassy phase amount was observed to be located at multigrain pockets. From this we can assume that the degree of crystallization of the secondary phase triple pockets did not change significantly. However, it is possible that some triple pockets did not crystallize. Many more pockets would have to be analyzed to say with complete certainty that all the pockets did or did not crystallize. If there were some pockets that cooled to form a glassy phase, then there would have to be a mechanism to selectively prevent crystallization of certain pockets. Such a selective mechanism would most likely have to be a chemical gradient, which seems unlikely in the materials studied here. Furthermore, the total amount of secondary phase, be it crystalline or not, was found to decrease as a function of increasing temperature and pressure. When one compares the micrographs of the as sintered state (SS1) and the high temperature high pressure condition (SS4) it is clearly seen that there is simply less secondary phase present in SS4 (Figures 4.42 and 4.43). From electron microscopy studies it seems convincing that there was a decrease in the amount of secondary phase, which was tantamount to the decrease in secondary crystalline phase as detected by XRD. Therefore , the prediction that the liquid phase was absorbed seems likely.

No measurements of the thickness of the amorphous film present at two-grain junctions were made, but it did not appear as though a thick film developed at two-grain junctions. Based on Clarke's (1987) predictions of the equilibrium thickness of amorphous films present in silicon nitride ceramics, it did not appear that the grain boundaries present in this material were outside of the thickness range of 0.5-2nm. Intuitively, it would be very improbable for the high pressure of the HIP to allow for any penetration of liquid into two-grain boundaries; the applied pressure would displace any liquid present at two-grain junctions to the multigrain pockets, so no increase in the two-grain boundary film could have been possible (assuming an isostatic pressure).

For the instance seen in Figures 4.44 and 4.45, where a rather large perimeter of amorphous phase was seen around the crystalline pocket phase, it was seen that the thickness of the amorphous region decreased from ~5 to ~1nm as it penetrated the two-grain boundary. If the dihedral angle of the boundary is measured at the corners of penetration one finds that it is less than $\pi/3$. Raj (1981) predicted that a glass (which would normally be incorporated into the matrix grains as a solid solution) could be stable in a triple junction if the dihedral angle of the boundary was less than $\pi/3$ (i.e. the glass would not be absorbed, nor would it wet the two-grain boundaries). This prediction was based on the argument that any penetration of glass along two-grain boundaries would require an increase in energy because of a larger interfacial area. Thus, the minimum energy geometry for the glass would be in a triple pocket if the angle between the grains was less than $\pi/3$. Questions about the crystallization behaviour of such triple pockets then arise, in particular, why is there only partial crystallization in some triple pockets? (e.g. Figure 4.44).

One may consider the study of Raj and Lange (1981) to explain the observation of partial crystallization of a triple pocket. When the liquid phase starts to crystallize there may be a volume expansion (crystalline solids are usually less dense than their glasses). As this volume expansion occurs the remaining liquid cannot flow down the two-grain boundaries because of the interfacial barriers, and so a hydrostatic stress is introduced into the liquid. The constraint on the liquid by the surrounding grains, and the volume increase during the transformation, thus introduce a strain energy into the liquid that prevents it from fully crystallizing.

From the triple pockets analyzed, recall that very few were noted to have a low degree of crystallization, and that the appearance of any left over liquid was only found at the corners of the triple pockets. It might have been possible that the different phases detected from XRD had different volume expansions when they crystallized, and so only some of the pockets exhibited partial crystallization.

Generally, the smallest pocket phases will have the least amount of crystallization possible, as observed by Cinibulk et al. (1990). The same authors also found that after annealing heat treatments nearly complete crystallization of the smallest pockets could be accomplished. Their interpretation of this result was that either the strain energy produced from the volume expansion was accommodated somehow, or that the amount of strain energy predicted by Raj and Lange (1981) was overestimated. Thus, the minimum free energy state of the pocket existed when the size of the transforming crystal was close to the triple pocket size. When we consider the high degrees of crystallization observed in this study, a similar interpretation can be made.

If one accepts the fact that minimal amorphous phase formed in the triple pockets in this study, the premise of absorption of the liquid phase needs to be contemplated. Assuming that absorption of the liquid phase did occur, we must determine how it was absorbed. Recall that the amount of β increased as temperature increased, but the amount of β was unvarying with pressure. As the increase in temperature caused more β to form, the β would require Al and O from the liquid phase. If the liquid was the only source of Al and O, and the growing β grains the only sink, then the amount of liquid phase would decrease as β grain coarsening progressed. However, the amount of α phase was found to decrease as the β amount increased. One would assume from this finding that a constant source of Al and O in the α phase supplied the liquid phase with the components for the necessary β grain coarsening. We cannot, however, neglect the fact that the α phase could have absorbed Al, O and Y from the liquid as well, even though the overall amount of α was found to decrease with increasing temperature. The unfortunate paradigm that one holds concerning phase transformations is the usual expectation that they proceed to completion. For the sake of α and β SiAlONs it has usually been presented that β is the high temperature polymorph, and that the α phase will tend to fully transform into the β phase. At this stage we must ponder the thermodynamic equilibrium of the present system, to see if we should expect all the α to transform into β. Based on where the composition for this material is thought to lie on the published behavioural diagrams [Sun et al. A and B, 1990; Huang and Chen 1996] we expect there to be both α and β SiAlON present in equilibrium (i.e. on a tie line between the β SiAlON single phase line and the α SiAlON boundary facing the β SiAlON line). This fact implies that once the equilibrium value of the α/α+β ratio has been met no further α→β transformation should occur. When the equilibrium permits, single phase α SiAlONs and decreasing amounts of β SiAlON (reverse α→β transformation) with increasing time and temperature of heat treatments have been observed [Bartek et al. 1992; Huang et al., 1983; Rosenflanz and Chen, 1999]. So, there is evidence that the α→β transformation does not always go to completion, or in only one direction.

At the equilibrium concentrations, both α and β could then absorb the liquid phase with little change in the α/α+β ratio so long as the changes in substitution in each phase did not alter the equilibrium value of the α/α+β ratio. The fact that the α and β SiAlON boundaries (tie line ends) are parallel to each other on the equilibrium diagram, supports the theoretical argument that changes in substitution could occur with no change in the $\alpha/\alpha+\beta$ ratio. A further implication to this idea would be that the secondary phases compatible with the changing α and β SiAlONs would either change, or their degree of substitution would shift. Of course, the high temperature equilibrium would be expected to differ from the low temperature equilibrium.

At lower temperatures, where the phase transformation is more sluggish, there would simply be less β grain coarsening and a very small change in the $\alpha/\alpha+\beta$ ratio. Another point to consider is the fact that the $\alpha \rightarrow \beta$ transformation occurs via a dissolution reprecipitation process (see Chapter 2). Thus, a liquid medium is required for materials transport and β grain growth, or $\alpha/\alpha+\beta$ ratio changes. Considering the low temperature at which the eutectic liquid phase forms during sintering (~1375°C) it is not surprising that the final $\alpha/\alpha+\beta$ ratio was 0.6 in the as sintered material of this study. However, upon cooling, the liquid phase crystallized into more refractory compounds. When subsequent heat treatments were performed on the previously sintered material these crystalline secondary phases did not liquefy at the temperature where the $\alpha \rightarrow \beta$ transformation would normally occur, so very little change in the $\alpha/\alpha+\beta$ ratio was observed because of a lack of liquid medium. If we investigate reports on the temperatures at which the refractory secondary crystalline phases are stable, we find for instance that the M phase is stable up to 1600°C [Huang and Chen, 1996]. With such a high melting point of the secondary phase, it is not surprising that there was little change in the $\alpha/\alpha+\beta$ ratio until after 1650°C because very little liquid would have been present to allow for diffusion.

When considering the long time annealing heat treatments at high temperature it was found that there was still some α phase present in sintered and previously HIP'd materials. This suggests that perhaps the equilibrium concentrations of α and β had only been approached more closely after long times, and that the sintered microstructure was not in a state of thermodynamic equilibrium. The fact that only some of the conditions had almost a complete elimination of secondary phase is interesting as well. Perhaps the M phase produced at lower pressure (SS3) was more stable than when it was formed at higher pressure and lower temperature (SS2). The increase in temperature at high pressure, and the increase in pressure at high temperature caused the M phase to revert back to the J phase after 1650°C (and after 10000psi) suggesting that the chemistry of the secondary phase had altered (i.e. N and Si, and possibly Al had been extracted from the liquid, as the J phase is not as rich in these components as the M phase). If then follows that there should have been changes in substitution levels of the β SiAlON (and perhaps α SiAlON) with increasing temperature and pressure, since the liquid was absorbed.

One can argue that the change in substitution would have had to be greater as a function of pressure rather than temperature due to the fact that increasing temperature changed the α/α+β ratio and grain size, thus requiring absorption of Si, N, Al, and O simply for β nucleation and growth. Thus, at a constant α/α+β ratio, with no grain growth, the disappearance of the liquid with increasing pressure would have caused an increase in the levels of substitution at higher pressures. However, we must realize that the levels of substitution would not be severely altered for this case. When we consider how much liquid was absorbed over the temperature and pressure ranges, and the volume of α and β that could have absorbed it, the average levels of the level of substitution change would most likely not have been detected by peak shifting in XRD. Since no lower pressure specimens were analyzed in the TEM no evidence of this postulate can be presented here. Also, the fact that bulk specimens were used in XRD analysis precludes any interpretation of peak shifts from being identified as either lattice volume changes (changes in substitution) or residual stress effects. On final point regarding the levels of substitution, and their presumed changes with HIP conditions, concerns the manner in which the levels would be increased. Recall from Chapter 4 that SiAlON grains can exhibit coring, and chemical gradients near boundaries of secondary phase. The inner cores of any grains with a radial gradient will have a higher degree of substitution because it was grown first when the liquid was richest in Al and O. Interestingly, one observation made in the SEM was that the number of β Si_3N_4 cores decreased as a function of increasing temperature. This was thought to be due to diffusion of Al and O into the core from the surrounding high substitution shell surrounding the core – essentially the cores were annealed out. After some time, there would come a point where the concentration of the Al and O in the secondary phase would approach that of the SiAlON grain and no further substitution would be possible. The question remains as to whether or not most of the liquid would have been absorbed at this time. It would be insightful to investigate the microstructure of the long time annealing treatments more thoroughly to determine if the substitution levels had increased, and to determine the degree of crystallinity of the triple pocket phases (recall that negligible amounts of crystalline secondary phase were detected via XRD, but the limit of detection was only a few volume percent).

The final analysis of this section concerns the amount of any amorphous film present at two-grain boundaries. In any material where an amorphous grain boundary phase is present, it is desirable to be able to predict what volume fraction of the secondary phase it accounts for. If we assume that the amorphous phase is a continuous layer along two-grain SiAlON junctions a simple calculation, based on the volume and surface area of the grains, can be performed. Reports of the volume fraction of amorphous phase located at grain boundaries have often used the approximations that the elongated β phase is a cylinder, and that it has a constant aspect ratio [Plucknett and Wilkinson, 1994]. For this study some of the parameters were altered to see how much these assumptions changed the value of the volume fraction of amorphous phase. The evolution of the essential mathematical relationships below was based on that of Plucknett and Wilkinson (1994).

The assumption that all grains were hexagonal prisms was made in place of the previous assumption that grains were cylinders. The volume and surface area of a hexagonal grain (V_g and A_g respectively) were then determined in terms of a ratio to a cylinder or radius r and length h (recall that a minimum diameter was measured in the grain size analysis, so $r = d_{min}/(2cos30^{\circ})$).

$$A_g = \left(\frac{\pi \cdot r^2}{1.209} + 6 \cdot r \cdot h \right)$$

$$V_g = \frac{\pi \cdot r^2}{1.209} \cdot h$$

With a very thin film of amorphous material at the grain boundary, such that the thickness of the boundary is much less that the grain dimensions ($t \ll d_{min}$, h) the amorphous phase volume (V_a) can be expressed as:

$$V_a = \pi \cdot r \cdot t \cdot \left(\frac{r}{1.209} + \frac{3}{\pi} \cdot h \right)$$

The volume fraction of the amorphous grain boundary phase (F_a) is then determined by the ratio of the volume of the amorphous phase to the volume of the grain:

$$F_a = \frac{V_a}{V_g} = \frac{\pi \cdot r \cdot t \cdot \left(\frac{r}{1.209} + \frac{3}{\pi} \cdot h \right)}{\frac{\pi \cdot r^2}{1.209} \cdot h} = t \cdot \left(\frac{r + 1.155 \cdot h}{r \cdot h} \right) \tag{5.1}$$

If we then do the same calculation that Plucknett and Wilkinson (1994) did for F_a, for values of t=2nm, a grain diameter of 1µm and an aspect ratio of 4 (i.e. $h = 4r$) we find that Equation 5.1 predicts F_a to be ~0.56%, whereas the aforementioned treatment found F_a to be ~0.45%. Equation 5.1 predicts a 20% higher volume fraction of amorphous phase at two-grain junctions when hexagonal, instead of cylindrical grains are used.

Realizing that the present material was a mixed α/β SiAlON it was thought that the different weight fractions (and hence volume fractions) of each phase might affect the volume fraction of amorphous phase. Equation 5.1 was modified, using a rule of mixtures approach, to account for the mixed phase composition, and most importantly, the difference in average grain size of the different phases. The new equation (Equation 5.2) is seen below, where f_α and f_β are the weight fractions of α and β respectively, (equivalent to the α/α+β ratio determined from XRD analysis: $1\text{-}f_\alpha = f_\beta$) and r_α and r_β are the radii of the α and β phases. Aspect ratios of 1 for the α phase and 7 for the β phase were assumed.

$$F_a = f_\alpha \cdot \left[t \cdot \left(\frac{2.155}{r_\alpha} \right) \right] + f_\beta \cdot \left[t \cdot \left(\frac{1.298}{r_\beta} \right) \right] \tag{5.2}$$

No parameters were included to account for the different grain size distributions of the two phases, nor were any attempts made to include a term for the incidence of having α-β grain junctions (α-α or β-β grain boundaries were assumed). These considerations might be a future investigation. If anything, Equation 5.2 should over-predict the amount of amorphous phase associated with the β phase, as there were much larger β grains observed than α grains. Recall from the SEM investigations (Section 4.2.1) that the α grains seemed to have a narrower size distribution and a higher mean grain size than the β grains.

Values of F_a for the grain dimensions observed in this study are found in Table 5.1 (an aspect ratio of 7 was assumed for all calculations). From the table one can see that the modification of the Plucknett and Wilkinson (1994) approach to account for hexagonal prismatic grains (Equation 5.1) did not yield a large increase in the volume fraction of amorphous phase at two-grain junctions (only +12%). However, when the inclusion of the alpha phase was made (Equation 5.2) the amount of amorphous phase decreased by 30% in comparison to the results of Equation 5.1, and 20% in comparison to Plucknett and Wilkinson's method (1994).

Sample Set	r_β§ [nm]	r_α* [nm]	t [nm]	F_a: Plucknett and Wilkinson (1994)	F_a: Eq. 5.1 Pure β	F_a: Eq. 5.2 Mixed α/β	f_α**
SS1	84	300	2	2.71	3.08	2.15	0.57
			1.5	2.03	2.31	1.61	
SS2	94	325	2	2.43	2.76	1.96	0.56
			1.5	1.82	2.07	1.47	
SS4	107	350	2	2.13	2.42	1.89	0.45
			1.5	1.60	1.82	1.42	

§ $r_\beta = d_{min}/(2\cos 30°)$

* estimated from SEM micrographs

** Batch 4 XRD α/α+β ratios

Table 5.1. Different determinations of the volume fraction of amorphous phase located at two-grain junctions for SS1, 2 and 4. Methods: Plucknett and Wilkinson (1994), and Equations 5.1 and 5.2.

From these calculations of the volume fraction of amorphous material present in the materials studied we have found that the small grain size of microwave sintered materials results in there being a rather high amount of amorphous phase volume at two-grain junctions. As the temperature of the post sinter heat treatment was increased the average grain size and β content increased, and resulted in a slightly smaller amount of amorphous material being present at two-grain junctions (-12% from SS1 to SS4). This small degree of change in the amount of amorphous phase at the grain boundaries (assuming that its thickness was constant) was not thought to have been responsible for the large changes in properties observed in this study. Certainly, the amount of amorphous phase present in these fine-grained materials may have implications in their creep response.

Now that we have a complete picture of how the secondary phase was thought to evolve with the other changes in the microstructure, we can discuss the fracture toughness trends, and determine why they occurred.

Based on SEM investigations of crack paths we concluded that fracture was largely intergranular. The apparent differences in the fracture behaviour of the toughest and least tough heat treatment conditions (SS1: $K_{IC} = 7.54\text{MPa}\sqrt{\text{m}}$ vs. SS4: $K_{IC} = 6.74\text{MPa}\sqrt{\text{m}}$) did not seem to be very great, but it appeared that more fiber rupture may have been present in the less tough of the two conditions. The secondary phase character was then analyzed and found to have changed in amount and distribution between the two conditions, but not in the degree of crystallinity. Therefore, how could the amount and distribution have affected the fracture toughness? We need to consider what the secondary phase was, in order to determine if there were any residual stresses at the boundaries. The density of the M phase has been reported to be 4.22 – 4.28g/cc [Tsuge et al., 1974; Wills et al., 1976] which is higher than the SiAlON phases (~3.16-3.18g/cc) and close to the density of YSiAlON liquid thought to be present at the processing temperatures (~3.90g/cc [Cinibulk et al., 1990; Kleebe et al., 1999]). No reports for the density of the J phase were found, but it was assumed that it was close to that of the M phase. Judging from the closeness in density, one can easily see that upon crystallization a volume *decrease* of the secondary phase should occur. If that were the case, there would be no stain energy resistance countering complete crystallization of the entire pocket phase region, and hence a high degree of crystallinity would be observed. The result of this phenomena would be that slightly tensile stresses, or no stresses whatsoever would exist across the secondary phase-SiAlON grain boundaries [Kleebe et al., 1999]. With no compressive residual stresses present at these boundaries an approaching crack would find an easy path along the secondary phase-SiAlON boundaries, as they would be the paths of least resistance. Kleebe et al. (ibid.) found that the degree of crystallinity of secondary phases increased with the density of the crystallizing phase, and that the resultant fracture toughness of materials with highly crystalline secondary phases was higher than those materials in which some residual amorphous phase was still present at the boundary between the secondary crystalline phase and the majority phase. The studies of Bonnell et al. (1987) and Bonnell (1989) on different crystalline secondary phases also found that the particular secondary crystalline phase was a determinant in the fracture toughness of silicon nitride ceramics, and more importantly that the grain boundary morphology was found to override any thermal mismatch effects. The presence of residual glass in the less tough materials was also found in comparison to the tougher material [Bonnell, 1989]. Therefore, the grain boundary morphology was found to be linked with toughness of the material. The same studies (ibid.) also found that as the volume fraction of the secondary phase (that gave a higher toughness) was increased, the fracture toughness also increased by a small amount. These observations are pertinent to the current study, as it was also found that an increase in the amount of secondary phase increased the fracture toughness slightly.

We therefore conclude that the presence of a dense crystalline phase crystallizing in triple pockets upon cooling from sintering temperatures can affect the toughness of the material. The negative volume expansion of crystallization causes tensile stresses across the secondary phase-SiAlON grain boundaries and thus presents an easy path for crack propagation. As the total amount of secondary phase increases, the toughness increases as well, since there is more opportunity for the crack to deflect in different directions with relatively little energy consumption. For the current study, this explanation seems to fit the observed trends very well, as it was found that dense secondary crystalline phases were found to exist in a state of high crystallinity in larger amounts in the toughest conditions tested. The fact that the fracture mode was mostly intergranular further supports the notion that the secondary phase was the microstructural parameter most responsible for the property of fracture toughness.

5.2 Processing Condition Effects

Up to this point the microstructural mechanisms responsible for hardness and toughness have been identified as being the $\alpha/\alpha+\beta$ ratio (and grain size) and the amount of secondary phase present in the microstructure respectively. The effects of the processing conditions has only been discussed in terms of the changes that were seen in the microstructure, and discussion of the specific reasons for why these changes in microstructure were effected due to the processing conditions has not been summarized.

This section will complete the story of how the processing conditions affected the microstructural parameters observed by analyzing any effects of temperature, pressure and time that have not already been explained.

The α/α+β ratio has been found by many authors to decrease as the sintering temperature is increased [Messier and Croft, 1982], the mechanism of solution reprecipitation being responsible for the transformation [Clarke and Thomas, 1978; Messier et al., 1978; Šajgalik, 1991]. From these studies, it was also found that increased time assisted in the transformation of α→β. Therefore, it was not surprising that this study showed the same trends in the α/α+β ratio with increasing temperature and time. As mentioned in Chapter 2, some debate as to the controlling mechanism of the α→β transformation exists, and hence there is some debate on the kinetics of transformation, which imposes different controlling mechanisms on β grain growth. The most recent study by Kleebe et al. (1999) on the rate controlling step concluded that the transformation (determined from grain size measurements with isothermal time) was diffusion controlled, whereas previous studies by Lee et al. (1988), Kang et al. (1995) concluded that interface reaction was the rate controlling mechanism of β grain growth. Krämer et al. (1993) proposed that the volume fraction of liquid had an influence on the rate controlling step, which seems to explain the discrepancy in the previously mentioned reports; the high volume fractions of liquid studied by Lee et al. (1988) and Kang et al. (1995) would show that the rate controlling step was reaction control, whereas the smaller volume fractions investigated in the study of Kleebe et al. (1999) would show a diffusion controlling mechanism.

We can then assume for the current study that the rate controlling step for β grain growth during HIP'ing was diffusion controlled, based on the small volume fraction of liquid present. From this assumption, the observation of grain coarsening of the β grains with increasing temperature seems to be valid. However, we must investigate the effect of pressure on diffusion. It was found by Shimada et al. (1983) that hot pressing (1.5GPa, or 217000psi) of high α content Si_3N_4 powder with no additives at 1500°C increased the rate of transformation of $\alpha \rightarrow \beta$. If we assume that the transformation occurs via a liquid phase materials transport mechanism, then this result seems puzzling, since the transformation should be diffusion controlled, and the diffusion rate should decrease with increasing pressure because of an apparent viscosity increase. However, the mechanism of transformation proposed by these researchers was in fact different: they assumed that the transformation occurred in plastically transformed α grains by the release of stored strain energy. Since such high pressures were not used the current study, this mechanism of transformation was not considered to be present.

Based on the unchanging $\alpha/\alpha+\beta$ ratio with pressure, we can also assume that any viscosity increases in the liquid phase due to high pressure at high temperature were negligible, and that the transformation (and grain growth of the β phase) was unaffected.

Another reason for believing that the pressure was not high enough to cause a significant increase in liquid viscosity is discovered when the secondary phase evolution is analyzed. If high pressure did cause a viscosity increase in the liquid, then the crystallization of the liquid would not have been as extensive because diffusion would have been limited. According to the Stokes-Einstein relation for the dependence of diffusion on the apparent viscosity:

$$D = \frac{kT}{3\pi\lambda\eta}$$

where D is the diffusion coefficient of either the Si, N, Al, and O for the case of β grain growth, or for Y, Si, Al, O, N for the secondary phase. λ is the molecular spacing, η is the apparent viscosity and k the Boltzmann constant. The effect of pressure on the viscosity is a direct relationship, meaning high pressures cause high viscosity. For these considerations we assume that the pressure was high enough to have had an effect of the viscosity. Usually, extremely high pressures (higher than those observed here) would be required to cause a substantial increase in the liquid viscosity, so we can conclude that no such effects were present for this study [Gerhart et al., 1992].

Despite the fact that the pressure was not high enough to limit diffusion, it was high enough have other effects on the liquid. There are three possible mechanisms whereby pressure could effect the microstructure: mechanical, kinetic, and thermodynamic. Before discussing these effects we need to consider the temperature conditions first. The effect of increasing temperature would have resulted in dissolution of the secondary crystalline phase, which would then allow for rearrangement processes to occur upon the application of pressure. From the crystalline phases found at all temperature conditions, we only noticed a decrease in the amount of the secondary phase at high temperature as pressure was increased. This fact leads us to believe that the crystalline phase did not soften until a temperature threshold (~1500-1650°C) was reached; there was no significant change in the secondary phase amount until these temperatures were surpassed.

At lower temperatures, no effects of pressure were observed on the toughness (unfortunately none of the MS samples were tested in XRD) so we conclude that the secondary phase amount and distribution did not change significantly at lower temperatures because a liquid had not formed. As the temperature increased under high pressure, rearrangement of the grains occurred, and absorption of the liquid phase was accomplished. At high temperature, a pressure effect was seen on the amount of secondary phase, and presumably a slight difference in its distribution was present as well. The secondary phase would have been dissolved into the liquid at high temperature for all the pressure conditions, so increasing pressure would have had more of a mechanical effect on the rearrangement of grains. It is possible that the increased pressure also had a kinetic and thermodynamic effect on the dissolution of the secondary phases due to increase chemical potentials under regions of high pressure.

This explanation of the effect of pressure and temperature on the evolution of the secondary phase seems to be reasonable, but we must also analyze the effect of time. It was found that increasing time at high temperature also decreased the amount of secondary crystalline phase as well. This was most likely because the thermodynamic equilibrium at high temperature dictated that the secondary phase be absorbed. Thus, it would make stronger the argument that pressure was merely a mechanical and kinetic effect (due to enhance solubility). However, the shorter HIP conditions seem to oppose this idea, which suggests that there are some competing processes. The lower fracture toughness conditions HIP'd at the same temperature and pressure, but for only 30 minutes, showed toughness values slightly below those of the 120 minute conditions. In the last section, this toughness difference was thought to be a β grain size effect, as the shorter HIP times would not have caused as large a β grain size increase. With the advent of the idea that the secondary phase character is ultimately responsible for the fracture toughness, we cannot ignore the fact that the β grain size also has a small effect on the same property.

Therefore, to optimize the toughness we would need to do some further processing experiments to determine the time at which the toughness starts to decrease after the initial toughness increase from 30 to 120 minutes. We would also have to vary the chemistry of the liquid phase of sintering so that more secondary crystalline phase would form upon cooling. It seems that the optimal conditions for this material were obtained in the as sintered state and no benefits of HIP'ing were realized. The fact that the temperature was so high as to cause dissolution of the secondary phase was definitely a drawback to the ultimate properties of the material for the HIP conditions studied. Nevertheless, such results have given sufficient insight into the fracture behaviour of this material: the fracture toughness is most strongly determined by the secondary phase amount and distribution, and to a lesser extent the morphology of the β grains.

6. CONCLUSIONS

The goal of the present study was to characterize the effects of different post sinter heat treatment conditions on the microstructure and mechanical properties of a microwave sintered silicon nitride. The HIP'ing temperature, pressure and time were varied, and the resultant microstructural changes were analyzed by x-ray diffraction, and scanning and transmission electron microscopy. Indentation hardness and toughness testing were performed to classify the mechanical properties.

Three main microstructural features were discovered to be responsible for the mechanical behaviour of the studied material: the $\alpha/\alpha+\beta$ ratio, the β SiAlON grain size, and the character of the secondary crystalline phase. These microstructural parameters followed known scientific theory in their response to temperature, pressure, and time.

Increasing temperature and time were determined to decrease the $\alpha/\alpha+\beta$ ratio in the microstructure, thereby causing a loss in hardness. An increase in β grain size was also observed with increasing temperature. The effects of this grain size increase could have been responsible for some of the loss in hardness, but its effects could not be isolated from the $\alpha/\alpha+\beta$ ratio. No pressure effects were observed in either the $\alpha/\alpha+\beta$ ratio, or the β grain size.

The major discovery of this work was the role of the secondary phase in the fracture behaviour of the material. It was found that the chemistry, degree of crystallinity, distribution, and amount of secondary phase were important for describing the observed changes in toughness with processing conditions. Large amounts of the secondary phase were found to enhance fracture toughness if the secondary phase was normally distributed, had a high density, and high degree of crystallinity. These variables led to intergranular fracture, and contributed to toughening by crack deflection, elastic bridging, pullout and fiber rupture.

Increasing temperature, pressure, and time caused decreases in the amount of secondary crystalline phase present in the microstructure, and therefore a decrease in toughness. Disappearance of the secondary phase was predicted to have been accomplished by dissolution and absorption into the SiAlON grains at high temperature. The combined effects of high temperature and high pressure caused rearrangement of the microstructure, along with increased dissolution of the secondary phase. Pressure was thought to be largely kinetic and mechanical in nature because reductions in the amount of secondary phase were accomplished at very low pressures after long times.

Based on the results of this study processing guidelines can be formulated. Essentially, very high temperature and pressure should be avoided at all costs. Temperature limits should be set at 1650°C maximum to maintain hardness and toughness. At this temperature there were some indications that the M phase was the most stable secondary phase. The M phase was found to have a high degree of crystallinity within the microstructure, and it has been reported to be more dense than the liquid phase in sintering [Huang et al., 1996]. These two properties of the M phase should therefore translate into a fracture toughness increase if the amount of M phase can be maximized. Below 1650°C it appears that the effect of pressure should be negligible, and one may find that application of pressure is profitless. The only possible benefit of any pressure would be to close porosity remnant from sintering if some dissolution of the secondary crystalline phases occurs (which will most likely not happen).

Already evident in these conclusions are some proposals for future work to expand on the discoveries that were made in this study. Due to the trends of this study, the amount of crystalline secondary phases should be increased if and only if the secondary crystalline phase is more dense than the liquid phase and is evenly distributed. Already mentioned is a processing method that may achieve this goal. An alternative route would be to alter the composition of the starting powder. The latter presents more difficulties.

The fact remains that the as sintered material seemed to have the best combination of hardness and toughness of all conditions explored. This discovery demonstrates the potential of microwave sintering to produce fine grained, hard and tough silicon nitride ceramics that do not need to be post sinter heat treated. This unique finding deserves more investigation to determine if the sintering schedule can be adjusted to further improve the properties of the material.

APPENDIX A

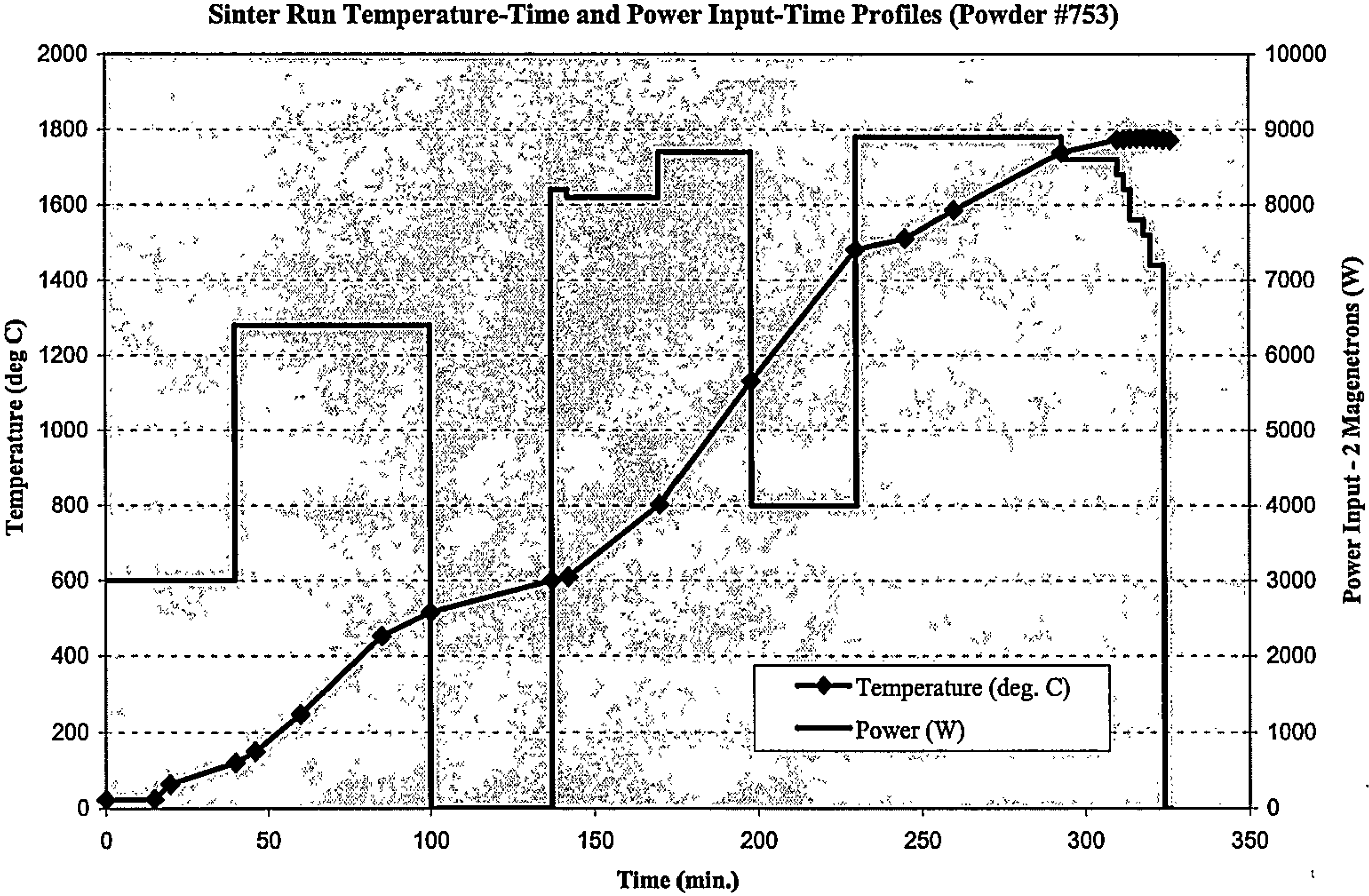

Figure A1. Microwave sintering profile showing the power input from both magnetrons, and the resulting temperature inside the furnace. Powder Batch #753 - not used in this study.

APPENDIX B: Batch 5 XRD Procedure

As mentioned in 3.4.3, Batch 5 XRD tests were done in order to try and eliminate some inconsistencies from the results obtained at McMaster University. Different geometrical configurations were tested, along with different surface preparations.

The direction of the incident x-ray beams was switched through 180° to determine if there were any preferred orientation effects. Polished and ground surfaces were tested to rule out the chance that the first set of data was performed on the polished side instead of the ground side. The effect of beam orientation was checked on both surfaces as well. In all there were four cases tried, as seen in Figure B1 below. Only sample SS5 A24-2 had all four Cases tested, whereas the other two samples in Batch 5 (SS3 A21-6 and SS6 A20-6) were scanned in Case D (Table B1).

Sample #	XRD Conditions	Test Case Geometry
A24-2	CuK_α, Ni filtered, short scan: 12 minutes (10-70° 2 theta)	A,B,C and D
A21-6	Same	D
A20-6	Same	D

Table B1. Summary of Test conditions for XRD Batch 5 Scans.

Case A: polished surface, x-rays incident from side ***without*** label

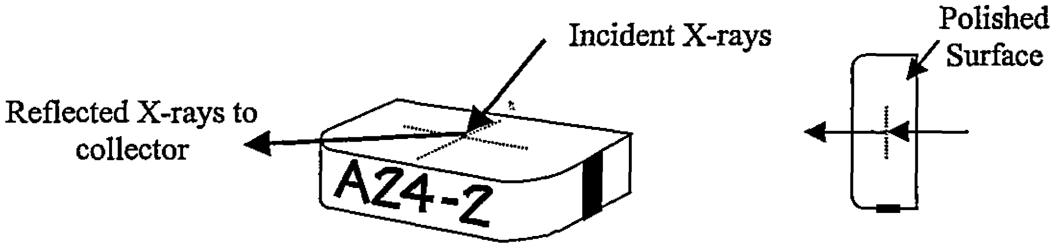

Case B: polished surface, x-rays incident from side ***with*** label

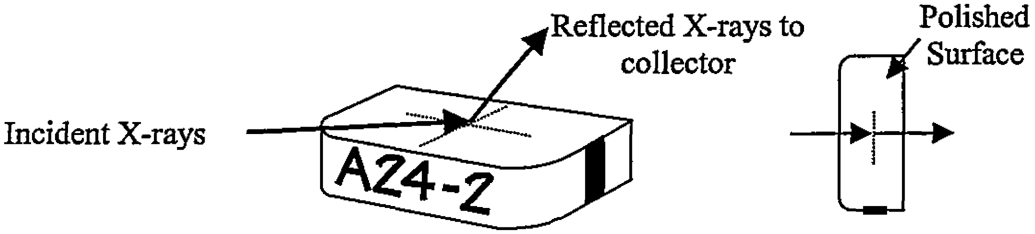

Case C: ground surface, x-rays incident from side ***without*** label

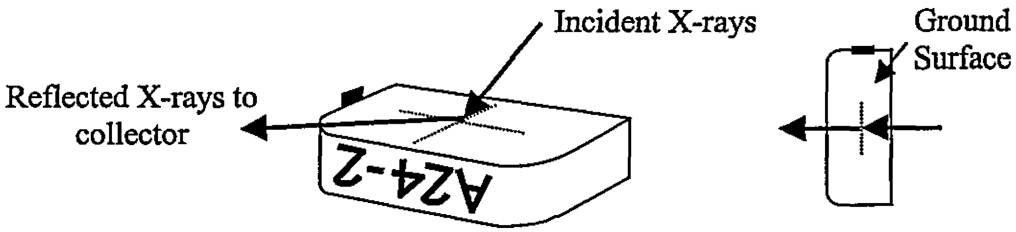

Case D: ground surface, x-rays incident from side ***with*** label

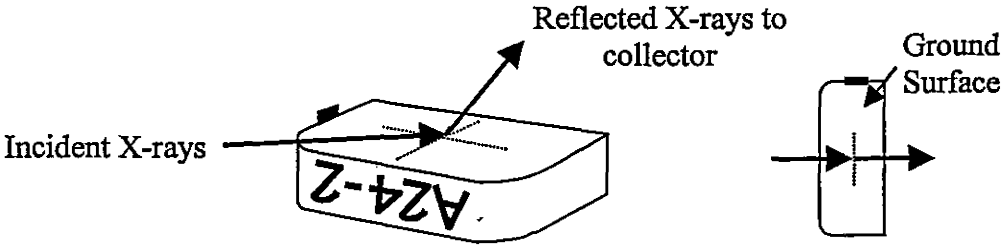

Figure B1. Geometrical Configurations for the four Cases tested in Batch 5.

The scans from the various tests are shown in Figures B2 and 3. Notice that the relative peak intensities of the α and β peaks between 33.5 and 36° 2θ varied between the polished and ground surfaces (Cases A and B vs. Cases C and D). There were no differences in the amount, or location of secondary peaks.

The results of the β fraction calculations (see Table B2) showed that the polished surfaces had roughly 3-4wt% more β than the ground surfaces because of the higher relative intensity of the β phase in comparison to the α phase. The physical explanation of the lower β content on the ground surface was thought to be a result of the different relative hardness of the α and β phases. Preferential damage (wear) and removal of the β phase during grinding seemed to be a reasonable explanation since β is softer than α phase. Another possibility for the difference could have been that the surfaces actually contained different amounts of β phase after processing, but this was not considered to be as possible as preferential damage effects of grinding.

Sample #	Test Case	Wt% β*
A24-2	A	48
	B	47.5
	C	44.5
	D	44.5

* Average of the Gazzara and Messier (1977) and Devlin and Amin (1990) results

Table B2. Batch 5 β weight fractions as a function of test case geometry for SS5 A24-2.

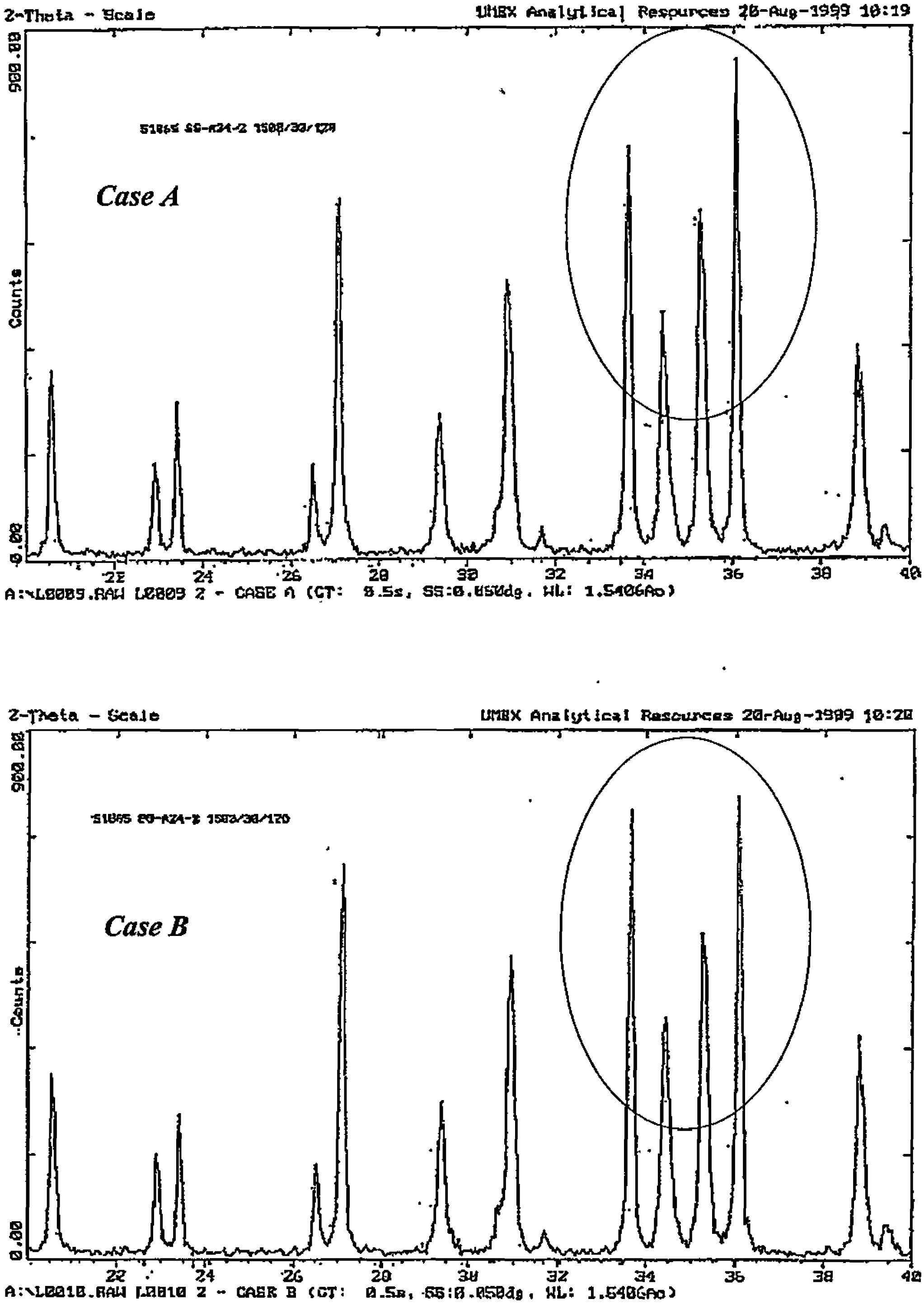

Figure B2. XRD scans of Batch 5 (SS5 A24-2) on polished surfaces: Cases A and B. Marked area includes the peaks seen to differ from ground surfaces, seen in Figure B3..

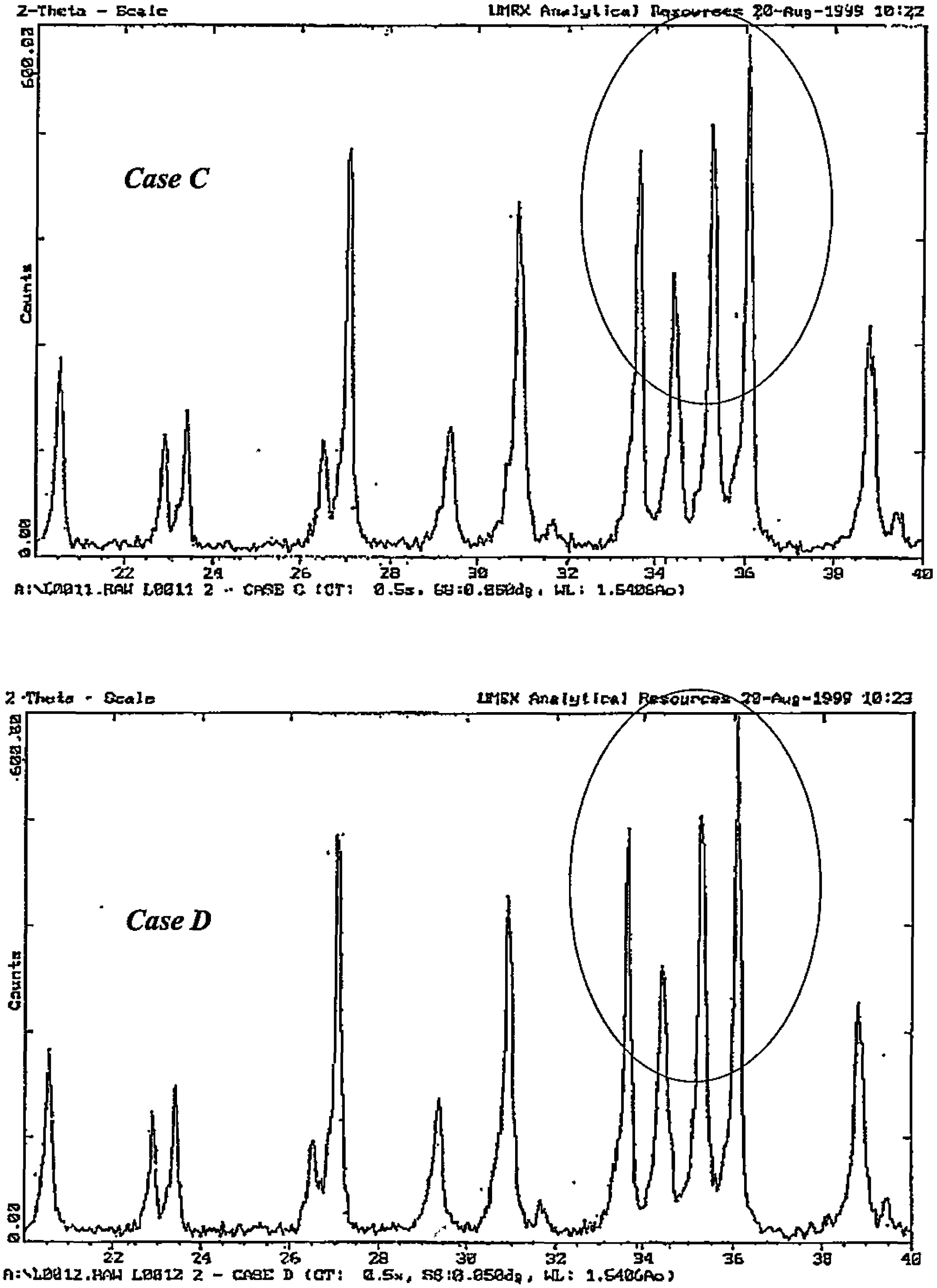

Figure B3. XRD scans of Batch 5 (SS5 A24-2) on ground surfaces: Cases C and D. Marked area includes the peaks seen to differ from polished surfaces, seen in Figure B2.

APPENDIX C

Raw Data: Peak Height Measurements

		Peak Height (mm)									
		Alpha						Beta			
Batch	Sample	101	110	200	201	102	210	110	200	101	210
1	SS1: A27-3	46.3	39.2	31.2	67.5	74.1	73.3	38.2	74.3	88	79.3
	SS2: A23-9	38	25.8	23.7	57.3	58.2	63.3	35.6	85.1	87.7	86
	SS3: A21-6	35.8	23.9	22.7	49.3	61	52.7	38.7	81.8	87.3	85.8
	SS4: A28-4	26.3	18	20.2	47.3	46.6	51.6	33.7	86.1	80.9	87.4
	SS5: A24-2	48.3	32	30.7	70.9	80.1	74.9	38.3	77.8	87.5	81.5
	SS6: A20-6	29.1	22.3	22.5	45	77.2	52	37.4	73.2	87	79.1
2	SS1: A22-6 (Annealed)	19.8	8.3	8	23	18.8	22.9	21.7	56.9	48.9	51.9
	SS3: A27-4 (Annealed)	14.2	7.5	7.2	20	17	20.4	21.5	56.7	47.1	51
	SS4: A29-3 (Annealed)	12.2	7	6.8	19.5	16.4	20	22	56.7	48.1	56
	SS5: A24-2	36.1	19.1	16.3	46.9	38.1	48.9	23.2	56.9	51.6	55.8
3	SS5: A24-2	51.2	27.9	24.8	68	56.8	74	35.9	87.1	79.6	82.9
4	SS1: A27-3	34.3	19.5	17.1	46.3	37.1	50.3	23.5	53.8	49.1	56.7
	SS2: A23-9	43.8	34.2	32	61.5	59.7	67.8	41	83	86.7	87.2
	SS4: A28-4	19.5	11.2	10.2	29.1	23.8	29.4	21.9	56.8	45.8	56.2
5	SS3: A21-6 Case D	23.3	11.6	11.9	39	37.5	49.8	29.5	73.9	82.9	100.9
	SS5: A24-2 Case A	45.7	23.1	22.7	66.3	59	83.5	37.9	86.1	98.6	119.3
	SS5: A24-2 Case B	44.5	25.5	23	73	58.1	78.3	34.9	94.7	107.7	111
	SS5: A24-2 Case C	42.2	29	28	84.9	68	103.2	34.8	97.2	97	124.3
	SS5: A24-2 Case D	46.2	31	24.4	83.1	66.3	102.6	32.5	97.5	99.4	126.1
	SS6: A20-6 Case D	20.1	12.8	12.1	46.2	36.9	54	33.1	91	92.9	119.2
	L	7.5	3.58	2.44	7.44	6.66	6.79	4.21	10.53	10.9	11.21

Table C1. Peak Height Measurements, Normalization, and Correction

Normalization

Peak heights divided by the value of L for each set of planes

		Normalized Peak Heights, Yi											
		Alpha						Beta					
Batch	Sample	101	110	200	201	102	210	110	200	101	210	Yavg Alpha	Yavg Beta
1	SS1: A27-3	6.17	10.95	12.79	9.07	11.13	10.80	9.07	7.06	8.07	7.07	12.18	7.82
	SS2: A23-9	5.07	7.21	9.71	7.70	8.74	9.32	8.46	8.08	8.05	7.67	9.55	8.06
	SS3: A21-6	4.77	6.68	9.30	6.63	9.16	7.76	9.19	7.77	8.01	7.65	8.86	8.16
	SS4: A28-4	3.51	5.03	8.28	6.36	7.00	7.60	8.00	8.18	7.42	7.80	7.55	7.85
	SS5: A24-2	6.44	8.94	12.58	9.53	12.03	11.03	9.10	7.39	8.03	7.27	12.11	7.95
	SS6: A20-6	3.88	6.23	9.22	6.05	11.59	7.66	8.88	6.95	7.98	7.06	8.93	7.72
2	SS1: A22-6 (Annealed)	2.64	2.32	3.28	3.09	2.82	3.37	5.15	5.40	4.49	4.63	3.50	4.92
	SS3: A27-4 (Annealed)	1.89	2.09	2.95	2.69	2.55	3.00	5.11	5.38	4.32	4.55	3.04	4.84
	SS4: A29-3 (Annealed)	1.63	1.96	2.79	2.62	2.46	2.95	5.23	5.38	4.41	5.00	2.88	5.00
	SS5: A24-2	4.81	5.34	6.68	6.30	5.72	7.20	5.51	5.40	4.73	4.98	7.21	5.16
3	SS5: A24-2	6.83	7.79	10.16	9.14	8.53	10.90	8.53	8.27	7.30	7.40	10.67	7.87
4	SS1: A27-3	4.57	5.45	7.01	6.22	5.57	7.41	5.58	5.11	4.50	5.06	7.25	5.06
	SS2: A23-9	5.84	9.55	13.11	8.27	8.96	9.99	9.74	7.88	7.95	7.78	11.14	8.34
	SS4: A28-4	2.60	3.13	4.18	3.91	3.57	4.33	5.20	5.39	4.20	5.01	4.34	4.95
5	SS3: A21-6 Case D	3.11	3.24	4.88	5.24	5.63	7.33	7.01	7.02	7.61	9.00	5.89	7.66
	SS5: A24-2 Case A	6.09	6.45	9.30	8.91	8.86	12.30	9.00	8.18	9.05	10.64	10.38	9.22
	SS5: A24-2 Case B	5.93	7.12	9.43	9.81	8.72	11.53	8.29	8.99	9.88	9.90	10.51	9.27
	SS5: A24-2 Case C	5.63	8.10	11.48	11.41	10.21	15.20	8.27	9.23	8.90	11.09	12.40	9.37
	SS5: A24-2 Case D	6.16	8.66	10.00	11.17	9.95	15.11	7.72	9.26	9.12	11.25	12.21	9.34
	SS6: A20-6 Case D	2.68	3.58	4.96	6.21	5.54	7.95	7.86	8.64	8.52	10.63	6.18	8.92

Table C1. Peak Height Measurements, Normalization, and Correction, continued

Correction

Yavg(phase) multiplied by *L* (hkl) to determine I(phase)(hkl)c, the corrected value of intensity

Correction is for any preferred orientation and particle size effects

		Corrected Intensity I (hkl)c									
		Alpha						Beta			
Batch	**Sample**	**101**	**110**	**200**	**201**	**102**	**210**	**110**	**200**	**101**	**210**
1	SS1: A27-3	91.4	43.6	29.7	90.6	81.1	82.7	32.9	82.3	85.2	87.7
	SS2: A23-9	71.6	34.2	23.3	71.1	63.6	64.8	33.9	84.9	87.9	90.4
	SS3: A21-6	66.4	31.7	21.6	65.9	59.0	60.2	34.3	85.9	88.9	91.4
	SS4: A28-4	56.7	27.0	18.4	56.2	50.3	51.3	33.0	82.7	85.6	88.0
	SS5: A24-2	90.8	43.4	29.5	90.1	80.6	82.2	33.5	83.7	86.6	89.1
	SS6: A20-6	66.9	32.0	21.8	66.4	59.4	60.6	32.5	81.3	84.1	86.5
2	SS1: A22-6 (Annealed)	26.3	12.5	8.6	26.1	23.3	23.8	20.7	51.8	53.6	55.1
	SS3: A27-4 (Annealed)	22.8	10.9	7.4	22.6	20.2	20.6	20.4	51.0	52.8	54.3
	SS4: A29-3 (Annealed)	21.6	10.3	7.0	21.4	19.2	19.6	21.1	52.7	54.6	56.1
	SS5: A24-2	54.1	25.8	17.6	53.7	48.0	49.0	21.7	54.3	56.2	57.8
3	SS5: A24-2	80.0	38.2	26.0	79.4	71.1	72.5	33.2	82.9	85.8	88.3
4	SS1: A27-3	54.3	25.9	17.7	53.9	48.3	49.2	21.3	53.3	55.2	56.8
	SS2: A23-9	83.6	39.9	27.2	82.9	74.2	75.7	35.1	87.8	90.9	93.5
	SS4: A28-4	32.6	15.6	10.6	32.3	28.9	29.5	20.9	52.2	54.0	55.5
5	SS3: A21-6 Case D	44.1	21.1	14.4	43.8	39.2	40.0	32.2	80.6	83.5	85.8
	SS5: A24-2 Case A	77.9	37.2	25.3	77.3	69.2	70.5	38.8	97.1	100.5	103.3
	SS5: A24-2 Case B	78.8	37.6	25.6	78.2	70.0	71.4	39.0	97.6	101.0	103.9
	SS5: A24-2 Case C	93.0	44.4	30.3	92.3	82.6	84.2	39.5	98.7	102.1	105.0
	SS5: A24-2 Case D	91.6	43.7	29.8	90.8	81.3	82.9	39.3	98.3	101.8	104.7
	SS6: A20-6 Case D	46.4	22.1	15.1	46.0	41.2	42.0	37.5	93.9	97.2	99.9
	L	7.5	3.58	2.44	7.44	6.66	6.79	4.21	10.53	10.9	11.21

Table C1. Peak Height Measurements, Normalization, and Correction, continued

Beta Phase Ratio Determinations: Gazzara and Devlin Methods

		Gazzara		Devlin			
Batch	**Sample**	**BPR**	**Wt % beta**	**Xa**	**Wt % beta**	**%Beta Difference**	**Percent Error**
1	SS1: A27-3	0.51	39	0.59	41	2	3.88
	SS2: A23-9	0.58	46	0.53	47	1	2.78
	SS3: A21-6	0.60	49	0.51	49	0	0.95
	SS4: A28-4	0.63	52	0.47	53	1	0.96
	SS5: A24-2	0.52	40	0.59	41	1	2.68
	SS6: A20-6	0.59	47	0.52	48	1	1.90
2	SS1: A22-6 (Annealed)	0.70	59	0.40	60	1	1.47
	SS3: A27-4 (Annealed)	0.72	62	0.37	63	1	1.43
	SS4: A29-3 (Annealed)	0.74	65	0.35	65	0	-0.16
	SS5: A24-2	0.54	42	0.57	43	1	2.78
3	SS5: A24-2	0.55	43	0.56	44	1	2.22
4	SS1: A27-3	0.54	43	0.57	43	0	-0.86
	SS2: A23-9	0.55	43	0.56	44	1	2.96
	SS4: A28-4	0.65	53	0.45	55	2	3.29
5	SS3: A21-6 Case D	0.68	57	0.42	58	1	1.81
	SS5: A24-2 Case A	0.59	47	0.51	49	2	3.22
	SS5: A24-2 Case B	0.59	47	0.52	48	1	2.88
	SS5: A24-2 Case C	0.56	44	0.55	45	1	1.24
	SS5: A24-2 Case D	0.56	44	0.55	45	1	1.90
	SS6: A20-6 Case D	0.70	59	0.39	61	2	2.52

Gazzara and Messier:

BPR = Ib(210)c/(Ib(210)c+Ia(210)c

Wt % beta = Read from calibration curve

[see Gazzara and Messier, 1977]

Devlin and Amin:

Xa = Ia(102)c+Ia(210)c/[0.647(Ib(101)c+Ib(21)c)+Ia(102)c+Ia(210)c]

Wt % beta = 100*(1-Xa)

[see Devlin and Amin, 1990]

Table C2. Beta Phase Ratio Calculations

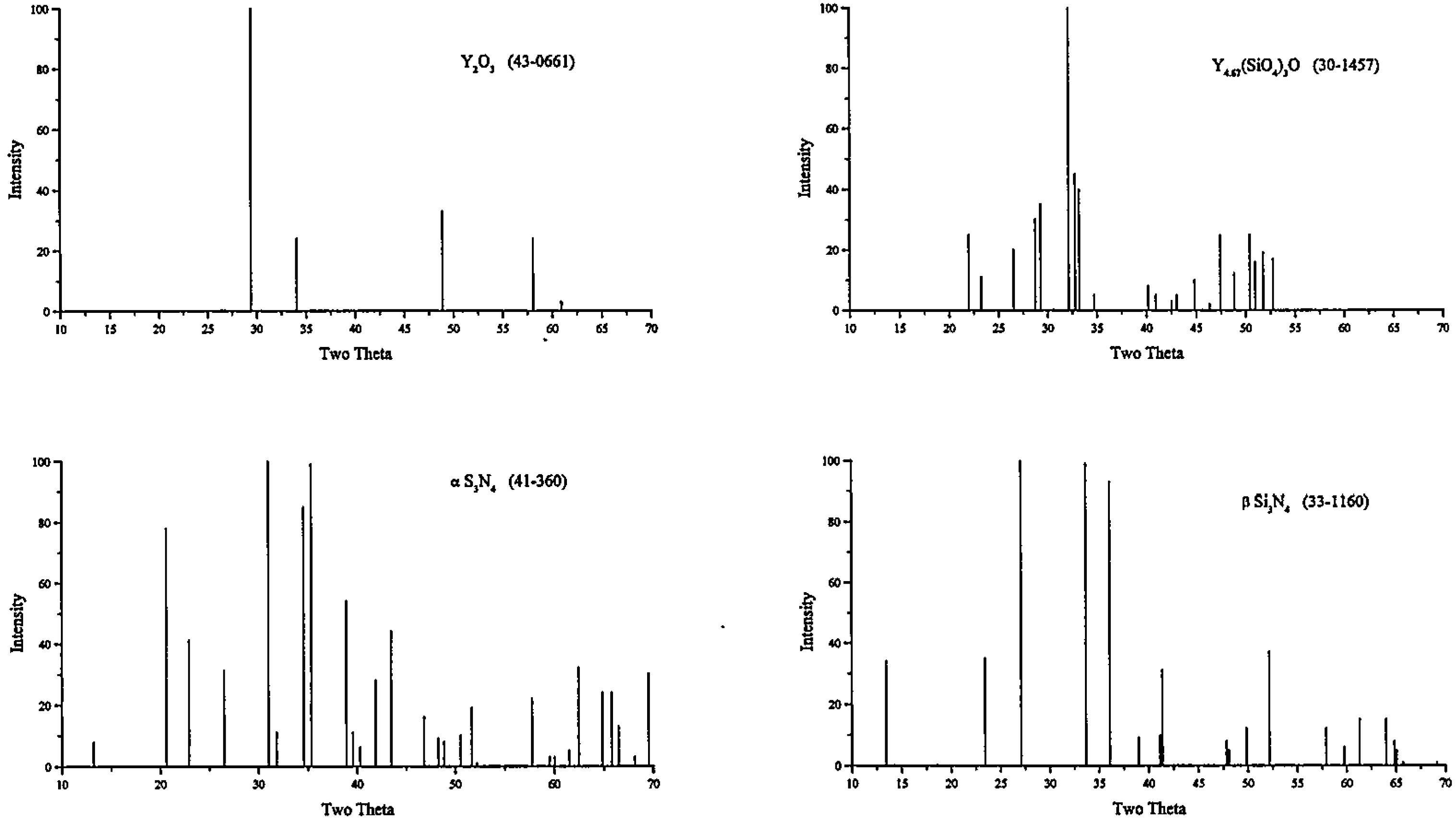

Figure C1. PDF Standards: 1

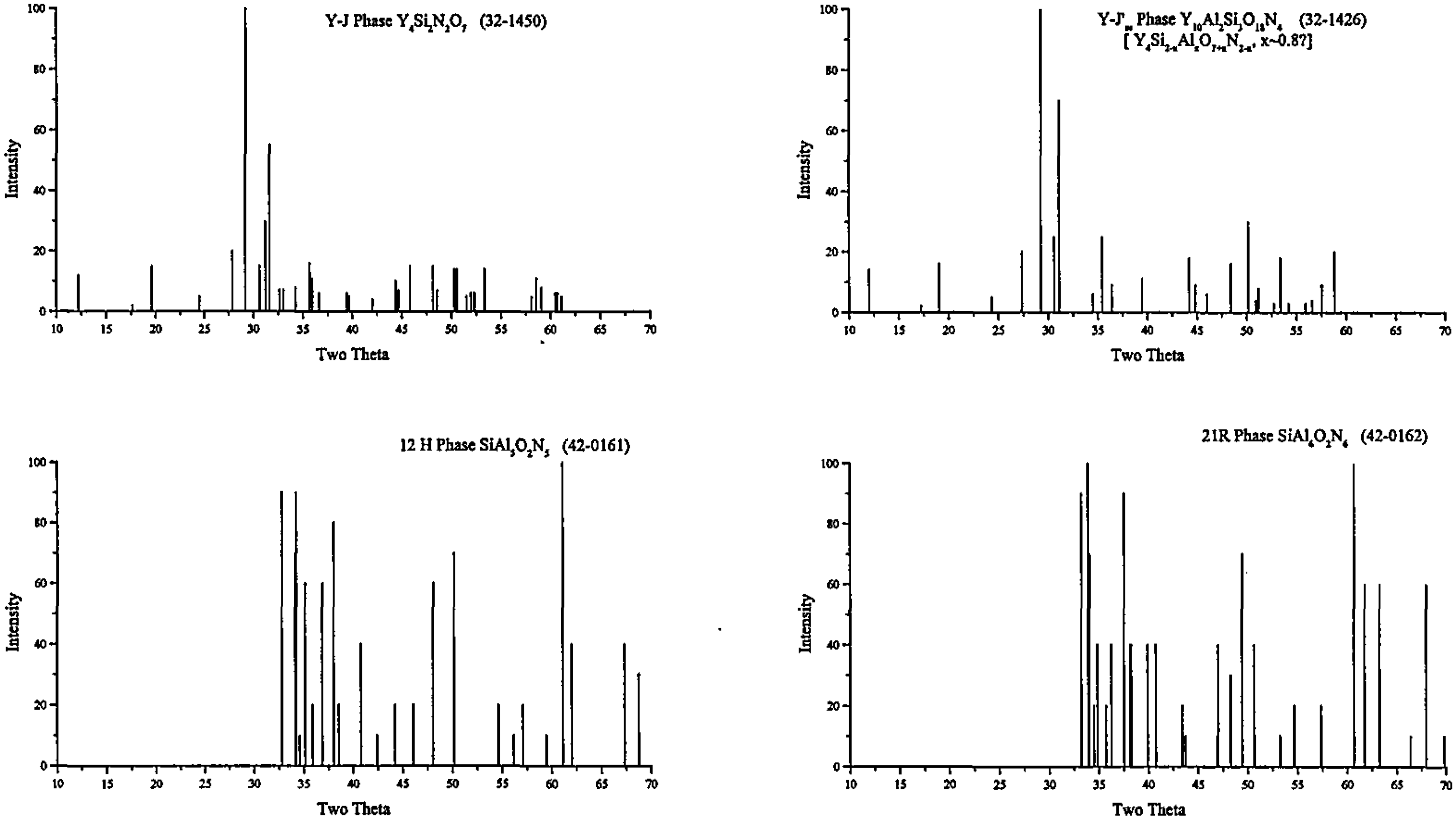

Figure C2. PDF Standards:2

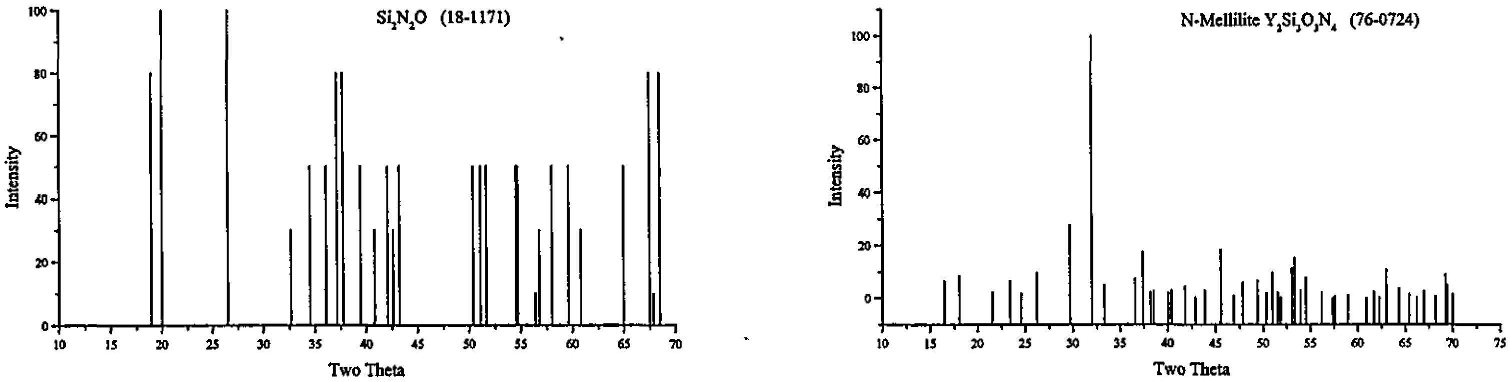

Figure C3. PDF Standards:3

APPENDIX D

Bottom Level

	Layer #									Ave. Column Density (g/cc)	Stnd Dev. (g/cc)
Column#	1	2	3	4	5	6	7	8	9		
A11	3.2477	3.2436	3.2449	3.2438	3.2458	3.2435	3.2450	3.2500	3.2500	**3.246**	**0.003**
A12	3.2442	3.2503	3.2461	3.2461	3.2448	3.2462	3.2470	3.2487	3.2487	**3.247**	**0.002**
A13	3.2477	3.2447	3.2441	3.2416	3.2422	3.2430	3.2433	3.2435	3.2455	**3.244**	**0.002**
A14	3.2487	3.2490	3.2471	3.2455	3.2421	3.2412	3.2425	3.2432	3.2460	**3.245**	**0.003**
A15	3.2488	3.2467	3.2464	3.2456	3.2442	3.2481	3.2453	3.2463	3.2474	**3.247**	**0.001**
A16	3.2474	3.2503	3.2499	3.2485	3.2488	3.2488	3.2492	3.2501	3.2482	**3.249**	**0.001**
A17	3.2482	3.2495	3.2475	3.2467	3.2479	3.2502	3.2502	3.2498	3.2481	**3.249**	**0.001**
Ave. Layer Density (g/cc)	**3.248**	**3.248**	**3.247**	**3.245**	**3.245**	**3.246**	**3.246**	**3.247**	**3.248**		
Stnd. Dev (g/cc)	**0.002**	**0.003**	**0.002**	**0.002**	**0.003**	**0.003**	**0.003**	**0.003**	**0.002**		

Top Level

	Layer #									Ave. Column Density (g/cc)	Stnd Dev. (g/cc)
Column#	1	2	3	4	5	6	7	8	9		
A21	3.2386	3.2392	3.2406	3.2402	3.2416	3.2429	3.2448	2.0000	3.2411	**3.103**	**0.414**
A22	3.2387	3.2403	3.2416	3.2426	3.2411	3.2362	3.2412	3.2437	3.2387	**3.240**	**0.002**
A23	3.2436	3.2453	3.2445	3.2406	3.2402	3.2410	3.2408	3.2432	3.2428	**3.242**	**0.002**
A24	3.2308	3.2336	3.2354	3.2377	3.2382	3.2394	3.2401	3.2409	3.2390	**3.237**	**0.003**
A25	3.2429	3.2448	3.2444	3.2438	3.2429	3.2425	3.2413	3.2416	3.2388	**3.243**	**0.002**
A26	3.2415	3.2417	3.2509	3.2437	3.2435	3.2441	3.2410	3.2449	3.2441	**3.244**	**0.003**
A27	3.2365	3.2358	3.2366	3.2380	3.2398	3.2385	3.2377	3.2388	3.2408	**3.238**	**0.002**
A28	3.2354	3.2356	3.2356	3.2354	3.2353	3.2364	3.2373	3.2364	3.2373	**3.236**	**0.001**
A29	3.2375	3.2402	3.2397	3.2399	3.2381	3.2406	3.2403	3.2413	3.2375	**3.239**	**0.001**
A20	3.2348	3.2376	3.2362	3.2379	3.2388	3.2384	3.2400	3.2390	3.2380	**3.238**	**0.002**
Ave. Layer Density (g/cc)	**3.238**	**3.239**	**3.241**	**3.240**	**3.240**	**3.240**	**3.240**	**3.117**	**3.240**		
Stnd. Dev (g/cc)	**0.004**	**0.004**	**0.006**	**0.003**	**0.003**	**0.003**	**0.002**	**0.003**	**0.002**		

Table D1. Raw Sintered Density Data.

Table D2. Raw HIP'd Density Data.

Sample Set	Sample ID	Mair (g)	Mwater (g)	HIP Density (g/cc)	Ave. HIP Density (g/cc)	Sinter Density (g/cc)
2	A22-8	17.7878	12.3236	3.2553	**3.256**	3.2437
	A22-5	17.8772	12.3870	3.2562		3.2411
	A22-2	18.1780	12.5941	3.2554		3.2403
	A21-7	17.5538	12.1626	3.2560		3.2448
	A21-4	17.6901	12.2583	3.2568		3.2402
	A21-1	17.5286	12.1401	3.2530		3.2386
	A23-9	17.4255	12.0686	3.2529		3.2428
	A23-6	17.6348	12.2151	3.2538		3.2410
	A23-3	18.5312	12.8428	3.2577		3.2445
	A26-7	17.8119	12.3422	3.2565		3.2410
	A26-4	18.2173	12.6248	3.2575		3.2437
	A26-1	18.2272	12.6321	3.2577		3.2415
	A27-8	17.5875	12.1828	3.2541		3.2388
	A27-5	17.5588	12.1677	3.2570		3.2398
	A27-2	18.0717	12.5219	3.2563		3.2358
3	A22-7	17.5546	12.1573	3.2525	**3.257**	3.2412
	A22-4	18.3763	12.7276	3.2532		3.2426
	A22-1	18.2009	12.6069	3.2536		3.2387
	A21-9	17.4444	12.0889	3.2573		3.2411
	A21-6	17.5786	12.1809	3.2567		3.2429
	A21-3	17.3112	11.9961	3.2570		3.2406
	A23-8	17.8845	12.3972	3.2593		3.2432
	A23-5	17.9902	12.4675	3.2575		3.2402
	A23-2	18.0343	12.4980	3.2575		3.2453
	A26-9	17.7125	12.2742	3.2570		3.2441
	A26-6	17.7284	12.2896	3.2596		3.2441
	A23-3	17.8360	12.3650	3.2601		3.2509
	A27-7	17.8742	12.3916	3.2602		3.2377
	A27-4	17.5606	12.1732	3.2596		3.2380
	A27-1	17.5943	12.1918	3.2567		3.2365

Sample Set	Sample ID	Mair (g)	Mwater (g)	HIP Density (g/cc)	Ave. HIP Density (g/cc)	Sinter Density (g/cc)
4	A29-9	17.2795	11.9790	3.2600	3.261	3.2375
	A29-6	17.9106	12.4185	3.2612		3.2406
	A29-3	17.7743	12.3233	3.2607		3.2397
	A20-8	17.7308	12.2931	3.2607		3.2390
	A20-5	17.9250	12.4274	3.2605		3.2388
	A20-2	17.6944	12.2707	3.2624		3.2376
	A28-7	17.7548	12.3138	3.2632		3.2373
	A28-4	17.7469	12.3061	3.2618		3.2354
	A28-1	17.7293	12.2933	3.2615		3.2354
	A25-8	17.8660	12.3885	3.2617		3.2416
	A25-5	18.0134	12.4918	3.2624		3.2429
	A25-2	17.5878	12.1927	3.2600		3.2448
	A24-9	17.5763	12.1837	3.2593		3.2390
	A24-6	17.7585	12.3151	3.2624		3.2394
	A24-3	17.8008	12.3442	3.2623		3.2354
5	A29-8	17.8856	12.3947	3.2573	3.260	3.2412
	A29-5	17.9130	12.4158	3.2586		3.2381
	A29-2	17.6547	12.2363	3.2583		3.2402
	A20-7	17.7970	12.3333	3.2573		3.2400
	A20-4	17.7050	12.2743	3.2602		3.2379
	A20-1	18.0224	12.4942	3.2601		3.2348
	A28-9	17.7223	12.2811	3.2571		3.2373
	A28-6	17.8854	12.3990	3.2600		3.2364
	A28-3	17.9204	12.4245	3.2607		3.2356
	A25-7	17.7950	12.3356	3.2595		3.2413
	A25-4	18.0082	12.4840	3.2599		3.2438
	A25-1	17.8114	12.3489	3.2607		3.2429
	A24-8	17.5137	12.1436	3.2613		3.2409
	A24-5	18.2147	12.6274	3.2600		3.2382
	A24-2	17.8912	12.4065	3.2620		3.2336

Table D2. Raw HIP'd Density Data, continued.

Sample Set	Sample ID	Mair (g)	Mwater (g)	HIP Density (g/cc)	Ave. HIP Density (g/cc)	Sinter Density (g/cc)
6	A29-7	17.6140	12.2092	3.2590	**3.257**	3.2403
	A29-4	18.0756	12.5313	3.2602		3.2399
	A29-1	17.5035	12.1307	3.2578		3.2375
	A20-9	17.0172	11.7782	3.2482		3.2380
	A20-6	17.9840	12.4656	3.2589		3.2384
	A20-3	17.6470	12.2319	3.2589		3.2362
	A28-8	17.5558	12.1651	3.2567		3.2364
	A28-5	17.7359	12.2924	3.2582		3.2353
	A28-2	17.7326	12.2923	3.2595		3.2356
	A25-9	17.8465	12.3541	3.2493		3.2388
	A25-6	17.5589	12.1691	3.2578		3.2425
	A25-3	17.6388	12.2278	3.2598		3.2444
	A24-7	17.8464	12.3662	3.2565		3.2401
	A24-4	17.7613	12.3050	3.2552		3.2377
	A24-1	17.5561	12.1658	3.2570		3.2308
MS1	A11-9	17.7805	12.3085	3.2494	**3.256**	3.2500
	A11-6	17.8637	12.3840	3.2600		3.2435
	A11-3	17.9631	12.4491	3.2577		3.2449
MS2	A12-8	17.6507	12.2364	3.2600	**3.258**	3.2487
	A12-5	17.8614	12.3728	3.2543		3.2448
	A12-2	17.7361	12.2967	3.2607		3.2503
MS3	A13-7	17.6562	12.2358	3.2574	**3.259**	3.2433
	A13-4	17.6819	12.2581	3.2601		3.2416
	A13-1	17.6678	12.2494	3.2607		3.2477
MS4	A14-8	17.3908	12.0484	3.2552	**3.254**	3.2432
	A14-5	17.4729	12.1018	3.2531		3.2421
	A14-2	17.6702	12.2400	3.2541		3.2490
MS5	A15-9	17.5471	12.1618	3.2583	**3.259**	3.2474
	A15-6	17.7517	12.3029	3.2579		3.2481
	A15-3	17.5170	12.1448	3.2607		3.2464

Table D2. Raw HIP'd Density Data, continued.

Before Grinding

Sample Set	Sample ID	Mair (g)	Mwater (g)	HIP Density (g/cc)	Ave. HIP Density (g/cc)	Sinter Density (g/cc)
1 (annealed)	A26-6	2.8816	1.9972	3.2583	**3.259**	3.2500
	A23-1	3.6610	2.5375	3.2586		3.2435
	A22-6	3.5884	2.4874	3.2592		3.2449
3 (annealed)	A27-4	3.7960	2.6329	3.2637	**3.266**	3.2487
	A26-6	3.5536	2.4660	3.2674		3.2448
	A21-9	3.7863	2.6269	3.2657		3.2503
4 (annealed)	A29-3	3.9302	2.7263	3.2646	**3.267**	3.2433
	A25-2	3.7291	2.5883	3.2688		3.2416
	A24-9	3.5757	2.4816	3.2682		3.2477

After Grinding

Sample Set	Sample ID	Mair (g)	Mwater (g)	HIP Density (g/cc)	Ave. HIP Density (g/cc)	Sinter Density (g/cc)
1 (annealed)	A22-6	2.4930	1.7244	3.2436	**3.252**	3.2500
	A23-1	2.9201	2.0223	3.2525		3.2435
	A22-6	2.9165	2.0217	3.2594		3.2449
3 (annealed)	A27-4	3.0889	2.1425	3.2638	**3.266**	3.2487
	A26-6	3.0464	2.1142	3.2680		3.2448
	A21-9	3.1344	2.1744	3.2650		3.2503
4 (annealed)	A29-3	3.1645	2.1949	3.2637	**3.267**	3.2433
	A25-2	3.1683	2.1991	3.2690		3.2416
	A24-9	3.0557	2.1208	3.2685		3.2477

Table D2. Raw HIP'd Density Data, continued.

Sample Set	Sample ID	HRA			Sample Ave.	Sample Set Average	Standard Deviation
1	A21-2	95.1	94.9	94.7	94.9	94.92	0.14
	A26-5	94.9	94.9	95	94.9		
	A27-3	94.7	95.1	95	94.9		
2	A22-2	95	95.2	95	95.1	94.99	0.09
	A23-9	94.9	94.9	95	94.9		
	A27-8	94.9	95	95	95.0		
3	A21-6	94.9	94.8	94.7	94.8	94.72	0.08
	A23-2	94.7	94.7	94.7	94.7		
	A26-9	94.7	94.6	94.7	94.7		
4	A25-5	94.8	94.8	94.7	94.8	94.69	0.12
	A28-4	94.7	94.7	94.8	94.7		
	A20-8	94.4	94.7	94.6	94.6		
5	A24-2	95.1	95	95	95.0	95.10	0.11
	A28-3	95.1	95.3	95.2	95.2		
	A29-8	95.2	95	95	95.1		
6	A24-7	94.6	94.5	94.5	94.5	94.58	0.10
	A25-9	94.5	94.5	94.5	94.5		
	A20-6	94.7	94.8	94.6	94.7		
1 (annealed)	A26-2	94.4	94.4	94.3	94.4	94.33	0.11
	A23-1	94.4	94.5	94.4	94.4		
	A22-6	94.2	94.2	94.2	94.2		
3 (annealed)	A26-6	94.1	94.4	93.8	94.1	94.09	0.22
	A27-4	94.2	94.4	94.1	94.2		
	A21-9	94	94	93.8	93.9		
4 (annealed)	A25-2	94.2	94.2	93.8	94.1	94.07	0.15
	A29-3	94.2	94.2	94	94.1		
	A24-9	94	94.1	93.9	94.0		
MS1	A11-9	95.1	95.1	95.1	95.1	95.10	0.00
MS2	A12-5	94.8	94.8	94.7	94.8	94.77	0.05
MS3	A13-7	95	95	95.1	95.0	95.03	0.05
MS4	A14-8	95	94.9	94.8	94.9	94.90	0.08
MS5	A15-3	95	94.9	94.8	94.9	94.90	0.08

Table D3. Raw Rockwell A Hardness Data.

Table D4. Raw Vicker's Mirohardness Data

Sample Set	Sample	D1(microns)	D2(microns)	Hv	Average Hv	Standard Deviation
1	a27-3	15.92	15.71	2224	2128	83
		15.89	15.89	2203		
		16.13	16.74	2060		
		16.07	16.02	2161		
	a26-5	16.69	16.79	1985		
		16.97	16.71	1962		
		16.21	16.1	2132		
		16.13	15.81	2181		
	a21-2	15.85	16.17	2170		
		15.83	16.31	2154		
		16	16	2173		
		16.15	16.16	2132		
1(annealed)	a22-6	17.07	16.34	1994	1944	123
		17.5	16.49	1926		
		16.31	16.45	2073		
		16.38	17.06	1990		
	a26-2	16.38	16.09	2111		
		17.99	17.44	1773		
		17.81	17.07	1829		
		18.2	17.91	1707		
	a23-1	16.57	16.82	1996		
		17.31	16.9	1901		
		16.28	16.61	2057		
		16.59	16.98	1975		
2	a23-9	15.86	15.86	2212	2090	127
		16.43	15.9	2129		
		17.48	17.03	1868		
		16.1	15.76	2192		
	a27-8	16.3	16.21	2105		
		16.86	16.43	2008		
		17.16	16.98	1909		
		16.41	16.28	2082		
	a22-2	15.93	15.93	2192		
		15.81	16.19	2173		
		15.48	15.95	2253		
		17.01	16.74	1954		

Sample Set	Sample	D1(microns)	D2(microns)	Hv	Ave Hv	Standard Deviation
3	a21-6	16.64	16.68	2004	1969	99
		16.48	16.03	2105		
		16.24	16.53	2072		
		17.05	17.11	1907		
	a23-2	17.56	17.57	1803		
		17.04	16.29	2003		
		16.73	16.33	2036		
		17.49	17.75	1792		
	a26-9	16.8	17.39	1904		
		16.44	16.78	2016		
		16.87	16.69	1976		
		16.98	16.29	2010		
3 (annealed)	a27-4	18.17	18.21	1681	1810	86
		17.79	17.72	1765		
		17.99	17.66	1751		
		17.25	17.49	1844		
	a26-6	17.36	17.31	1851		
		17.76	17.23	1818		
		17.16	18.29	1771		
		16.55	17.2	1954		
	a21-9	17.03	16.56	1972		
		17.94	17.92	1730		
		17.86	17.53	1777		
		17.47	17.58	1811		
4	a28-4	16.32	16.45	2072	1891	129
		16.23	16.24	2111		
		16.86	16.64	1983		
		17.49	16.81	1891		
	a20-8	17.24	17.89	1803		
		16.97	17.18	1908		
		18.16	17.84	1717		
		17.57	18.5	1710		
	a25-5	17.76	17.62	1778		
		16.86	17.24	1914		
		17.36	17.49	1832		
		16.73	16.84	1975		
4 (annealed)	a29-3	18.01	16.99	1817	1849	74
		17.46	17.56	1814		
		17.76	17.14	1827		
		17.76	16.75	1868		
	a25-3	16.88	16.98	1941		
		18.07	17.55	1754		
		17.2	17.08	1894		
		17.45	17.53	1819		
	a24-9	16.74	16.78	1980		
		17.7	17.7	1776		
		17.82	17.73	1761		
		16.83	17.1	1933		

Sample Set	Sample	D1(microns)	D2(microns)	Hv	Ave Hv	Standard Deviation
5	a24-2	15.91	16.73	2089	2149	107
		15.88	15.88	2206		
		15.78	16.18	2179		
		16.15	16.96	2030		
	a29-8	15.69	15.94	2224		
		16.86	17.36	1900		
		16.34	15.91	2140		
		15.64	16.02	2220		
	a28-3	16.04	16.2	2141		
		15.59	15.63	2283		
		15.68	15.71	2258		
		16.32	16.11	2116		
6	a25-9	16.13	16.16	2134	1936	103
		16.29	16.69	2046		
		17.41	17.95	1780		
		17.8	16.83	1856		
	a20-6	16.39	16.67	2036		
		16.82	17.03	1942		
		17.71	16.84	1864		
		16.8	16.8	1971		
	a24-7	17.04	17.56	1859		
		17.12	17.74	1831		
		16.86	16.66	1980		
		16.59	17.39	1927		

Sample Set	Sample	D1(microns)	D2(microns)	Hv	Ave Hv	Standard Deviation
MS1	a11-9	16.44	16.21	2087	2073	49
		16.39	16.27	2086		
		16.27	16.16	2116		
		16.49	16.85	2002		
MS2	a12-5	16.39	17.19	1973	1983	16
		16.15	17.31	1988		
		16.38	17.24	1969		
		16.59	16.74	2003		
MS3	a13-1	17.47	17.47	1823	1979	116
		16.84	16.8	1966		
		16.41	16.21	2091		
		16.29	16.76	2037		
MS4	a14-8	17.55	17.76	1785	1858	88
		17.4	17.53	1824		
		16.91	16.57	1985		
		17.13	17.68	1836		
MS5	a15-3	16.52	17.03	1977	1928	83
		17.42	17.41	1834		
		16.66	16.57	2015		
		17.09	17.28	1884		

Table D4. Raw Vicker's Microhardness Data, continued

TableD5. Vicker's Indentation Fracture Toughness Raw Data.

Sample Set	Sample ID	L1 (microns)	L2 (microns)	Ave. L (microns)	KIC (MPaM^1/2)	AVE. KIC (MPaM^1/2)
1	A21-2	473.49	459.24	466.37	7.84	7.54
		457.09	477.78	467.43	7.82	
		484.23	440.65	462.44	7.94	
		493.87	484.82	489.34	7.30	
	A26-5	474.89	494.88	484.89	7.40	
		471.14	496.55	483.84	7.42	
		479.69	483.14	481.42	7.48	
		477.22	501.95	489.59	7.29	
	A27-3	457.74	496.10	476.92	7.58	
		436.97	501.89	469.43	7.77	
		460.84	506.80	483.82	7.42	
		490.44	496.75	493.59	7.20	
2	A22-2	464.35	468.58	466.46	7.84	7.54
		450.23	473.43	461.83	7.96	
		471.12	462.43	466.78	7.83	
		458.89	495.46	477.18	7.58	
	A23-9	471.91	487.93	479.92	7.51	
		449.35	498.57	473.96	7.66	
		492.80	488.91	490.86	7.26	
		499.32	521.66	510.49	6.85	
	A27-8	455.36	491.32	473.34	7.67	
		448.96	493.74	471.35	7.72	
		500.65	477.00	488.83	7.31	
		479.73	496.33	488.03	7.33	

Sample Set	Sample ID	L1 (microns)	L2 (microns)	Ave. L (microns)	KIC (MPaM^1/2)	AVE. KIC (MPaM^1/2)
3	A21-6	465.89	475.84	470.87	7.73	7.45
		466.05	547.04	506.55	6.93	
		462.03	465.31	463.67	7.91	
		461.84	502.67	482.25	7.46	
	A23-2	465.04	483.81	474.42	7.64	
		433.84	473.53	453.69	8.17	
		458.27	455.84	457.06	8.08	
		476.18	451.55	463.86	7.91	
	A26-9	497.12	533.08	515.10	6.76	
		469.06	553.90	511.48	6.83	
		494.31	510.06	502.19	7.02	
		499.88	511.80	505.84	6.94	
4	A25-5	454.57	515.47	485.02	7.40	6.74
		509.15	548.28	528.71	6.50	
		500.55	491.41	495.98	7.15	
		453.62	514.00	483.81	7.42	
	A28-4	498.15	556.71	527.43	6.52	
		471.52	542.95	507.24	6.92	
		509.37	527.00	518.19	6.70	
		553.21	547.10	550.16	6.12	
	A20-8	504.96	589.01	546.99	6.18	
		499.80	564.62	532.21	6.43	
		543.60	501.26	522.43	6.62	
		506.13	509.58	507.85	6.90	

TableD5. Vicker's Indentation Fracture Toughness Raw Data, continued.

Sample Set	Sample ID	L1 (microns)	L2 (microns)	Ave. L (microns)	KIC (MPaM^1/2)	AVE. KIC (MPaM^1/2)
5	A24-2	507.46	493.89	500.68	7.05	7.28
		465.33	489.65	477.49	7.57	
		473.65	466.17	469.91	7.76	
		494.22	502.41	498.31	7.10	
	A28-3	492.70	494.10	493.40	7.21	
		484.43	491.31	487.87	7.33	
		483.45	484.77	484.11	7.42	
		499.79	494.73	497.26	7.12	
	A29-8	480.42	504.10	492.26	7.23	
		491.94	504.16	498.05	7.11	
		517.51	470.59	494.05	7.19	
		485.08	496.85	490.97	7.26	
6	A24-7	450.54	466.35	458.45	8.05	7.99
		425.66	455.45	440.56	8.54	
		459.69	442.02	450.85	8.25	
		461.28	469.18	465.23	7.87	
	A25-9	461.27	483.44	472.35	7.70	
		446.96	486.31	466.63	7.84	
		472.04	497.71	484.88	7.40	
		458.46	524.30	491.38	7.25	
	A20-6	448.32	460.28	454.30	8.16	
		431.00	455.72	443.36	8.46	
		451.46	454.50	452.98	8.19	
		447.04	459.57	453.31	8.19	

Table D5. Vicker's Indentation Fracture Toughness Raw Data, continued.

Sample Set	Sample ID	L1 (microns)	L2 (microns)	Ave. L (microns)	KIC (MPaM^1/2)	AVE. KIC (MPaM^1/2)
1 (annealed)	A26-2	549.71	536.76	543.23	6.24	6.42
		572.65	447.33	509.99	6.86	
		574.18	473.82	524.00	6.59	
		541.17	473.92	507.55	6.91	
	A23-1	499.88	470.99	485.44	7.39	
		587.13	511.34	549.23	6.14	
		609.26	599.38	604.32	5.32	
		629.06	541.67	585.36	5.58	
	A22-6	567.16	505.86	536.51	6.36	
		553.49	474.53	514.01	6.78	
		533.56	506.10	519.83	6.67	
		553.31	540.76	547.04	6.17	
3 (annealed)	A26-6	452.58	658.97	555.78	6.03	6.84
		523.21	449.71	486.46	7.36	
		568.20	526.04	547.12	6.17	
		549.31	469.05	509.18	6.88	
	A27-4	507.37	480.22	493.79	7.20	
		536.98	443.22	490.10	7.28	
		519.47	487.47	503.47	6.99	
		522.50	505.27	513.89	6.78	
	A21-9	541.66	494.91	518.28	6.70	
		530.92	454.78	492.85	7.22	
		446.87	580.25	513.56	6.79	
		523.96	516.21	520.09	6.66	

Table D5. Vicker's Indentation Fracture Toughness Raw Data, continued.

Sample Set	Sample ID	L1 (microns)	L2 (microns)	Ave. L (microns)	KIC (MPaM^1/2)	AVE. KIC (MPaM^1/2)
4 (annealed)	A25-2	568.04	449.01	508.53	6.89	6.63
		546.13	420.56	483.34	7.43	
		566.23	535.25	550.74	6.11	
		535.17	524.99	530.08	6.47	
	A29-3	562.64	506.08	534.36	6.40	
		519.34	445.01	482.17	7.46	
		442.57	569.43	506.00	6.94	
		580.02	536.25	558.13	5.99	
	A24-9	600.72	475.96	538.34	6.32	
		590.72	461.64	526.18	6.55	
		577.78	493.00	535.39	6.38	
		515.86	528.41	522.13	6.62	

Table D5. Vicker's Indentation Fracture Toughness Raw Data, continued.

Sample Set	Sample ID	L1 (microns)	L2 (microns)	Ave. L (microns)	KIC (MPaM^1/2)	AVE. KIC (MPaM^1/2)
MS 1	A11-9	475.13	504.81	489.97	7.28	7.42
		451.76	488.13	469.94	7.75	
		501.81	470.50	486.15	7.37	
		491.81	488.35	490.08	7.28	
MS 2	A12-5	545.79	525.93	535.86	6.37	6.23
		524.78	541.18	532.98	6.42	
		540.11	558.29	549.20	6.14	
		575.80	538.28	557.04	6.01	
MS 3	A13-7	465.83	481.24	473.53	7.67	7.43
		473.26	484.39	478.82	7.54	
		487.75	484.21	485.98	7.37	
		480.42	513.37	496.89	7.13	
MS4	A14-8	480.22	497.08	488.65	7.31	7.08
		486.91	503.74	495.32	7.17	
		494.14	515.51	504.82	6.96	
		491.99	526.61	509.30	6.87	
MS 5	A15-3	492.06	493.34	492.70	7.22	7.30
		451.56	499.71	475.63	7.62	
		490.04	495.39	492.72	7.22	
		479.80	511.88	495.84	7.15	

Table D5. Vicker's Indentation Fracture Toughness Raw Data, continued.

APPENDIX E

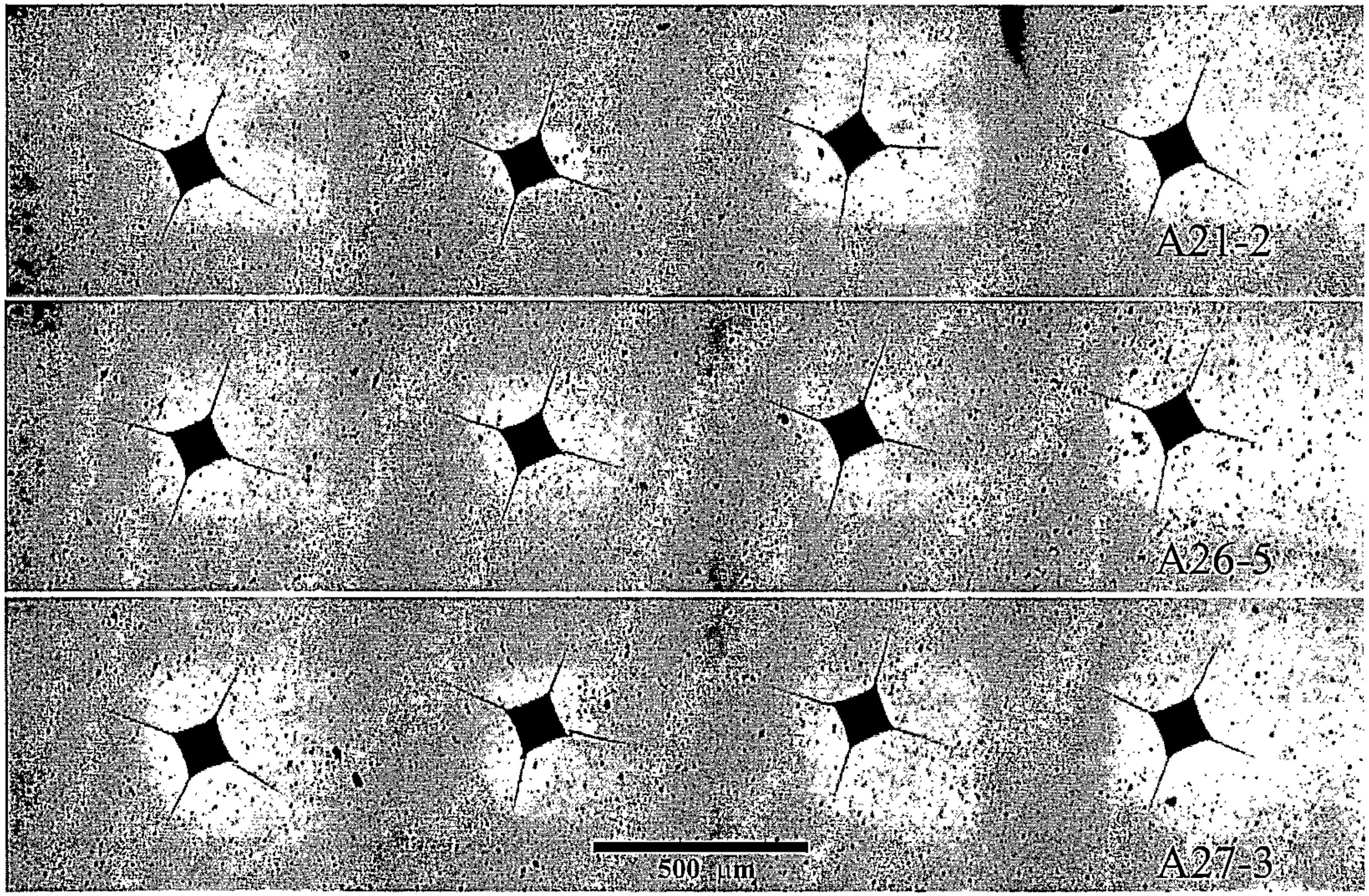

Figure E1. Optical micrographs of fracture toughness indents for SS1. Indents 1 through 4 are seen left to right.

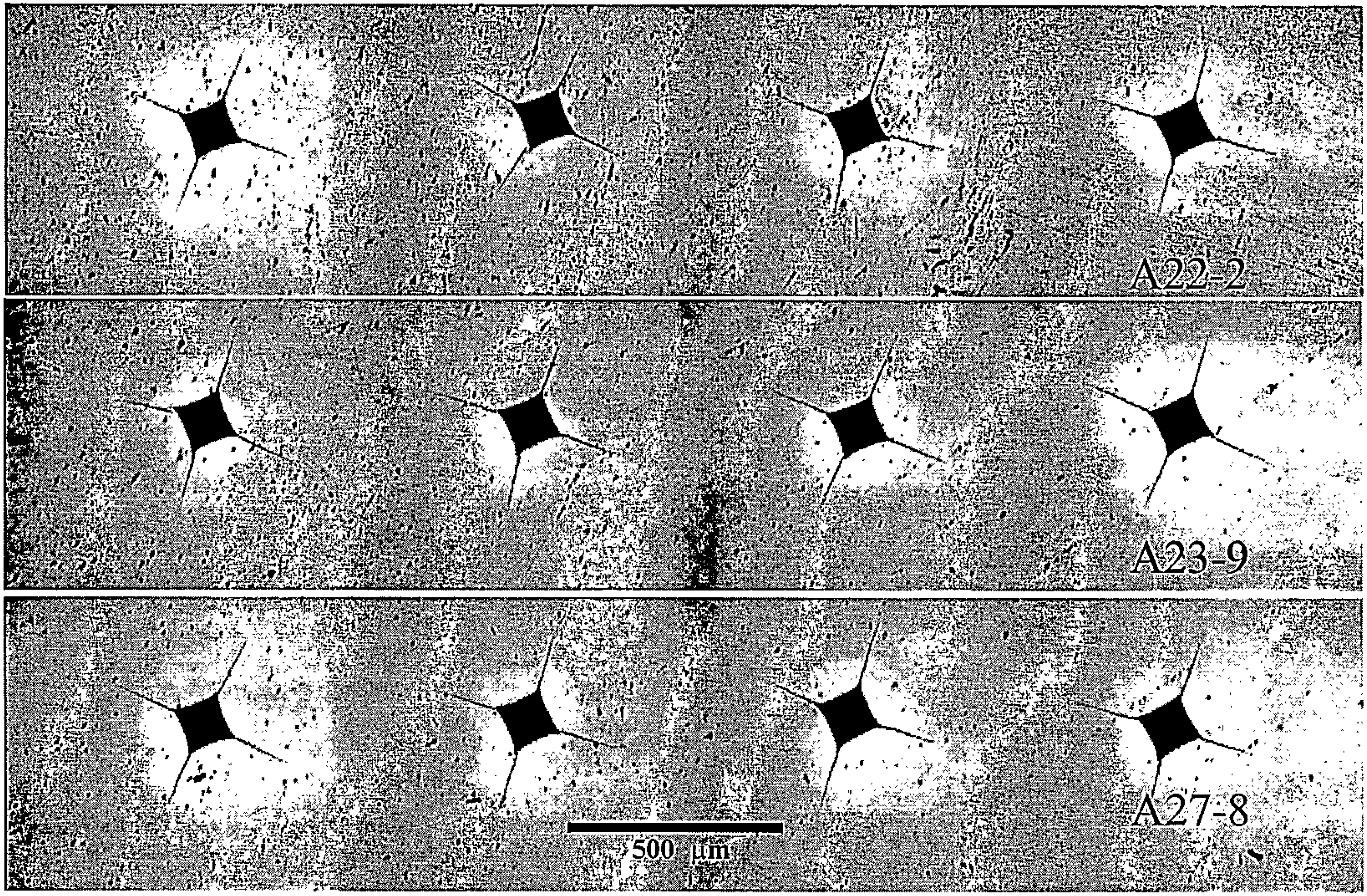

Figure E2. Optical micrographs of fracture toughness indents for SS2. Indents 1 through 4 are seen left to right.

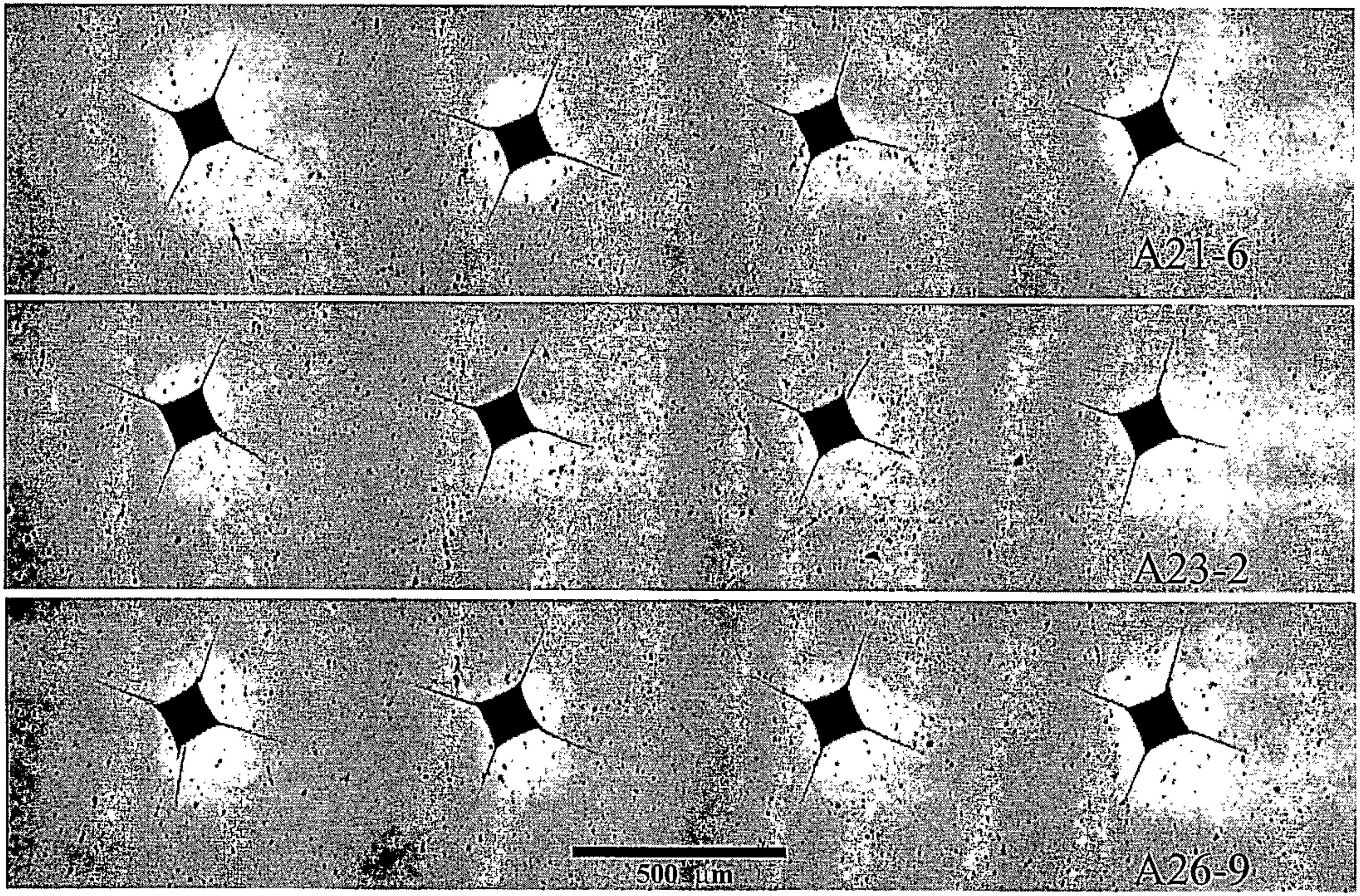

Figure E3. Optical micrographs of fracture toughness indents for SS3. Indents 1 through 4 are seen left to right.

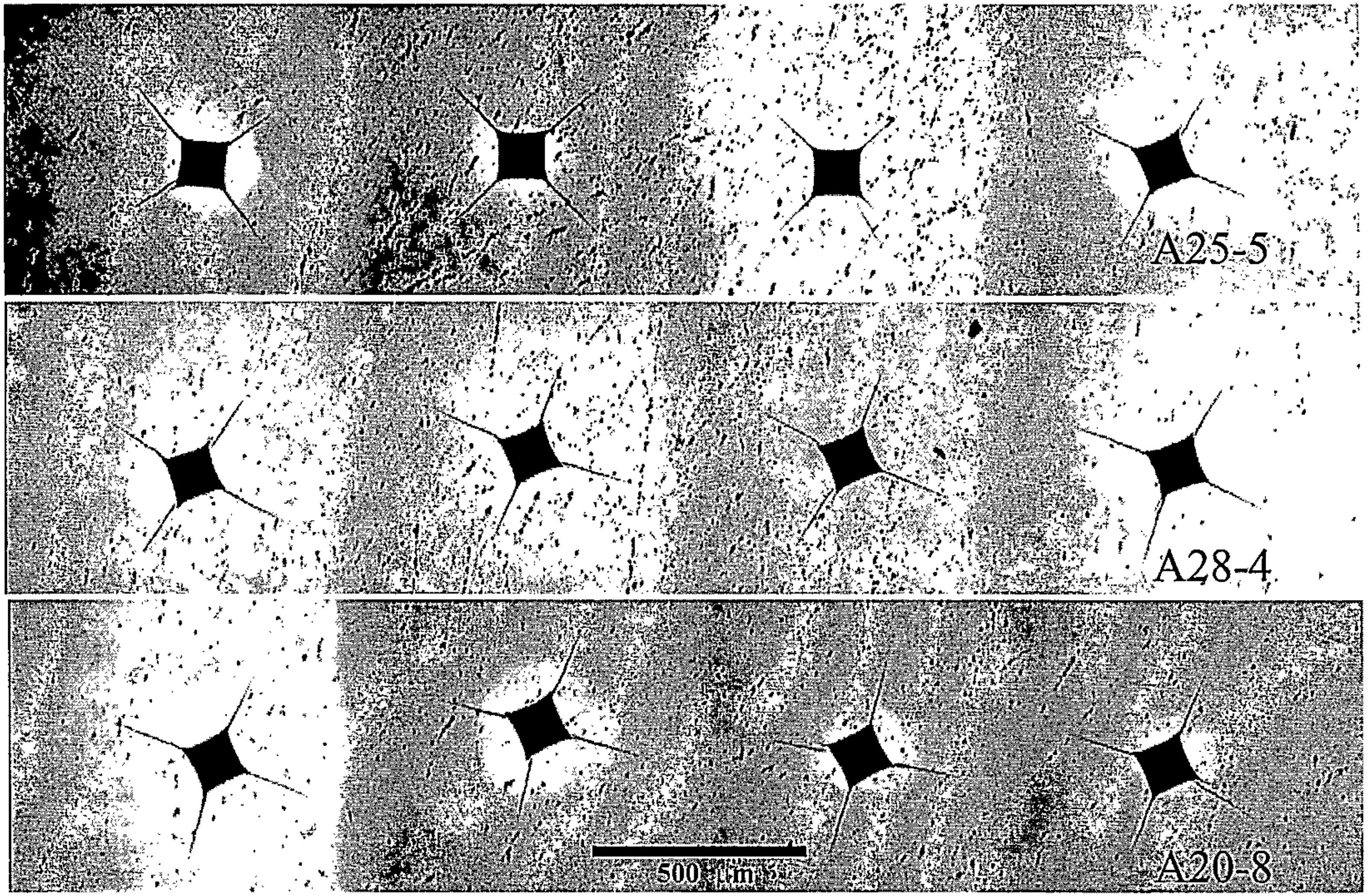

Figure E4. Optical micrographs of fracture toughness indents for SS4. Indents 1 through 4 are seen left to right.

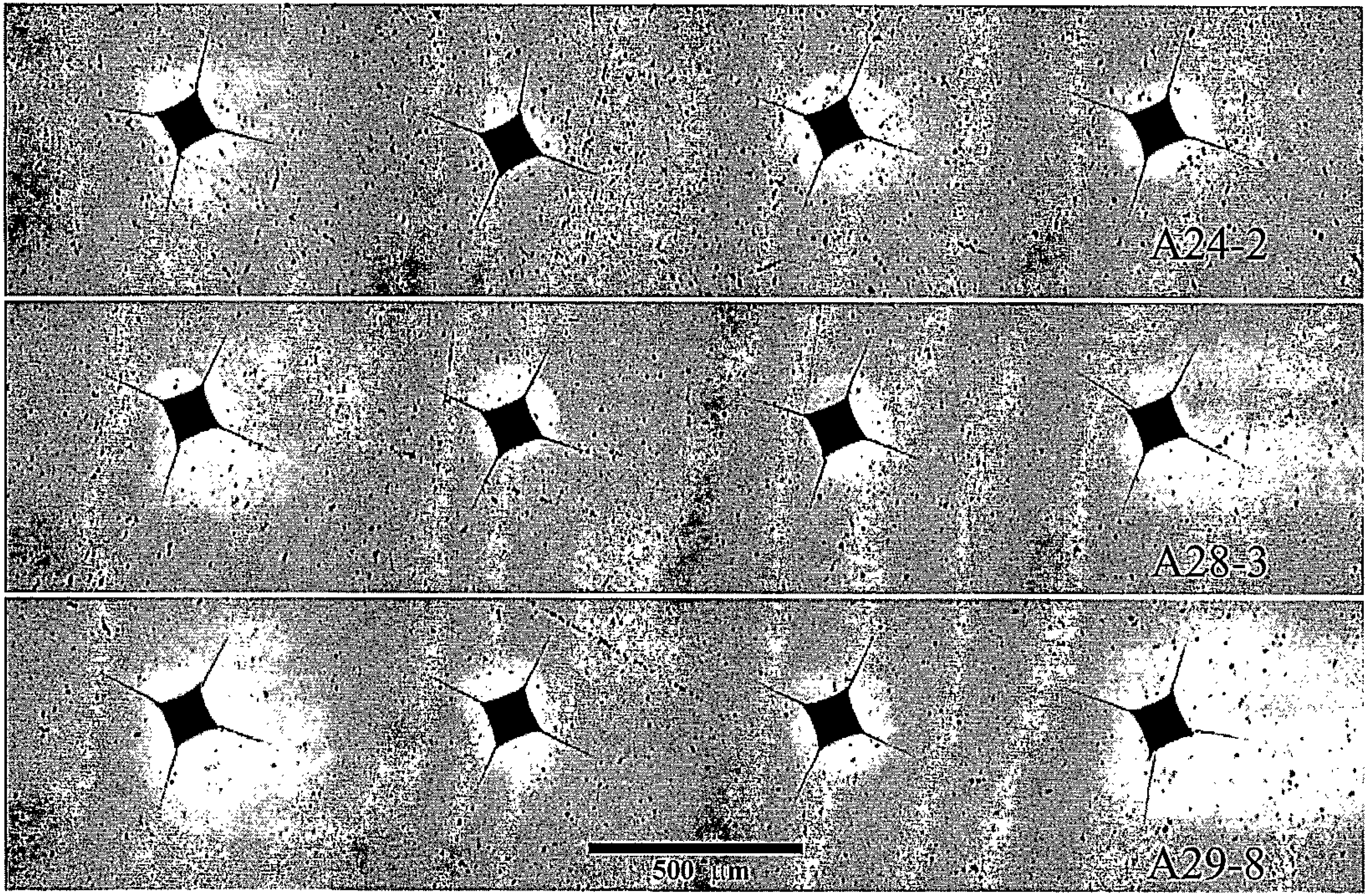

Figure E5. Optical micrographs of fracture toughness indents for SS5. Indents 1 through 4 are seen left to right.

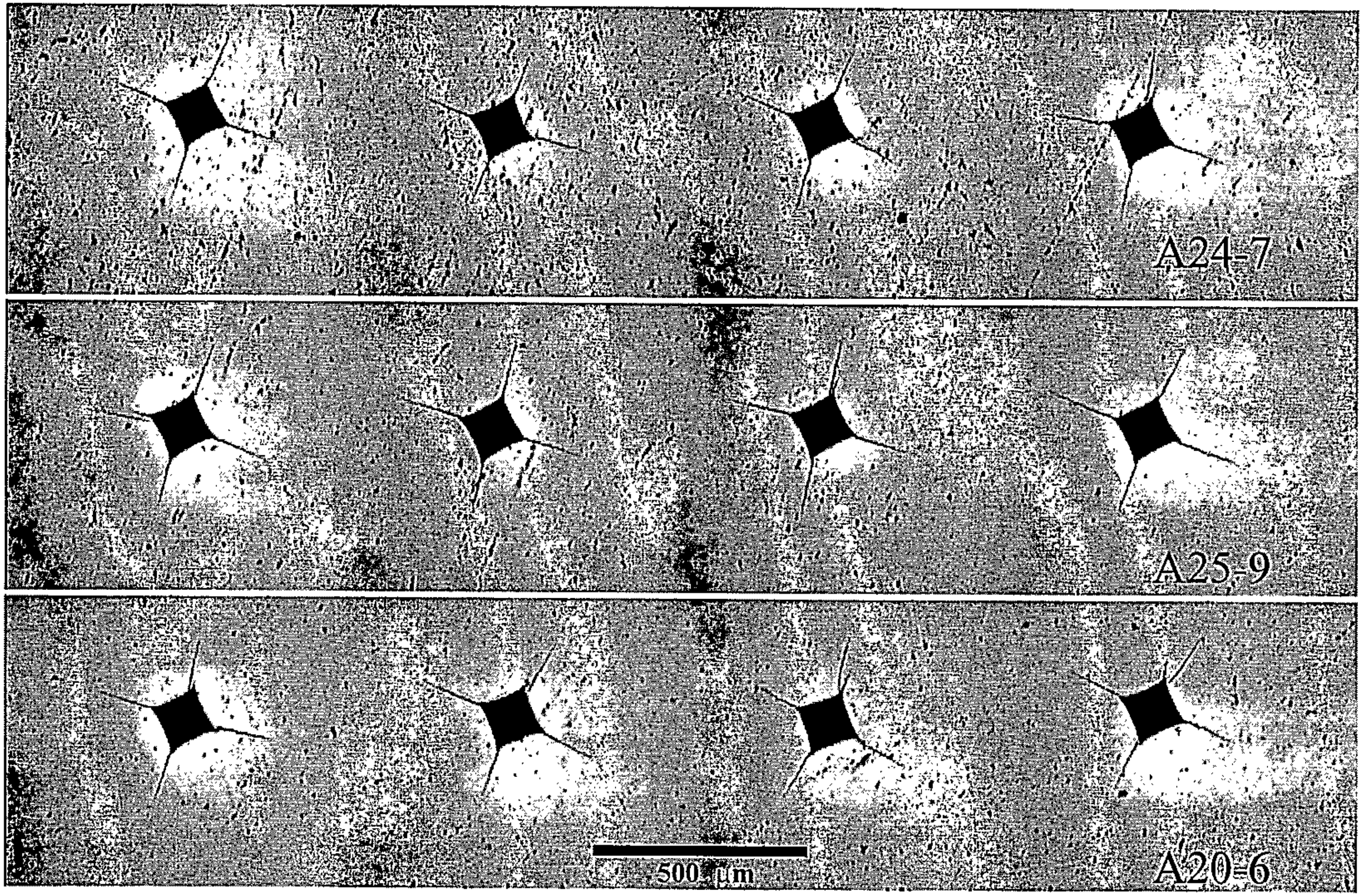

Figure E6. Optical micrographs of fracture toughness indents for SS6. Indents 1 through 4 are seen left to right.

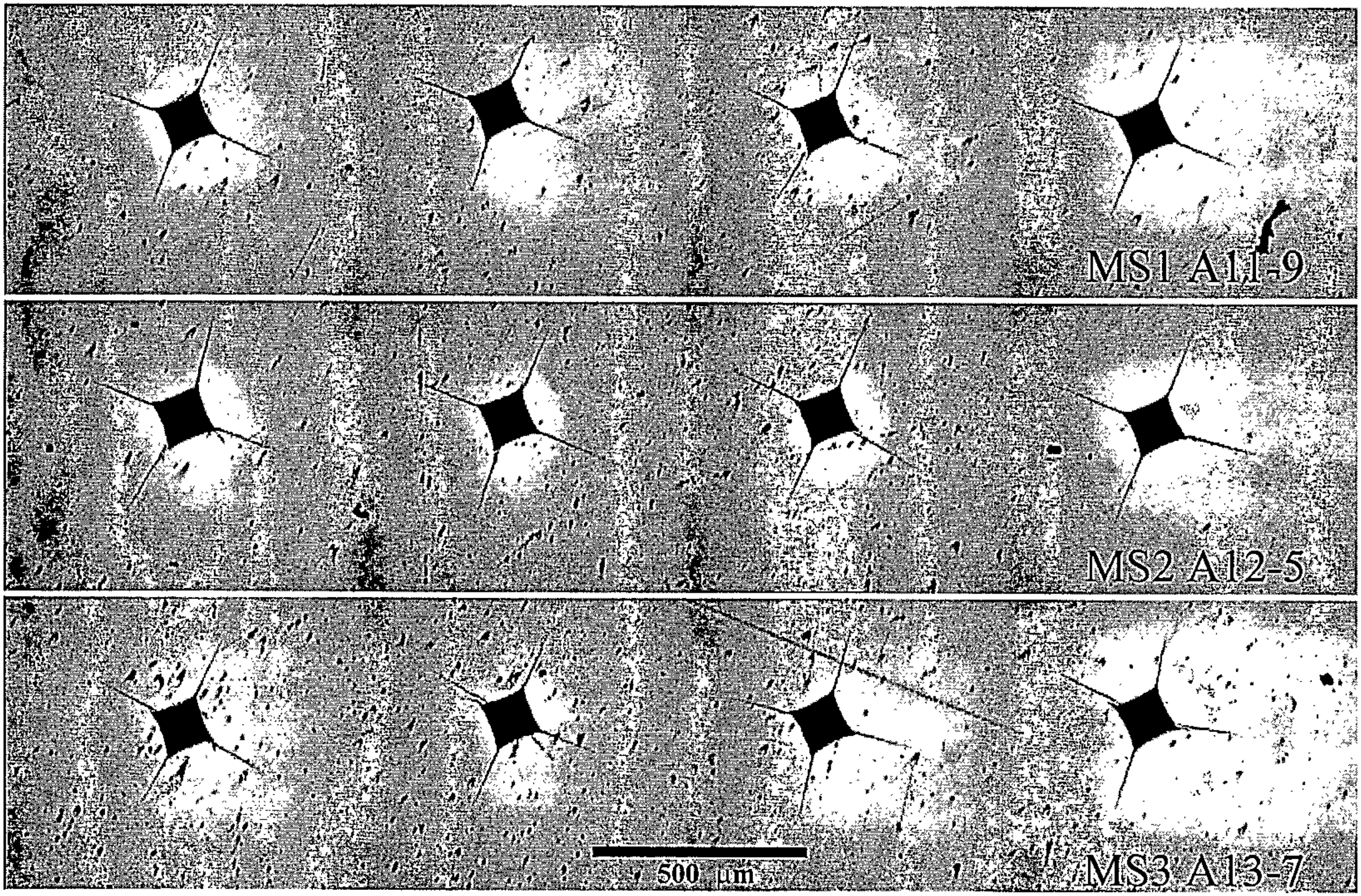

Figure E7. Optical micrographs of fracture toughness indents for MS1-3. Indents 1 through 4 are seen left to right.

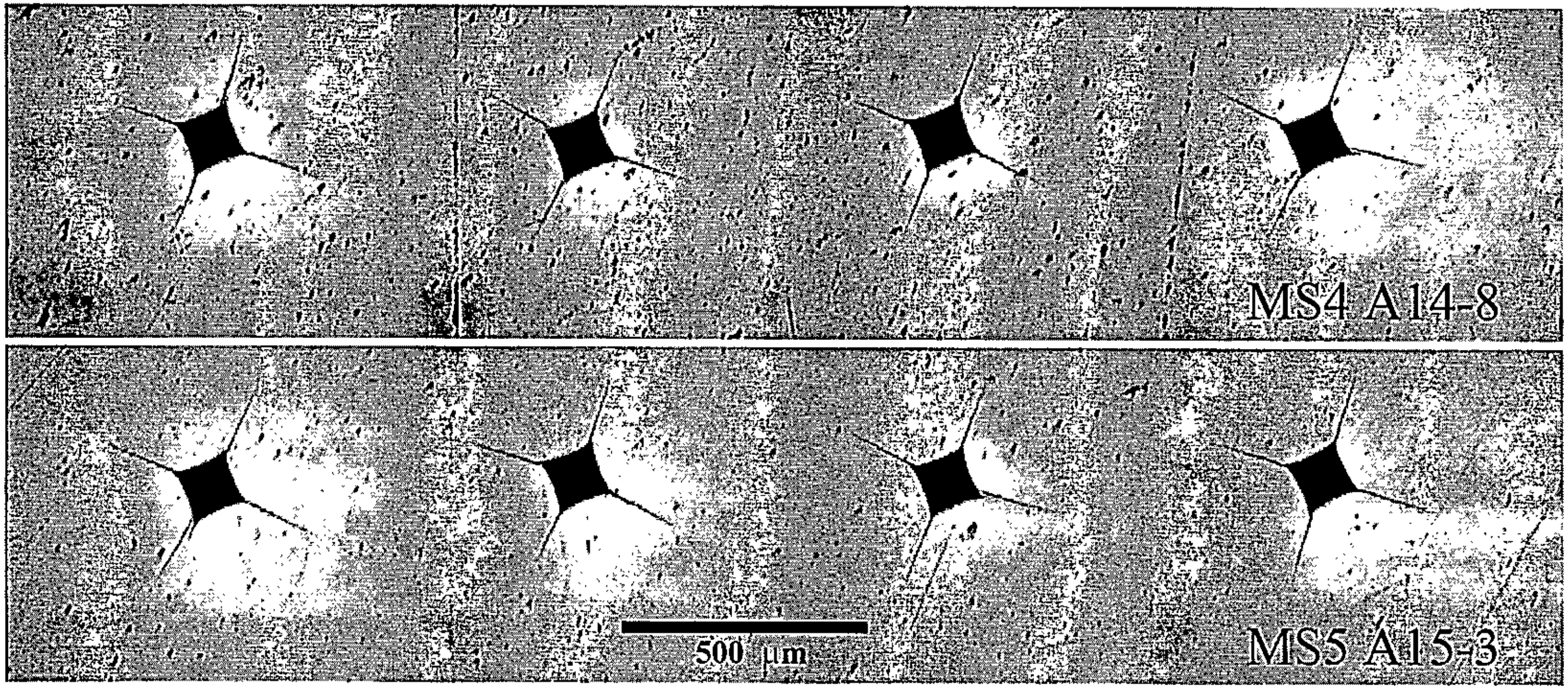

Figure E8. Optical micrographs of fracture toughness indents for MS4 and 5. Indents 1 through 4 are seen left to right.

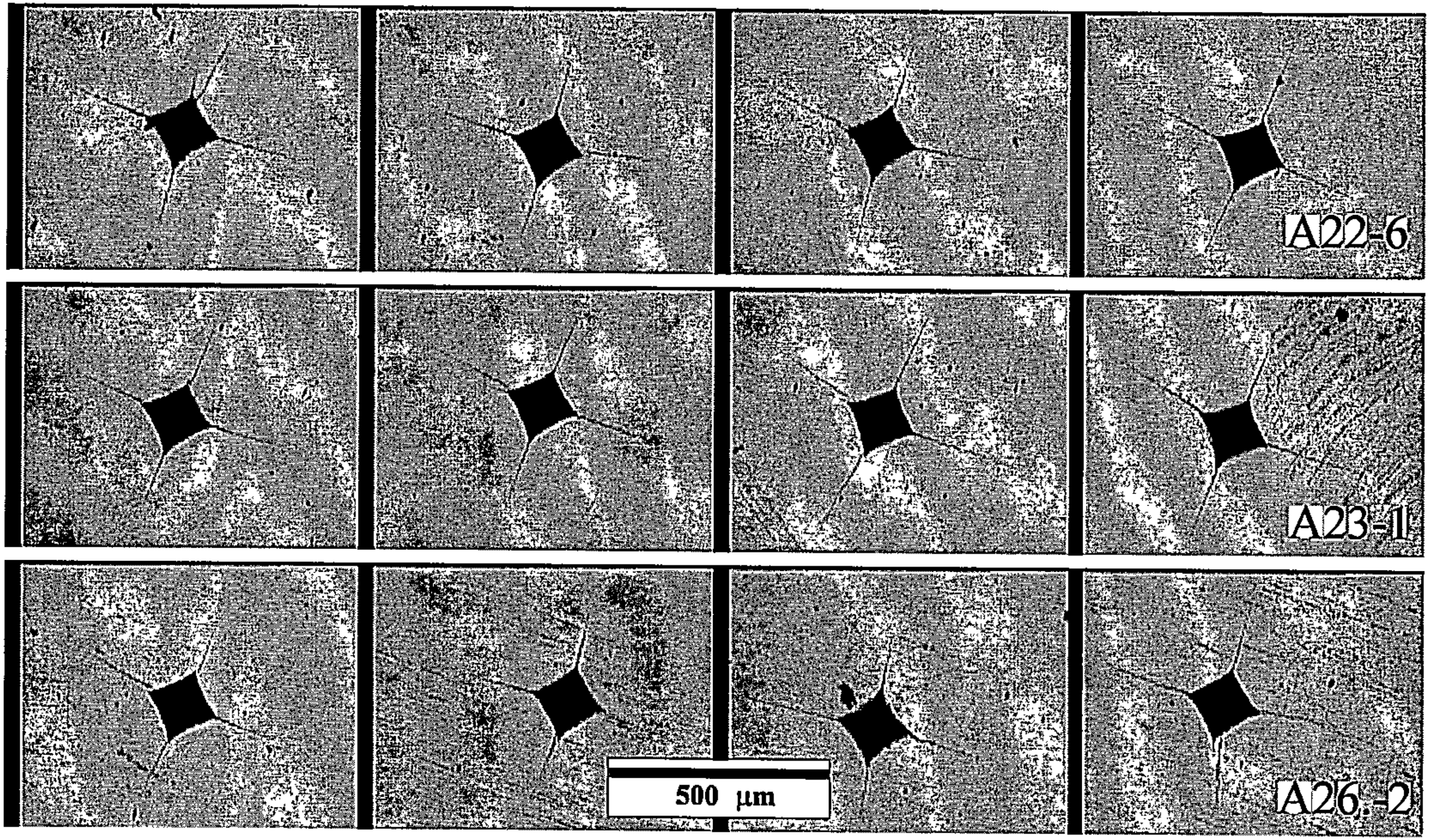

Figure E9. Optical micrographs of fracture toughness indents for SS1 annealed. Indents 1 through 4 are seen left to right.

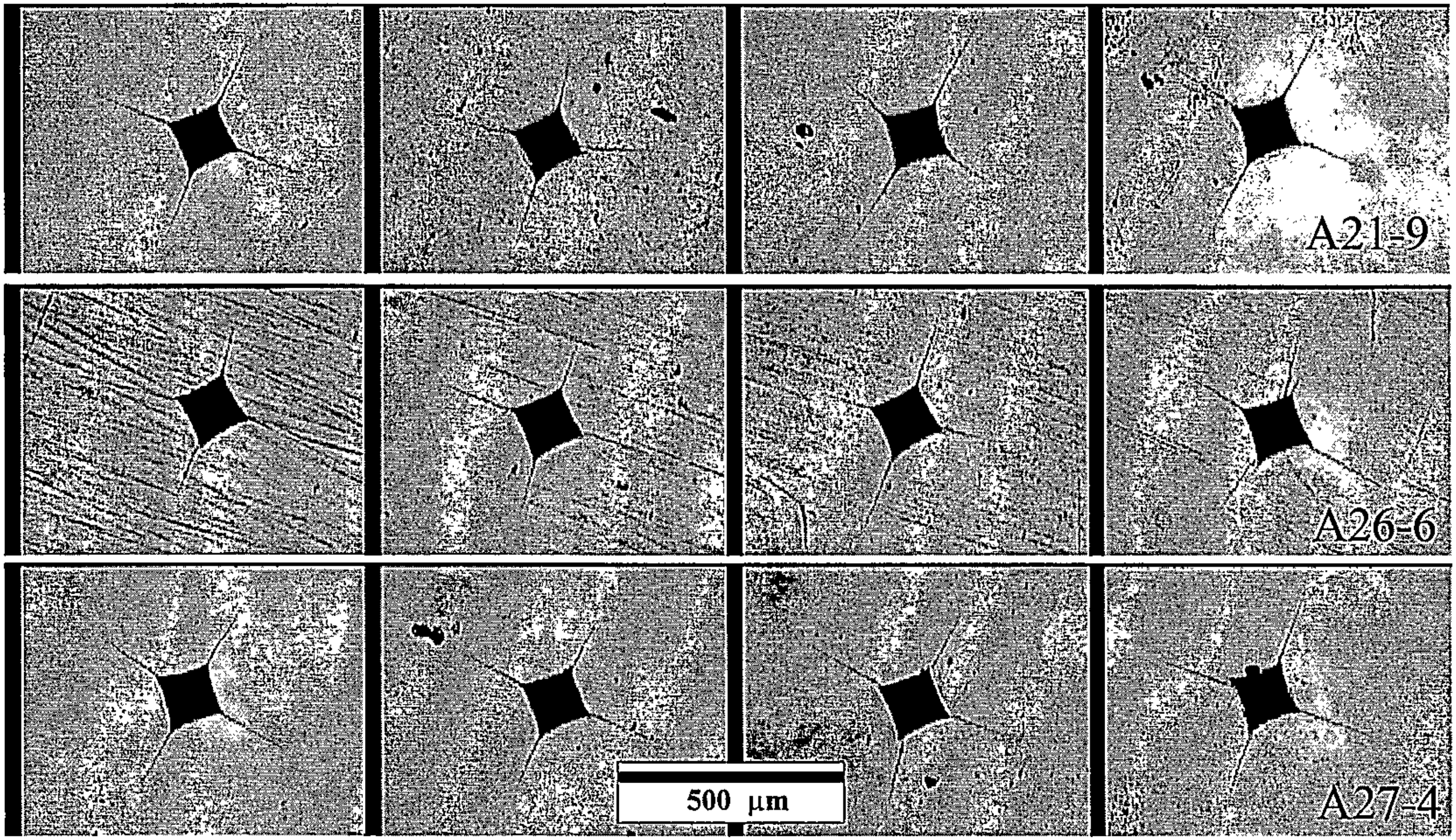

Figure E10. Optical micrographs of fracture toughness indents for SS3 annealed. Indents 1 through 4 are seen left to right.

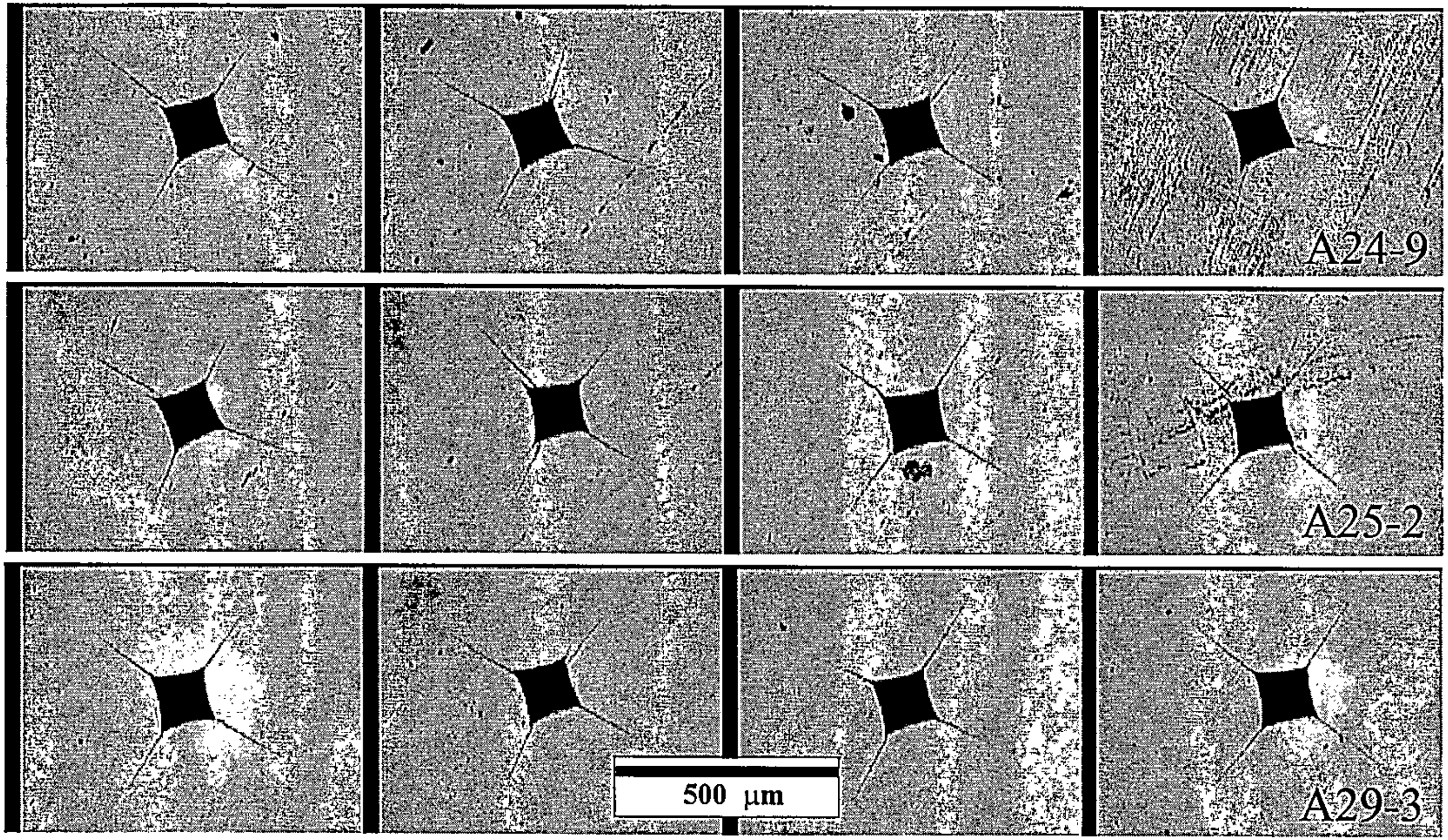

Figure E11. Optical micrographs of fracture toughness indents for SS4 annealed. Indents 1 through 4 are seen left to right.

BIBLIOGRAPHY

Ahmad, I and Clark, D.E. "Effect of Microwave Heating on the Mass Transport in Ceramics", Ceramic Transactions Volume 36, Microwaves: Theory and Application in Materials Processing II, D.E. Clark, W.R. Tinga, and J.R. Laia Jr., Eds. Ohio: The American Ceramic Society, 1993, 287-95.

Ahn, C.C. and Thomas, G. "Microstructure and Grain-Boundary Composition of Hot-Pressed Silicon Nitride With Yttria and Alumina", Journal of the American Ceramic Society, **[66]** (1983), 14-17.

ASM Handbook Vol. 8: Mechanical Testing, 9th ed., ASM International, USA (1985) 90-114.

ASTM E 384-89, "Standard Test Method of Microhardness of Materials", Annual Book of ASTM Standards, (1990).

Bartek, A., Ekström, T., Herbertsson, H. and Johansson, T. "Yttrium α-Sialon Ceramics by Hot Isostatic Pressing and Post-Hot Isostatic Pressing", Journal of the American Ceramic Society, **[75]** (1992), 432-39.

Beals, J.T. and Bar-on, I. "Fracture Toughness and Fatigue Crack Propagation of Silicon Nitride with Two Different Microstructures", Ceramic Engineering and Science Proceedings, **[11]** (1990), 1061-71.

Becher, P.F. "Microstructural Design of Toughened Ceramics", Journal of the American Ceramic Society, **[74]** (1991), 255-69.

Becher, P.F., Fuller, E.R. Jr., Angelini, P. "Matrix-Grain-Bridging Contributions to the Toughness of Whisker-Reinforced Ceramics", Journal of the American Ceramic Society, **[74]** (1991), 2131-35.

Becher, P.F., Hsueh, C.-H., Angelini, P. and Tiegs, T.N. "Toughening Behavior in Whisker-Reinforced Ceramic Matrix Composites", Journal of the American Ceramic Society, **[71]** (1988), 1050-61.

Becher, P.F., Hwang, S.-L. and Hsueh, C.-H. " Using Microstructure to Attack the Brittle Nature of Silicon Nitride Ceramics", MRS Bulletin, February, 1995, 23-27.

Binner, J.G.P. "Microwave Processing of Ceramics", British Ceramic Proceedings No. 45: Fabrication Technology, R.W. Davidge and D.P. Thompson, Eds. United Kingdom: The Intistute of Ceramics, 1990, 97-108.

Bonnell, D.A. "Structure of Grain Boundary Phases in Silicon Nitride", Materials Science Forum, **[47]** (1989), 132-42.

Bonnell, D.A., Ruhle, M., and Tien, T.-Y. "Redistribution of Aluminum Ions during Processing of Sialon Ceramics", Journal of the American Ceramic Society, **[69]** (1986), 623-27.

Bonnell, D.A., Tien, T.-Y. and Ruhle, M. "Controlled Crystallization of the Amorphous Phase in Silicon Nitride Ceramics", Journal of the American Ceramic Society, **[70]** (1987), 460-65.

Brenner, S.S. "Tensile Strength of Whiskers", Journal of Applied Physics, **[12]** (1957), 1484-91.

Chadwick, M. "Analytical Electron Microscopy and Creep Behaviour of Sintered Silicon Nitride" Ph.D. Thesis, McMaster University, 1990.

Cinibulk, M.K, Thomas, G. and Johnson, S.M. "Grain-Boundary-Phase Crystallization and Strength of Silicon Nitride Sintered with a YSiAlON Glass", Journal of the American Ceramic Society, **[73]** (1990), 1606-12.

Clark, D.E., Folz, D.C., Schulz, R.L., Fathi, Z. and Cozzi, A.D. "Recent Developments in the Microwave Processing of Ceramics", MRS Bulletin, November, 1993, 41-46.

Clarke, D.R. "The Microstructure of Nitrogen Ceramics", Progress in Nitrogen Ceramics. (NATO ASI series. Series E, Applied Sciences; no.65) Proceedings of the 2nd NATO Advanced Study Institute on Nitrogen Ceramics, F.L. Riley, Ed. Netherlands: Martinus Nijhoff Publishers, 1983, 341-57. (United States and Canada: Kluwer Boston Inc.)

Clarke, D.R. "On the Equilibrium Thickness of Intergranular Glass Phases in Ceramic Materials", Journal of the American Ceramic Society, **[70]** (1987), 15-22.

Clarke, D.R., and Thomas, G. "Microstructure of Y_2O_3 Fluxed Hot-Pressed Silicon Nitride", Journal of the American Ceramic Society, **[61]** (1978), 114-18.

Devlin, D.J., and Amin, K.E. "A Method for Quantitative Phase Analysis of Silicon Nitride by X-Ray Diffraction", Powder Diffraction, **[5]** (1990), 121-24.

Eitel, W. Silicate Melt Equilibria, New Jersey: Rutgers University Press, 1951.

Ekström, T, and Ingelström, N. "Characterisation and Properties of Sialon Materials", Non-Oxide Technical and Engineering Ceramics, S. Hampshire, Ed. England: Elsevier Applied Science Publishers Ltd., 1986, 231-54. (Canada: Elsevier Science Publishing Co., Inc.)

Ekström, T, and Nygren, M. "SiAlON Ceramics", Journal of the American Ceramic Society, **[75]** (1992), 259-76.

Ekström, T, and Olsson, P.-O. "β-SiAlON Ceramics Prepared at 1700°C by Hot Isostatic Pressing", Journal of the American Ceramic Society, **[72]** (1989), 1722-24.

Ekström, T, and Persson, J. "Hot Hardness Behaviour of Yttrium Sialon Ceramics", Journal of the American Ceramic Society, **[73]** (1990), 2834-28.

Freeman, S.A., Booske, J.H., Cooper, R.F., Meng, B., Kieffer, J. and Reardon, B.J. "Studies of Microwave Field Effects on Ionic Transport in Ionic Crystalline Solids", Ceramic Transactions Volume 36, Microwaves: Theory and Application in Materials Processing II, D.E. Clark, W.R. Tinga, and J.R. Laia Jr., Eds. Ohio: The American Ceramic Society, 1993, 213-20.

Gazzara, C.P., and Messier, D.R. "Determination of Phase Content of Si_3N_4 by X-Ray Diffraction Analysis", Ceramic Bulletin, **[56]** (1977), 777-80.

Gerhart, P.M., Gross, R.J. and Hochstein, J.I. Fundamentals of Fluid Mechanics, 2nd Ed. USA: Addison-Wesley Publishing Company, Inc., 1992, 13. (Ontario: Addison-Wesley Publishing Company, Inc.)

German, R.M. Liquid Phase Sintering, New York: Plenum Press, 1985.

Gnesin, G.G. and Yaroshenko, V.P. "Structure and Characteristics of Si_3N_4-Based Ceramic Cutting Tools", Key Engineering Materials, **[89-91]** (1994), 737-42.

Herdan, G. Small Particle Statistics. Great Britain: Butterworths & Co. Limited, 1960. (New York: Academic Press Inc.)

Himsolt, G. and Knoch, H. "Mechanical Properties of Hot-Pressed Silicon Nitride with Different Grain Structures", Journal of the American Ceramic Society, **[62]** (1979), 29-32.

Huang, Z.-K. and Chen, I.-W. "Rare-Earth Melilite Solid Solution and Its Phase Relations with Neighboring Phases", Journal of the American Ceramic Society, **[79]** (1996), 2091-97.

Huang, Z.-K., Liu, S.-Y., Rosenflanz, A., and Chen, I.-W. "SiAlON Composites Containing Rare-Earth Melilite and Neighboring Phases", Journal of the American Ceramic Society, **[79]** (1996), 2081-90.

Hwang, C.J.and Tien, T,-Y. "Microstructural Development in Silicon Nitride Ceramics", Materials Science Forum, **[47]** (1989), 84-109.

Jack, K.H. "Review: Sialons and related nitrogen ceramics" Journal of Materials Science, **[11]** (1976), 1135-58.

Jack, K.H. "Sialons: A Study in Materials Development", Non-Oxide Technical and Engineering Ceramics, S. Hampshire, Ed. England: Elsevier Applied Science Publishers Ltd., 1986, 1-30. (Canada: Elsevier Science Publishing Co., Inc.)

Jänecke, E. Zeitschrift für anorganische und allgemeine Chemie **[53]** (1907), 319.

Jack, K.H. "The Relationship of Phase Diagrams to Research and Development of Sialons", Phase Diagrams: Materials Science and Technolgy, A.M. Alper, Ed. New York: Academic Press, 1978, 241-85.

Janney, M.A. and Kimrey, H.D. "Microwave Sintering of Alumina at 28GHz", Ceramic Powder Science II, G.L. Messing, E.R. Fuller and H. Hausner, Eds. Ohio: The American Ceramic Society, 1988, 919-24.

Janney, M.A., Kimrey, H.D. and Kiggans, J.O. "Microwave Processing of Ceramics: Guidelines Used at the Oak Ridge National Laboratory", Materials Research Symposium Proceedings Volume 269: Microwave Processing of Materials III, Pennsylvania:Materials Research Society, 1993, 173.

Johnson, D.L. "Microwave Heating of Grain Boundaries in Ceramics", Journal of the American Ceramic Society, **[74]** (1991), 849-50.

Johnson, D.L., Skamser, D.J. and Spotz, M.S. "Temperature Gradients in Microwave Processing: Boon and Bane", Ceramic Transactions Volume 36, Microwaves: Theory and Application in Materials Processing II, D.E. Clark, W.R. Tinga, and J.R. Laia Jr., Eds. Ohio: The American Ceramic Society, 1993, 133-46.

Kang, S.-J.L. and Han, S.-M. "Grain Growth in Si_3N_4-Based Materials", MRS Bulletin, February (1995), 33-37.

Käll, P. "Quantitative Phase Analysis of Si_3N_4-based Materials", Chemica Scripta, **[28]** (1988), 439-446.

Katz, J.D., Blake, R.D. and Kenkre, V.M. "Microwave Enhanced Diffusion?", Materials Research Symposium Proceedings Volume 124: Microwave Processing of Materials I, Pennsylvania: Materials Research Society, 1988, 219.

Kleebe, H.-J., Pezzotti, G. and Ziegler, G. "Microstructure and Fracture Toughness of Si_3N_4 Ceramics: Combined Roles of Grain Morphology and Secondary Phase Chemistry", Journal of the American Ceramic Society, **[82]** (1999), 1857-67.

Krämer, M., Hoffmann, M.J., and Petzow, G. "Grain Growth Kinetics of Si_3N_4 During α/β-Transformation", Acta Metallurgica et Materialia, **[41]** (1993), 2939-47.

Kuriakose, A.K, Wheat, T.A., Llewellyn R.J. "The abrasive wear rates of certain ceramics and cermets relative their microhardess and fracture toughness", Developments & Applications of Ceramics & New Metal Alloys: Proceedings of the International Symposium on Developments and Applications of Ceramics and New Metal Alloys, R.A.L. Drew and H. Mostaghaci, Eds. Canada: Canadian Institute of Mining, Metallurgy and Petroleum, 1993, 615-23.

Lai, K.-R., and Tien, T.-Y. "Kinetics of β-Si_3N_4 Grain Growth in Si_3N_4 Ceramics Sintered under High Nitrogen Pressure", Journal of the American Ceramic Society, **[76]** (1993), 91-96.

Lange, F.F. "Fracture Toughness of Si_3N_4 as a Function of the Initial α-Phase Content", Journal of the American Ceramic Society-Discussions and Notes, **[62]** (1979), 428-30.

Lange, F.F. "Relation Between Strength, Fracture Energy and Microstructure of Hot-Pressed Si_3N_4", Journal of the American Ceramic Society, **[56]** (1973), 518-22.

Lawn, B.R. Fracture of Brittle Solids, Great Britain: Cambridge University Press, 1993, 2nd ed. Reprinted 1995.

Lee, D.-D., Kang, S.-J.L., Petzow, G., and Yoon, D.N. "Effect of α to $\beta[\beta']$ Phase Transition on the Sintering of Silicon Nitride Ceramics", Journal of the American Ceramic Society, **[73]** (1990), 767-69.

Lee, D.-D., Kang, S.-J.L., and Yoon, D.N. "Mechanism of Grain Growth and α-β' Transformation During Liquid-Phase Sintering of β'-Sialon", Journal of the American Ceramic Society, **[71]** (1988), 803-6.

Lee, S.K., Lee, K.S., and Lawn, B.R. "Effect of Starting Powder on Damage Resistance of Silicon Nitrides", Journal of the American Ceramic Society, **[81]** (1998), 2061-70.

Li, C.-W. and Yamanis, J. "Super-Tough Silicon Nitride with R-Curve Behaviour", Ceramic Engineering and Science Proceedings, **[10]** (1989), 632-45.

MacDonald, W. *MicroWear*. Personal communication with author, 1998.

McClure, F. *MicroWear*. A: Personal communication with author, 1998.

McClure, F. *MicroWear*. B: Personal communication with author, 1998.

Mendenhall, W. and Sincich, T. Statistics fo Engineering and the Sciences, USA: Dellen Pubslishing Co., 1992, 3rd ed.(Toronto: Maxwell Macmillan Canada, Inc.).

Messier, D.R.and Croft, W.J. "Silicon Nitride", Preparation and Properties of Solid State Materials, **Vol. 7**, 132-213. New York: Marcel Dekker Inc., 1982.

Messier, D.R., Riley, F.L., and Brook R.J. "The α/β silicon nitride phase transformation", Journal of Materials Sceince, **[13]** (1978), 1199-1205.

Mitomo, M., Hirotsuru, H., Suematsu, H., Nishimura, T. "Fine-Grained Silicon Nitride Ceramics Prepared from β-Powder", Journal of the American Ceramic Society, **[78]** (1995), 211-14.

Moreira da Silva, C.R., Lourenço de Melo, F.C., Moreira de Macedo Silva, O. "Mechanical Properties of Sialon", Materials Science and Engineering, **A209** (1996), 175-79.

Mott, B.W. Micro-Indentation Hardness Testing, London: Butterworths Scientific Publications, 1956, 1-14. (Toronto: Butterworth & Co. Ltd.)

Mukhopadhyay, A.K., Datta, S.K., and Chakraborty, D. "On the Microhardness of Silicon Nitride and Sialon Ceramics", Journal of the European Ceramic Society, **[6]** (1990), 303-11.

Mussler, B., Swain, M.V. and Claussen, N. "Dependence of Fracture Toughness of Alumina on Grain Size and Test Technique", Journal of the American Ceramic Society, **[65]** (1982), 566-72.

Nair, S.V. "Crack-Wake Debonding and Toughness in Fiber- or Whisker-Reinforced Brittle-Matrix Composites", Journal of the American Ceramic Society, **[73]** (1990), 2839-47.

Ordoñez, S., Iturriza, I. and Castro, F. "The influence of amount and type of additives on α→β Si_3N_4 transformation", Journal of Materials Science, **[34]** (1999), 147-53.

Pan, X., Gu, H., Werren, R. van, Danforth, S.C., Cannon. R.M., and Rühle, M. "Grain-Boundary Microstructure and Chemistry of a Hot Isostatically Pressed High-Purity Silicon Nitride", Journal of the American Ceramic Society, **[79]** (1996), 2313-20.

Patterson, M.C.L., Kimber. R.M. and Apté, P.S. "Mechanical Properties of Microwave Sintered Alumina", Proceedings of the Riso International Symposium on Metallurgy and Materials Science Structural Ceramics Processing, Microstructure and Properties Proceedings of the 11th Riso International Symposium on Metallurgy and Materials Science, Denmark: Riso National Laboratory, 1990, 167-74.

Pezzotti, G., Ota, K., and Kleebe, H.-J. "Grain-Boundary Relaxation in High–Purity Silicon Nitride", Journal of the American Ceramic Society, **[79]** (1996), 237-46.

Plucknett, K.P and Wilkinson, D.S. "Microstructural Characterisation of a Microwave Sintered Silicon Nitride Based Ceramic", Journal of Materials Research, **[10]** (1994), 1387-96.

Raj, R. "Morphology and Stability of the Glass Phase in Glass-Ceramic Systems", Journal of the American Ceramic Society, **[64]** (1981), 245-48.

Raj, R. and Lange, F.F. "Crystallization of Small Quantities of Glass (or a Liquid) Segregated in Grain Boundaries", Acta Metallurgica, **[29]** (1981), 1993-2000.

Reimanis, I.E., Suematsu, H., Petrovic, J.J., and Mitchell, T.E. "Mechanical Properties of Single-Crystal α-Si_3N_4", Journal of the American Ceramic Society, **[79]** (1996), 2065-73.

Rice, R.W., Freiman, S.W. and Becher, P.F. "Grain-Size Dependence of Fracture Energy in Ceramics: I, Experiment", Journal of the American Ceramic Society, **[64]** (1981), 345-49.

Rice, R.W. and Freiman, S.W. "Grain-Size Dependence of Fracture Energy in Ceramics: II, A Model for Noncubic Materials", Journal of the American Ceramic Society, **[64]** (1981), 350-54.

Rosenflanz, A. and Chen, I.-W. "Phase Relationships and Stability of α'-SiAlON", Journal of the American Ceramic Society, **[82]** (1999), 1025-36.

Roy, R. *MicroWear*. Personal communication with the author, 1999.

Šajgalik, P. "α/β-Phase Transformation Si_3N_4 without Sintering Additives", Journal of the European Ceramic Society, **[8]** (1991), 21-27.

Shelby, J.E., Minton, S.M., Lord, C.E. and Tuzzolo, M.R. "Formation and properties of yttrium aluminosilicate galsses", Physics and Chemistry of Glasses, **[33]** (1992), 93-98.

Shimada, M., Tanaka, A., Yamada, T. and Koizumi, M. "Densification and Phase Transformation of Si_3N_4 by High Pressure Sintering", Ceramic Powders, P. Vincenzini, Ed. Amsterdam: Elsevier Scientific Publishing Company, 1983, 871-79.

Sun, W.-Y., Tien. T.-Y., Yen, T.-S. **A:**"Solubility Limits of α'- SiAlON Solid Substitutions in the System Si, Al, Y/N, O", Journal of the American Ceramic Society, **[74]** (1991), 2547-50.

Sun, W.-Y., Tien. T.-Y., Yen, T.-S. **B:**"Subsolidus Phase Relationships in Part of the System Si, Al, Y/N,O: The System Si_3N_4-AlN-YN-Al_2O_3-Y_2O_3", Journal of the American Ceramic Society, **[74]** (1991), 2753-58.

Sutton, W.H. "Key Issues in Microwave Processing Technology", Ceramic Transactions Volume 36, Microwaves: Theory and Application in Materials Processing II, D.E. Clark, W.R. Tinga, and J.R. Laia Jr., Eds. Ohio: The American Ceramic Society, 1993, 3-18.

Sutton, W.H. "Microwave Processing of Ceramic Materials", Ceramic Bulletin, **[68]** (1989), 376-86.

Sutton, W.H. "Microwave Processing of Materials", MRS Bulletin, November, 1993, 22-24.

Tabor, D. The Hardness of Metals, London: Oxford University Press, 1951.

Tabor, D. "Indentation Hardness and Its Measurement: Some Cautionary Comments", Microindentation Techniques in Materials Science and Engineering, ASMT STP 889, P.J. Blau and B.R. Lawn, Eds. Philadelphia: American Society for Testing and Materials, 1986, 129-159.

Terwilliger, G.R. and Lange F.F. "Pressureless sintering of Si_3N_4", Journal of Materials Science, **[10]** (1975), 1169-1174.

Tiegs, T.N., Kiggans, J.O. and Menchhofer, P.A. "Microwave Sintered Silicon Nitride Ceramics", Proceedings of the European Ceramic Society Second Conference, 1991.

Tiegs, T.N., Kiggans, J.O. and Ploetz, K.L. "Sintered Reaction-Bonded Silicon Nitride by Microwave Heating", Materials Research Symposium Proceedings volume 287: Silicon Nitride Ceramics: Scientific and Technological Advances, I.-W. Chen, P.F. Becher, M. Mitomo, G. Petzow and T.-S. Yen, Eds. Pennsylvania: Materials Research Society, 1993, 277.

Tinga, W.R. "Fundamentals of Microwave-Material Interactions and Sintering", Materials Research Symposium Proceedings Volume 124: Microwave Processing of Materials, W.H. Sutton, M.H. Brooks and I.J. Chabinsky, Eds. USA: Materials Research Society, 1988, 33-43.

Tinga, W.R. "Microwave Material Interactions and Process Design Modeling", Ceramic Transactions Volume 36, Microwaves: Theory and Application in Materials Processing II, D.E. Clark, W.R. Tinga, and J.R. Laia Jr., Eds. Ohio: The American Ceramic Society, 1993, 29-43.

Tsuge, A, Kudo, H. and Komeya, K. "Reaction of Si_3N_4 and Y_2O_3 in Hot-Pressing", Journal of the American Ceramic Society-Discussions and Notes, **[57]** (1974), 269-70.

Ukyo, Y. and Suda, A. "Effect of a Small Amount of SiO_2 on the Reaction during Sintering in the Si_3N_4-Y_2O_3-AlN System", Journal of the Ceramic Society of Japan, **[104]** (1996), 371-76.

Varadan, V.K., Ma, Y., Lakhtakia, A. and Varadan, V.V. "Microwave Sintering of Ceramics", Materials Research Symposium Proceedings Volume 124: Microwave Processing of Materials, W.H. Sutton, M.H. Brooks and I.J. Chabinsky, Eds. USA: Materials Research Society, 1988, 45-57.

Walls, P.A., and Ueki, M. "Preferential Reactive Plasma Etching of Sialon Ceramics", Submitted to the Journal of the American Ceramic Society.

Wills, R.R., Cunningham, J.A., Wimmer, J.M. and Stewart, R.W. "Stability of the Silicon Yttrium Oxynitrides", Journal of the American Ceramic Society-Discussions and Notes, **[59]** (1976), 269-70.

Wood, C.A., Zhao, H. and Cheng, Y.-B. "Microstructural Development of Calcium α-SiAlON Ceramics with Elongated Grains", Journal of the American Ceramic Society, **[82]** (1999), 421-28.

Wötting, G and Ziegler, G. "Influence of Powder Properties and Processing Conditions on Microstructure and Properties of Sintered Si_3N_4", Ceramic Powders, P. Vincenzini, Ed. Amsterdam: Elsevier Scientific Publishing Company, 1983, 951-62.

Wötting, G and Ziegler, G. "Powder Characteristics and Sintering Behaviour of Si_3N_4-Powders", Powder Metallurgy International, **[18]** (1986), 25-32.

Ziegler, G., Heinrich, J. and Wötting, G. "Review: Relationships between processing, microstructure and properties of dense and reaction-bonded silicon nitride", Journal of Materials Science, **[22]** (1987), 3041-3086.